Artificial and Natural Disturbances in the Equatorial Ionosphere: Results from the MOSC Experiment and the C/NOFS satellite mission

Author: Dev Raj Joshi

Boston College Electronic Thesis or Dissertation, 2019

Artificial and Natural Disturbances in the Equatorial Ionosphere: Results from the MOSC Experiment and the C/NOFS satellite mission

Dev Raj Joshi

A dissertation

submitted to the Faculty of

the department of Physics

in partial fulfillment

of the requirements for the degree of

Doctor of Philosophy

Boston College
Morrissey College of Arts and Sciences
Graduate School

February 2019

Recommended Citation
Joshi, Dev Raj (2019), *Artificial and Natural Disturbances in the Equatorial Ionosphere: Results from the MOSC Experiment and the C/NOFS satellite mission,* Ph.D. Dissertation, Boston College, United States.

Artificial and Natural Disturbances in the Equatorial Ionosphere: Results from the MOSC Experiment and the C/NOFS satellite mission

Dev Raj Joshi

Advisors: Professor Michael Naughton and Dr. Keith Groves

Committee Members: Professor Pradip Bakshi

Professor Krzysztof Kempa

Dr. Charles Carrano

ABSTRACT: The low-latitude ionosphere is characterized by large-scale instabilities in the post-sunset hours due to the distinct geometry of the earth's magnetic field lines at the equator. The magnetic field lines are horizontal at the equator contributing to the high vertical drift velocity of the plasma bubbles growing from the bottomside of the ionospheric F-region. The phenomenon, commonly known as equatorial spread F, is an important problem in aeronomy as it can cause radio wave scintillation effects representing the most critical impacts of space weather on man-made technologies, such as satellite communications and global navigation satellite systems (GNSS). Here, we present results from an artificial ionospheric modification experiment as well as from naturally occurring instabilities in the equatorial ionosphere. An artificial plasma cloud was created in the bottomside of the ionospheric F-layer during the Metal Oxide Space Cloud (MOSC) experiment in May 2013 to study the interactions of artificial ionization with the background plasma under the hypothesis that the artificial plasma might

suppress the occurrence of natural instabilities. While the suppression hypothesis remains open to debate, the propagation results confirm that the injection of artificial ionization in the lower F–region causes dramatic changes to the ambient HF propagation environment. We also calculate various parameters needed to evaluate the growth rate of Rayleigh-Taylor instability created in the F-region bottomside of the ionosphere from the thirteen days of High-Frequency (HF) radar data during the MOSC campaign. These parameters have been used to calculate the growth rate to predict the diurnal variability of the spread F occurrence. The growth rate has also been calculated from model ionospheric profiles optimized by ray-tracing techniques to match actual delays as observed in the oblique HF links. The calculated growth rate provides a close prediction of spread F development as seen in its correlation with the ground scintillation observations. With regard to natural processes, data from the Air Force Research Laboratory (AFRL) / the National Aeronautics and Space Administration (NASA) Communications/Navigations Outage Forecasting System (C/NOFS) satellite mission has been analyzed to investigate the characteristics of equatorial ionospheric irregularities from in situ observations. We present a comprehensive investigation on the variation of apex-altitude distribution of equatorial ionospheric irregularities with solar activity supported by modeling, simulation and comparisons with ground- and space-based in situ density observations. We also analyze Physics Based Model (PBMOD) ionospheric model results to determine if a physics-based model can reproduce the observed dependence of bubble height on solar activity.

TABLE OF CONTENTS

Acknowledgements

First and foremost, I would like to thank my thesis advisor Dr. Keith Groves for his continuous support and guidance to pursue the investigation presented in this work. His insightful discussions and vast experience in the field contributed immensely to my understanding of the research questions pursued in this dissertation. His unwavering support at all steps through my graduate research work contributed immensely to the completion of this delightful journey. I would also like to thank my committee members – Professor Michael Naughton, Professor Pradip Bakshi and Dr. Charles Carrano – for their time, support and motivation to pursue this research work. I would like to thank Professor Michael Naughton for his continuous motivation throughout my graduate studies to ensure timely accomplishment of the Ph.D. goals.

I would also like to thank Patricia Doherty, Director, Institute for Scientific Research (ISR) for the opportunity to pursue research at the Institute. The support at the Institute has been generous and resourceful which enabled me to focus on my work without any constraint. I am also indebted to senior colleagues at ISR – Dr. Rezy Pradipta, Dr. Kathleen Kraemer, Dr. Endawoke Yizengaw, Dr. Vadym Paznukhov – for the opportunity to discuss scientific ideas throughout my work and also during the completion of this dissertation. I also thank my colleagues in the Department of Physics and the Institute for Scientific Research for the opportunity to grow with them during my graduate studies. I specially would like to thank Dr. Binod Rizal and Dr. Sovit Khadka for helping me at many instances.

I finally dedicate my Ph.D. to my family. It is their support and belief in me which helped me to complete my graduate studies.

List of Figures

Chapter 1

Chapter 2

Chapter 3

Chapter 4

Chapter 5

List of Tables

Chapter 2

Chapter 3

Chapter 4

Chapter 5

CHAPTER 1 INTRODUCTION

1.1 Introduction:

This dissertation is aimed at studying irregularities in the equatorial ionosphere with the aid of the data from the Metal-Oxide Space Cloud (MOSC) experiment and the Communications/Navigation Outage Forecasting System (C/NOFS) mission. We analyze data from the Metal Oxide Space Cloud (MOSC) experiment conducted in May 2013 to study the interaction of artifical ionization with the background ionospheric plasma and its effects on the High-Frequency (HF) radio wave propagation. The C/NOFS mission data has been analyzed to understand the effects of the solar activity on the occurrence of the equatorial plasma irregularities in the background ionosphere. We also seek to investigate the apex-altitude distribution of the equatorial plasma irregularities as a function of the solar activity.

The existence of an ionized region in the earth's upper atmosphere was first speculated in 1839 by Carl Gauss as he hypothesized the existence of electric currents in the atmosphere to explain the observed variations of the geomagnetic field at the surface of the earth [1]. In 1901, G. Marconi transmitted radio wave signals across the Atlantic and in 1902, A. E. Kennelly and O. Heaviside suggested the transmission could be possible due to the reflection of the waves by free electric charges in the upper atmosphere. It is O. Lodge who, in a letter [2] to the editors in the *Nature* journal, gave the first physical explanation of the existence of free electric charges in the upper atmosphere as due to the influence of ultra-violet solar radiation. The term 'ionosphere' itself was coined by Robert Watson-Watt in 1926 [3]. Since these early discoveries of the ionosphere, it has been extensively explored as a wall-less natural plasma laboratory in scientific research leading to significant enhanced understanding of the complex physical processes involved in the ionosphere. The region has been an active area of research ever since the discovery of diffuse echoes from the F-region of the ionosphere by Booker and Wells [4] despite which many phenomena in the region continue to remain enigmatic and scientifically challenging. While the early phase of research mainly focused in the morphological description and statistical characterization of the phenomenon [5], the advance in diagnostics tools and analytical technology [6, 7, 8, 9, 10, 11] has led to newer insights in the complex physical processes undergoing in the region. This has also opened newer avenues to investigate the science questions pertaining to the dynamics of the disturbances in the region.

The equatorial ionosphere is a region of great interest as many spectacular and complex physical phenomena occur there. The region is characterized by large-scale instabilities in the post-sunset hours due to the distinct geometry of the earth's magnetic field lines at the equator. The magnetic field lines are horizontal at the equator contributing to the high vertical drift velocity of the plasma bubbles growing from the bottomside of the ionospheric F-region. The phenomenon, commonly known as equatorial spread F, is an important problem in aeronomy as it can cause radio wave scintillation effects representing the most critical impacts of space weather on man-made technologies, such as satellite communications and global navigation satellite systems (GNSS).

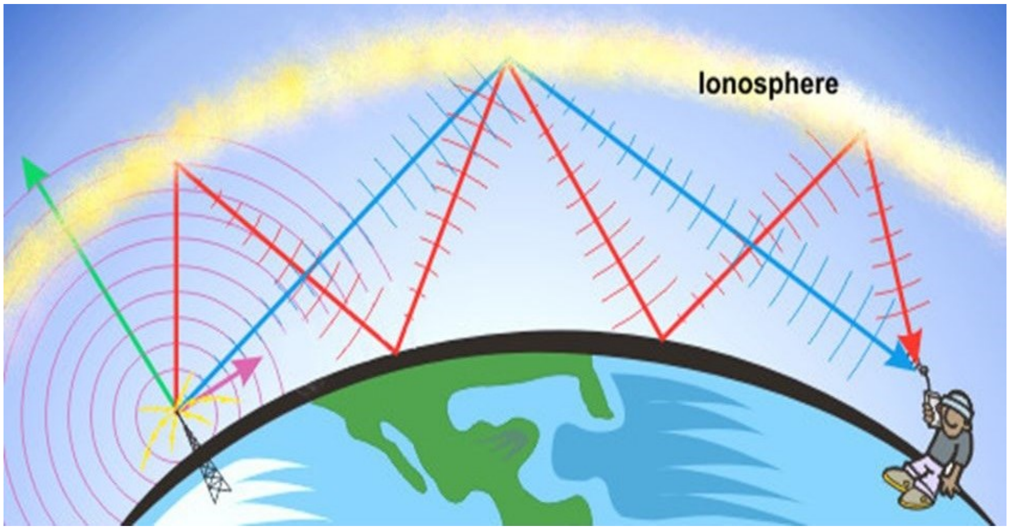

Figure 1.1: Illustration of radio wave reflection from the ionosphere. Marconi transmitted radio wave signal across the Atlantic in 1901 and the following year, it was suggested a conducting layer of electrons could have reflected the waves.

Overview of this work

In this thesis, it is our hope to exploit the equatorial ionospheric natural plasma laboratory – to understand the interaction of artificial ionization with the background ionosphere in an artificial modification experiment and to investigate the characteristics of the naturally occurring irregularities in the background ionosphere using in-situ observations from satellite. While studying the interaction of the artificial ionization with the background ionosphere, we focus on understanding the high frequency propagation effects caused by an artificial plasma cloud created at the bottomside of the F-region. While studying the irregularities in the background ionosphere in the equatorial region, we seek to understand how solar activity influences the rise of the ionospheric irregularities at the magnetic equator. The study of both artificial ionization and natural irregularities has important practical implications. In the former, modifications to the HF wave propagation environment have a dramatic impact on HF communications over the horizon radar performance while the latter phenomenon can determine the limits of satellite communication and GNSS navigation accuracy at low latitudes.

In chapter 2, we present an overview of the ionosphere. We discuss some of the basic topics in the ionospheric physics. We also briefly discuss artificial modification experiments. We then present the theoretical treatment of the radio wave propagation through an ionized layer of the upper atmosphere.

In Chapter 3, we present the High Frequency propagation results from the Metal Oxide Space Cloud (Experiment). In the experiment, the Air Force Research Laboratory (AFRL) launched two sounding rockets in the Kwajalein Atoll, Marshall Islands in May

2013 with support from the National Aeronautics and Space Administration (NASA). We analyze data from ALTAIR incoherent scatter radar and high frequency (HF) radio links to understand the impacts of the artificial ionization on the radio wave propagation. We also present a brief theoretical overview of ray-tracing which has been applied to model the HF propagation through the ionosphere. We then present the modeling results done with the aid of the HF radio wave ray-tracing toolbox PHaRLAP along with ionospheric models.

In Chapter 4, we present the calculation of the various parameters in the growth rate of the Rayleigh-Taylor Instability from thirteen days of High-Frequency (HF) radar data during the Metal-Oxide Space Cloud (MOSC) campaign. We calculate the growth rate as well. The parameters and the growth rate are also calculated from model ionospheric profiles optimized to match time-delays in corresponding HF observations. We then make comparisons of the calculated growth rate with the ground based scintillation observations.

In Chapter 5, we present an investigation on the apex-altitude distribution of equatorial plasma bubbles as a function of solar activity. We analyze data from the Communications/Navigations Outage Forecasting System (C/NOFS) satellite mission to understand the effects of the solar activity on the occurrence of the equatorial plasma irregularities. We also analyze results from the Physics Based Model (PBMOD) ionospheric model to determine if a physics-based model can reproduce the observed dependence of bubble height on solar flux.

In the final Chapter 6, we review the important results of this dissertation work. We present our conclusions and make suggestions for possible future work based on this dissertation.

References:

[1] Schunk, R. W., and Nagy, A. F. (2000), Ionospheres: Physics, Plasma Physics, and Chemistry, New York, NY, Cambridge University Press.

[2] Lodge, O. (1902), Mr. Marconi's results in day and night wireless telegraphy, Nature, 66, 222, doi:10.1038/066222c0.

[3] Rishbeth H. (2002), High above the Earth, Nature, 418:23, doi: 10.1038/418023a.

[4] Booker, H. G., and H. W. Wells (1938), Scattering of radio waves by the *F*-region of the ionosphere, Terr. Magn. Atmos. Electr., 43(3), 249–256, doi: 10.1029/TE043i003p00249.

[5] Rao P B & Patra A K, Recent Advances on equatorial spread-F, *Proc Indian Natl Sci Acad A (India),* 64 (1998) 365.

[6] Farley, D. T., and D. L. Hysell (1996), Radar measurements of very small aspect angles in the equatorial ionosphere, J. Geophys. Res., 101(A3), 5177–5184, doi: 10.1029/95JA02640.

[7] Woodman, R. F., and C. La Hoz (1976), Radar observations of *F* region equatorial irregularities, J. Geophys. Res., 81(31), 5447–5466, doi: 10.1029/JA081i031p05447.

[8] Hysell, D. L., M. C. Kelley, W. E. Swartz, and R. F. Woodman (1990), Seeding and layering of equatorial spread *F* by gravity waves, J. Geophys. Res., 95(A10), 17253–17260, doi: 10.1029/JA095iA10p17253.

[9] Sultan, P. J. (1996), Linear theory and modeling of the Rayleigh-Taylor instability leading to the occurrence of equatorial spread *F*, J. Geophys. Res., 101(A12), 26875–26891, doi: 10.1029/96JA00682.

[10] Hysell, D. L., R. Jafari, M. A. Milla, and J. W. Meriwether (2014), Data-driven numerical simulations of equatorial spread *F* in the Peruvian sector, J. Geophys. Res. Space Physics, 119, 3815–3827, doi: 10.1002/2014JA019889.

[11] Woodman, R. F. (2009), Spread F – An old equatorial aeronomy problem finally resolved? Ann. Geophys., 27, 1915-1934.

CHAPTER 2 BACKGROUND

In this chapter, we review the theoretical background of the topics relevant to this dissertation. We start with the introduction of the Ionosphere, its structure, formation, composition and the variance in its profiles. We then discuss about the artificial modification experiments which make the prelude to the Metal-Oxide Space Cloud (MOSC) experiment. We then briefly review the theory of radio wave propagation through the ionospheric layers.

2.1 The Ionosphere

The ionosphere can be defined as the region of the upper atmosphere which contains significant numbers of free electrons and ions to affect the propagation of radio waves. While the atmospheric structure can be organized based on the temperature profile, the ionosphere is instead better organized based on the plasma density profile (Fig. 2.1) [1].

Since the ionosphere is within the neutral atmosphere, the neutral atmosphere plays an important role in the formation, dynamics, and energetics of the ionosphere [2], and therefore, it is essential to gain, at least, an introductory knowledge of the neutral atmosphere before seeking to delve deeper into the ionosphere. The temperature profile of the neutral atmosphere is primarily determined by the chemical composition of the atmosphere and radiation absorption coming from the sun. The temperature decreases with altitude in the lowest region of the atmosphere called as troposphere which contains 80% of the total mass of the atmosphere. It extends upto the tropopause (12-15 km) from the earth's surface and is the region associated with atmospheric weather. The region is heated due to the radiation from the surface of the earth. As the radiation is emitted radially, its intensity, and hence the temperature, decreases farther from the earth's surface. The trend reverses at the tropopause - the boundary between the troposphere and the stratosphere. The rise in temperature is due to absorption of the ultraviolet portion of the solar radiation by the ozone layer contained in the stratosphere. The stratosphere extends upto 45-50 km. Radiative cooling [3] again causes a decrease in temperature in the mesosphere which extends upto mesopause at 85-95 km. The mesopause, the upper boundary of the mesosphere, is the coldest region in the atmosphere with the temperature falling as low as 180 K. Above the mesopause is the region called as thermosphere in which the temperature first increases with altitude to values well above 1000 K and then remains constant with altitude. The temperature increase in the thermosphere is due to the absorption of the solar ultraviolet spectrum. The photo-dissociation of the molecular neutrals such as N_2 and O_2 produces atomic neutrals N and O in the thermosphere which causes the heavy molecular constituents dominate at low-altitudes and the atomic neutrals dominate at high altitudes of the atmosphere. Above 500 km, the atmosphere is called as exosphere where the neutrals behave like individual particles as collisions become unimportant due to low neutral densities. The lower boundary of the exosphere is called as exobase. The neutral densities in the exosphere become so low that the atmosphere can no longer be treated as a fluid. The exosphere is the transitional region between the Earth's atmosphere and the interplanetary space.

The neutral atmosphere, briefly described in the preceding paragraphs, is ionized to a maximum level of 1% primarily due to the solar radiation. The vertical-layering or stratification of the ionosphere is due to the combination of decreasing intensity of the solar radiation and increasing neutral density as one moves to lower altitudes into the ionosphere (Fig. 2.2) which causes the competing effects of different ionization production and loss processes at different altitudes. Figure 2.2 shows the various bands in the electromagnetic spectrum of the solar radiation penetrating the various altitudes leading to the creation of different layers in the ionosphere. But as we see in Fig 2.1, the existence of these layers varies depending upon the presence or the absence of sunlight in day and night. The plasma density of the ionospheric layers also varies according to the change in solar flux through a solar cycle as seen in Fig 2.1. The neutral approximation or quasi-neutrality which requires the number of ion density equal the number of electron density in any ionized gas is valid in the ionosphere. Hence, the electron density can be interchangeably called as the ion density or the plasma density. The F-region is the layer with maximum plasma density. The region extends from 150 km to the upper boundary of the bottom-side ionosphere at ~500 km. The ionization in the region is due to the extreme ultraviolet (UV, 10 - 100 nm) radiation ionizing atomic oxygen. The dominant ions in the region are O+ corresponding to the high concentration of atomic oxygen in the neutral gas. The O+ ions are also converted to NO+ by molecular nitrogen. Since the region has the maximum plasma density, it acts as the reflecting layer to the radio waves. Radio waves transmitted from the earth's surface but not reflected by the F region escape into the space penetrating the region. The region is divided into two F1 and F2 layers during the day. The F1 layer disappears during the night because of recombination of the NO^+ ions with the electrons whereas the F2 layer persists throughout the night since the small supply of N2 leads to slow conversion of O^+ to NO^+ and hence only a small reduction in the number of electrons. The layer is simply called as F-region during the night. The F1 layer extends from 150 to 200 km whereas the F2 layer extends from 200

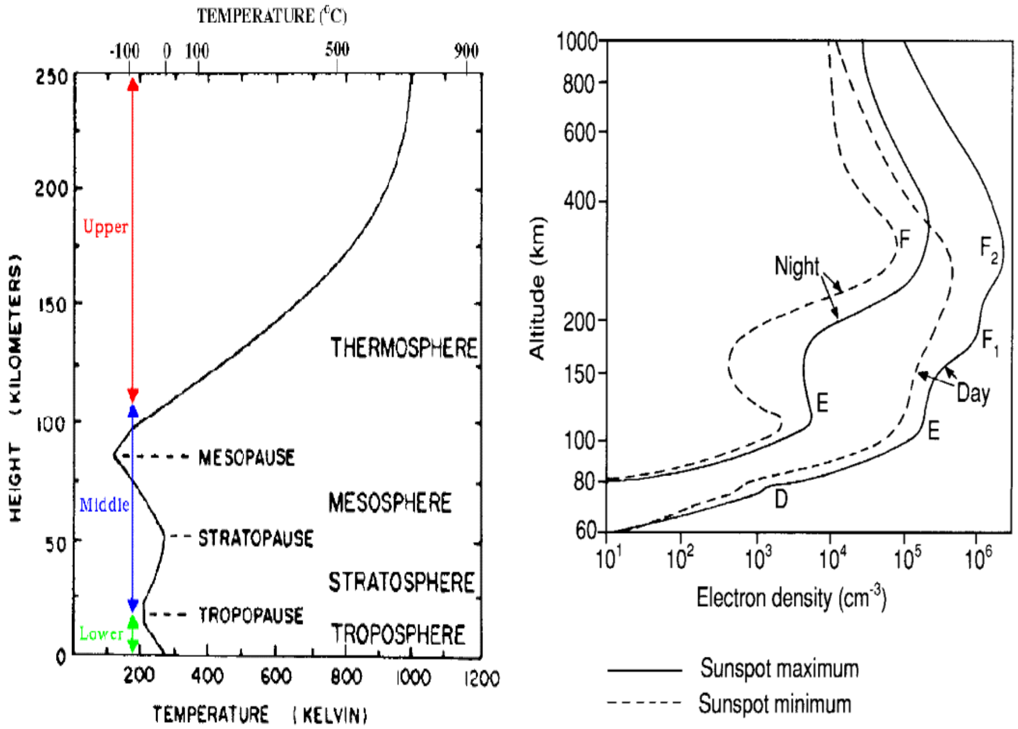

Figure 2.1: Profile of atmospheric temperature (left). Profile of ionospheric plasma density during day and night with various layers of the ionosphere (right).

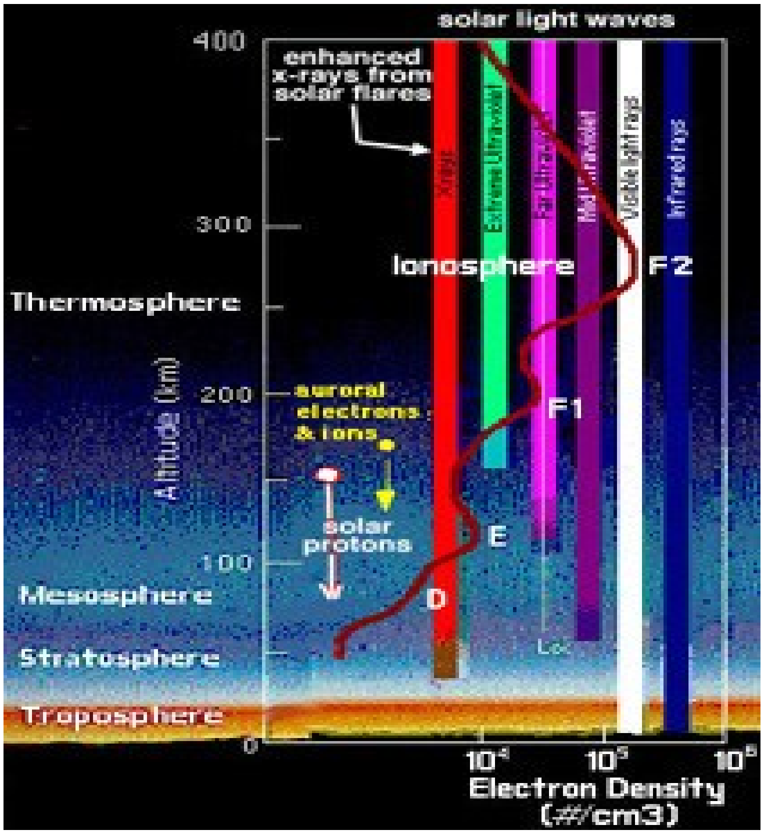

Figure 2.2: The intensity of the solar radiation and the chemical composition of the neutral density cause the stratification of laug5ayers in the ionosphere.

km to 500 km. Below the F-region, the altitude range 90 -150 km is called as the E-region. The ionization in the region is due to the soft X-ray (1-10 nm) and the extreme ultraviolent solar radiation (90-103 nm) ionizing the molecular oxygen (O_2) and also the meteoric vapors which exist in the region. The electrons recombine with the molecular ions (O_2^+ and NO^+) during the night. But the layer persists throughout the night although with diminished plasma density due to the slower recombination and presence of metallic ions such as Na^+ (Sodium) and Fe^+ (Iron). Electrons recombine with the atomic ions (Na^+ or O^+) very inefficiently. There can also be distinct region of enhanced electron densities called as sporadic-E region in the altitudes corresponding to E-region. As the name suggests, these regions are sporadic and can be caused by meteors, electrical storms, auroral activity and upper atmospheric winds. Below the E-region, the D-region exists in the altitude range of 60-90 km. The ionization in the D-region is due to the Lyman–α solar radiation ionizing the nitric oxide (NO) and also due to the solar X-rays (< 20nm) ionizing nitrogen (N_2) and oxygen (O_2) molecules. The molecular ions also react with water vapor to produce water cluster ions. The layer disappears at night as the production ceases and electrons undergo rapid recombination and attachment.

The comparison of night-time and day-time profiles in Fig. 2.1 reveals that the plasma density near F-peak decreases less rapidly than the density at the lower altitudes. The ion and the neutral compositions in the atmosphere (Fig. 2.3) provide a clue to the reason for the difference which is the molecular ions dominating the lower altitudes have a much higher recombination rate than the atomic ions dominating the higher altitudes. For example,

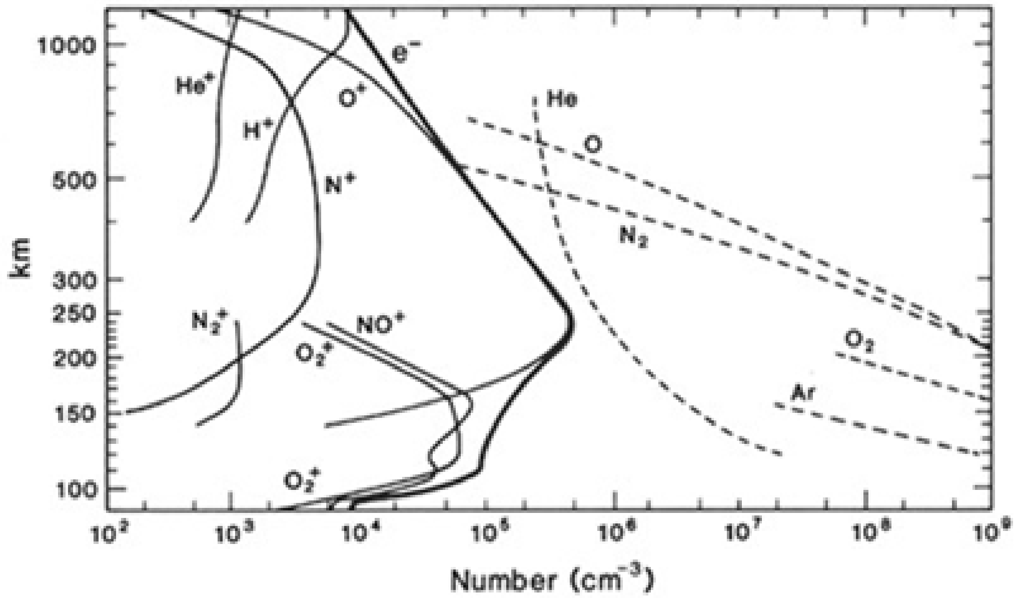

Figure 2.3: Ions and Neutral compositions in the atmosphere. The composition explains why the F-peak decreases less rapidly than the densities at lower altitudes.

$$NO^{+} + e^{-} \rightarrow N + O$$

and

$$O^{+} + e^{-} \rightarrow O + h\nu \text{ (photon)}$$

The former process in the above illustrations is called as dissociative recombination whereas the latter is called radiative recombination since photon-emission takes place to conserve energy and momentum in the process. The dissociative recombination reaction rate is nearly 1000 times higher than that of the radiative recombination which is why, after night when the ion production is reduced, rapid recombination quickly reduces the plasma concentration at lower altitudes whereas O^{+} ions at higher altitudes survives the night at concentrations between 10^4 and 10^5 cm^{-3}.

Table 2.1: Ionospheric Constituents

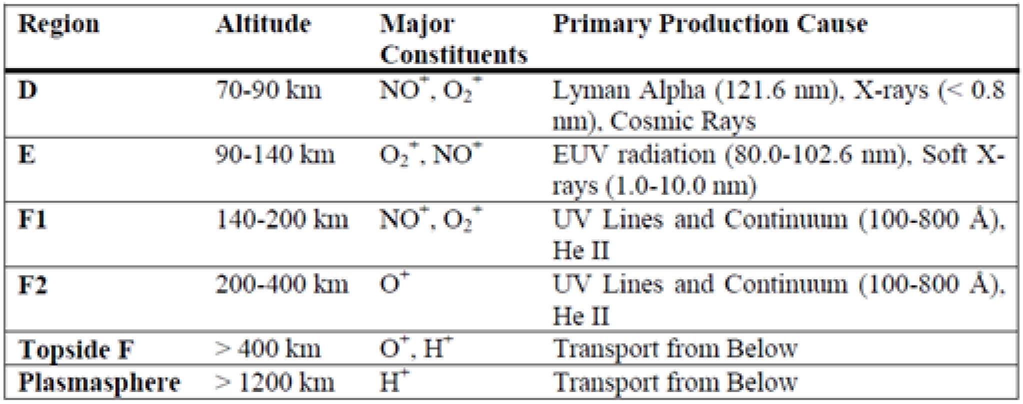

Region	Altitude	Major Constituents	Primary Production Cause
D	70-90 km	NO^{+}, O_2^{+}	Lyman Alpha (121.6 nm), X-rays (< 0.8 nm), Cosmic Rays
E	90-140 km	O_2^{+}, NO^{+}	EUV radiation (80.0-102.6 nm), Soft X-rays (1.0-10.0 nm)
F1	140-200 km	NO^{+}, O_2^{+}	UV Lines and Continuum (100-800 Å), He II
F2	200-400 km	O^{+}	UV Lines and Continuum (100-800 Å), He II
Topside F	> 400 km	O^{+}, H^{+}	Transport from Below
Plasmasphere	> 1200 km	H^{+}	Transport from Below

The ionosphere is thus a ‘battleground between the earth’s neutral atmosphere and the sun’s fully ionized atmosphere in which the earth is embedded’. [1] Towards its upper end, the ionosphere is coupled to the magnetosphere through more exotic phenomena such as the current inflow into the ionosphere and the plasma outflow from the ionosphere. We do not intend to treat these vast and important topics in this dissertation.

2.2 Artificial Ionospheric Modification

“ To explore the upper atmosphere man first used kites, then ballons, then aircraft.”

– Homer E. Newell

In an NASA Sounding Rocket Historical Summary Report (1958 -1968), William R. Corliss [4] lists the disadvantages of sounding rockets in scientific campaigns as restricted time of observation, localized coverage, payload limitations and lack of glamour. But in the NASA Sounding Rockets Annual Report 2017 [5], Philip Eberspeaker states the Sounding Rockets Program’s ‘mobile capability, coupled with the unique ability to collect in-situ measurements at specific altitudes of interest, continues to make the program an important element of NASA’s research activities’. Before enumerating the disadvantages,Corliss also mentions the advantages of sounding rockets as simplicity, informality, low cost, recoverability, geographic and temporal flexibility. With Eberspeaker’s statement, we observe that the advantages of sounding rockets have far outweighed their few disadvantanges and they continue to remain in the forefront of space research, more often than not, being the ‘only’ means to achieve certain scientific objectives. The idea that rockets could be used for upper atmosphere research was first proposed by Robert H. Goddard [6]. It is but scientific inquisitiveness to seek to go beyond the observation of nature and try to reproduce the observations in controlled environment. Termed as active experiment or controlled experiment or artificial ionospheric modification, the first chemical release into the high atmosphere from a sounding rocket was done in 1955 [7]. It involved the release of sodium vapor from rocket-borne multiple cannisters igniting the vapor initated by internal timing mechanisms forming a sodium vapor cloud [8].

James C. G. Walker [9] has surveyed four techniques of active experimentation with Ionospheric Plasma. The four techniques are: i) the modification of ionospheric electron densities by the release of reactive gases or clouds of plasma, ii) using charged particles to modify ionospheric properties creating artificial auroras, and to investigate beam-plasma interactions, iii) using Very Low Frequency (VLF) radiation to stimulate instabilities in the magnetospheric plasma that generate hydromagnetic emissions and cause particle precipitation, and iv) using ground based transmitters at High Frequency (HF) or higher frequencies to modify ionospheric propoerties and to generate instabilities in the ionospheric plasma. The fourth technique is commonly called as heating experiment and a number of HF heating facilities exist around the world. The Metal Oxide Space Cloud (MOSC) experiment in which two sounding rockets were launched by Air Force Research Laboratory (AFRL) with support from the NASA Sounding Rocket Program is the first of the techniques described by Walker in his paper. The rockets were launched to artificially modify the ambient environment in the bottomside of F-region of the ionosphere for the purpose of tailoring the radio-wave propagation environment. Since the early days of 'active experiments' involving sounding rockets, numerous chemical release experiments have been conducted using suborbital rockets and orbital platforms. *Caton et al.*[10], in their paper,while providing an overview of the MOSC experiment list many of these experiments inolving the release of Barium in the upper atmosphere. While Barium is the most commonly released chemical, but sodium, strontium, lithium,europium,calcium,and several others have also been used [11] to study global neutral winds, electric field strengths, auroral physics, critical ionization velocity, magnetosphere and magnetotail phenomena,cross-field skidding, cometary physics,ionospheric instabilities,magnetic field tracing and many other applications. There is an extensive literature in the field reviewing these works [12, 13, 14, 15]. Releases are normally done at the dusk time because the chemicals require solar photons or particle collisions for ionization. The effects of the ionospheric modification chemicals can be two ways: plasma enhancement or plasma depletion. Plasma enhancement chemicals add up to the pre-exisiting ions in the ambient enovironment whereas the plasma depletion chemicals deplete the pre-exisiting plasma density [16]. It is also desirable to seek to modify the ambient environment in the atmosphere after the sunset in complete absence of sunlight, for example, to understand phenomena which occur in the post-sunset hours. The solution is to use chemi-ionizing elements instead of the photo-ionizing elements as has been mostly used in past active experiments. Lathanides are the strong candidates for the modification experiments requiring chemi-ionizing elements. Researchers at the U.S. Air Force Research Laboratory (AFRL) worked with the lanthanide series of metals to examine the materials with exothermic chemi-ionization reactions which chould potentially create long-lived artificially generated plasma clouds.

$$\mathrm{LM} + \mathrm{O} \rightarrow \mathrm{LMO}^{+} + e^{-} \quad \text{; LM indicates a lathanide metal.}$$

Samarium among the lanthanides was chosen due to its achievable vaporization temperature when mixed with an intermetallic heat source. Canister payloads packed with a titanium/boron mixture (TiB) and powdered samarium (Sm) consisting of a ~30% mixture of Sm by volume were developed to be used in the MOSC experiment. The

MOSC experiment would provide an opportunity for the first comprehensive diagnosis of an artificially plasma cloud generated by the release of Sm vapor in the ionosphere. The primary objective of the experiment was to examine the extent to which the radio frequency propagation environment can be tailored through artificial ionospheric modification. The second objective, somewhat more ambitious, was to potentially seek to suppress ionospheric irregularities caused by the Rayleigh-Taylor instability in the nighttime equatorial ionosphere. The site selection for the experiment was motivated by the low-latitude geometry and also the availability of a Scatter Radar facility - ALTAIR radar - in the region capable of tracking the artificial plasma clouds.

The Advanced Research Projects Agency (ARPA) Long-Range Tracking and Instrumentation Radar (ALTAIR) was developed and built at Roi-Namur in the Reagan Test Site between 1968 and 1970 [17]. ALTAIR (Fig. 2.4) is highly-sensitive dual-frequency radar designed specifically to study the physical interactions between a ballistic missile in flight and its natural environment [18]. It supports several operating modes, including tracking and signature collection at VHF and UHF. The target resolution in VHF is 37 meters and in UHF, it is 15 meters. Its antenna is 150 foot (45.7 m) diameter paraboloid, which produce a beamwidth of 1.1^{o} at UHF and 2.8^{o} at VHF. The antenna can rotate at an angular rate of 10 degrees/second. The ARPA itself was formed in early 1958 by the Department of Defense in reaction to the successive news from USSR of developing Inter-Continental Ballistic Missile (ICBM) and launch of Sputnik I, the first artificial satellite. The ARPA had broad jurisdiction of research and development of space projects and anti-missile systems [19, 20]. It was *Gordon* [21] who suggested that a powerful radar can detect the incoherent backscatter from the free electrons in and above the earth's ionosphere. Because the incoherent scatter radar (ISR) employs radar signal well above the maximum plasma frequency of the ionosphere, the problem of reflection only from the bottomside of the ionosphere encountered by the ionosondes are circumvented with ISR [1]. It gives us the full – topside which is the region above the F-region peak and bottomside which is the region below the F-region peak – profile of the ionosphere. We provide references for the theoretical treatment [22, 23] of the incoherent scattering. When amplitude of fluctuations of plasma instabilities grows much greater than the thermal level in ionosphere, it can lead to coherent scattering of the incident waves from the radar. The fluctuations can contribute to the constructive interference amongst the scattered signals from the ionosphere and hence, a reception of strong signals by the radar is possible. ALTAIR is capable of performing both coherent and incoherent scatter observations of the ionosphere. We have used ALTAIR radar profiles in our MOSC related work in Chapter 3 to model the artificial plasma cloud and the background ionospheres the clouds evolved in.

The high-frequency radars are the reflectometry instruments which have continued to remain the mainstay of ionospheric research since the days of discovery of diffuse echoes (spread F) by these instruments. We briefly recapitulate the idea of radio refractive index of the ionosphere in the next section of this chapter which gives us the working principle of the HF radars, commonly called as, ionosondes. A longer discussion on the diagnostics involved in the MOSC experiment along with other aspects of the campaign is detailed in the paper by *Caton et al.* [10].

Advanced Research Project Agency (ARPA) Long-range Tracking and Identification Radar (ALTAIR)

- Dual Frequency:150 MHz/422 MHz
- Max Bandwidth: 7 MHz/18 MHz
- Steerable 46 m dish
- Beamwidth 1.1° UHF and 2.8° VHF
- Peak Power
  VHF: 6.0 MW
  UHF: 6.4 MW
- Pulse-repetition frequency 300 Hz

Figure 2.4: The ARPA Long-range Tracking and Instrumentation Radar (ALTAIR) in the Marshall Islands and its operating characteristics

2.3 Radio Waves in the Ionosphere

We seek to understand and model the effects caused by the artificial plasma cloud on High Frequency (HF) radio wave propagation evironment. In Chapter 3, we present the results from the experiments and our modeling efforts for two launches of the sounding rockets on May 1st and May 9th. In this section, we review the radio wave propagation theory through the ionosphere.

Radio waves propagating through an ionosphere must satisfy two conditions [24]: (i) Maxwell's equations relating electric and magnetic fields, and (ii)the constitutive relationships relating the response of the medium to wave fields.

The maxwell's equations in differential forms are:

$\nabla . \in E = \rho$; --- (1)

ρ is charge density , $\in$ is dielectric permittivity , E is electric field.

$\nabla . B = 0$; --- (2)

B is magnetic field.

$\nabla \times \mathrm{H} = J + \dot{D}$; --- (3)

H is magnetic intensity, J is electric current density, D is displacement field.

$\nabla \times \mathrm{E} = -\dot{B}$; --- (4)

where the 'dot' on the the top of the letter represents time derivative.

The constitutive relations are :

$$D \;= \in E = \in_o E + P; \quad \text{---} \quad (5)$$

$\in_o$ is the permittivity of free space, P is the volume Polarization.

$$B \;=\; \mu_o H\,; \quad \text{---} \quad (6)$$

μ_o is permeability in free space.

The equation (6) suggests the magnetic permeability for the ionospheric plasma is approximated to be of free space.

With the polarization P, the charge density ρ and the current J all being zero in a homogenous anisotropic medium in free space, ,the refractive index for an infinite transverse plane wave traveling in the x-direction can be calculated to be:

$$\mu^2 \;=\; 1 + \frac{P_y}{\in_o E_y} \;=\; 1 + \frac{P_z}{\in_o E_z}\;; \quad \text{---} \quad (7)$$

We use this result to obtain the refractive index for plane waves in a homogeneous plasma consisting of electrons and positive ions in the presence of a uniform magnetic field B_o , and of electron collision frequency υ. The following properties are assumed:

Wave :

1. Simple harmonic progressive waves with small amplitude
2. Steady-state solution
3. Plane waves with fixed polarization

Medium :

- iv. Electrically neutral
- v. Charges distributed with statistical uniformity
- vi. Uniform external magnetic field
- vii. Electron collisions independent of electron energy
- viii. Thermal motions of the electrons neglected,i.e., Cold Plasma
- ix. Magnetic properties of free space

Taking an equation of motion for a plane electromagnetic wave traveling in the x-direction of an orthogonal system with the external magnetic field in x-y plane making an angle Θ with the direction of propagation of the wave, we obtain the famous Appleton formula which gives us the complex refractive index :

$$n^2 = (\mu - i\,\chi)^2 = 1 - \frac{X}{1 - iZ - \frac{Y_T^2}{2(1 - X - iZ)} \pm \left[\frac{Y_T^4}{4(1 - X - iZ)^2} + Y_L^2\right]^{\frac{1}{2}}} \quad \text{---} \quad (8)$$

where,

$$X = \frac{N\,e^2}{\epsilon_0 m\omega^2}\ , Y_L = \frac{e\,B_L}{m\omega}\ ,\ \ Y_T = \frac{e\,B_T}{m\omega}\ , Z = \frac{\upsilon}{\omega}$$

When collisions are negligible (i.e. Z ≈ 0),

$$n^2 = \mu^2 = 1 - \frac{2X\,(1-X)}{2(1-X) - Y_T^2 \pm \left[Y_T^4 + 4(1-X)^2 Y_L^2\right]^{\frac{1}{2}}} \quad \text{---} \quad (9)$$

When the magnetic field is negligible (i.e. Y << 1),

$$n^2 = (\mu - i\,\chi)^2 = 1 - \frac{X}{1-iZ} \quad \text{---} \quad (10)$$

When both collision and magnetic field effects are negligible,

$$n^2 = \mu^2 = 1 - X = 1 - \left(\frac{f_N}{f}\right)^2 \quad \text{---} \quad (11)$$

where $f_N = \frac{\omega_p}{2\pi} = \sqrt{\left(\frac{Ne^2}{\epsilon_0 m}\right)}$ is the plasma frequency

$f_N \approx 9\sqrt{N}$; N is in electrons per cubic meter , f is in Hz.

The equation (11) sets the working principle for the ionosonde. It shows vertical reflection occurs when the plasma frequency equals the wave frequency as the refractive index equals zero. The radio pulses from ionosondes are reflected at an altitude where the plasma frequency equals the radio wave frequency and the returned signals also known as echoes are received by the receivers. The sounding can occur in both vertical propagation and oblique propagation. In case of vertical propagation, the transmitter and the receiver are collocated.

To find the reflection conditions for vertical propagation in the presence of external magnetic field, setting $\mu = 0$ in the equation (9) gives for the + sign

$$X = 1 \quad \text{---} \quad (12)$$

For the negative sign in the equation (9),

$$X = 1 - Y \quad \text{---} \quad (13a)$$

or, $X = 1 + Y$ --- (13b)

The wave with the +ve sign in equation (9) is called as the ordinary wave and the waves with the –ve sign in equation (9) are called as extraordinary waves. There is more discussion on these waves in the reference [24] and the references therein.

References:

[1] Kelley, M.C. (1989), The Earth's Ionosphere, San Diego, CA, Academic Press.

[2] Schunk, R. W., and Nagy, A. F. (2000), Ionospheres: Physics, Plasma Physics, and Chemistry, New York, NY, Cambridge University Press.

[3] Allen, D. C., J. D. Haigh, J. T. Houghton, C. J. S. M. Simpson (1979), Radiative cooling near the mesopause, Nature, 281, 660, doi:10.1038/281660a0.

[4] Corliss, W.R. (1971), NASA sounding rockets, 1958–1968: A historical summary. *Technical Report NASA SP- 4401,* National Aeronautics and Space Administration, Washington, D.C.

[5] Sounding Rockets 2017 Annual Report, https://sites.wff.nasa.gov/code810/download_archive.html.

[6] Goddard, R. H. (1920), A method of Reaching Extreme Altitudes, Nature 105, 809-811, doi: 10.1038/105809a0.

[7] Edwards H.D., Bedinger J. F., Manring E. R., and Cooper C. D.(1955), The Airglow and the Aurorae (edited by E. S. Armstrong and A. Da!gamo), Pergamon Press, Ltd., London; p. 122.

[8] Davis, T.N. (1979), Chemical releases in the ionosphere, *Rep. Prog. Phys.*, *42*, 1565, doi: 10.1088/0034-4885/42/9/003.

[9] Walker, J. C. G. (1979), Active experimentation with the ionospheric plasma, Rev. Geophys., 17(4), 534–544, doi:10.1029/RG017i004p00534.

[10] Caton, R. G., et al. (2017), Artificial ionospheric modification: The Metal Oxide Space Cloud experiment, Radio Sci., 52, 539–558, doi: 10.1002/2016RS005988.

[11] Shuman, N. S., D. E. Hunton, and A. A. Viggiano (2015), "Ambient and Modified Atmospheric Ion Chemistry: From Top to bottom," *Chem. Rev.*, *115* (10)*,* pp 4542–4570, doi: 10.1021/cr5003479.

[12] Raitt, W. J. (1995), Stimulating our piece of the universe: Active experiments in space, Rev. Geophys., 33(S1), 559–564, doi: 10.1029/95RG00102.

[13] Reasoner, D. L. (1992), Chemical-release mission of CRRES, J. Spacecr. Rockets, 29, 580.

[14] Valenzuela, A., et al. (1986), The AMPTE artificial comet experiments, *Nature*, **320**, 700.

[15] Pongratz, M. B. (1981), Large scientific releases, *Adv. Space Res.*, **1**, 253–273.

[16] Bernhardt, P. A. (1987), A critical comparison of ionospheric depletion chemicals, *J. Geophys. Res., 92*(A5)*,* 4617–4628, doi: 10.1029/JA092iA05p04617.

[17] U.S. Army Space and Missile Defense Command, Factsheet, "ARPA Long-Range Tracking and Instrumentation Radar," available at: https://www.smdc.army.mil/KWAJ/RangeInst/ALTAIR.html.

[18] Tsunoda, R. T., M. J. Baron, J. Owen, and D. M. Towle (1979), Altair: an incoherent scatter radar for equatorial spread *F* studies, Radio Sci., 14(6), 1111–1119, doi: 10.1029/RS014i006p01111.

[19] Melvin F. Stone and Gerald P. Banner (2000), “Radars for the Detection and Tracking of Ballistic Missiles, Satellites, and Planets,” *Lincoln Laboratory Journal*, Vol. 12, No. 2, pp. 217-24.

[20] Philip A. Ingwersen and William Z. Lemnios (2000), “Radars for Ballistic Missile Defense Research,” *Lincoln Laboratory Journal*, Vol. 12, No. 2, pp. 245-66.

[21] Gordon, W. E. (1958), “Incoherent scattering of radio waves by free electrons with applications to space exploration by radar’’, *Proc. IRE*, **46**, 1824 -1829, doi: 10.1109/JRPROC.1958.286852.

[22] Beynon, W. J. G., P. J. S. Williams (1978), Incoherent scatter of radio waves from the ionosphere, *Rep. Progr. Phys.*, **41**, 909–956.

[23] Dougherty, J. P., D. T. Farley (1960), A theory of incoherent scattering of radio waves by a plasma, *Proc. Roy. Soc. London, A*, **259**, 79–99.

[24] Davies, K. (1990), *Ionospheric Radio*, Peter Peregrinus, London, U. K.

CHAPTER 3 METAL OXIDE SPACE CLOUD (MOSC) EXPERIMENT: HF PROPAGATION RESULTS

3.1 Introduction

Since the 1950s after the availability of rockets for research purposes, experiments have been conducted to inject various materials into the atmosphere for the purpose of creating perturbations to the ambient medium [1, 2, 3, 4, 5, 6]. Such ionospheric modification experiments in the form of chemical releases have been used for various goals such as to measure neutral wind directions and shears, to detect plasma drift velocities and electric fields, to exploit the ionosphere as a plasma laboratory without walls, to modify the plasma density in the ionosphere to trigger larger scale phenomena, and many other uses [7, 8, 9]. The Air Force Research Laboratory (AFRL) launched two sounding rockets in the Kwajalein Atoll, Marshall Islands, in May 2013 known as the Metal Oxide Space Cloud (MOSC) experiment. The sounding rockets, each carrying a payload of two 2.5 kg canisters of powdered samarium metal in a thermite mixture, released samarium metal vapor at dusk at 170 and 180 km altitude, respectively. A fraction of the samarium metal vapor ionized in the ambient environment, creating an additional layer of plasma. The objectives of the experiments were to understand the dynamics, evolution, and chemistry of Sm atoms in the Earth's upper atmosphere; to understand the interactions of artificial ionization and the background plasma; and to measure the effects on high-frequency (HF) radio wave propagation. A host of diagnostic instruments were used to probe and characterize the cloud including the Advanced Research Project Agency Long-range Tracking and Identification Radar (ALTAIR) incoherent scatter radar, multiple GPS, and optical instruments, satellite radio beacons, and a dedicated network of high-frequency (HF) radio links [10]. In this chapter, we report the results from the HF sounder observations and modeling those results with the ALTAIR radar data using the HF radio wave ray-tracing MATLAB toolbox PHaRLAP [17]. The modeling results enable us to understand the changes caused by the samarium plasma cloud in the HF propagation environment and thus validate the extent to which we can model HF propagation for other specified plasma perturbations. We have developed a new technique to model an anomalous background ionosphere by assimilating oblique ionosonde data specifically to match observed HF signal delays. The approach may have numerous applications for ionospheric specification for HF propagation. The angle of arrival (AoA) measurements would have been very helpful to validate the ray-tracing calculations which could also have been assimilated to optimize the ionospheric model. Since we did not have the AoA measurements from the experiment, we recommend these measurements to be made in future studies which would help in refining the ionospheric model and its predictive capabilities.

In Figure 3.1, the site locations corresponding to the HF links and the ALTAIR incoherent scatter radar are shown. In this work, we focus on the signals received at Wotho from transmitters at Rongelap and Likiep. The Rongelap-Wotho link geometry is predominantly N-S and the release region is far from the great-circle path, whereas the Likiep-Wotho path is nearly magnetic E-W and the release point lies close to the mid-point of the link. Geographic coordinates for the sites may be found in Table 3.1. The first sounding rocket launch occurred on 1 May 2013 at 07:38 UT and the samarium metal vapor release occurred at 07:40:40 UT. The second sounding rocket launch

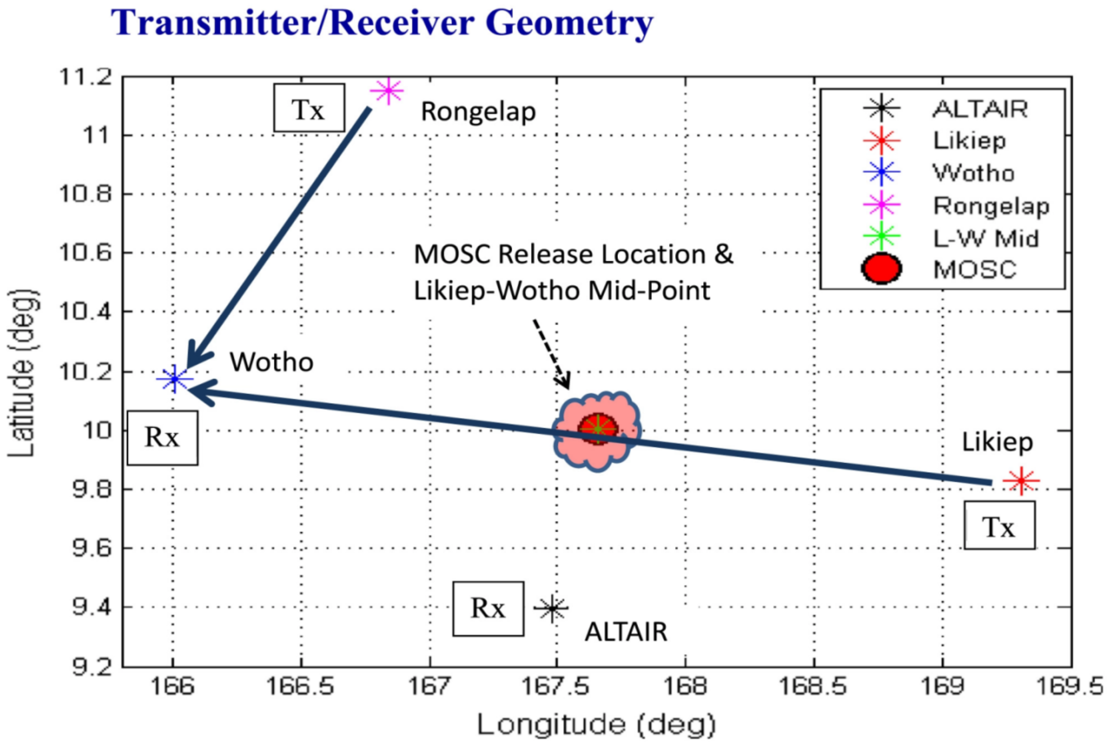

Figure 3.1: Site Locations in Marshall Islands. Tx = Transmitter, Rx = Receiver. The MOSC release point is at the mid-point between Likiep-Wotho.

occurred on 9 May 2013 at 07:23 UT and the release occurred at 07:25:40 UT. In both releases, approximately 10% of the samarium metal in the canisters ionized.

Table 3.1: Geographic Site Co-ordinates in Marshall Islands

Site	Latitude (°N)	Longitude (°E)
Rongelap	11.1523	166.8378
Likiep	9.8262	169.30673
Wotho	10.17404	166.0046
ALTAIR	9.3954	167.4793

3.2 OBSERVATIONS

The Advanced Research Project Agency Long-range Tracking and Identification Radar (ALTAIR) at Kwajalein Atoll was used to monitor the ionospheric state and track the evolution of the metal oxide space cloud. Range-time-intensity displays of each release event are shown in Figure 3.2. The data gap during the first release shown in Figure 3.2 (a) was an intentional data management action to avoid a data file size limitation.

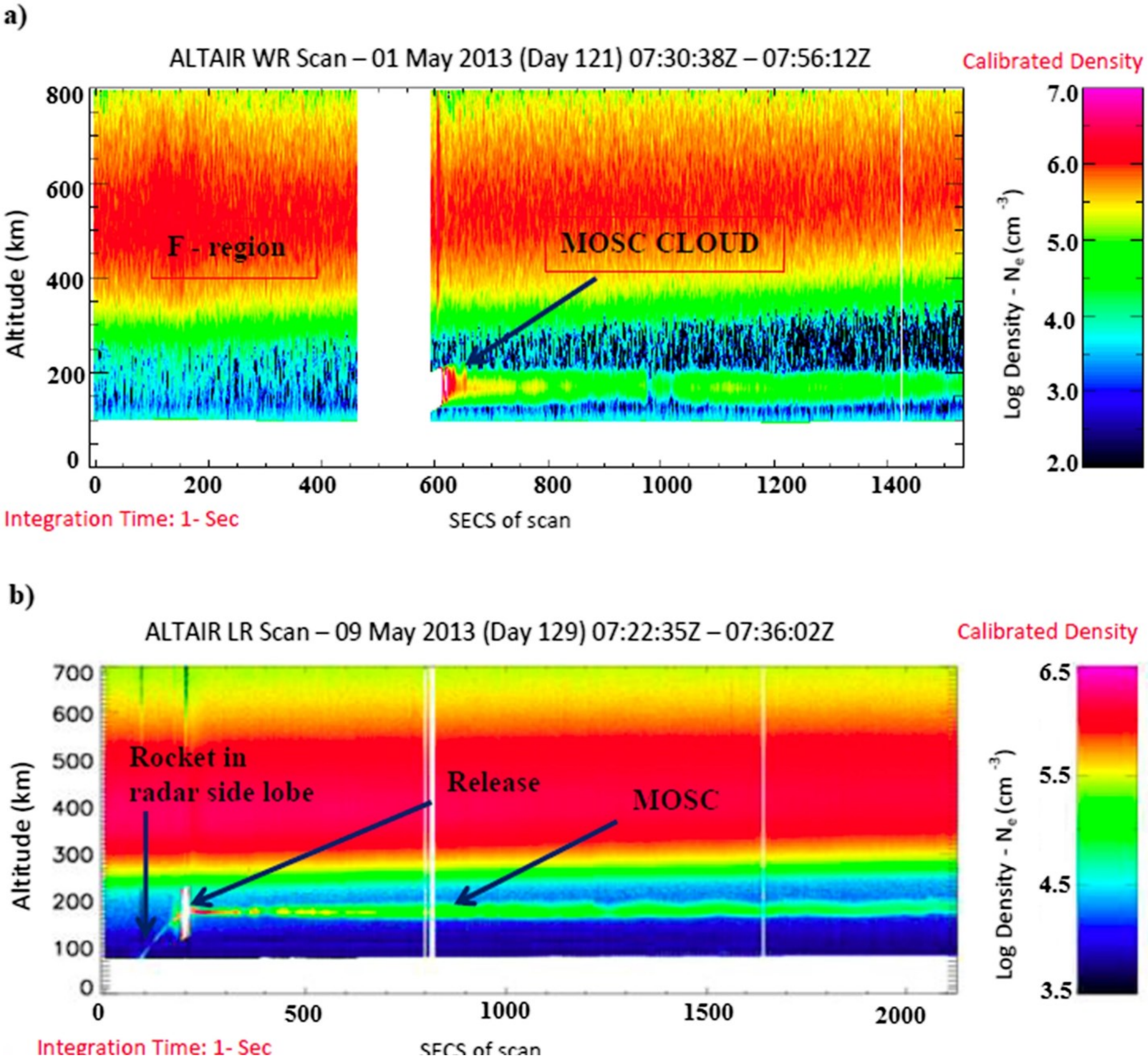

Figure 3.2: First release: (top) the ALTAIR radar range-time-intensity (RTI) plot shows a rapidly rising *F*-layer of the ionosphere (disturbed condition). (b) Second release: (bottom) the RTI plot shows a quiescent ionosphere typical of the equatorial region just prior to the onset of the prereversal enhancement period.

Recording was turned off for a period of about 2 min and turned back on approximately 30 s prior to the samarium release. Improved prelaunch file management on the night of 9 May precluded the need to limit data sampling during the second rocket flight as shown in Figure 3.2 (b).

The ionograms (Figures 3.3 and 3.4) from the oblique sounder data for the releases on 1 and 9 May 2013 show the evolution of the ionosphere before and after the release of the samarium metal vapor in the ambient environment. An ionogram is a graph of time-of-flight, commonly called time-delay, against transmitted frequency. Both Likiep and Rongelap used broadband folded dipole transmit antennas approximately 12 m long connected to 100 W power amplifiers to transmit swept frequency waveforms from 2–30 MHz every 5 min at the rate of 100 KHz/s. The timing for both transmitters and receivers was synchronized by GPS-disciplined clocks. The ionograms shown in the figures were recorded at Wotho using a simple 1 m diameter loop antenna. Plots show data from only 2–14 MHz since no signatures were observed at higher frequencies. The titles include the start time of the frequency sweep (2 MHz); end time at 14 MHz is 120 s later. In prerelease sweeps on 1 May, *E*-layer traces are also seen in the ionograms in addition to the ground wave and *F* region traces, whereas the *E*-layer trace is not seen on 9 May, suggesting that the *E* region is not present during the second release. The *E*-layer echoes present on 1 May are due to sporadic *E* [11], as the traces extend to 10 MHz or so, well beyond the peak plasma frequency expected in the *E* region at this local time (approximately 18:20 LT). The *F* region traces are further seen to be split into two characteristic components: ordinary and extraordinary waves. The effects of the artificial plasma cloud are clearly seen in the post release sweeps along both Rongelap-Wotho and

Likiep-Wotho paths. Two additional traces, denoted as the “MOSC” layer and the secondary *F* region echo, are evident, suggesting significant change in the propagation environment of the HF radio waves due to the metal oxide plasma cloud. SmO+ layer density (approximately 10 MHz at early times) is similar in both cases and observed initially on all links. The density of the artificial cloud is observed to fall rapidly over time scales of a few minutes, and the signatures disappear completely within about 15 min. The difference between the secondary *F* region echo and *F* region trace is smaller along the Likiep-Wotho path compared to the Rongelap-Wotho path, the reason of which is explained in section 4.2. A more detailed description of the cloud's evolution can be found in *Pedersen et al.* [12]; here we focus on modeling the HF propagation observed during the first few minutes after the release. The SmO+ plasma also triggered significant modification of HF propagation in the *F* region.

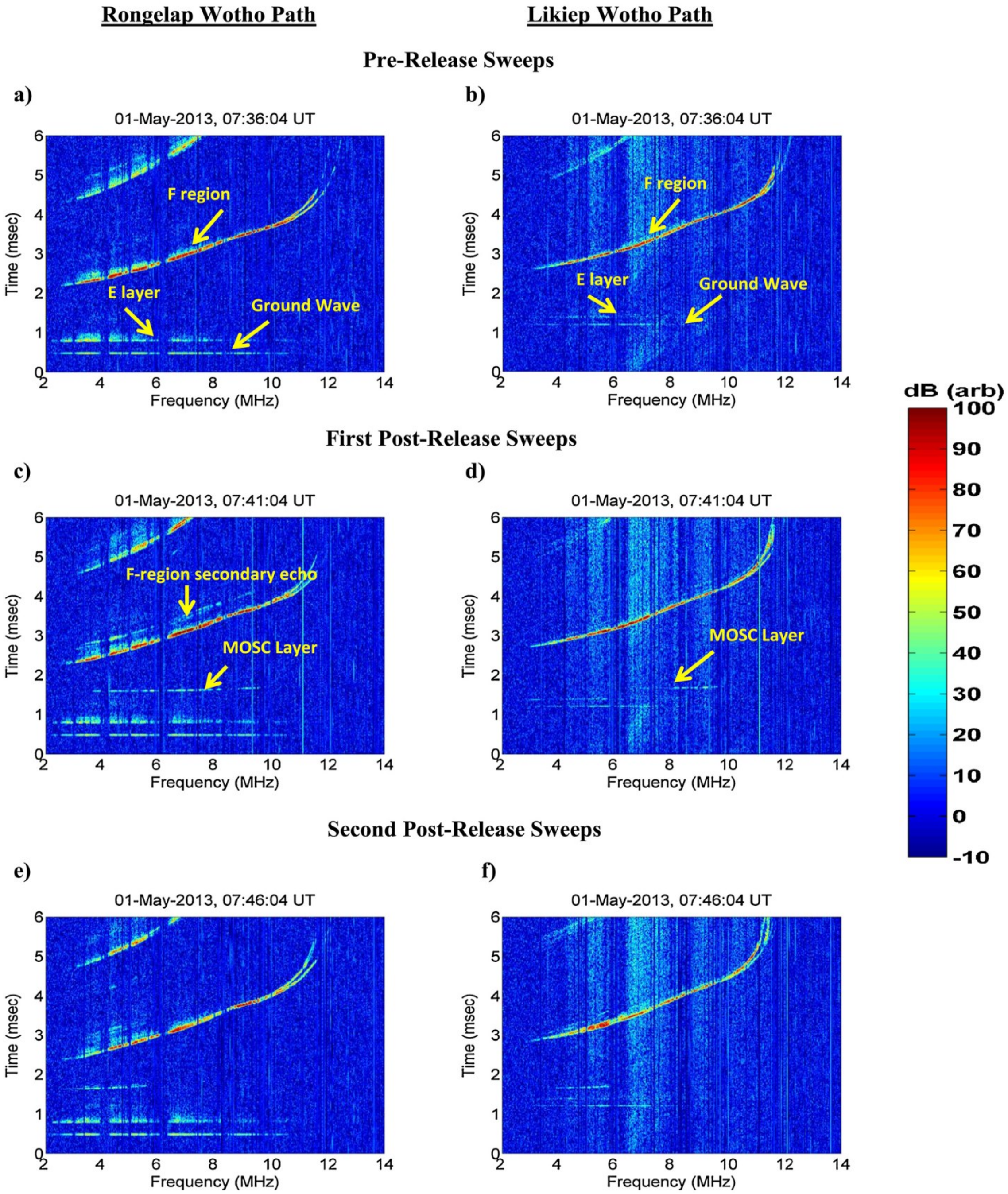

Figure 3.3: First Release: Sounder Observations of the ionosphere before and after the release of the samarium metal vapor along Rongelap-Wotho path (left column, panels a, c, e) and along Likiep-Wotho path (right column panels b, d, f).

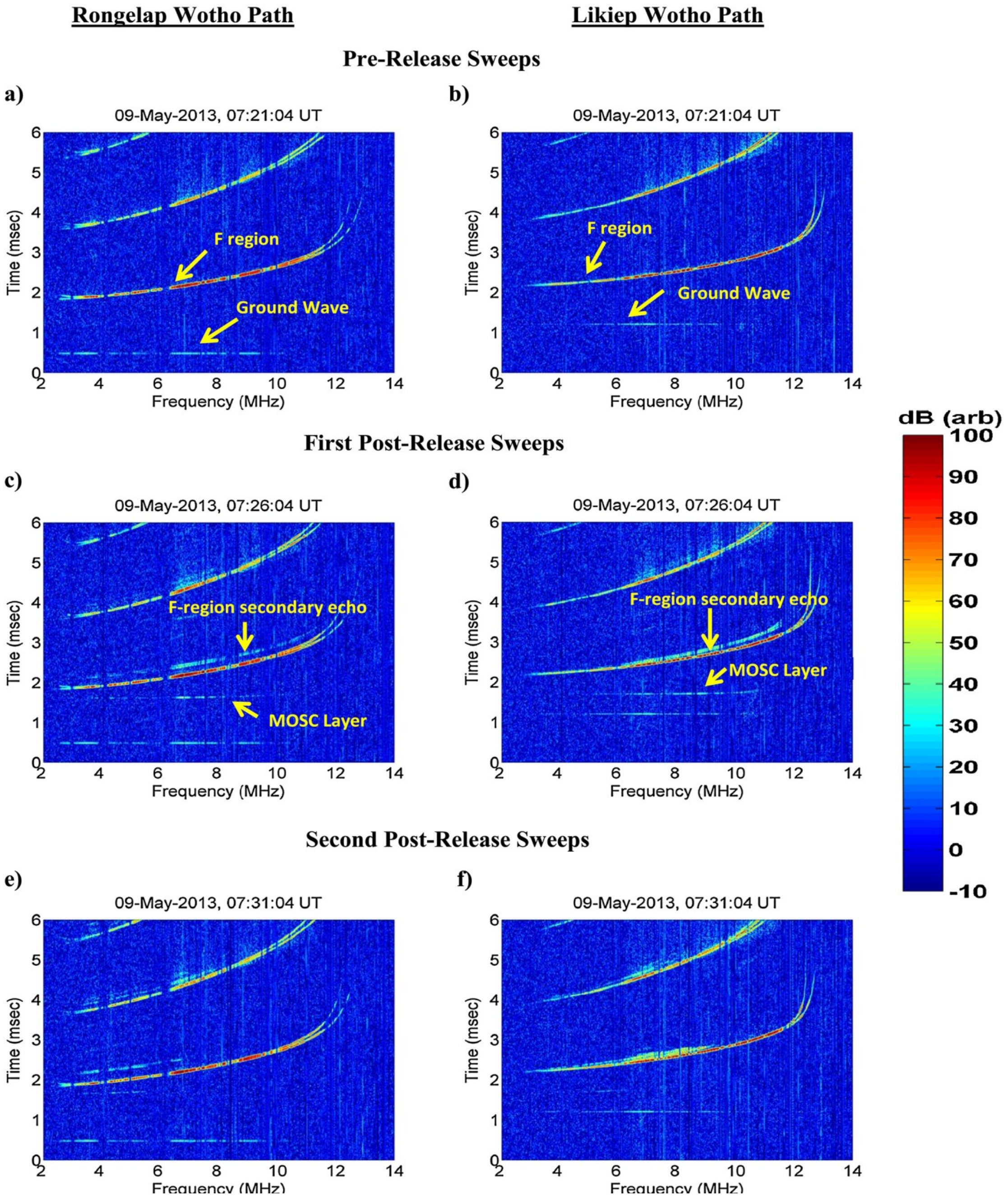

Figure 3.4: Second Release: Sounder Observations of the ionosphere before and after the release of the samarium metal vapor along Rongelap-Wotho path (left column, panels a, c, e) and along Likiep-Wotho path (right column, panels b, d, f).

In the first post release frequency sweep initiated less than 40 s after the release on 1 May, the Likiep-Wotho path has an MOSC signature only in the high end of the frequency sweep above $f = 8$ MHz (Figure 3.3d), yet the Rongelap link shows a robust signature beginning at less than 4 MHz (Figure 3.3c). The subsequent sweep 5 min later shows a solid MOSC trace at lower frequencies only on both paths (Figures 3.3e and 3.3f). Moreover, MOSC signature is present across most of the frequency bands on both links in the second release during all phases of the observations (Figures 3.4c –3.4f). Potential reasons for the lack of signals on the Likiep-Wotho path in the lower portion of the HF frequency band during the first release will be discussed later in this chapter.

3.3 MODELING:

Since *Haselgrove* [13] set down the differential equations governing ray paths in an anisotropic medium for numerical integration techniques, the equations have been used extensively [14, 15, 16] to study the propagation of HF energy through the ionosphere. In our work to model the HF sounder observations, we have used PHaRLAP, a HF radio wave ray tracing MATLAB toolbox developed by Dr. Manuel Cervera, that contains a variety of ray tracing engines of various sophistications from 2-D ray tracing to full 3-D magnetoionic ray tracing [17].

Modeling the sounder observations involved insertion of a three-dimensional plasma cloud representing the MOSC into a background ionosphere and then using full 3-D magnetoionic ray-tracing to understand the various propagation modes induced by introduction of Sm+ ions in the ambient plasma. Prior to the first release on 1 May the ionosphere was rising rapidly ($v_z \geq 50$ m/s), potentially responding to a minor magnetic perturbation ($Dst \sim -50$), and spread F - in which the equatorial region ionosphere is reshaped after sunset due to hydrodynamic instabilities - formed within minutes after the release as observed in the sounder data and ALTAIR radar scan. For the second release, the ionosphere was quiescent as seen in the sounder observations and the radar scan. Hence, we present the modeling efforts for the background ionosphere and samarium cloud for the second release in section 3.1 before those for the first release (section 3.2).

At early times immediately after the release, the cloud appeared to be symmetric optically and the ALTAIR radar scan also showed a symmetric density profile [*Caton et al.*, 2017]. Before- and after-release density profiles along with the symmetric 3-D representation for the samarium plasma cloud derived from ALTAIR are shown in Figure 3.5 where a prerelease electron density profile (Figure 3.5 (a)) and a post release profile (Figure 3.5 (b)) clearly show the contribution of the samarium plasma. The dual peaks seen in the post-release profile (Figure 3.5 (b)) correspond to the cloud (lower peak) and the rocket (upper peak) as detected by the ALTAIR radar scan. A model cloud based on these observations was inserted into the background ionosphere for ray-tracing. A graphical representation of the digitized cloud is shown in Figure 3.5 (c), while a false-color image of the cloud itself is shown in Figure 3.5 (d). The image was acquired with the AFRL bare CCD camera through a 630 nm filter approximately 4 min after release. The cloud still appears spherical at this time which corresponds to the end of the first post-release HF frequency scans presented in Figure 3.4.

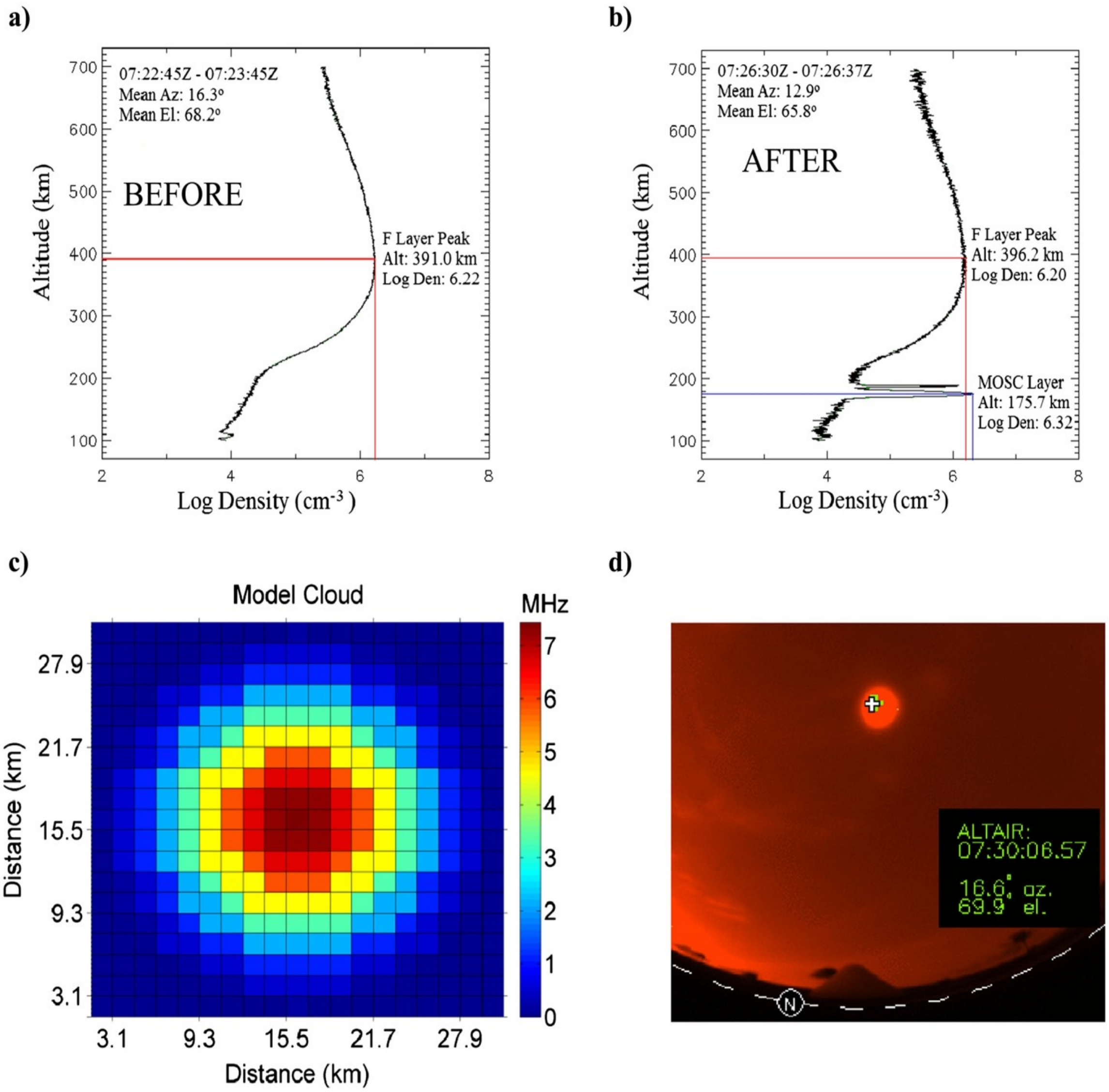

Figure 3.5: a) The ALTAIR radar profile before the release of the samarium metal vapor b) The radar profile approximately 30 seconds post-release c) The two dimensional view of the model cloud through its center is shown . The central pixel corresponds to f_{pe} = 7.44 MHz. d) An optical image of the cloud.

An ionospheric model was used for the background because we did not have adequate knowledge of the ionosphere across the whole region of interest. The approach was to constrain the background model with calibrated ALTAIR radar observations at a specific location and then use the model to represent the ionosphere across a region that extended approximately 200 km north and ± 200 km E-W from the point of the radar observations. We used the Parametrized Ionospheric Model (PIM) [18] and the International Reference Ionosphere (IRI-2012) [19] as the background model ionospheres for ray-tracing. The reason for using two models rather than just one will be made clear shortly.

The International Reference Ionosphere (IRI) is an empirical model ionosphere developed as a joint project of the Committee on Space Research (COSPAR) and the International Union of Radio Science (URSI). For a given location, time, and date, IRI provides the median monthly values of electron density, the electron temperature, and ion composition in the altitude range 50 km to 2000 km. The major data sources for the IRI model are the worldwide network of ionosondes, the powerful incoherent scatter radars, (Jicamarca, Arecibo, Millstone Hill, Malvern, St. Santin), the International Satellites for Ionospheric Studies (ISIS) and Alouette topside sounders, and in situ instruments on several satellites and rockets.

The Parameterized Ionospheric Model (PIM) is a global ionospheric and plasmaspheric model based on combined output from the Global Theoretical Ionospheric Model (GTIM) model for low and middle latitudes. PIM produces electron density profiles between 90 and 2500 km altitude, in addition to other profile parameters such as corresponding critical frequencies and heights for the ionospheric E and F2 regions, and Total Electron Content (TEC).

3.3.1 Ionospheric Model for Samarium Release on 9 May

For the second release in which the background ionosphere exhibited typical characteristics, good agreement between the PIM model and the ALTAIR radar observations were obtained by making a small change in the F10.7 flux input to the model. The objective was to obtain a good fit primarily in the bottomside to insure accurate HF propagation modeling.

3.3.2 Ionospheric Model for Samarium Release on 1 May

For the first release which had a disturbed and rapidly rising ionosphere, no standard model could be fitted to match the background ionosphere. We tried to minimize the difference between the model ionospheric profile and ATLAIR radar profile at the MOSC release location by an optimization technique known as the Nelder-Mead Downhill Simplex method [20, 21]. We used the native “fminsearch” function in MATLAB to optimize the difference between the ALTAIR radar ionospheric profile and the model profile (Fig 3.7a). Since PIM didn’t have enough accessible degrees of freedom, this optimization technique gave good results only with the IRI model. An altitude-dependent scale vector was obtained by dividing the optimized IRI profile by the initial IRI profile and this was subsequently used to scale the entire IRI 3D grid. However, when the optimized results were used on the Rongelap-Wotho path (~150 km NW of ALTAIR scan), the modeled delay did not match observations with sufficient accuracy, presumably because the disturbed ionosphere gradients were not well represented by the scaled model output. After experimenting with a number of approaches we succeeded in modeling the background ionosphere along the raypath by applying frequency-specific

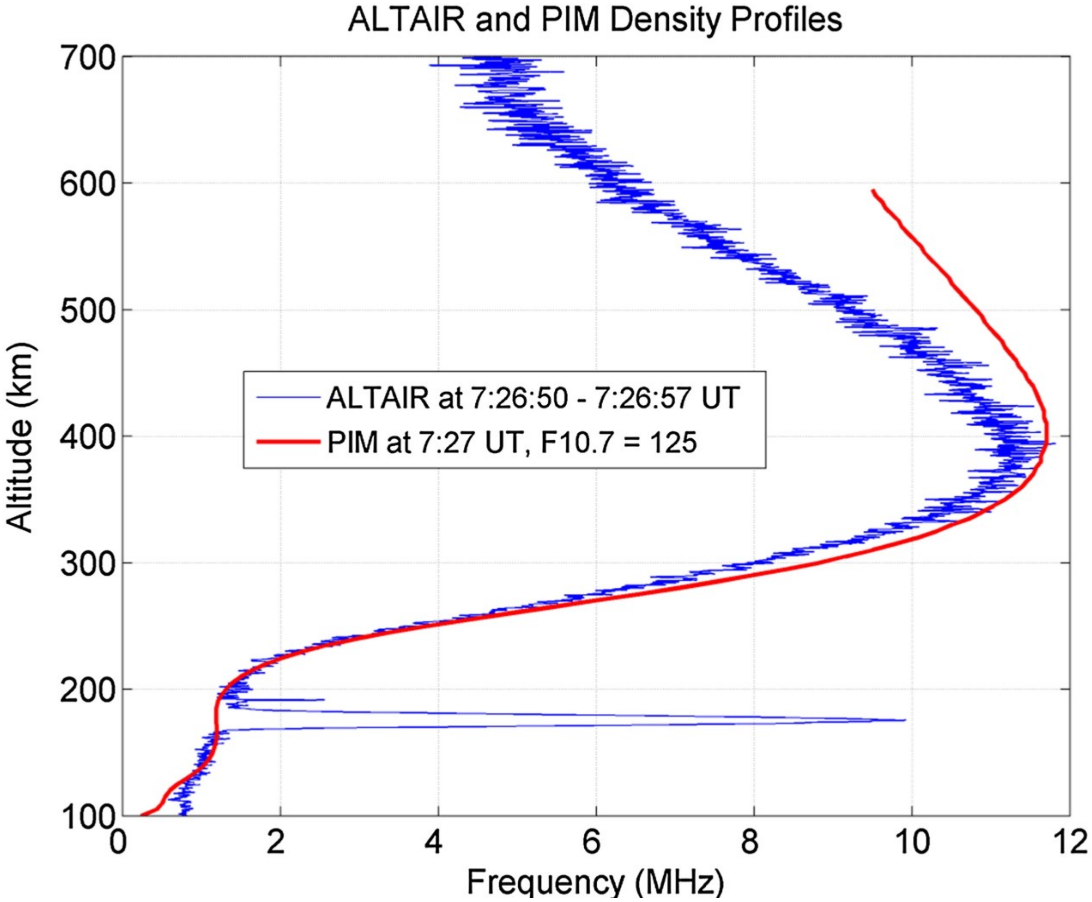

Figure 3.6: PIM and ALTAIR radar electron density (N_e) profiles displayed as equivalent plasma frequency ($f_p \approx \sqrt{N_e}$, in MKS units). The PIM bottomside fits well with the observed ATLAIR profile. The disparity below about 125 km corresponds to a very low density/frequency ($<10^3$ cm^{-3}/1 MHz) that will not have an appreciable effect on radio waves propagating above about 2 MHz.

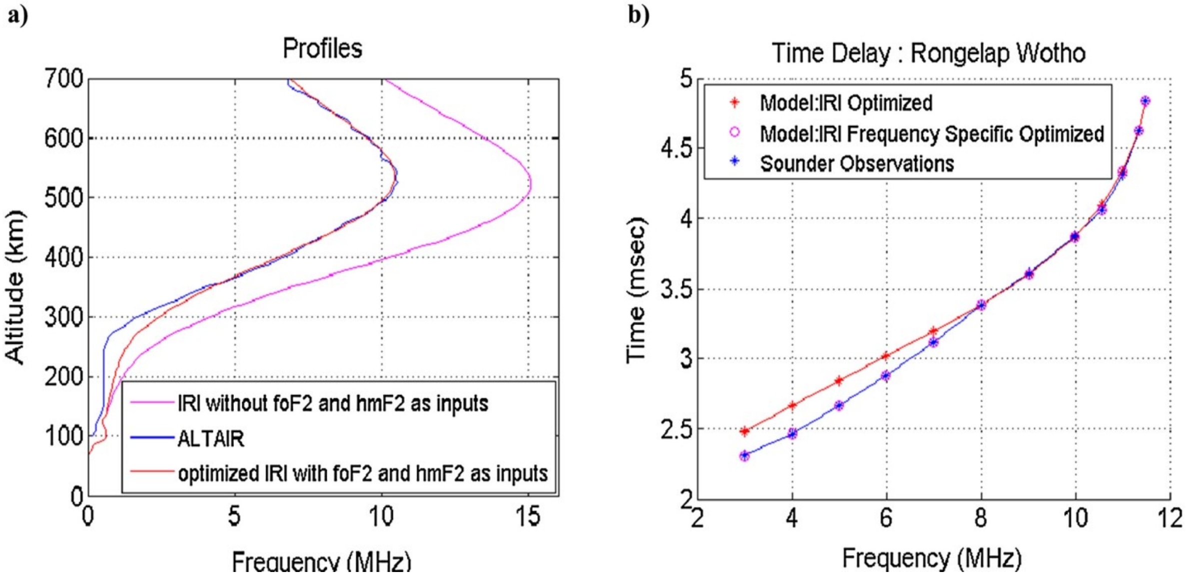

Figure 3.7: a) The Nelder-Mead Downhill Simplex method applied to optimize IRI in the vicinity of ALTAIR radar data b) A second frequency dependent optimization procedure was applied to assimilate the sounder data along the R-W path.

multipliers to the altitude-dependent scale vector; results are shown in Figure 3.7b. The variations in the multipliers were not large, but they facilitated a good fit between the modeled and observed profiles. The multipliers were determined by adjusting the ionosphere using ray tracing to minimize the difference between the observed and modeled signal delays. The primary objective is not to develop a good model of the ionosphere, but rather, to optimize our ability to model the HF propagation environment. The priority is for the primary *F* region modes to match the observations with high fidelity, so when the samarium cloud is introduced one can have high confidence in the propagation model results.

3.4 HF Propagation Modeling Results and Discussion

Ray-tracing was performed for both the releases after inserting the 3-D plasma cloud into the background ionosphere. It confirmed and explained the changes in propagation modes of the HF radio waves due to the artificial plasma cloud.

3.4.1 Rongelap-Wotho Path

As shown in Figure 3.8a, the Rongelap-Wotho path is nearly N-S and the release point is well off the great circle path connecting the two atolls. Up to three paths for the received HF energy have been identified. Rays reflected directly from the transmitter off the cloud account for the low altitude MOSC layer. Meanwhile the secondary F-region traces may be formed in two ways. One path consists of refraction first from the F-layer to the MOSC cloud and subsequent refraction to the receiver site (high elevation). The other path is defined by waves that travel first to the samarium cloud, refract to the F-region and are then refracted to the receiver (low elevation). Figure 3.8b shows a graphical representation of the various propagation modes identified to model the time delays shown in Figure 3.8c. The match between the observations and the model results suggest that both the high and low elevation angle paths contributed to the observed F-region secondary layers. From the geometry all the observed signatures confirm that the cloud scattered and/or refracted HF energy well off the great circle path. Rays were traced for a number of selected frequencies. Ray-tracing gave excellent results which agree with the sounder observations (Fig. 3.8c and 3.8d). For the first release (Fig. 3.8d), the additional MOSC and F-region secondary layers are also modeled to be close to the observed layers validating the modeling approach and the technique developed to build a disturbed background ionosphere.

For both the releases, the sounder observations show greater frequency extent for both the MOSC samarium layer and the F-region secondary layer than the model results. Reasons for the discrepancy include inadequate spatial resolution of the MOSC plasma cloud in the model and a low estimate of the peak plasma density in the cloud obtained from the radar observations. The high density center of the cloud is contained within just a few cubic kilometers which represents a very small target for ray tracing calculations, particularly for accurately homing rays from a transmitter to a receiver. Moreover, the high density center of the cloud is also challenging to resolve in both space and time with the ALTAIR radar. The observations presented in Figure 3.5b are the true cloud density convolved spatially with the radar beam width and pulse resolution and the time period over which the measurements were integrated. The measurements provide a good estimate of the average parameters of the cloud over a 60-second window, but they do not represent an exquisite characterization of the plasma cloud at the sub-kilometer resolution

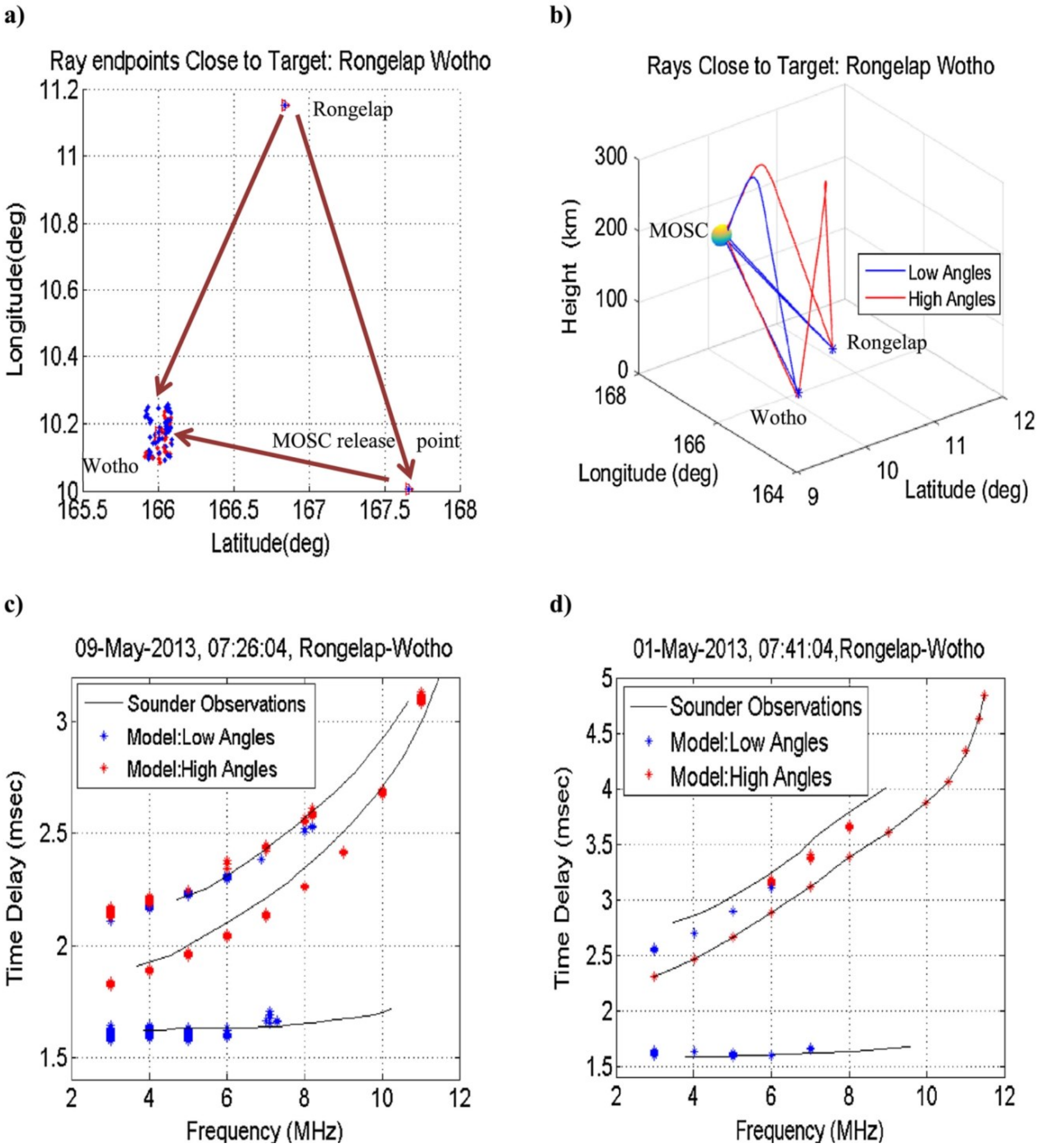

Figure 3.8: a) Rongelap-Wotho geometry; b) Various Propagation modes for 6 MHz in Second Release; Excellent agreement between model and observations c) second release and d) first release

needed to describe the structure in full detail. This does not present a critical problem, however, because the primary objectives to identify and characterize the new propagation modes introduced by the cloud can be achieved without an extremely high fidelity representation of the electron density in the cloud. The radar-derived spatial and plasma parameters are sufficient for this purpose.

3.4.2 Likiep-Wotho Path

Similar analysis was performed along the Likiep-Wotho path, shown in Figure 3.9a. This path was selected because the samarium release point lies nearly at the mid-point of the great circle path between the transmitter (Likiep) and the receiver (Wotho). The same modes to/from the cloud and the F-region were observed in this geometry, but the differences in delay between the normal F-layer path and the delayed paths (F-region to cloud; cloud to F-region) were significantly smaller than for the Rongelap-Wotho geometry as expected due to the co-planar geometry (see Fig 3.9b). Rays traced for various frequencies reproduced the additional MOSC and F-region secondary layers close to the observations for both releases (Fig. 3.9). As mentioned previously, one significant feature of the observations that remains to be explained is the absence of lower frequency signals (below ~ 8 MHz) refracted directly from the samarium cloud to the receiver on the Likiep-Wotho path within the first few minutes post-release on 1 May 2013.

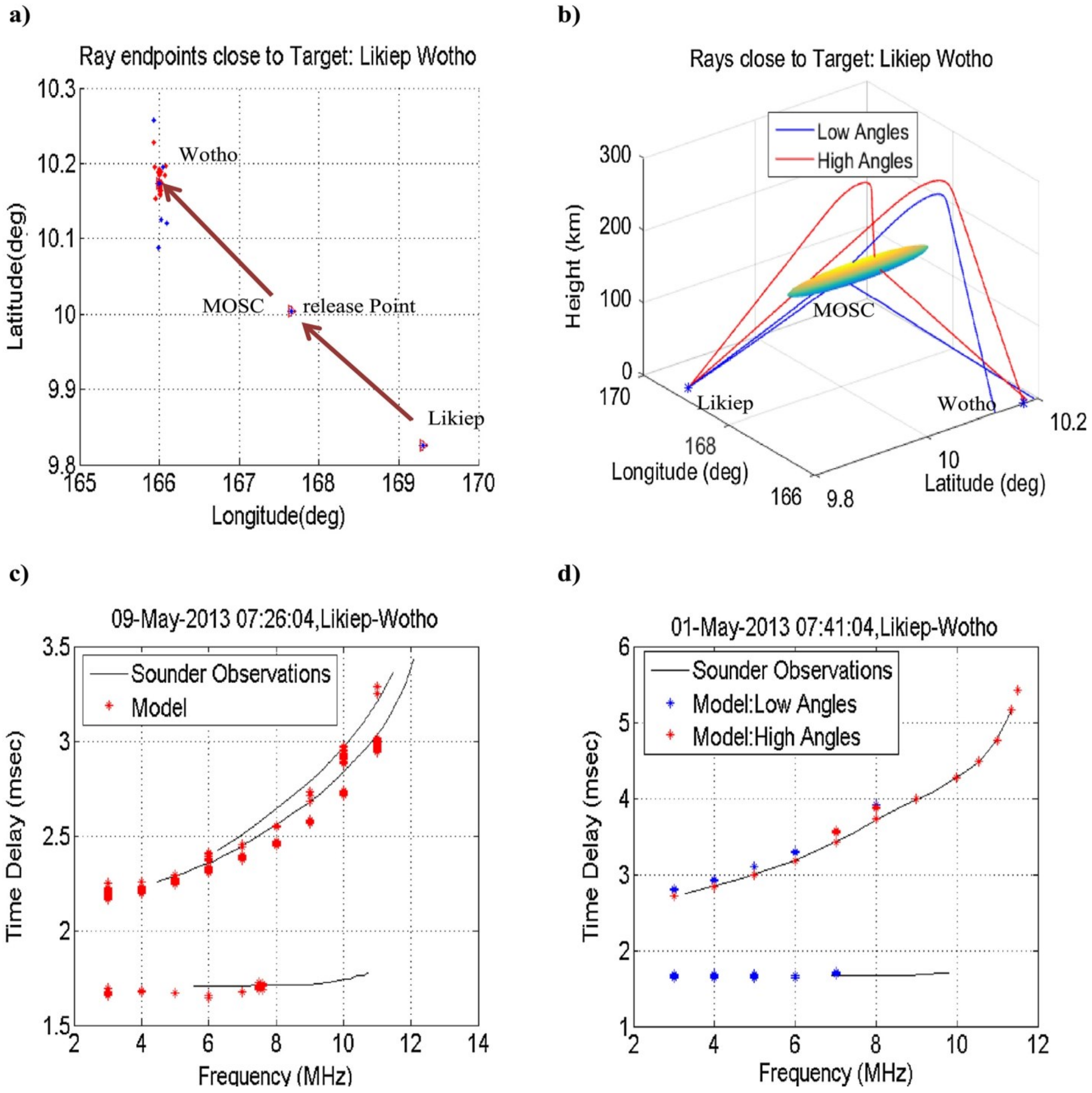

Figure 3.9: a) Likiep -Wotho geometry; b) Various Propagation modes for 6 MHz in Second Release; Close agreement between model and observations c) second release and d) first release

The lack of lower frequency signals on the nearly great circle path is noteworthy because relatively strong lower frequency signals are observed on the distinctly non great circle Rongelap-Wotho link at the same time. Moreover, lower frequency signals are present on both links throughout the observing period during the second release on 9 May. One possible explanation is enhanced absorption during the early scan period on the Likiep-Wotho path. This absorption is frequency-dependent and would normally be associated with an enhanced *E*- or *D* region not expected to be present at the time of the observations (18:47 SLT). A comparison of the relative intensities of the *F* region traces at frequencies below 8 MHz clearly shows that there is little to no difference between the first and second post release scans on 1 May or the scans from the second release on 9 May. Absorption does not appear to be a viable mechanism for the observed absence of power.

The primary geophysical difference between the 1 May and the 9 May releases was the presence of sporadic *E* (Es) on the night of the first release. A reasonably strong Es layer is visible on the Rongelap-Wotho link (Figures 3.3a, 3.3c, and 3.3e) extending to about 10 MHz frequency. A faint Es trace may be observed during the same time on the Likiep-Wotho path. On neither path does the layer appear to be blanketing in terms of masking the *F* region returns or the return from the samarium cloud on the Rongelap path. But that does not preclude the possibility that the path to the samarium cloud from Likiep, which is significantly different than the direct paths to both the *F* and *E* regions, may have been partially or wholly obscured by local sporadic *E* at the lower frequencies consistent with the lack of power observed below 6 MHz on the night of 1 May.

The severity of the effect may have been exacerbated by the reduced received power at low frequencies on the Likiep-Wotho path relative to the Rongelap-Wotho path. HF transmissions at Likiep were weaker overall than those from Rongelap and considerably weaker at frequencies below 8 MHz. In fact, between 2 and 6 MHz the observed average signal strengths at Wotho were more than 20 dB below the corresponding signals from Rongelap, as shown in Figure 3.10. The curve in the figure shows the ratio of power from Likiep/Rongelap as a function of frequency and was derived from averaging 10 scans during different quiet periods characterized by an absence of spread *F* and low *E* region density. A straight line fit to the data is also plotted to demonstrate the trend of the frequency dependence. Differences in path length between the two sites account for some of the observed SNR differences, approximately 6 and 2.5 dB for *E* and *F* region paths, respectively. A more significant contribution to the disparity may result from the transmit antenna installations at the two sites. The antenna at Rongelap was mounted on a tower some 18 m above ground, while the Likiep antenna was suspended from trees at a height of just 4 m. Although we do not have sufficient details to calculate the exact differences in gain at the two sites, it is well known that the impedance of a dipole antenna changes dramatically as the installation height decreases below one-fourth wavelength (see, e.g., *ARRL Antenna Handbook* [22]); the resulting impedance mismatch greatly reduces the radiation efficiency of the antenna. The 18 m height of the antenna at Rongelap corresponds to one-fourth wavelength at about 4.2 MHz; the 4 m high antenna at Likiep would transmit much less efficiently at this frequency, though the relative response would be expected to improve rapidly as the frequency increases, as has been observed. Similarly, one would expect the masking efficiency of Es to decrease as the transmitted frequency increases. Thus, we believe that a combination of factors including path length, antenna efficiency, and E_s masking effectiveness was responsible for the absence of lower frequency signals scattered by the samarium cloud from Likiep on the evening of 1 May. Of course, differences in the path lengths and antenna efficiencies were common to all the observations, while sporadic *E* was present only during the first release. However, the reduced signal strengths imposed by the common propagation factors from Likiep mean that relatively modest Es masking is needed to explain the observations.

A high density plasma sphere placed in a low density plasma background behaves as a divergent lens for radio waves; the signals will always be refracted away from the center. The top panel of Figure 3.11 shows just 2-d view of such a simulated cylinder while the bottom panel displays the relative signal strength for an 8-MHz plane wave traveling from left to right in the Figure. The propagation results, derived from a wave-optics calculation, show clearly how the power diverges as the wave propagates through the sphere. In this scenario it is plausible that the power from waves below 8-MHz was refracted off-axis passing through the samarium cloud and was not received along the great circle path at Wotho; signals at higher frequencies would suffer less refraction and could thus reach Wotho. Meanwhile the same plasma cloud could refract (or scatter) energy through acute angles such that signals from Rongelap were observed far off the great circle path, consistent with the actual observations. A detailed analysis of the cloud and geometry for the MOSC releases was performed. The results show that the region where refractive effects would be most effective in creating a signal void lies beyond Wotho. Indeed, the ray tracing results shown in Figure 3.9d specifically predict a

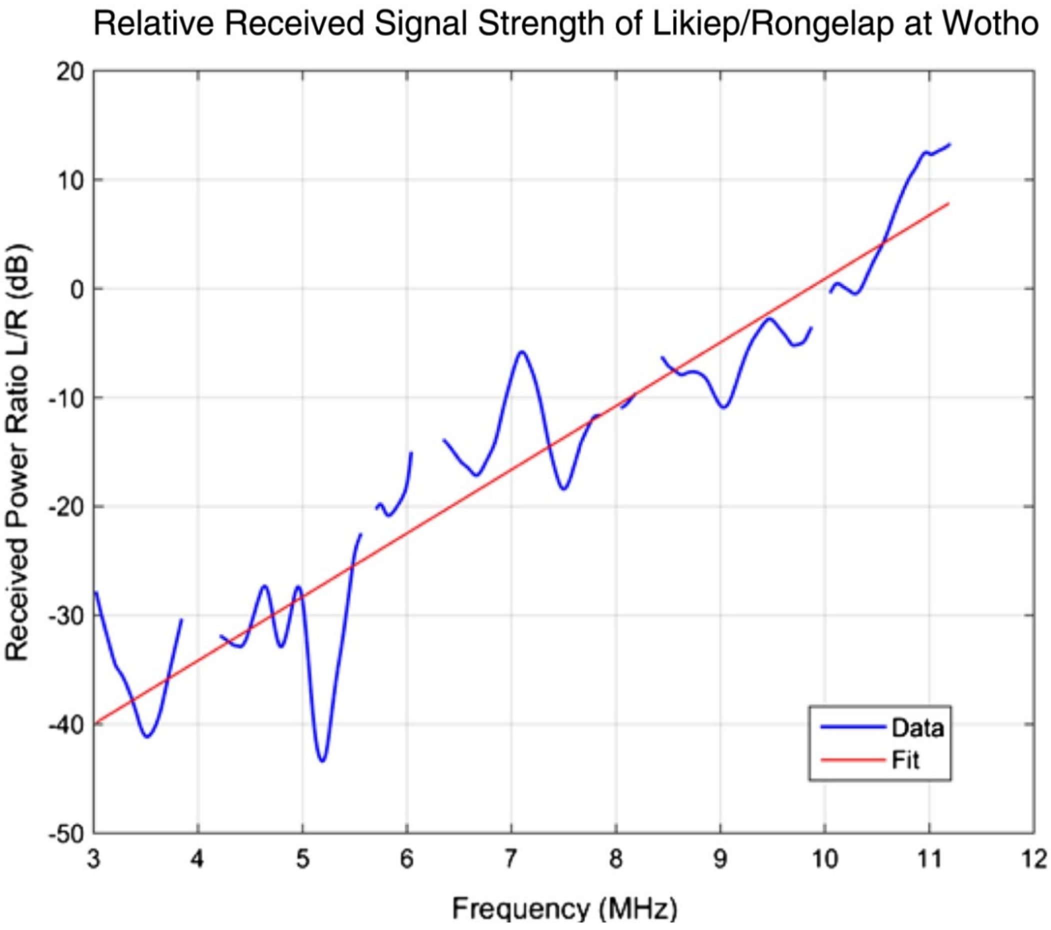

Figure 3.10: HF power received at Wotho from Likiep relative to Rongelap as a function of signal frequency (Likiep/Rongelap). The straight line shows a linear fit of the data. The received power from Rongelap was considerably higher at low frequencies.

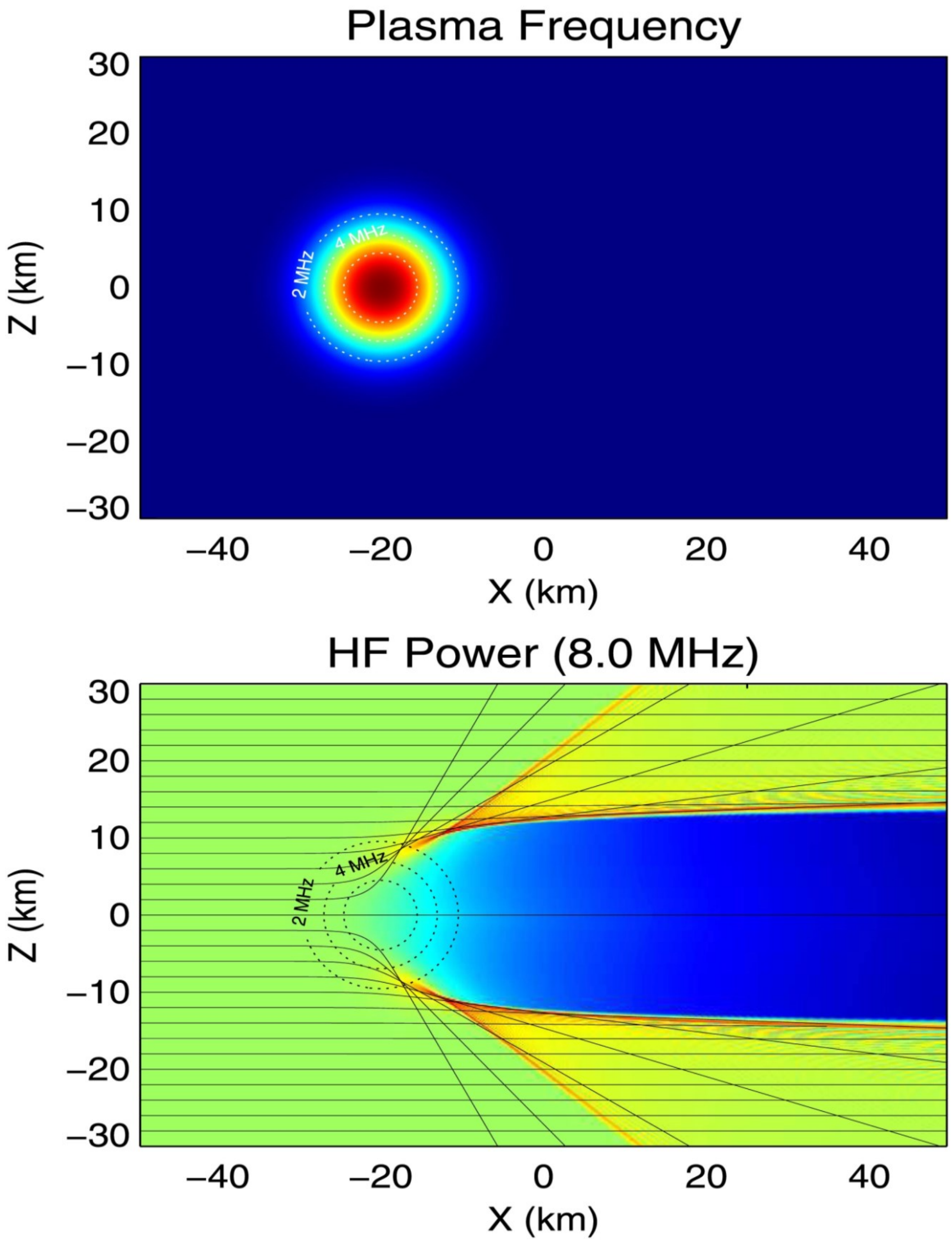

Figure 3.11: (top) Background environment and plasma distribution for a cylindrical artificial cloud. (bottom) Wave-optical calculation for 8 MHz radio wave propagation through the artificial cloud.

signature at the lower frequencies where none is observed. Nevertheless, divergent effects of the artificial plasma cloud remain the most probable cause for the signal drop-out from Likiep to Wotho (Fig 3.3d). Signals at the lower frequencies appeared in the subsequent scan five minutes later (Fig 3.3f), presumably as the cloud evolved and decayed. Although it is treated as a sphere in our model, the actual shape and density distribution of the cloud determine the detailed HF propagation effects. Some elongation along the magnetic field is expected, even at early times, and the true shape undoubtedly differs from our simple model. Interestingly the divergent effects of the cloud would be expected to persist much longer than the effects visible on the oblique ionograms shown in Figures 3.3 and 3.4. The divergence effect requires only small refraction angles along the direction of propagation, while large refraction angles are required to generate traces directly from the artificial plasma cloud.

CONCLUSIONS

The results presented here account for the features of the modified HF propagation environment observed at early times during the MOSC samarium release experiments. We have shown that ray tracing techniques may be used to model the disturbances caused by artificial ionospheric modification. The samarium plasma clouds created at least three additional HF propagation paths in the ionosphere. One path is directly from the transmitter to the cloud to the receiver, while two others involve propagation between the F-region and the cloud; in one case interacting with the cloud first, refracting off the F-region to the receiver, and in the other reflecting from the F-region first and then reaching the receiver antenna by refraction from the cloud. These effects were observed both on a great circle path and a markedly non-great circle path where the refraction angle exceeds 90°. Additionally, a drop-out in the lower portion of the HF band was observed on the great circle path between Likiep and Wotho minutes after the first release. While we were not able to simulate this effect using a simple spherical cloud model, the rejection of other explanations such as absorption and reduced SNR, suggests that the divergent properties of a dense plasma "sphere" provide the most plausible reason for the drop-out.

For modeling the background plasma, when constrained by ALTAIR radar electron density profiles, the Parameterized Ionospheric Model (PIM) provided an excellent representation of the low latitude ionosphere during quiet conditions. Not surprisingly, neither PIM nor IRI were able to accurately specify local gradients during a modest magnetic disturbance. However, IRI's flexibility and convenient access to parameters within the model supported the use of a minimization technique to optimize the difference between the IRI model and observed time delays for constructing a valid regional ionosphere. Ray tracing confirms the sounder observations to a high degree of fidelity. Changes in the natural propagation environment can thus be successfully modeled, and the effects from arbitrary artificial plasma environments can be predicted with accuracy [23].

REFERENCES

[1] Bedinger, J. F., E. R. Manring, and S. N. Ghosh (1958), Study of sodium vapor ejected into the upper atmosphere, *J. Geophys. Res., 63*(1)*,* 19-29, doi: 10.1029/JZ063i001p0019.

[2] Rosenberg, N. W. (1963), Chemical releases in the upper atmosphere (Project Firefly), A summary report, *Geophys. Res., 68*(10), 3057–3063, doi: 10.1029/JZ068i010p03057.

[3] Corliss, W.R. (1971), NASA sounding rockets, 1958–1968: A historical summary. *Technical Report NASA SP- 4401,* National Aeronautics and Space Administration, Washington, D.C.

[4] Davis, T.N. (1979), Chemical releases in the ionosphere, *Rep. Prog. Phys.*, *42*, 1565, doi: 10.1088/0034-4885/42/9/003.

[5] Wand, R. H., and M. Mendillo (1984), Incoherent scatter observations of an artificially modified ionosphere, *J. Geophys. Res*., *89*(A1)*,* 203–215, doi: 10.1029/JA089iA01p00203.

[6] Bernhardt, P. A., et al. (2012), Ground and space-based measurement of rocket engine burns in the ionosphere, *IEEE Trans. Plasma Sci., 40,* 1267-1286, doi: 10.1109/TPS.2012.2185814.

[7] Bernhardt, P. A. (1987), A critical comparison of ionospheric depletion chemicals, *J. Geophys. Res., 92*(A5)*,* 4617–4628, doi: 10.1029/JA092iA05p04617.

[8] Hu, Y., Z. Zhao, and Y. Zhang (2011), Ionospheric disturbances produced by chemical releases and the resultant effects on short-wave ionospheric propagation, *J. Geophys. Res*., 116, A07307, doi: 10.1029/2011JA016438.

[9] Shuman, N. S., D. E. Hunton, and A. A. Viggiano (2015), "Ambient and Modified Atmospheric Ion Chemistry: From Top to bottom," *Chem. Rev.*, *115* (10)*,* pp 4542–4570, doi: 10.1021/cr5003479.

[10] Caton, R.G., et al. (2017), Artificial Ionospheric Modification – The Metal Oxide Space Cloud (MOSC) Experiment, *Radio Science, 52* , doi: 10.1002/2016RS005988.

[11] Davies, K. (1990), *Ionospheric Radio*, Peter Peregrinus, London, U.K.

[12] Pedersen, T. R., R. G. Caton, D. Miller, J. M. Holmes, K. M. Groves, and E. Sutton (2017), Empirical modeling of plasma clouds produced by the Metal Oxide Space Clouds experiment, *Radio Sci.*, **52**, doi:10.1002/2016RS006079.

[13] Haselgrove, J. (1955), Ray Theory and a new method for raytracing, in *Physics of the Ionosphere,* pp. 355-364, Physical Society, London.

[14] Jones, R. M., and J. J. Stephenson (1975), A versatile three-dimensional ray tracing computer program for radio waves in the ionosphere, *NASA STI/Recon Tech. Rep., 76,* 25,476, U.S. Department of Commerce, Off. of Telecommun., Washington, D. C.

[15] Coleman, C. J. (1993), A general purpose ionospheric ray tracing procedure, *Tech. Rep.,* SRL-0131-TR, Defence Science Technology Organization, Adelaide, Australia.

[16] Zawdie, K. A., D. P. Drob, J. D. Huba, and C. Coker (2016), Effect of time-dependent 3-D electron density gradients on high angle of incidence HF radio wave propagation, *Radio Sci., 51*, 1131–1141, doi: 10.1002/2015RS005843.

[17] Cervera, M. A., and T. J. Harris (2014), Modeling ionospheric disturbance features in quasi-vertically incident ionograms using 3-D magnetoionic ray tracing and atmospheric gravity waves, *J. Geophys. Res. Space Physics*, *119*, 431–440, doi: 10.1002/2013JA019247.

[18] Daniell, R. E., Jr., L. D. Brown, D. N. Anderson, M. W. Fox, P. H. Doherty, D. T. Decker, J. J. Sojka, and R. W. Schunk (1995), Parameterized ionospheric model: A global ionospheric parameterization based on first principles models, *Radio Sci*., *30*(5), 1499–1510, doi:10.1029/95RS01826.

[19] Bilitza, D., D. Altadill, Y. Zhang, C. Mertens, V. Truhlik, P. Richards, L.-A. McKinnell, and B. Reinisch (2014), The International Reference Ionosphere 2012 – a model of international collaboration, *J. Space Weather Space Clim*. *4*, A07, doi: 10.1051/swsc/2014004.

[20] Nelder, J. and R. Mead (1965), "A simplex method for function minimization", *Computer Journal*, *7*, 749-756, doi: 10.1093/comjnl/7.4.308.

[21] Press, W. H., S. A. Teukolsky, W. T. Vetterling, and B. P. Flannery (2007), Numerical Recipes 3rd Edition: The art of scientific computing, *Cambridge University Press,* New York.

[22] American Radio Relay League (1974), *The ARRL Antenna Handbook,* 13th ed., edited by G. Hall, pp. 49-57, American Radio Relay League, Newington, Conn.

[23] Joshi, D., K. Groves, W. McNeil, C. Carrano, R. Caton, R. T. Parris, T. Pedersen, P. Cannon, M. Angling, and N. Jackson-Booth (2017), HF propagation results from the Metal Oxide Space Cloud (MOSC) Experiment, *Radio Sci., 52*, doi:10.1002/2016RS006164.

CHAPTER 4 INVESTIGATION OF THE GENERALIZED RAYLEIGH TAYLOR INSTABILITY (GRTI) GROWTH RATE FACTORS OF EQUATORIAL IONOSPHERIC IRREGEULARITIES USING OBLIQUE HF LINKS

4.1 Introduction

In this chapter, we seek to calculate the various parameters influencing the growth rate of the Generalized Rayleigh Taylor Instability (GRTI) in the equatorial ionosphere from oblique High Frequency (HF) data and from model ionospheric profiles optimized by ray-tracing techniques to match actual delays as observed in HF data. The goal is to calculate the growth rate of the RTI to predict the diurnal variability of the spread F occurrence using simple HF link data. In the chapter following this, we seek to characterize the spatial distribution of the equatorial ionospheric irregularities and also try to understand the dependence of equatorial plasma bubble altitude at magnetic equator on solar activity by analyzing an elliptical satellite in-situ observations spanning half a solar cycle (2008-2014). The physics based ionospheric models lack the real-time knowledge of the ionospheric state to drive them to predict the occurrence of spread F. Hence, data from oblique HF links are used in this chapter to calculate the GRTI growth rate to compare with scintillation activity observed by ground-based receivers. The scintillation is the random fluctuation in phase and amplitude of the signals which can occur when the radio waves traverse through the plasma irregularities in ionosphere.

The MOSC campaign provided several days of HF data which we seek to analyze to understand the factors influencing the growth rate of generalized Rayleigh Taylor

Instability (GRTI). The irregularities in the ionosphere were first identified in ionograms by *Booker and Wells* [1] in which they reproduced records showing diffuse echoes from the F-region of the ionosphere continuously at night in equatorial regions over a wide range of wave-frequency. The irregularities, commonly called as equatorial spread F (ESF) owing to the spread nature of the traces in the ionogram, have since been studied extensively using host of diagnostic instruments including ionosondes, Very High Frequency (VHF) radars, airglow observations, VHF and Global Positioning System (GPS) scintillations, in situ rockets and satellite measurements, GPS-TEC map, etc. The total electron content (TEC) is the total number of electrons along a path between a radio transmitter and receiver which is generally measured in electrons per square meter. It was *Dungey* [2] who first proposed the idea that Rayleigh-Taylor instability could initiate ESF on the bottomside of the F region. Following *Dungey's* paper, several other works [3, 4, 5] have invoked Rayleigh-Taylor instability to explain the ESF. The in-situ rocket, satellite and radar observations [6, 7, 8, 9] also interpreted the structures in the plasma density as Rayleigh-Taylor instabilities. These early theoretical and observational works led the basis for accepting RT instability as the main mechanism for the creation of ESF [10]. Although the full-fledged plasma instability in the ionosphere occurs in non-linear state, the linear theory is valuable in understanding the onset and the basic physical mechanism of the instability [11]. The growth rates of the Rayleigh Taylor instability obtained from the linear treatment of the problem can also be useful to forecast/identify the possible regions of the equatorial ionosphere where plasma instabilities and radio-wave scintillation may occur. The non-linear evolution of the generalized Rayleigh Taylor (RT) instability in which the bottomside low-density plasma drifts upward into

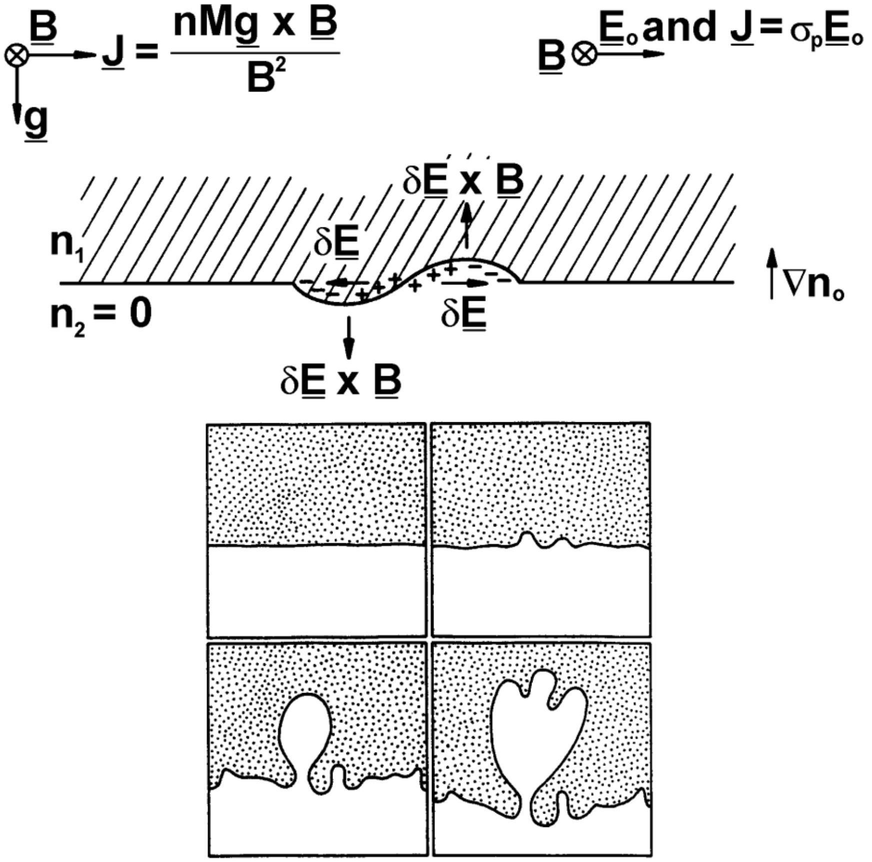

Figure 4.1: Illustration showing the initiation and development of plasma bubbles in equatorial ionosphere. The dense plasma is initially stacked on top of light plasma.

the high-density plasma much like the rise of air bubbles in a liquid [12] as shown in Figure 4.1 [13].

In section two of this chapter, we present the theoretical foundation of ionospheric plasma physics leading to the derivation of the growth rate expression and discuss the roles of various factors in the formula. In section three, we present oblique HF data from two nights representing cases of ‘disturbed’ and ‘quiet’ nights. We also apply numerical ray-tracing through a 2-D plane of model ionosphere to optimize the ionospheric profiles to match the observed oblique ionosonde delays of the respective nights. In section four, we present results from the VHF radar reporting scintillation activity for the chosen two nights. We also show the results for the various parameters of the growth rate calculated from the frequency-specific F-region delays and optimized ionospheric profiles. In section five, we present similar calculations made for thirteen nights during the campaign. We compare the growth rate values with the total hourly mean S4 (THMS4) index calculated from the VHF data. We describe the quantity THMS4 in detail in the corresponding section. In the final section, we discuss our conclusions and future work.

4.2 Review of Generalized Rayleigh Taylor Growth Rate

We deduce the growth rate for the Rayleigh-Taylor instability in the ionospheric F-region. Owing to the complexity involved, we exclude the independent heat equations and hence the thermal analysis [13]. The following set of dynamic and electrodynamic equations are applicable in description of the plasma fluid in the ionosphere:

$$\frac{\partial \mathrm{n}_\alpha}{\partial \mathrm{t}} + \nabla.(\mathrm{n}_\alpha \mathrm{V}_\alpha) = \mathrm{P} - \upsilon_\mathrm{R} \mathrm{n}_\alpha \qquad --- (1)$$

$$-T_e \nabla n_e - e n_e \left(-\nabla \phi + \frac{V_e \times B_o}{c} \right) = 0 \quad --- (2)$$

$$m_i n_i \left(\frac{\partial}{\partial t} + V_i . \nabla \right) V_i$$

$$= -T_i \nabla n_i - e n_i \left(-\nabla \phi + \frac{V_i \times B_o}{c} \right) + m_i n_i \mathbf{g} - m_i n_i \upsilon_{in} V_i \quad --- (3)$$

$$\nabla . J = 0 \qquad --- (4)$$

$$J = ne(V_i - V_e) \quad --- (5)$$

where, α (subscript) = species (e = electron, i = ion)

n = density,

V = Velocity,

P = Production,

B_o = the ambient magnetic field,

e = the electronic charge,

c = the speed of light,

m = mass,

g = the gravity,

υ_{in} = the ion-neutral collision frequency,

J = the current.

Equations (1-5) are taken from the review paper by *Ossakow* [14, 15] and we follow the treatment in the paper while calculating the growth rate expression. Equation (1) is the continuity equation which can be derived applying the principle of conservation of mass. Equation (2) and (3) are electron and ion momentum equations which can be derived from the principle of conservation of momentum. The momentum equation relates the fluid velocity to the forces acting on the fluid. Equation (4) is assuming the divergence of current to be zero as small charge differences create large electric fields in an ionized medium. Equation (5) is the current equation. The electrostatic approximation $E = -\nabla\phi$ has been used to find the electric field.

We take the harmonic solution of the form $\exp^{-i\,(k.x_{\perp}\ -\ \omega t)}$, where $\perp$ denotes perpendicular to ambient magnetic field. The solution gives us the linear growth rate,

$$\Upsilon = \frac{\left[-\upsilon_{\text{in}} + \left(\upsilon_{\text{in}}^2 - 4\,g.\frac{\nabla n_o}{n_o}\right)^{\frac{1}{2}}\right]}{2} - \upsilon_R \quad ---(6)$$

The growth rate is defined in the angular frequency as:

$$\omega = \omega_{\Upsilon} + i\,\Upsilon ;$$

Equation (6) further reduces to:

$$\Upsilon = \frac{g}{\upsilon_{\text{in}}\,L} - \upsilon_R\,, \qquad \upsilon_{in}^2 \gg 4\,g/L \quad ---(7a)$$

$$= \frac{(g)^{1/2}}{L} - \upsilon_R\,, \qquad \upsilon_{in}^2 \ll 4\,g/L \quad ---(7b)$$

where,

$$\frac{1}{L} = \left|\frac{\nabla n_o}{n_o}\right|$$

The equations 7(a) and 7(b) represent growth rate of the Rayleigh-Taylor instability.

By taking non-linear evolution of the collisional R-T instability which involves neglecting the inertial terms in the equation (3) and applying quasi-neutral approximation, $n_e \approx n_i \approx n$ and linearizing the equations, the linear growth rate can also be calculated as:

$$\Upsilon \quad = -\frac{\vec{g}}{\upsilon_{in}\, L} - \upsilon_R \quad ---(8)$$

The equation (8) shows that the bottomside of the F region can be linearly unstable in case of a positive gamma which happens when the first term is positive and exceeds the second term in magnitude. This indeed can happen in the bottomside of the F region where the density gradient is positive and the acceleration due to gravity is negative as we go upwards.

Sultan [16], in his paper, discusses that the locally determined growth rate is inadequate for determining the realistic onset conditions for equatorial spread F as it misses the actual physical phenomenon taking place. The actual physical process which occurs in the equatorial ionosphere is the coupling of the ionosphere above the equator to the ionosphere away from the equator due to the equipotential nature of earth's magnetic field lines and the faster transport of electrons and ions along the magnetic field than perpendicular to it. As the depletion of the ionospheric plasma grows into a bubble and rises to higher altitudes at the magnetic equator, the disturbances are mapped along the magnetic field lines towards both the hemispheres to lower altitudes. In order to calculate the growth rate of Rayleigh-Taylor instability for the entire flux-tube, we shall integrate the current and the ion velocity equations along the magnetic field lines. We present the final expression for the flux-tube integrated growth rate [16]:

$$\Upsilon = \frac{\Sigma_P^F}{\Sigma_P^E + \Sigma_P^F} \left(V_p - U_n^P + \frac{g_L}{\upsilon_{in}^{eff}} \right) \frac{1}{L_n} - R_T \qquad \text{--------} \ (9)$$

where,

Σ_P^F = the F-region integrated Pederson conductivity

Σ_P^E = the E region integrated Pederson conductivity

V_p = the integrated plasma drift

U_n^P = the integrated neutral wind,

g_L = the effective gravity,

υ_{in}^{eff} = the effective collision frequency,

L_n = gradient scale length,

R_T = the effective recombination rate.

Zalesak and Ossakow [17], in their work, have stated the following expression without derivation as an extension of the local growth rate formula combining local terms ($\overrightarrow{\mathbf{v}_p}$, $\overrightarrow{\mathbf{u}_n}$, and υ_{in}) with flux tube terms (Σ_P, R and N).

$$\Upsilon = \frac{\Sigma_P^F}{\Sigma_P^E + \Sigma_P^F}\left(\overrightarrow{\mathbf{v}_p} - \overrightarrow{\mathbf{u}_n} - \frac{\vec{\mathbf{g}}}{\upsilon_{\mathrm{in}}}\right)\frac{1}{\mathrm{N}}\frac{\partial N}{\partial h} - R_{\mathrm{T}} \quad --- (10)$$

Note that it has been realized that recombination rates that are linear in the plasma density (which constitute the largest part of the recombination rate at F region altitudes) do not contribute to the term R_T [18], because they reduce the density proportionally everywhere at the same rate, thus this term can usually be neglected.

4.3 Observations

In this section, we seek to analyze thirteen nights of HF data during the Metal-Oxide Space Cloud (MOSC) campaign to understand the parameters influencing the generalized Rayleigh Taylor Instability (GRTI). We illustrate our methodology by taking two nights of data representative of quiet and disturbed nights during the pre-reversal enhancement period (07:26 – 07:51 UTC) prior to the occurrence of the spread F. The pre-reversal enhancement [19] is the brief and intense increase in the eastward electric field in the equatorial ionosphere when the E-region conductivity decreases rapidly immediately after the sunset. Here, the goal is to create ionospheric time delay contours of F-region layers of certain frequencies (4.39 MHz, 5.54 MHz, 7.15 MHz, 9.12 MHz) in the evening period which would possibly observe pre-reversal enhancement and spread-F.

In Figure 4.2, the site locations corresponding to the HF links are shown. While there were two HF receivers and two transmitters in the site making four possible paths, we focus on the signals received at Wotho from transmitter at Rongelap. The Rongelap-Wotho link geometry is predominantly N-S. Geographic coordinates for the sites are given in Table 4.1. After examining the ionograms of all thirteen evenings, we found the possible pre-reversal enhancement and spread F would occur within the time period 06:31 – 09:26 UTC. The four frequencies taken are 4.39, 5.54, 7.15 and 9.12 MHz. We analyze the power-spectrum data to find the weighted average of the time-delay for a range of F-region reflected HF energy corresponding to a frequency. The range is determined by going above and below the peak power of reflected HF energy by 30 dB. In Figure 4.3, we show hourly ionograms beginning at 07:31 UT on the night of 27th April, 2013 showing the growth of the spread F. The time-delay contours of the frequency specific F-region layers show the F-region is drifting upward. In Figure 4.4, the hourly ionograms beginning at 07:31 UT on the night of 3rd May, 2013 show significantly less spread than 27 April. The contour image shows the frequency specific layers of the F-region aren't rising as rapidly as on 27 April.

Table 4.1: Geographic Site Co-ordinates in Marshall Islands

Site	Latitude	Longitude
Rongelap	11.1523	166.8378
Likiep	9.8262	169.30673
Wotho	10.17404	166.0046
ALTAIR	9.3954	167.4793

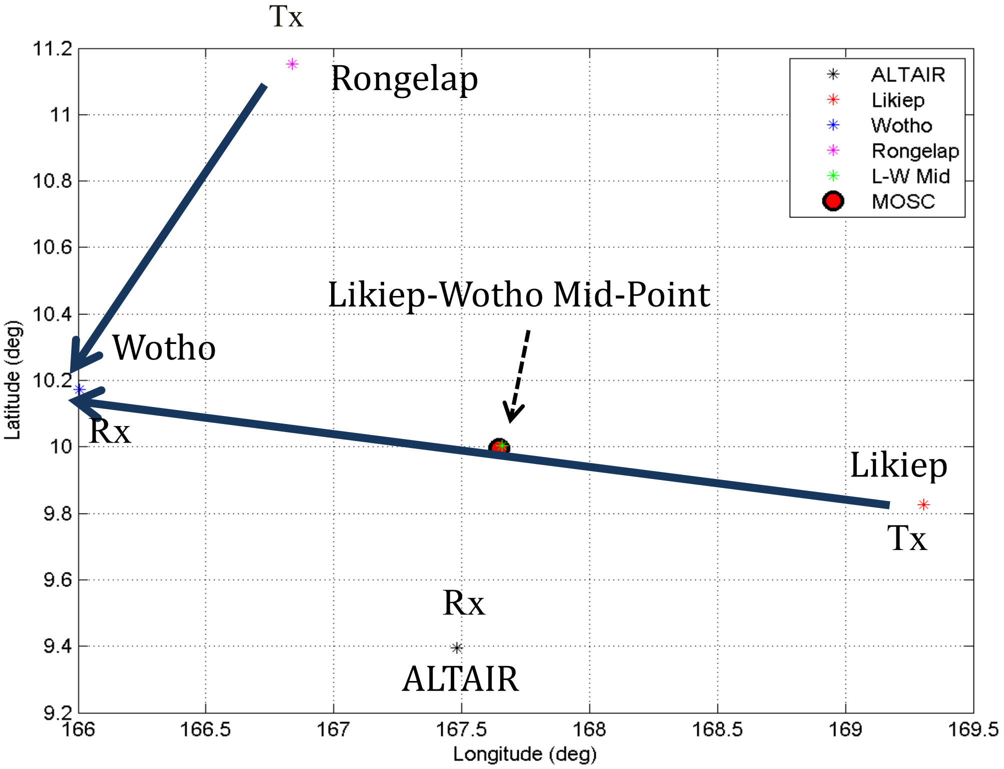

Figure 4.2: Site Locations in Marshall Islands. Tx = Transmitter, Rx = Receiver.

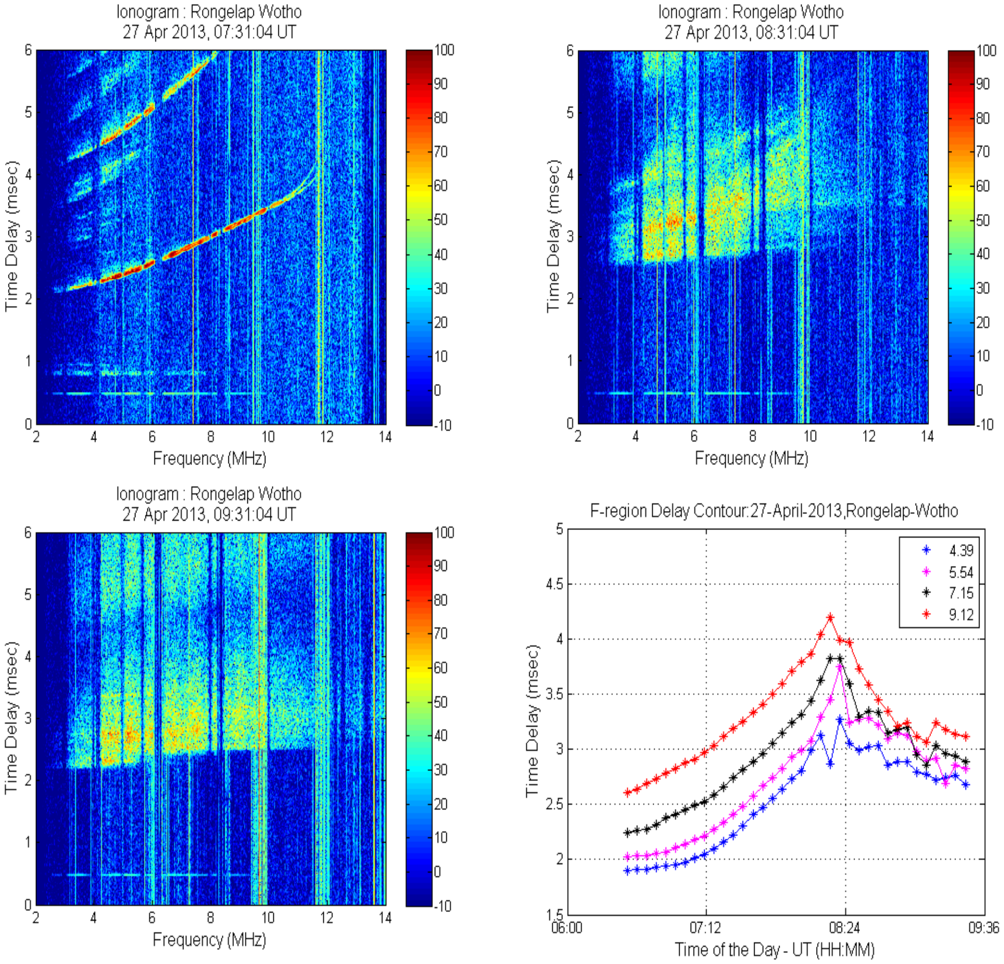

Figure 4.3: The hourly ionograms beginning at 07:31 UT on the night of 27th April. The contours of the frequency specific F-region layers show strong upward drift of the F-region before spread F.

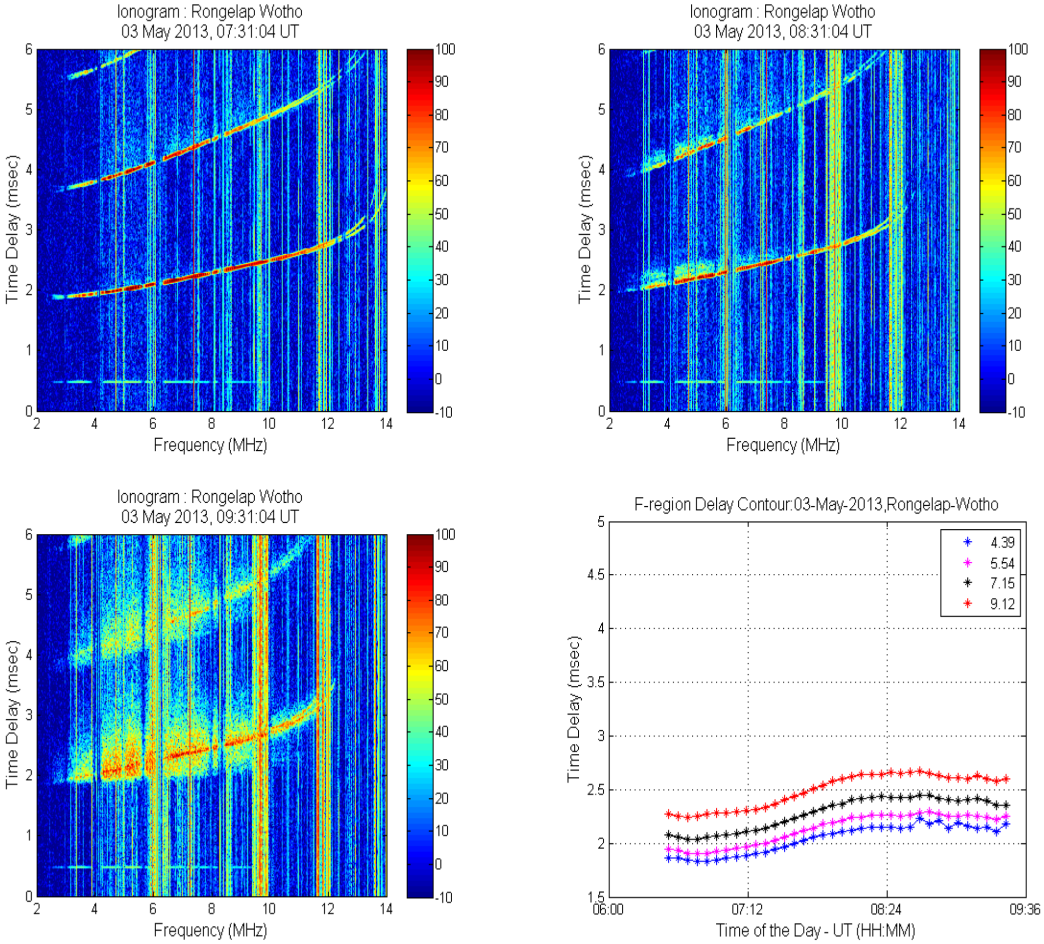

Figure 4.4: The hourly ionograms beginning at 07:31 UT on the night of the evening of 3 May, 2013, which shows considerably less spread than 27 April. The time-delay contours of the frequency specific F-region layers show weak upward drifts.

From the F-region layer contours, we can derive:

i) Upward Plasma Drift (V_p)

ii) Gradient Scale Length

$\frac{1}{L} = \frac{1}{Ne}\frac{dNe}{dh}$; N_e is the electron density, h is height

iii) Ion Collision frequency

$v_{in}^{eff} = (2.6 \times 10^{-9})\,(n_n + n_i)\,A^{-1/2}\ s^{-1}$; n_n is neutral density and n_i is the ion concentration in reciprocal cubic centimeters, and A is the mean molecular weight of the neutrals and ions. The gradient scale length between two frequency layers can be calculated by converting the electron density variation to change in frequency. The ion concentration can be calculated from the quasi-neutral approximation, $n_e \approx n_i$ and the neutral density and the mean molecular weight at a certain height can be calculated from the Mass-Spectrometer-Incoherent-Scatter (MSIS) model [20].

The Mass-Spectrometer-Incoherent-Scatter (MSIS) model describes the neutral temperature and densities in the upper atmosphere (above about 100 km) [21]. MSIS-86 constitutes the upper part of the Committee on Space Research (COSPAR) International Reference Atmosphere (CIRA) 1986. The MSIS model is based on the extensive data compilation and analysis work of A. E. Hedin and his colleagues. Data sources include measurements from several rockets, satellites (OGO 6, San Marco 3, AEROS-A, AE-C, AE-D, AE-E, ESRO 4, and DE 2), and incoherent scatter radars (Millstone Hill, St. Santin, Arecibo, Jicamarca, and Malvern). The MSIS-E-90 is the extended MSIS-86 model taking into account data derived from space shuttle flights and newer incoherent scatter results [22].

The local values of the above mentioned quantities can be calculated from the frequency specific F-region time-delay contours to compare the relative change in the growth rate. We can take the height needed to calculate the neutral density in the collision frequency expression from the virtual heights determined from the time-delay contours by applying the simple formula:

$$\text{Virtual height} = \frac{\text{speed of light}}{2} \times \text{time delay}$$

The equivalent virtual heights for the time-delay contours in Fig 4.3 and Fig 4.4 are shown in Fig 4.5. The ‘virtual’ plasma drift can also be calculated from the height contours.

Since virtual height will always be larger than the ‘true’ height, calculation of ion-neutral collision frequency at the virtual heights will produce bias because the neutral densities will be small there lowering the value of ion-neutral collision frequency and thus, increasing the RT growth rate value. To circumvent the bias, we instead use the ‘true’ heights from the digisonde and the ALTAIR radar data to compute the ion-collision frequency. The drift velocity and the gradient scale length shall not be appreciably different calculated from either the virtual heights or the true heights as it is change of heights involved in differentiation to calculate these quantities. We explain it in a little more detail in the next section.

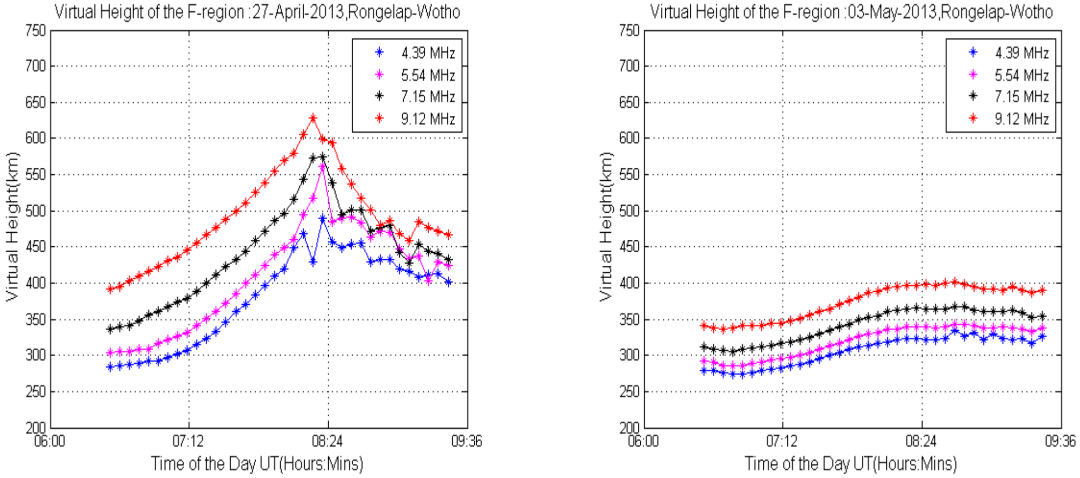

Figure 4.5: Virtual height contours of frequency F-region layers for the nights of April 27 and May 03, 2013 along the Rongelap-Wotho path. The equivalent time delays contours are in Fig 4.3 and 4.4.

We can also compute the above-mentioned quantities using the optimized model ionospheric profiles instead of the virtual height contours. We seek to use the numerical ray-tracing through a 2-D plane of ionosphere along the Rongelap-Wotho path to optimize the IRI profiles (Fig 4.6) to match the observed oblique ionosonde delays. The Nelder-Mead Downhill Simplex [23, 24] method is applied to optimize the IRI profiles to be used in lieu of the true profiles to calculate the quantities in the growth rate of the linearized Gravitational Rayleigh Taylor Instability (GRTI) equation. We used the native 'fminsearch' function in MATLAB to optimize the IRI profiles.

The International Reference Ionosphere (IRI) [25] is an empirical model ionosphere developed as a joint project of the Committee on Space Research (COSPAR) and the International Union of Radio Science (URSI). For a given location, time, and date, IRI provides the median monthly values of electron density, the electron temperature, and ion composition in the altitude range 50 km to 2000 km. The major data sources for the IRI model are the worldwide network of ionosondes, the powerful incoherent scatter radars, (Jicamarca, Arecibo, Millstone Hill, Malvern, St. Santin), the International Satellites for Ionospheric Studies (ISIS) and Alouette topside sounders, and in situ instruments on several satellites and rockets.

Since *Haselgrove* [26] set down the differential equations governing ray paths in an anisotropic medium for numerical integration techniques [26, 27, 28], the equations have been used extensively [29, 30, 31] to study the propagation of HF energy through the ionosphere. In this work we apply numerical ray-tracing through a 2-D plane of ionosphere to optimize the IRI profiles to match the observed oblique ionosonde delays using PHaRLAP, a HF radio wave ray tracing MATLAB toolbox developed by Dr.

Manuel Cervera, that contains a variety of ray tracing engines of various sophistication from 2-D ray tracing to full 3-D magnetoionic ray tracing [32]. We build the 2-D ionospheric plane along the Rongelap-Wotho path using the 2-D ionospheric grid generator file in the PHaRLAP package. We used a modified IRI 2016 subroutine developed at Institute for Scientific Research, Boston College:

[a, b] = iri2016bcw (yyyy, mmdd, UT, Lat, Lon, foF2, hmF2, foF1, foE, B0, B1)

where,

YYYY – Year,

Mmdd – Month and Day,

UT – Time in UT

Lat, Lon – Geographic latitude and longitude in degrees

foF2, foF1, foE – peak densities in MHz

hmF2 – peak height of F2 layer in km

B0, B1 – thickness parameters

a – 1× 1000 array of plasma freq. profile in MHz (from 65 km and up with 1 km step),

b – IRI output array.

We take the IRI profile at the mid-point along the Rongelap-Wotho path and use the same profile for the entire plane along the path. We fix the shape parameter B1 at 3.5.

The B0 parameter is defined as the difference between hmF2 and the altitude where the electron density equals to 0.24*NmF2 (h0.24) [33]. Hence, B0 makes a measure of the thickness of the bottomside profile. The B1 parameter determines the shape of the profile between maximum hmF2 and h0.24. The higher B1 corresponds to the larger densities in the region between hmF2 and h0.24. We also fix the highest frequency the ionosphere will reflect (foF2) as according to the observations in the ionograms of the oblique HF links. We used the secant law to change the observations from the oblique links to equivalent foF2 for vertical HF propagation:

$\mathrm{f_{ob}} = \mathrm{f_{vert}}\ \sec(\Theta_i)$; Θ_i = angle of incidence of a ray path with the plane of ionosphere

Any of the six parameters (foF2, hmF2, foF1, foE, B0, B1) in above subroutine can be left to IRI to calculate. Obviously, the first five parameters (yyyy, mmdd, UT, Lat, Lon) need to be given as inputs. So, we fix two parameters foF2 and B1 and let IRI determine the values for foF1 and foE. We let the optimization vary hmF2 and B0 so as the profile evolves to create a plane which would produce ray-traced time-delays matching the observed time-delays in HF sounder data.

We seek to compare the calculated growth rate with the scintillation activity reported in the ground-based observations. We use the Total Hourly Mean S4 (THMS4) index [34, 35] which is the accumulated sum of 5 hourly S4 means with a nightly accumulation window from 800 to 1300 UT as measured by the VHF receiver (Fig 4.7) at the Kwajalein Atoll. The S4 is amplitude scintillation index defined as the ratio of the standard deviation of the signal intensity and the average signal intensity.

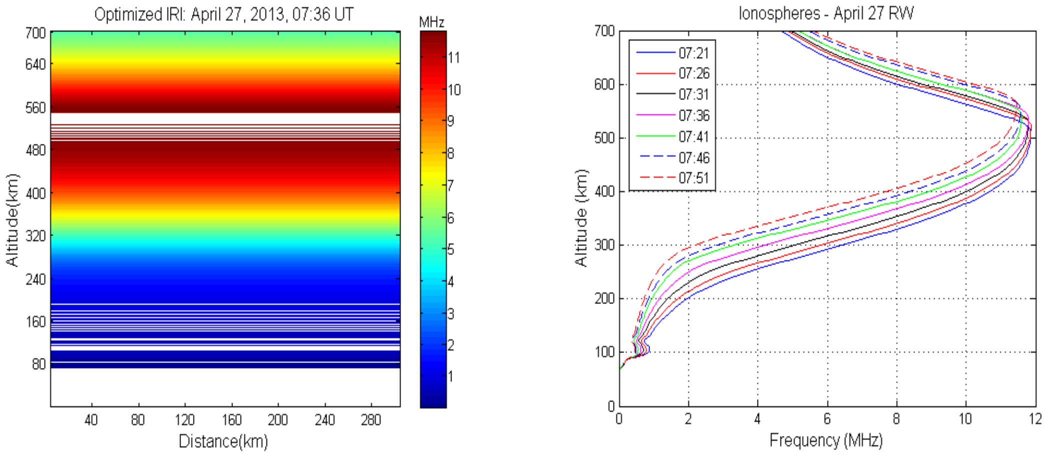

Figure 4.6: Numerical ray-tracing through a 2-D plane of ionosphere (left) is used to optimize the IRI profiles (right) to match the observed oblique ionosonde delays.

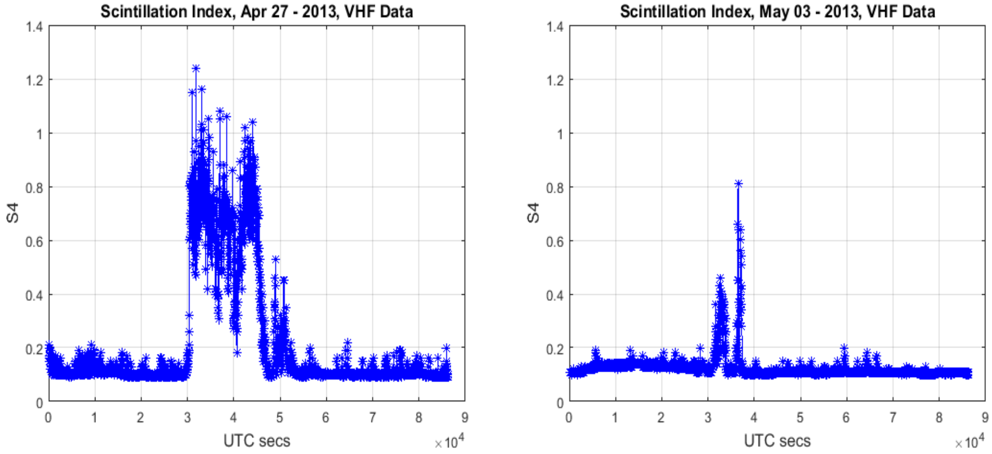

Figure 4.7: S4 indices of VHF signal, 244 MHz received at Kwajalein Atoll in Marshall Islands. The THMS4 index calculated from 8:00 to 13:00 UT takes the values 3.0126 and 0.7486 on April 27 and May 03 respectively.

$$S4 = \sqrt{\frac{< I^2 > - < I >^2}{< I >^2}}$$

where, I is the signal intensity and the upper limit of the S4 is 1.

4.4 Results and Discussion

The quantities we seek to calculate from the virtual height contours or the optimized model ionospheric profiles are: drift velocity, gradient scale length and the ion collision frequency. While calculating drift velocity and gradient scale length from the virtual height contours is straightforward, we use the 'true' heights from the digisonde and the ALTAIR radar data to compute the ion-collision frequency. For a given day, we take the average 'true' heights from the available digisonde data between the 07:26 – 07:51 UTC and calculate the collision frequency at that height corresponding to ion frequency of 7.15 MHz and the neutral densities taken of top three constituents O, N2 and N from the MSIS-E-90 model. Similarly, the gradient scale length for a given day is taken to be the average of the quantity between the virtual height contours of 5.54 and 7.15 MHz during the period 07:26 – 07:51 UTC. The drift velocity for a day is calculated by averaging the average of drift velocities corresponding to all four frequencies during the time period 07:26 – 07:51 UTC.

We use similar approach while calculating these quantities from the ray-traced optimized profiles. The advantage in using the ray-traced optimized profile is we can obtain these quantities for the entire frequency-range of the ionospheric profile than just the four frequencies we had for the virtual heights and time-delays (Figure 4.8). In Figure 4.8, we show the drift velocity and the gradient scale length calculated from the ray-traced

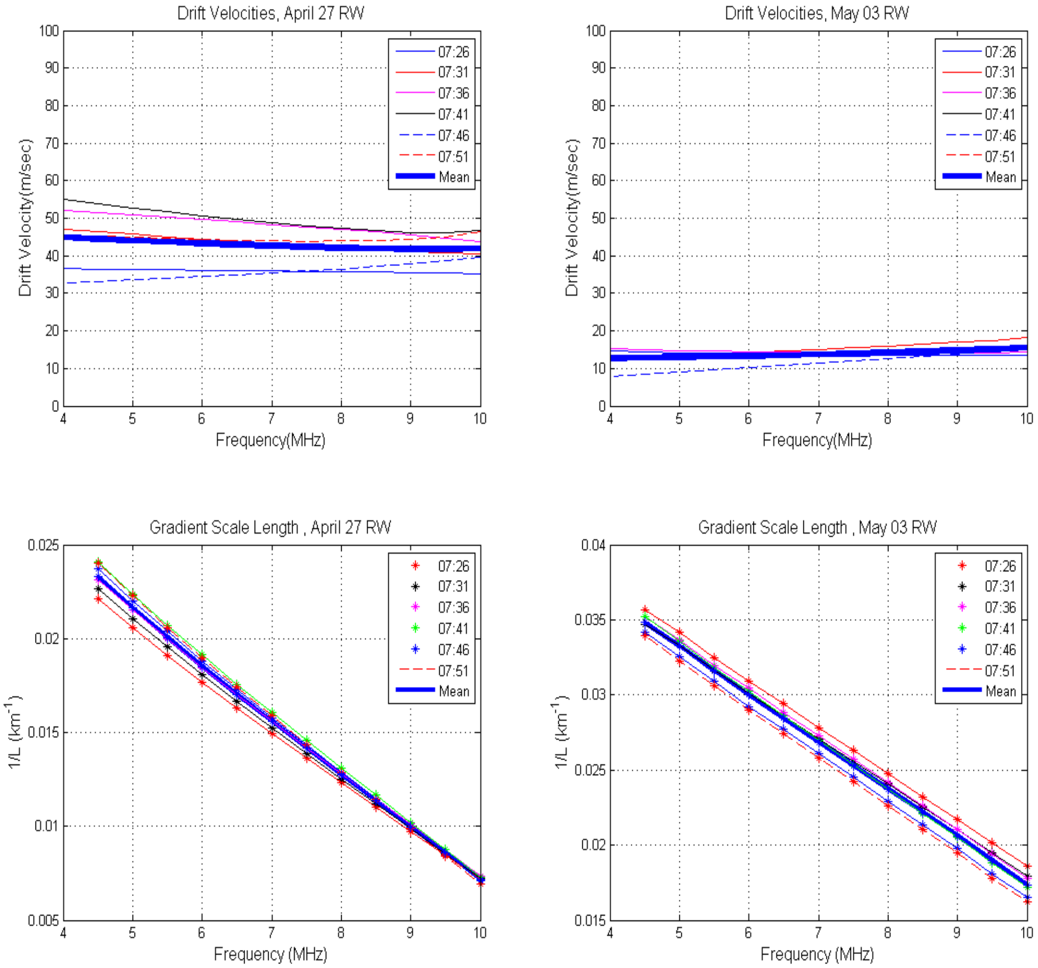

Figure 4.8: Plasma drifts calculated from the optimized profiles on April 27 and May 3 (Upper Row); Gradient Scale Lengths on April 27 and May 3 (Lower Row)

optimized ionospheric profiles during the time period 07:26 – 07:51 UTC for the two days – Apr 27 and May 3. The mean of these quantities plotted in the images in Figure 4.8 are the average of these quantities calculated from six profiles during the time period 07:26 – 07:51 UTC in successive five minutes as the HF frequencies were transmitted/received every five minutes. For a given day, the drift velocity is then taken to be of 8 MHz of the mean drift velocity. The gradient scale length is taken to be that between 7.5 and 8 MHz of the mean gradient scale length. And the collision frequency is calculated for the average height of 8 MHz for each day -- the average height taken out of all the profiles for the time-window for a day. The quantities and the growth rate calculated from either of the two approaches are shown in the Fig 4.9. The corresponding scintillation activity represented by total hourly mean S4 (THMS4) index which is highly correlated with the calculated linear growth rate is also shown.

Sultan [17], in his paper, has used atmospheric and ionospheric density model inputs to make quantitative calculations of the growth rate for a range of geophysical conditions. In the work, comparison of the growth rate calculated from the flux-tube formalism is made with the local growth rate. While it is concluded in the aforementioned paper that magnetic flux tube formalism better duplicates the physics of the equatorial ionosphere and locally determined growth rates are inadequate for determining the onset conditions for ESF, *Mendillo et al.* [36] in their work do acknowledge the local growth rates to be instructive in understanding the growth-rate characteristics. *Mendillo et al.* further assert the use of local growth rate avoids the uncertainties and assumptions applied in models of flux-tube-integrated quantities. *Rappaport* [37] shows that the equipotential approximation along the magnetic field lines made in flux-tube formalism produces a

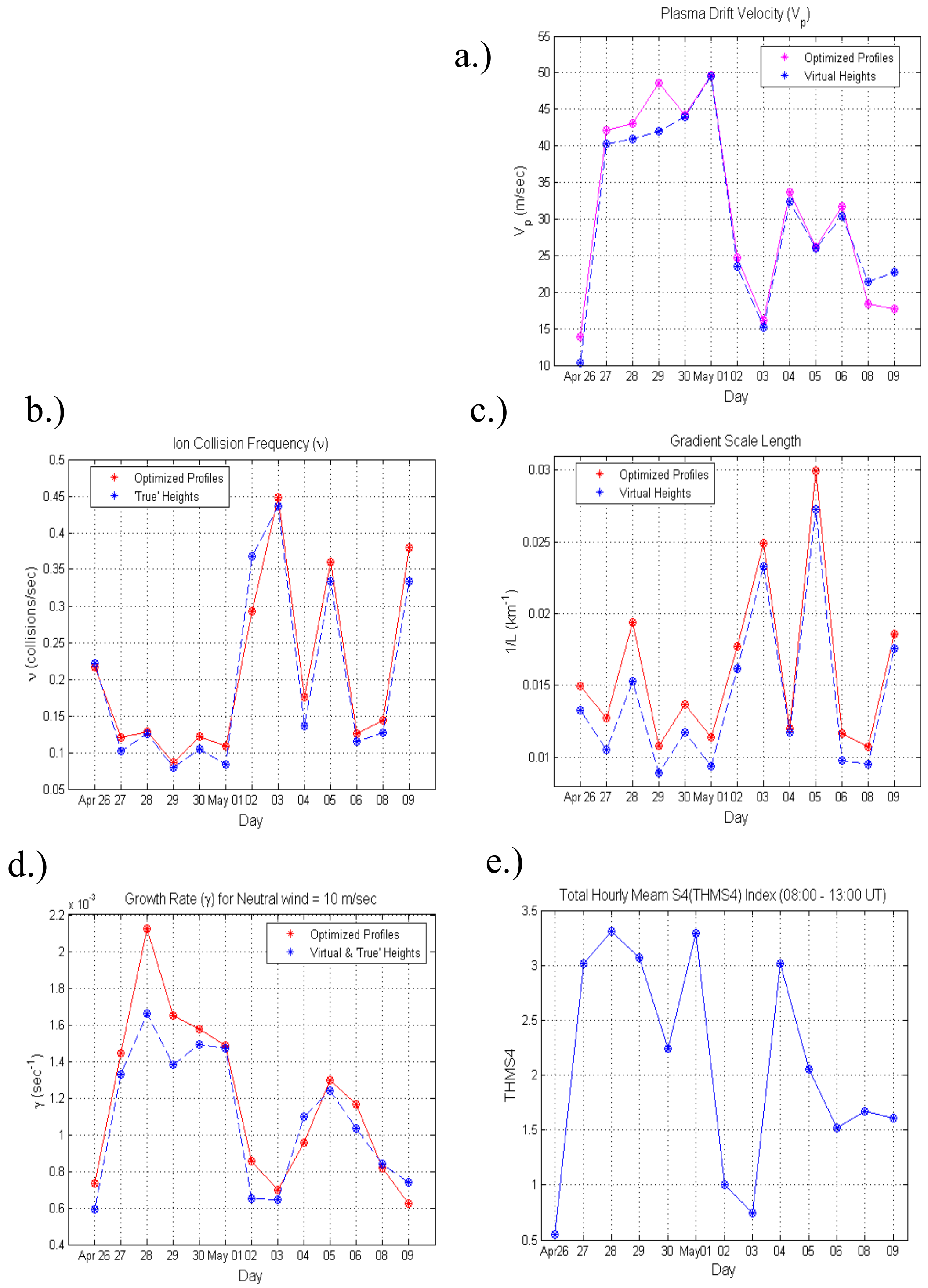

Figure 4.9 : Growth rate parameters plotted during the pre-reversal enhancement period (07:26 – 07:51 UT) prior to the occurrence of spread F. a) Drift Velocity b) Ion Collision Frequency c) Gradient Scale Length. Results for growth rate are shown in panel d) above where the neutral wind component (U_n^P) = 10 m/sec for each day is assumed. The corresponding scintillation activity represented by total hourly mean S4 (hourly mean S4 integrated from 08:00 to 13:00 UT) is shown in panel e, highly correlated (> 80 %) with the calculated linear growth rate.

lower bound for the true growth rate whereas local growth rate provides an upper bound. *Basu* [11], in his paper, compares the different descriptions on the linear theory of equatorial plasma instability. In addition to the local and the flux-tube formalism, he also discusses the so-called ballooning-mode type description of the problem. In this work, we don't intend to get into the theoretical aspects of the problem and try to make comparisons of one approach against another. Instead we seek to adopt an approach to compute the growth rate to understand its relative change in the thirteen days of the campaign and compare it with the ground scintillation observations. The local values of the drift velocity, the gradient scale length and the collision frequency are calculated to obtain the growth rate as given as:

$$\Upsilon = \left(V_p - U_n^P + \frac{g}{\upsilon_{\mathrm{in}}}\right)\frac{1}{L_{\mathrm{n}}} \quad \text{----- (11)}$$

Since the growth rate is computed during the pre-reversal enhancement period 07:26 – 07:51 UTC, the fraction appearing in equation (9) or (10) $\frac{\sum_P^F}{\sum_P^E + \sum_P^F}$ equals 1 as we assume the E-region, and hence the E-region Pedersen conductivity, disappears during this period. The chemical recombination rate is neglected and we assume the neutral wind component (U_n^P) = 10 m/sec for each day. The density scale length factor $(\frac{1}{L_{\mathrm{n}}})$ in equation (11) is the 'initial source of free energy' [17] that permits the Rayleigh-Taylor instability process to occur. The terms inside the bracket are the multiplicative factor to the density scale length factor which is positive in the bottom-side of the F-region. The role of drift velocity, the first term inside the bracket in equation (11), has been wellrecognized as an important, parameter controlling the generation of spread F [38, 39]. It also lifts the F layer, so that the collision frequency is smaller, making the gravity term bigger. The question amongst the researchers is if there is a threshold value for the upward drift velocity during pre-reversal enhancement for the generation of plasma bubbles. *Huang and Hairston* [40] offer a good review of past works on this question. As *Sultan* [17] argues in his paper, offering a 'threshold value' for any single parameter to predict spread F can easily be refuted by 'counter-examples' in which ESF didn't occur when the parameter was higher than the 'threshold value'. Hence, relying on the growth rate – which captures the cumulative effect of the various parameters involved in the equation – can be a more nuanced approach. In Fig 4.9, the panel (a) showing the drift velocity correlates well with high values of the calculated growth rate (panel (d)) and the THMS4 (panel (e)) on April 27, 28, 29, 30, May 1. The drift velocity on other days also correlate well with the scintillation activity – low drift velocity on low scintillation activity days of April 26, May 2 and May 3. The ion-collision frequency is inversely proportional to the growth rate. Hence, a low (high) value of ion-collision frequency is expected to cause high (low) value of growth rate. This is true for most of the days except May 5 in Fig 4.9 – panels (b) and (d). The high value of inverse gradient scale length (panel (c)) and the moderately high value of the drift velocity make the growth rate high despite having the collision frequency high. The values ($5\times10^{-2} – 5\times10^{-1}$) of ion-collision frequency is within the range of the results ($\sim 1\times10^{-2} – 1\times10$) in previous studies [10, 34] and (~0 – 100) in *Sultan*'s paper [17]. It also compares well with the results in *Basu*'s [11] paper in which the quantity is calculated along an entire field line. The paper defines the dipole coordinate system (ρ, ψ, s) in terms of the spherical coordinate system (r, ψ,Θ) as:

$$\rho = \frac{r}{cos^2\, \theta}, \; \mathrm{s} = \frac{r_o^3}{r^2}\, sin\theta$$

where θ is magnetic latitude measured from the equatorial plane and r_o is the radial distance from the Earth's center at which a field line intersects the equatorial plane. For $\hat{s}$(≡ *s/l*) value of ~ 0.33 corresponding to the magnetic latitude of the Marshall Islands, where 2*l* (*l* = 1.5×10^3 km, $\hat{s} = 0$ is magnetic equator) is the length of the field line along which the quantity is calculated, the ion-collision frequency has value in the range of $1\times10^{-1} - 1\times10$ (Fig. 1 and Fig. 4 in the paper [11]). In panel (c), the inverse density gradient scale length is plotted and has its value within the range of 0.005 – 0.030 km^{-1} which is close to that in the works of *Mendillo et al.* [33] (0- 5×10^{-2} km^{-1}) , *Lee* [10] (0.3 – 1.1×10^{-2} km^{-1}) , *Basu* [11] (0.005 – 0.040 km^{-1}) but smaller than that in the work of *Ossakaw et al.* [41] (0.1 -- 0.2 km^{-1}). From the equation (11), we would expect the growth rate to increase (decrease) with the increase (decrease) of inverse gradient scale length. But, the inverse scale length in our results has mostly anti-correlated with the growth rate with few days of correlation as well. This can be seen in the panels (c), (d) and (e) where, for example, both the days April 26 and May 03 with low growth rate (scintillation observations) respectively have low and high inverse scale length. There is no threshold of inverse gradient scale length we have marked as 'low' or 'high' as there will be consequences with any such choice. But taking any reasonable value as a threshold for the inverse gradient scale length will continue to show both correlation and anti-correlation with the calculated growth rate or the THMS4. It shows again that the growth rate and consecutively the occurrence of spread F is essentially a culmination of the cumulative effects of all the factors in the growth rate expression. The growth rate calculated from above factors is shown in the panel (d) which is in the same order of magnitude with the values in the work of *Basu* [11] and in the work of *Sultan* [17], within the range of the values in the work of *Lee* [10]. It is also in the same order of magnitude with the values in the work of *Mendillo* [36],but the negative values in their work is due to the inclusion of recombination rate in the growth rate expression. In Figure 4.9, the calculated growth rate in panel (d) correlates very well with the THMS4 index in panel (e) except for three days May 4, 8 and 9 for which the correlation isn't as obvious. It doesn't suggest anti-correlation for these days. The growth rate calculated from either of the two approaches – virtual heights/time delays or optimized ray-traced model ionospheric profiles – give us similar growth rate as seen in the panel (d).

Overall, the patterns of day-to-day variation of the calculated growth rate and scintillation strength match each other well. The small discrepancies between the calculated growth rate with the scintillation observations could be ascribed to the assumptions we have made in our approach: (i) constant neutral wind (10 m/sec) for all thirteen nights of observations, (ii) the vanishing of E-region conductance for all nights, (iii) negligible role of the recombination rate. We also note that scintillation is dependent on more than linear instability, it requires nonlinear development of short-scale irregularities, and also depends on the magnitude of the initial seed irregularities that get amplified by the linear instability. We made the assumptions not to avoid complexity but to permit us to deduce the growth rate from HF data. The HF sounding observations do not avail us information about the neutral wind and conductance. The neutral wind in the growth rate expression is in the perpendicular direction to the magnetic field and hence, this is quite a small value

[42] in both cases – if we take it locally or flux-tube-integrate in both hemispheres. The flux-tube-integrated neutral wind is a small value as the vertical component of the wind in two hemispheres act to counteract each-other and the resultant effect of an integration over an ionosphere symmetric with respect to the magnetic equator is cancelling out of the wind [17]. The prevailing belief is that meridional neutral winds act to suppress the instability in the equatorial ionosphere by creating (i) a tilt in the ionosphere in the direction of the wind and (ii) by transporting plasma between hemispheres [17,36]. However, in a recent paper, *Huba and Krall* [43] revisit the question and show that the meridional winds can be destabilizing for the equatorial ionospheric instability. But it is the vertical neutral wind – the component of the meridional neutral wind perpendicular to the magnetic field line – which appears in the growth rate expression. *Sekar and Raghavarao* [44] and *Krall et al.* [45] have shown that the upward vertical winds are a stabilizing influence while downward neutral winds are destabilizing influence on the development of ESF. Hence, although we assumed a small constant value of upward neutral wind in the growth rate expression, the day-to-day variations in the vertical neutral wind may have contributed some spread in the values of the growth rate.

The growth rate has been calculated in the pre-reversal enhancement period 07:26 - 07:51 LT. It is for this reason we assumed the disappearance of the E-region Pedersen conductivity as the E-region plasma vanishes after sunset due to rapid recombination with the molecular ions at the E-region altitudes. The disappearance of E-region conductivity allows us to take the conductivity ratio before the parentheses in the growth rate formula as 1. *Zalesak et al.* [46] have showed through numerical simulations that E region Pedersen conductivity effects result in slowing down of equatorial spread F and attendant bubble evolution. But as *Tsunoda* [47] shows in his paper that instead of the simple early unloading of the F region dynamo, longitudinal gradient in the integrated E region Pedersen conductivity is the likely source of free energy to enhance the irregularity generation. While we assumed the E-region Pedersen conductivity to be zero, the treatment of the longitudinal gradient in the E-region Pedersen conductivity is beyond the scope of this study. We note that such features are part of the structure which gives rise to the prereversal enhancement of the vertical plasma drift. Because we have used empirical data for this parameter, we have taken the longitudinal gradients of the ionospheric E-region into effect.

Mendillo et al.[36] identify the nighttime requirements for the R-T instability growth as: "(i) postsunset rise of the F region, (ii) the availability of a seed perturbation to launch the R-T mechanism, and (iii) the absence of a strong transequatorial thermospheric wind." In our work, we didn't analyze the HF data to detect the presence of seed and/or wind in any given night. But, we note that this factor is likely one of the sources of the small discrepancies between the daily patterns of the calculated growth rate and the scintillation observations. (The other primary factor being that strong scintillation is dependent on the nonlinear development of the plasma instability into the strong turbulence regime.) The choice of scintillation index to quantify the ground based spread-F observations could also have been the source of possible discrepancy between the calculated growth rate and scintillation observations.

Conclusions

The research results discussed in this chapter present a simple method to calculate various parameters needed to evaluate the growth rate of Rayleigh-Taylor instability created in the F-region bottomside of the ionosphere. These parameters have been used to calculate the growth rate to predict the diurnal variability of the spread F occurrence using HF link data. The growth rate has also been calculated from model ionospheric profiles optimized by ray-tracing techniques to match actual delays as observed in the oblique HF links. The growth rate calculated from either of the aforementioned two methods provide a close prediction of spread F development as seen in the correlation between the calculated growth rate and the scintillation observations quantified by THMS4. We summarize our investigation results as following:

1. The vertical plasma drift is shown to be an important factor in the growth of instability in the equatorial F-region. The $V_p \sim 20$ m/sec is seen to be a threshold value for moderate/high level of scintillation observations as quantified by THMS4 index.

2. The growth rate captures the cumulative effect of the various ionospheric parameters and hence is a better indicator to predict scintillation activity instead of any single parameter in the growth rate expression.

3. The growth rate calculated from the HF link data or optimized model ionospheric profiles based on HF link delays accurately predicts the instability development as observed in the scintillation index THMS4.

4. The small discrepancies in the calculated growth rate and the scintillation observations can possibly be due to assumptions made in our work: constant vertical neutral wind, disappearance of E-region conductivity.

5. The discrepancies can also be possibly due to seed perturbations in the bottomside F-layer, transequatorial neutral wind and choice of scintillation index.

This investigation also opens wide avenues for future research in investigating other requirements for Rayleigh-Taylor growth rate in the F-region bottomside region. In particular, the HF data can be analyzed to investigate the precursor signatures such as large scale wave structures in pre-sunset hours to expand upon existing works in this interesting field of research [48].

References:

[1] Booker, H. G., and H. W. Wells (1938), Scattering of radio waves by the *F*-region of the ionosphere, *Terr. Magn. Atmos. Electr.*, 43(3), 249–256, doi: 10.1029/TE043i003p00249.

[2] Dungey, J. W.(1956), Convective diffusion in the equatorial F region, *J. Atmos. Terr. Phys.*, 9, 304-310.

[3] Balsley, B. B., G. Haerendel, and R. A. Greenwald (1972), Equatorial spread *F*: Recent observations and a new interpretation, *J. Geophys. Res.*, 77(28), 5625–5628, doi: 10.1029/JA077i028p05625

[4] Hudson, M. K., and C. F. Kennel (1975), Linear theory of equatorial spread *F*, *J. Geophys. Res.*, 80(34), 4581–4590, doi: 10.1029/JA080i034p04581

[5] Haerendel, G. (1973), Theory of equatorial spread F, technical report, Max Planck Inst. fur Extraterr. Phys. Munich, Germany.

[6] McClure, J. P., W. B. Hanson, and J. H. Hoffman (1977), Plasma bubbles and irregularities in the equatorial ionosphere, *J. Geophys. Res.*, 82(19), 2650–2656, doi: 10.1029/JA082i019p02650.

[7] Morse, F. A., et al. (1977), Equion, an Equatorial Ionospheric Irregularity Experiment, *J. Geophys. Res.*, 82(4), 578–592, doi: 10.1029/JA082i004p00578.

[8] Kelley, M. C., Haerendel, G., Kappler, H., Valenzuela, A., Balsley, B. B., Carter, D. A., Ecklund, W. L., Carlson, C. W., Häusler, B. and Torbert, R. (1976), Evidence for a

Rayleigh-Taylor type instability and upwelling of depleted density regions during equatorial spread F, *Geophys. Res. Lett.*, 3: 448–450.

[9] Woodman, R. F., and C. La Hoz (1976), Radar observations of *F* region equatorial irregularities, *J. Geophys. Res.*, 81(31), 5447–5466, doi: 10.1029/JA081i031p05447.

[10] Lee, C. C. (2006), Examine the local linear growth rate of collisional Rayleigh-Taylor instability during solar maximum, *J. Geophys. Res.*, 111, A11313, doi: 10.1029/2006JA011925.

[11] Basu, B. (2002), On the linear theory of equatorial plasma instability: Comparison of different descriptions, *J. Geophys. Res.*, 107(A8), doi: 10.1029/2001JA000317.

[12] Kil, H., L. J. Paxton, and S.-J. Oh (2009), Global bubble distribution seen from ROCSAT-1 and its association with the evening prereversal enhancement, *J. Geophys. Res.*, 114, A06307, doi: 10.1029/2008JA013672.

[13] Kelley, M.C. (1989), The Earth's Ionosphere, San Diego, CA, Academic Press.

[14] Ossakow, S. L. (1979), A review of recent results on spread F theory, NRL Memorandum Report 3909.

[15] Ossakow, S. L. (1981), Spread-F theories - A review, *J. Atmos. Terr. Phys.*, **43**, 437–452.

[16] Sultan, P. J. (1996), Linear theory and modeling of the Rayleigh-Taylor instability leading to the occurrence of equatorial spread *F*, *J. Geophys. Res*., 101(A12), 26875–26891, doi: 10.1029/96JA00682.

[17] Zalesak, S. T., and S. L. Ossakow (1982), On the prospect for artificially inducing equatorial spread F, Memo. Rep. 4899, Nav. Res. Lab., Washington D. C.

[18] Huba, J. D., P. A. Bernhardt, S. L. Ossakow, S. T. Zalesak (1996), The Rayleigh-Taylor instability is not damped by recombination in the *F* region, *J. Geophys. Res.*, **101**, 24,553–24,556, https://doi.org/10.1029/96JA02527.

[19] Kelley, M. C., R. R. Ilma, and G. Crowley (2009), On the origin of pre-reversal enhancement of the zonal equatorial electric field, *Ann. Geophys.*, **27**, 2053–2056, doi: 10.5194/angeo-27-2053-2009.

[20] https://omniweb.gsfc.nasa.gov/vitmo/msis_vitmo.html.

[21] https://ccmc.gsfc.nasa.gov/modelweb/atmos/msis.html.

[22] Hedin, A. E. (1991), Extension of the MSIS Thermosphere Model into the middle and lower atmosphere, *J. Geophys. Res*., 96(A2), 1159–1172, doi: 10.1029/90JA02125.

[23] Nelder, J. and R. Mead (1965), "A simplex method for function minimization", *Computer Journal*, 7, 749-756, doi: 10.1093/comjnl/7.4.308.

[24] Press, W. H., S. A. Teukolsky, W. T. Vetterling, and B. P. Flannery (2007), Numerical Recipes 3rd Edition: The art of scientific computing, Cambridge University Press, New York.

[25] Bilitza, D., et al. (2014), The International Reference Ionosphere 2012 – a model of international collaboration, *J. Space Weather Space Clim*. 4, A07, doi: 10.1051/swsc/2014004

[26] Haselgrove, J. (1955), Ray Theory and a new method for raytracing, in Physics of the Ionosphere, pp. 355-364, Physical Society, London.

[27] Haselgrove, C.B., and J. Haselgrove (1960), Twisted ray paths in the ionosphere, Proc. Phys. Soc. London, 75,357-363, doi: 10.1088/0370-1328/75/3/304.

[28] Haselgrove, J. (1963), The Hamiltonian ray path equations, *J. Atmos. Terr. Phys.*, 25, 397-399, doi:10.1016/0021-9169(63)90173-9.

[29] Jones, R. M., and J. J. Stephenson (1975), A versatile three-dimensional ray tracing computer program for radio waves in the ionosphere, NASA STI/Recon Tech. Rep., 76, 25,476, U.S. Department of Commerce, Off. of Telecommun., Washington, D. C.

[30] Coleman, C. J. (1993), A general purpose ionospheric ray tracing procedure, Tech. Rep., SRL-0131-TR, Defence Science Technology Organization, Adelaide, Australia.

[31] Zawdie, K. A., D. P. Drob, J. D. Huba, and C. Coker (2016), Effect of time-dependent 3-D electron density gradients on high angle of incidence HF radio wave propagation, *Radio Sci.*, 51, 1131–1141, doi: 10.1002/2015RS005843.

[32] Cervera, M. A., and T. J. Harris (2014), Modeling ionospheric disturbance features in quasi-vertically incident ionograms using 3-D magnetoionic ray tracing and atmospheric gravity waves, *J. Geophys. Res. Space Physics*, 119, 431–440, doi: 10.1002/2013JA019247.

[33] Bilitza, D., et al. (2000), New B0 and B1 models for IRI, *Adv. Space Res.*, 25, 89–95.

[34] Caton, R., and K. Groves (2006), Longitudinal correlation of equatorial ionospheric scintillation, *Radio Sci.*, 41, RS5S22, doi: 10.1029/2005RS003357.

[35] Redmon, R. J., D. Anderson, R. Caton, and T. Bullett (2010), A Forecasting Ionospheric Real-time Scintillation Tool (FIRST), *Space Weather*, 8, S12003, doi:10.1029/2010SW000582.

[36] Mendillo, M., J. Baumgardner, X. Pi, P. J. Sultan, and R. Tsunoda (1992), Onset conditions for equatorial spread *F*, *J. Geophys. Res.*, 97(A9), 13865–13876, doi: 10.1029/92JA00647.

[37] Rappaport, H. L. (1996), Field line integration and localized modes in the equatorial spread *F*, *J. Geophys. Res.*, 101(A11), 24545–24551, doi: 10.1029/96JA02174.

[38] LaBelle, J., M. C. Kelley, and C. E. Seyler (1986), An analysis of the role of drift waves in equatorial spread *F*, *J. Geophys. Res.*, 91(A5), 5513–5525, doi: 10.1029/JA091iA05p05513.

[39] Fejer, B. G., L. Scherliess, and E. R. dePaula (1999), Effects of the vertical plasma drift velocity on the generation and evolution of equatorial spread *F*, *J. Geophys. Res.*, 104(A9), 19859–19869, doi: 10.1029/1999JA900271.

[40] Huang, C., and M. R. Hairston (2015), The postsunset vertical plasma drift and its effects on the generation of equatorial plasma bubbles observed by the C/NOFS satellite*, J. Geophys. Res. Space Physics*, 120, 2263–2275. doi: 10.1002/2014JA020735.

[41] Ossakow, S. L., S. T. Zalesak, B. E. McDonald, and P. K.Chaturvedi (1979), Nonlinear equatorial spread *F*: Dependence on altitude of the *F* peak and bottomside background electron density gradient scale length, *J. Geophys. Res.*, 84(A1), 17–29, doi: 10.1029/JA084iA01p00017.

[42] Zalesak, S. T., and S. L. Ossakow (1982), On the prospect for artificially inducing equatorial spread F, Memo. Rep. 4899, Nav. Res. Lab., Washington, D.C.

[43] Huba, J. D., and J. Krall (2013), Impact of meridional winds on equatorial spread F: Revisited, *Geophys. Res. Lett.*, **40**, 1268–1272, doi:10.1002/grl.50292.

[44] Ramanathan, S. & R. Raghavarao (1987), Role of vertical winds on the Rayleigh-Taylor mode instabilities of the night-time equatorial ionosphere, *Journal of Atmospheric and Terrestrial Physics*, **49**, 981-985, doi: 10.1016/0021-9169(87)90104-8.

[45] Krall, J., J. D. Huba, and D. C. Fritts (2013), On the seeding of equatorial spread F by gravity waves, *Geophysical Research Letters*, **40**, 661–664, https://doi.org/10.1002/grl.50144.

[46] Zalesak ST, Ossakow SL, Chaturvedi PK (1982), Nonlinear equatorial spread F: the effect of neutral winds and background Pedersen conductivity, *J Geophys Res* 87(A1):151–166, https://doi.org/10.1029/JA087iA01p00151.

[47] Tsunoda, R. T. (1985), Control of the seasonal and longitudinal occurrence of equatorial scintillations by the longitudinal gradient in integrated *E* region Pedersen conductivity, *J. Geophys. Res.*, 90 (A1), 447–456, doi: 10.1029/JA090iA01p00447.

[48] Abdu, M. A., Souza, J. R., Kherani, E. A., Batista, I. S., MacDougall, J. W., & Sobral, J. H. A. (2015), Wave structure and polarization electric field development in the bottomside *F* layer leading to postsunset equatorial spread F, *Journal of Geophysical Research: Space Physics*, **120**, 6930–6940, https://doi.org/10.1002/2015JA021235.

CHAPTER 5 AN INVESTIGATION INTO THE ALTITUDE DISTRIBUTION OF EQUATORIAL IONOSPHERIC IRREGULARITIES BASED ON SOLAR ACTIVITY: RESULTS FROM THE C/NOFS MISSION

5.1 Introduction

In this chapter, we seek to characterize the spatial distribution of equatorial ionospheric irregularities and try to understand the dependence of the peak heights of the irregularities at the magnetic equator, also called as apex-altitude, on solar flux by analyzing in-situ observations from a low-earth orbit (LEO) satellite spanning half a solar cycle (2008-2014). The goal is to understand the physical processes that control the altitude of the instabilities, also known as bubbles. Because the irregularities map along the magnetic field lines, their height above the magnetic equator determines the spatial extent of the irregularities in latitude allowing us to identify regions affected by space weather impacts. Due to high parallel conductivity along the magnetic field lines, the field lines act like equipotentials and disturbance electric fields, along with associated instabilities, map efficiently parallel to magnetic field. To confirm the results from our space-based observations, we compare these with ground-based scintillation observations by invoking the flux-tube paradigm of equatorial plasma bubble growth. In doing so, we also validate the flux-tube paradigm of equatorial plasma bubble growth in which the latitudinal extent of the irregularities is determined by the height of the bubbles at the magnetic equator (Figure 5.1). We also seek to study the apex-altitude distribution of the equatorial ionospheric irregularities for low and high solar activity years and understand the variation of apex-altitude distribution with solar flux. These observational findings are further combined with modeling results from the Physics-Based Model (PBMOD) to attempt to understand what controls the rise of the equatorial ionospheric irregularities at the magnetic equator.

Equatorial plasma irregularities are caused by the non-linear evolution of the generalized Rayleigh Taylor (RT) instability [1, 2] in which the bottomside low-density plasma drifts upward into the high-density plasma much like the rise of air bubbles in a liquid [3] as shown in Fig 4.1 [4]. The ionospheric irregularities are generically called 'spread F' owing to the spread observed in the ionograms (Figure 5.2) when they were first observed but are also known by various other names such as 'plasma bubbles', 'plasma depletions', 'plasma plumes', etc. [5]. Since their first discovery by Berkner and Wells [6] in 1934, these irregularities have been extensively studied in a variety of experiments involving sounding rockets, ground-based radars, satellites, in-situ probes, conventional ionosondes, topside ionosondes, airglow measurements and satellite beacons [7,8]. The irregularities have been an active field of research due to both academic interest and practical applications as these irregularities cause radio wave scintillations disrupting satellite, communication, navigation, surveillance and aviation systems. Despite these extensive studies contributing to an enhanced understanding of the physical mechanism of the generation of the plasma bubbles, it continues to be a formidable challenge to predict their occurrence. Under seemingly identical ionospheric conditions in two days, there may or may not be similar ionospheric disturbances [9]. In this work, we seek to understand the occurrence statistics of these enigmatic equatorial ionospheric irregularities based on the analysis of several years of C/NOFS satellite data spanning both low and high solar activity years.

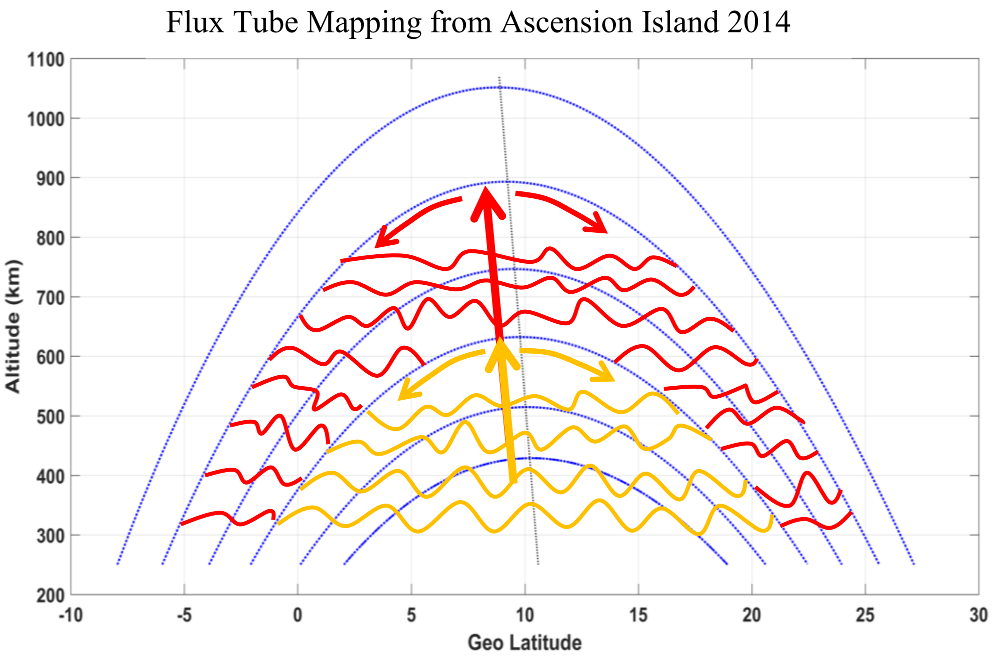

Figure 5.1: Illustration showing the flux-tube paradigm of the equatorial plasma bubble growth. The latitudinal extent of the irregularities is determined by the height it rises at the magnetic equator. The irregularities are mapped along the equipotential magnetic field lines while rising at the magnetic equator.

The primary purpose [10] of the Communications/Navigations Outage Forecasting System (C/NOFS) mission was to forecast ionospheric irregularities and radio wave scintillations with the aid of in-situ observations made by the sensors on board the C/NOFS satellite and complementary ground-based observations through scintillation receivers and Global Positioning System (GPS) receivers as well as other ground-based instruments such as ionosondes, optical instruments, Fabry Perot Interferometers and radars. The major component of the mission is the C/NOFS satellite which was launched in April 2008 into a low inclination (13^o), elliptical (~ 400 x 850 km) orbit and had a period of approximately 93 minutes. The satellite decayed in November 2015 [11, 12].

The C/NOFS mission had three broad objectives [10]:

1. Advance the understanding of physical processes of equatorial ionospheric plasmas
2. Understand the main drivers of the non-linear instability causing the depletion of plasma and associated radio wave scintillations
3. Model radio wave propagation through the ionosphere for various propagation geometries

To achieve these scientific objectives, the C/NOFS satellite included the following suite of *in situ* sensors and a multi-frequency beacon [10]:

1. *The Planar Langmuir Probe (PLP)* to measure the low time-resolution density and high time-resolution density irregularity measurements,

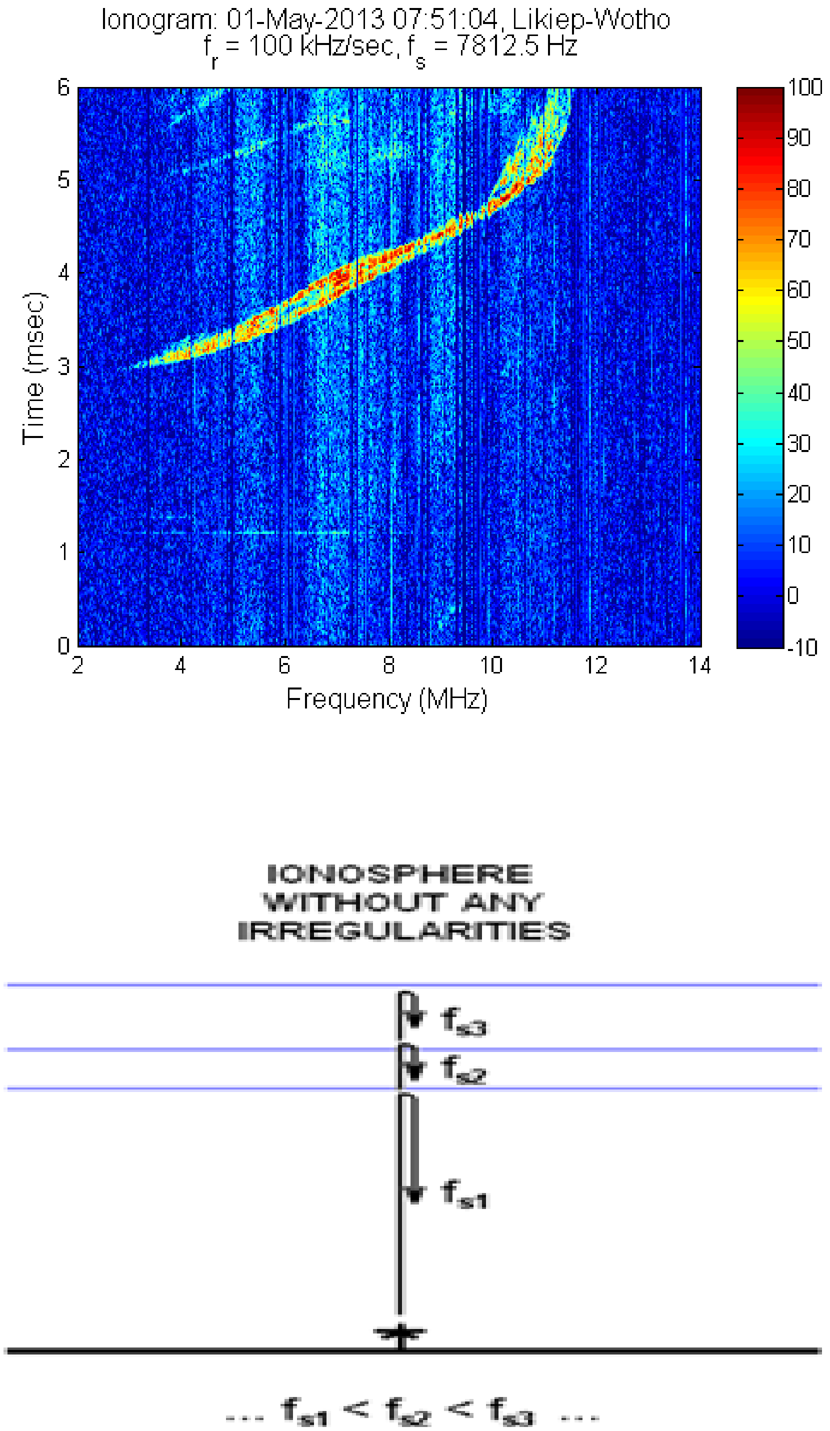

Figure 5.2: An example of spread F as seen in an oblique ionosonde data (top). Illustration of vertical ionosonde as Reflectometry diagnostic instrument (bottom).

2. *The Ion Velocity Meter (IVM)* to measure vector ion velocity, ion composition and ion temperature,
3. *The Neutral Wind Meter (NWM)* to measure vector neutral wind velocity,
4. *The Vector Electric Field Instrument (VEFI)* to measure vector AC and DC electric fields,
5. *The Coherent Electromagnetic Radio Tomography* (*CERTO*) to specify plasma conditions between the location of C/NOFS and the Earth and for the tomographic reconstruction of electron density profiles,
6. *The C/NOFS Occultation Receiver for Ionospheric Sensing and Specification (CORISS)* to measure total electron content (TEC) along the Lines-Of-Sight (LOS) between C/NOFS and GPS satellites.

The apogee and perigee of the elliptical orbit of the C/NOFS satellite ranges between 400 and 850 km and hence, provides a unique opportunity to analyze data at all altitudinal ranges between 400-850 km. This is helpful to compare the results from past experiments flying similar sensors such as Atmospheric Explorer E (AE-E: 1975-1981) [19], Republic of China Satellite (ROCSAT-1: 1999-2004) [3, 21] and Defense Meteorological Satellite Program (DMSP : 1962 - current) [2] satellites. AE-E, although initially designed to fly in an elliptical orbit, was changed to a circular orbit ~ 400 km after mid-1977. ROCSAT-1 was a low-inclination satellite in circular orbit ~ 600 km and the DMSP spacecraft fly in circular, sun-synchronous polar orbits at an altitude of ~ 840 km. In section two of this chapter, we discuss our methodology of identifying the equatorial ionospheric irregularities while comparing with other techniques applied in the literature.

a.)

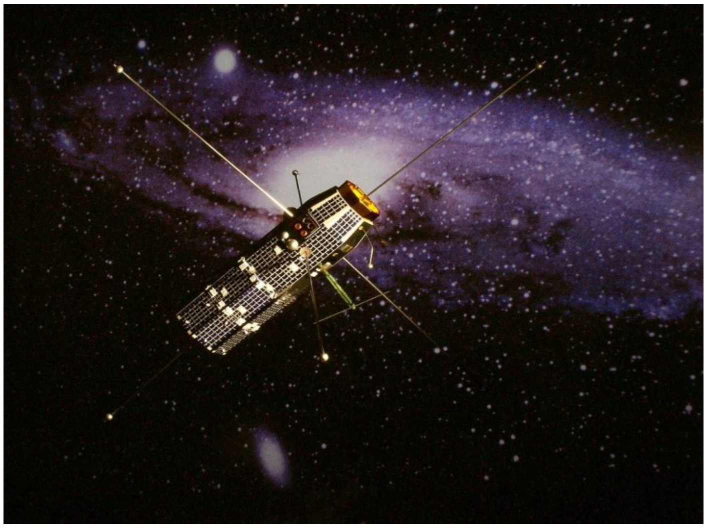

b.)

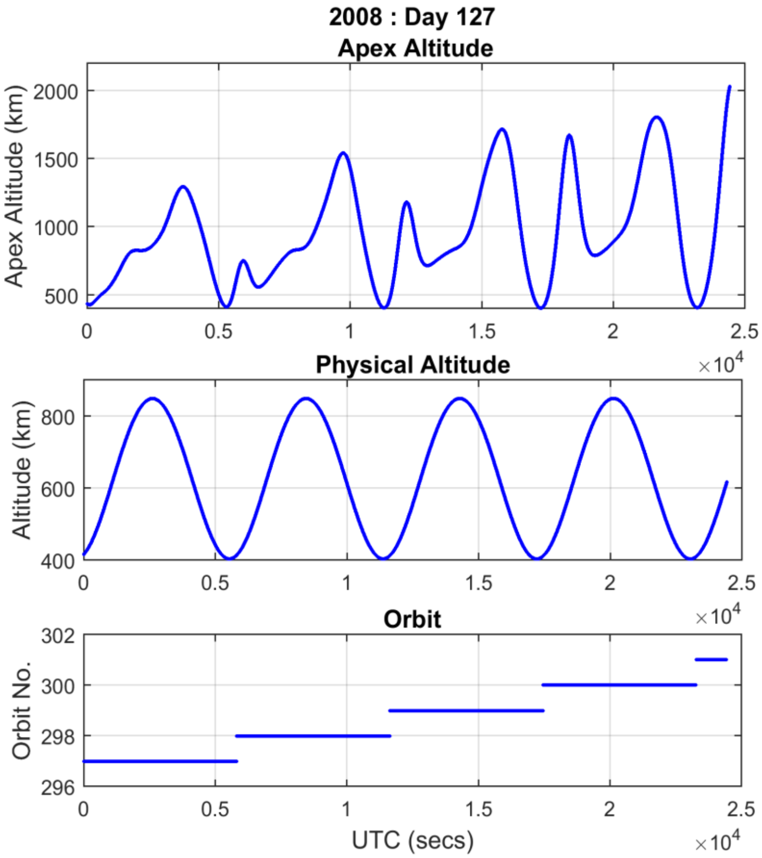

Figure 5.3: (a) An artist's rendition of C/NOFS space-craft [13]. **(b)** The variation of apex-altitude (top), physical altitude (middle) in C/NOFS Orbits 297-301 (bottom) on Day 127, 2008. The apex-altitude varies from 403 – 2013 (~ 1600) km as C/NOFS orbits around the earth in varying magnetic latitude in low inclination elliptical path while the physical altitude varies from 400 – 850 (~ 450) km.

In section three, we present climatological results obtained from these methodologies. In section four, we seek to validate our climatological results by making comparison of the space-based observations with ground-based scintillation measurements. In section five, we look at the apex-altitude distribution results for yearly C/NOFS data between the period 2008 - 2014. In section six, we confirm the apex-altitude distribution results of the C/NOFS data through a numerical simulation. In section seven, we study the local time effects on the apex-altitude distribution of equatorial ionospheric irregularities. In section eight, we present modeling results to compare with the C/NOFS observations on the change of maximum apex-altitude of equatorial ionospheric irregularities with solar flux. And in the final section, we discuss our results, conclusions and future work.

5.2 Observations and Methodology

We developed an algorithm to identify irregularities in the C/NOFS satellite PLP sensor electron density data. Langmuir probes have been a major plasma diagnostics tool installed in both the laboratory and in spacecrafts in scientific missions for more than five decades to observe the plasma characteristics [14]. The simplest Langmuir probe is a metallic electrode placed in plasma with an external DC bias to measure current (I) and voltage (V). This I-V curve is then analyzed to calculate various plasma parameters, principally electron density. But behind this simple description of the probe lays the theoretical and practical complexities involved in the charge collection processes from a plasma. We do not seek to treat the problem in its full detail in this work.

Roddy et al. [15] describe the PLP sensors in their paper, "The PLP on-board C/NOFS satellite included advances in electronic capability compared to past designs. These

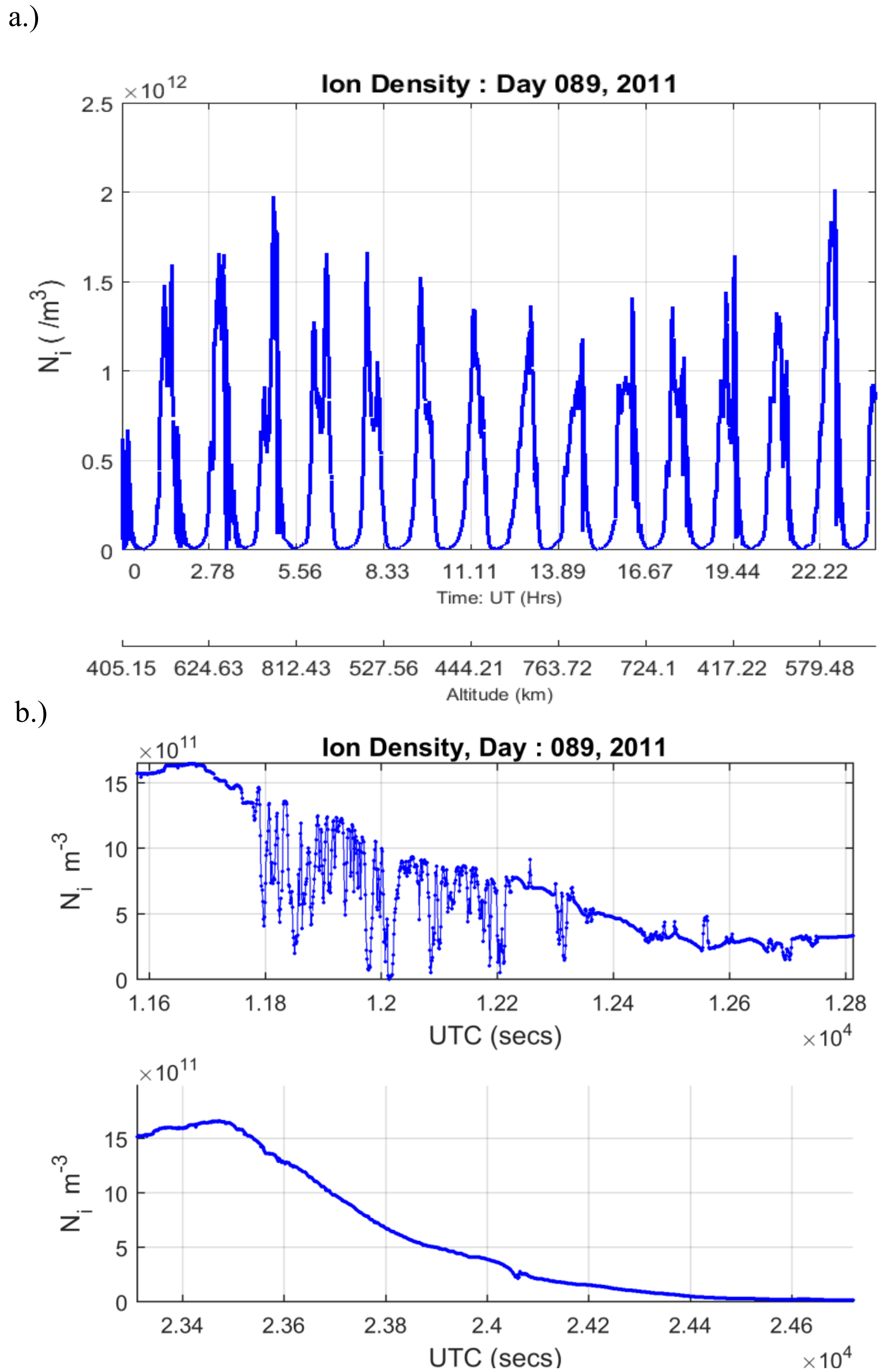

Figure 5.4: (a) An example of ion-density measurements for UTC day 089, 2011 made by C/NOFS PLP sensor (top).**(b)** Ionospheric Irregularities in upper subplot and smooth ion density measurements on the same day in lower subplot (below).

include : significant improvements in the range, linearity, and high-frequency time response of the logarithmic amplifiers; microprocessor control of software antialias filters; hardware filters that increase the effective sampling range of the A/D converters by flattening the typical power spectral density curve prior to sampling; hardware antialias filters; and, suppression of photoelectron effects and amplifier drift by injection of a variable calibration current into the ion trap logarithmic amplifier." PLP observations are available in individual daily files with 1-Hz resolution. Each 1-s record is associated with the Universal Time (s) to the corresponding average ion density, ion density fluctuations and various other quantities such as latitude, longitude, altitude, local-time, orbit number, etc. The ion density and ion density fluctuation values are sampled at 512 Hz during eclipse times. Other sample rates used during measurement by PLP sensors are 32, 256 and 1024 Hz. Nominally, PLP was operated at 32 Hz during day and 512 Hz during eclipse hours [15]. In a UTC day without any data gap, there are 86400 seconds of measurements of the ion-density (Fig 5.4 (a)). The ion-density measurements may have structures in them as signatures of irregularities in the equatorial ionosphere. It is these structures (Fig 5.4 (b) – upper subplot) we want to identify by our algorithm, we are interchangeably calling them ionospheric irregularities, plasma bubbles or plasma depletions. When the ionosphere is undisturbed, the change in the ion density isn't irregular (Fig 5.4 (b) – lower subplot) suggesting an absence of any kind of irregularity in the ionosphere. Here, the smooth decrease in density is caused simply by the increasing altitude of the satellite. We have similar observations starting from low solar activity year 2008 to high solar activity year 2014 with data a few gaps in some years (2008, 2013 and 2014). Later in this chapter, we discuss our approaches to handle these data-gaps while

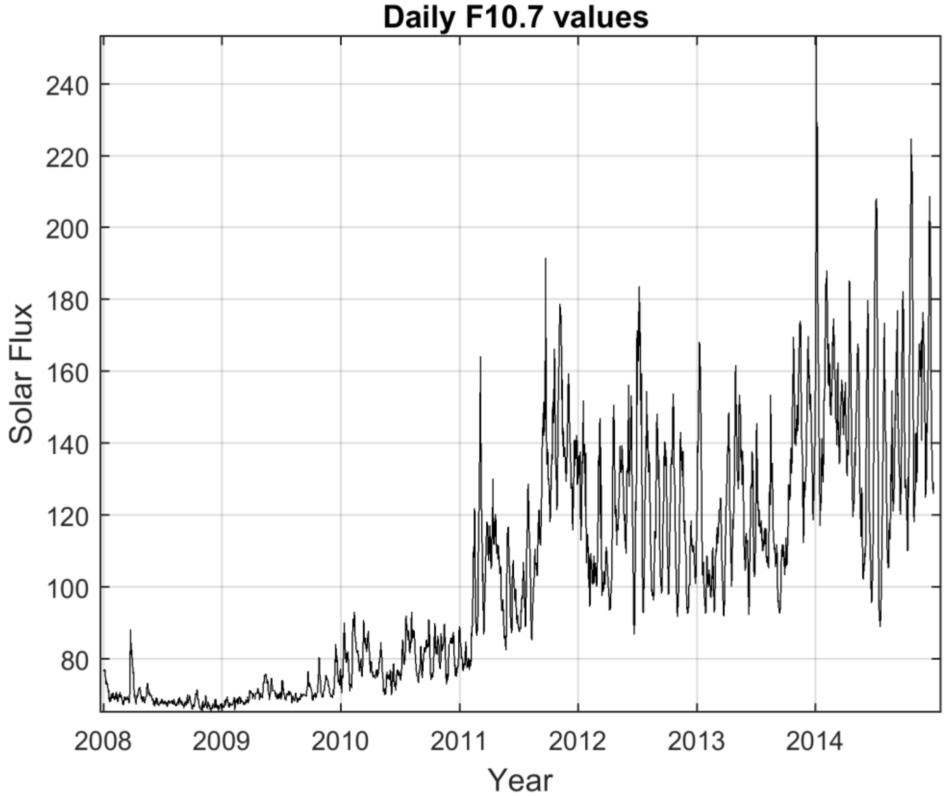

Figure 5.5: F10.7 solar radio flux (10^{-22} W m^{-2} Hz^{-1}) for the years 2008-2014.

making yearly comparisons of the maximum apex-altitude of ionospheric irregularities with respect to solar activity.

The 10.7 cm solar radio flux is a widely, if not the most widely, used index of solar activity. Each value of F10.7 is a measurement of the total emission at a wavelength of 10.7 cm from all sources present on the solar disk, made over a 1 h period centered on the epoch given for the value [16]. It describes solar UV forcing of the upper atmosphere and has been measured daily since 1947 [17]. The 12-month average F10.7 value is commonly used as an index for ionospheric models as a proxy for the EUV radiance and has been shown to correlate with ambient electron density. Other indices used to represent the solar activity are Sunspot Number (SSN) which measures the number of dark sun-spots on the surface of the sun and Ap index which is a measure of geomagnetic activity. We chose F10.7 as the index of solar activity as it correlates linearly with Total Electron Content (TEC) and Scintillation Index (S4) index. In our period of observations (2008 -2014), the maximum daily F10.7 value is 253.3 in the year 2014 whereas the minimum value is 65.2 in the year 2008. We take the period 2008-2010 as low solar activity years and the period 2011-2014 as high solar activity years.

In our work, we use the following parameter σ to identify ionospheric irregularities:

$$\sigma\,(\,\%) \;=\; 100 \times \frac{\left[\frac{1}{11}\sum_{i=1}^{11}(\log N_{\mathrm{i}} - \log N_{\mathrm{oi}}\,)^2\right]^{1/2}}{\left[\frac{1}{11}\sum_{i=1}^{11}\log N_{\mathrm{oi}}\,\right]} \qquad \text{--------}\ (1)$$

where N_i and N_{oi} are the ion density and linearly fitted value at the ith data position. This definition has been used in previous studies aimed [18, 21, 22] at investigating ionospheric irregularities. Equation (1) is the standard deviation of ion density variation in logarithmic scale for an 11-s segment of data. *Huang et al*. [18] and *Su et al*. [21] used the same parameter but with a 10-s segment of data in their work involving C/NOFS and ROCSAT (Republic of China Satellite) satellite observations respectively. To linearly fit data value at ith position to calculate N_{oi} , *Huang et al.*[18] used a moving average over 60 secs whereas *Su et al.*[21] used linear detrending over 10-sec data segment. *Kil et al.* [22] apply the same definition but with a 100-s segment of ROCSAT data instead of the 10-s data and N_{oi} was calculated using an 11-point smoothing curve. They claimed that the plasma bubbles could be determined more accurately by using multipoint smoothing curve as background density instead of linearly fitted values. Retterer and Roddy used a similar algorithm, taking the deviations from a fitted upper envelope of a section of the tabulated C/NOFS density [23].

The relative ion density variation in linear scale has also been used to identify ionospheric irregularities in previous studies [19, 20]:

$$\frac{\Delta N}{N_{\mathrm{o}}} = \frac{\left[\frac{1}{10}\sum_{i=1}^{10}(N_{\mathrm{i}} - N_{\mathrm{oi}})^2\right]^{1/2}}{\left[\frac{1}{10}\sum_{i=1}^{10}N_{\mathrm{oi}}\right]} \qquad \text{---------} \ (2)$$

Kil and Heelis [19] apply this definition using the 8-sec segment linear-scale ion density data from the AE-E satellite. *McClure et al.* [20] apply a similar definition but have an elaborate scheme of examining first 3-s data segment in an 8-s sample for eight contiguous samples to identify the ionospheric irregularities. *Huang and Hairston* in their recent work [24] have used only the numerator in equation (2) to calculate plasma density perturbation value and have used the threshold of $\Delta N > 1 \times 10^{10}$ m^{-3} to identify

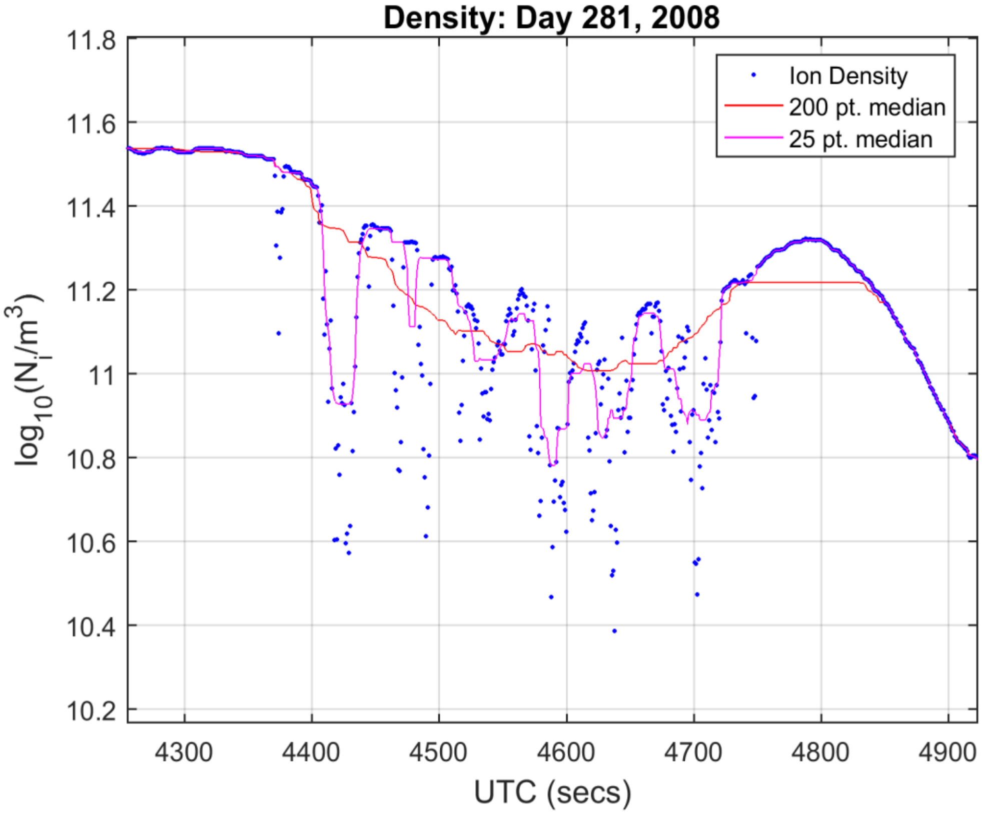

Figure 5.6: The ion-density values measured by the C/NOFS satellite on day 281, 2008. The 200-points-median line ‘separates better’ than the 25-point-median line from the ion density values.

occurrence of plasma bubbles. So, despite using similar definition, the differences in the calculation of the background density and in the number of data-points taken in a segment can lead to different identifications of the plasma bubbles and the plasma bubble occurrence statistics as well which in turn will affect the forecasting and modeling efforts of these bubbles. Hence, different authors have set different threshold values for the parameters they have chosen to identify the ionospheric plasma bubbles. For example, *Gentile et al*. [2] visually inspected data for every orbit in a month-longitude window bin to identify equatorial plasma bubbles. *Su et al.* [21] and *Kil et al*. [22] used a threshold value of $\sigma > 0.3$ % to identify the bubbles although the definition of σ used by each of them is slightly different. *McClure et al.* [20] have used $\sigma > 0.5$ % albeit their definition of σ has ion density values in linear scale. *Huang et al.* [16] have used $\sigma > 1$ % with 10-s data bins in the definition to identify ionospheric irregularities. So, there is no unanimous approach, definition and value to identify the ionospheric irregularities. In our work, while applying σ defined in equation (1) as the parameter to identify irregularities, we have taken the background density (N_{oi}) to be moving median of 200 points/secs. We chose to take median of a longer time-window as the 'base-line (N_{oi})' in equation (1) to ensure the algorithm identifies the depleted regions in the ion densities as equatorial plasma bubbles (EPBs). A shorter time-window causes the base line to move along the ion-density values (Fig 5.6) – thereby it could possibly sometimes miss to identify a 'structure' as an EPB irrespective of the threshold chosen for the parameter, σ. The inclusion of more data-points in the base-line ensures the median value is affected not only due to 'local' disturbances in the data but also by 'farther' data-points as well. There is another interesting aspect of the parameter in equation (1). The value for the

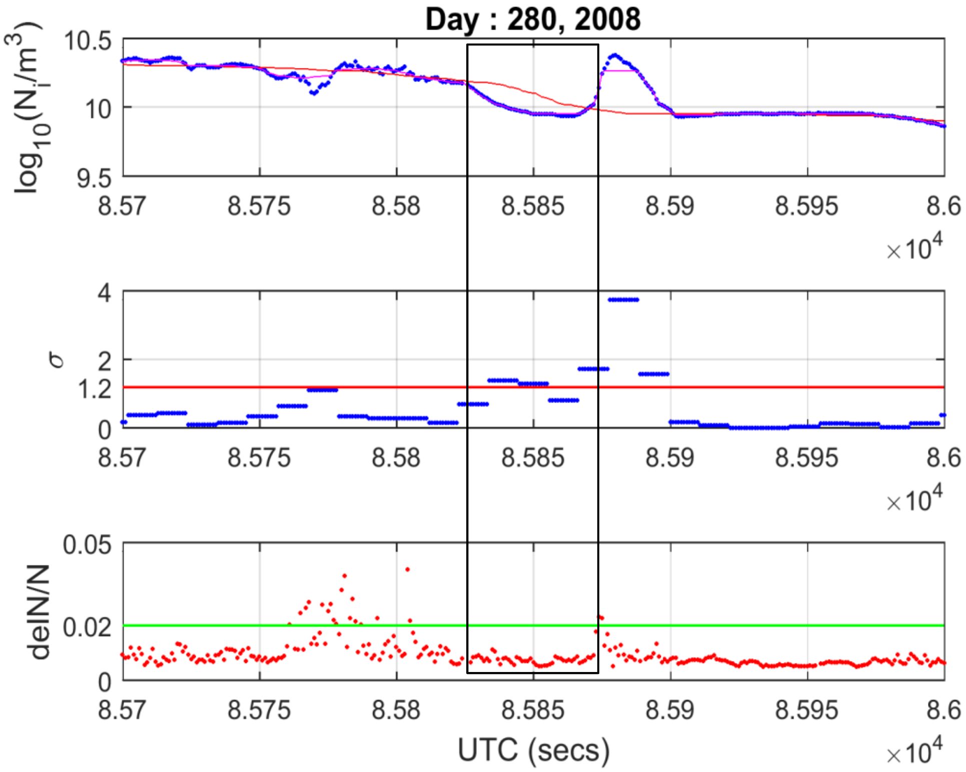

Figure 5.7: An example of 'smooth decrease' in density values (first subplot) at 8.585e4 UTC secs on day 80, 2008 which flags σ > 1.2 (second subplot) but delN/N < 0.02 (last subplot).

parameter depends upon the units chosen for the ion densities in the formula as it involves logarithm of the ion density values. The equation can be simplified in the form $\frac{\log(\frac{a}{b})}{\log(b)} = \frac{A}{B}$. It is seen the choice of units affects its value as the denominator (B) changes with the units whereas the effect in the numerator (A) gets canceled. Authors who have applied this parameter in their works previously have not explicitly revealed the units chosen while deciding a value as the criterion to capture the ionospheric density roughness. In this work, we set $\sigma > 1.2$ % as the criterion to identify the ionospheric irregularities with ion-density units taken to be in m^{-3}.

Although $\sigma > 1.2$ % as criterion with 200-point median base line well identifies irregular structures in the ionospheric density values, it is also possible to erroneously flag smoothly varying ion-density values as structures (Fig 5.7). To avoid such situation, we also check the value ΔN/N, the ion density standard deviation divided by the ion density, in addition to the parameter σ . The quantity ΔN/N is calculated from the 50-Hz resolution data and hence can capture roughness in the irregularities at smaller scales. We visually inspected many days' of data and decided to set delN/N > 0.02 as an additional requirement to ascertain 'roughness' of the structures flagged by $\sigma > 1.2$ % in the ion density data.

5.2.1 What is a structure?

In this subsection, we seek to further qualify the definition of the irregularities we intend to capture with our algorithm. With $\sigma > 1.2$ and ΔN/N > 0.02 as the conditions, we succeed in identifying equatorial ionospheric irregularities. But these irregularities are of various types and not all these are just the depletions like those in Figure 5.6 in which

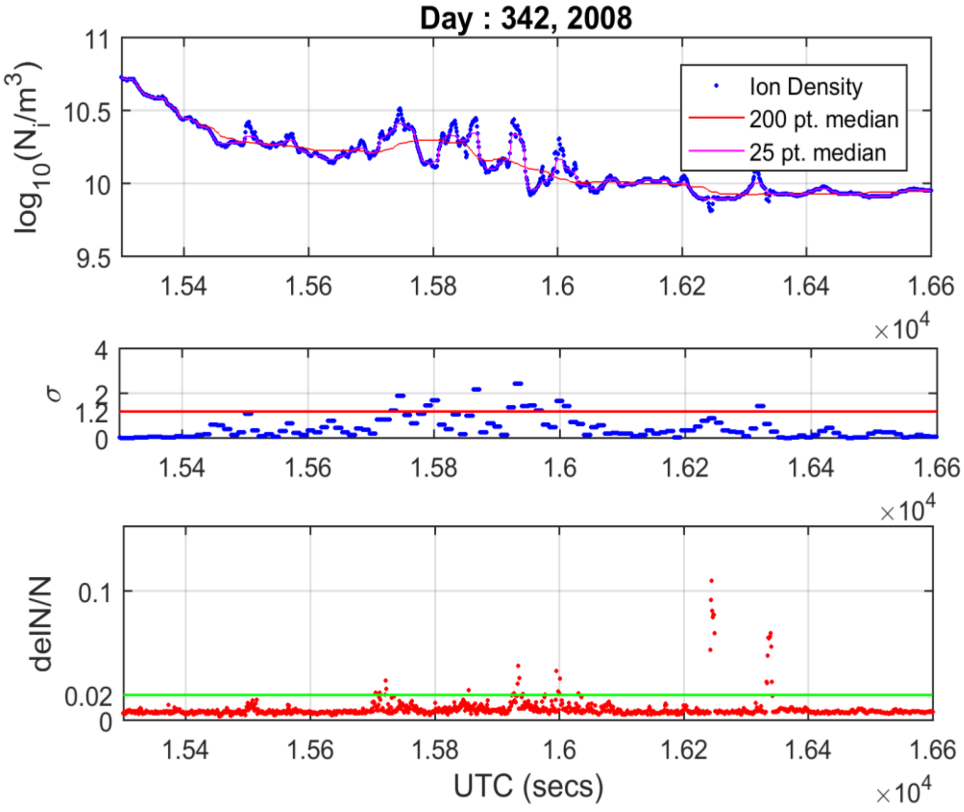

Figure 5.8: An example of ‘sinusoidal fluctuations’ in density values (first subplot) at 1.58e4 UTC secs on day 342, 2008 which flags σ > 1.2 (second subplot) but delN/N > 0.02 (last subplot).

there is a significant drop in the ion-density values from the background ion density values. There are also wave-like structures in which ion-density values fluctuate 'sinusoidally' (Fig. 5.8).

There are also plasma density enhancements of the ion-density values which could be both 'isolated' and 'contiguous' with the 'depletions'. Observational studies by *Huang et al.* [25] on these enhancements have hypothesized a causal relationship between the bubbles and the enhancements but in a recent paper, *Kil et al.* [26] assert that the enhancements, also called blobs, are independent of the bubbles. In this work, we seek to treat the depletions independent of the enhancements and hence will not be including enhancements. For any eleven-point ion-density which constitutes a bin for the parameter σ, this will be accomplished by excluding the bin for which the median ion density is higher than the median density of the corresponding 200-point baseline bin. While applying this approach, we also exclude the enhancements associated with 'sinusoidal' structures as well – which could be part of a Large Scale Wave Structure (LSWS) or Traveling Ionospheric Disturbances (TIDs). The Large Scale Wave Structures (LSWS) are quasi-periodic altitude modulation of electron-density contours in the bottomside F layer [9]. TIDs are wave-like fluctuations of the electron density induced by atmospheric gravity waves in the neutral atmosphere [27]. While it is challenging to ascribe an exact number as the scale size of any ionospheric 'wave structure', researchers have presented the scale size of LSWS as varying between 100 – 800 km [28, 29]. The TIDs are categorized as large-scale TIDs (LSTID) and medium-scale TIDs (MSTID) based on the wave characteristics such as wavelength, velocity and period. The scale size of LSTID is reported to be larger than 1000 km and that of MSTID is reported to be several hundred kilometers [30, 31]. While we didn't investigate the C/NOFS data extensively to look for wave-like structures, the structure in Figure 5.8 is seen to have a scale-size of ~ 780 km (100 secs) which is comparable to the reported scale-sizes of LSWS or LSTID. As we seek to understand what controls the occurrence and altitude distribution of ionospheric irregularities at the magnetic equator, the apex-altitudes of the depletion 'bins' which exist contiguously with enhancement bins will be well-represented in the apex-altitude statistics. The isolated plasma blobs are not represented in our study as the characterization and source of blobs is still an ongoing discussion in the literature to be associated directly with bubbles, which are the primary phenomenon of interest in our investigation.

We choose 20 – 24 hours Local Time (LT) for the statistical studies of equatorial plasma bubbles to focus on understanding active bubbles. The altitude profile during the early hours of evening (before 20 LT) may be determined by the growth characteristics rather than the terminal altitude of the bubble. Bubble growth may even continue after 20 LT, statistically we desire to make the time window as large as possible. Later on in this chapter, we examine differences between early and late periods in the window. Since these bubbles start at the bottomside F-region at the magnetic equator and move pole-wards in both hemispheres along the magnetic field lines, the latitudinal extent chosen also influences the climatology map of the bubbles. To make comparisons with similar studies in the past, we use data within ± 10 magnetic latitude to construct the climatology maps of the occurrence probability of ionospheric irregularities but later on as we study the apex-altitude distribution, we relax this restriction. The climatology map is made out of a matrix of dimensions 12 (months) x 18 (longitude sectors) – where each month-longitude bin displays the occurrence probability percentage of the plasma bubble defined as:

Occurrence Probability Percentage

$$= \frac{No.of\ orbits\ satisfying\ the\ plasma\ bubble\ criterion\ at\ least\ once}{No.of\ orbits\ through\ a\ cell} \text{ x } 100\ \%$$

5.3 Climatology Results

We take the period 2008-2010 as low solar activity years and the period 2011-2014 as high solar activity years (Fig. 5.5). The observed monthly mean F10.7 values during the low solar activity years range ~ (67 – 84 solar flux units (s.f.u.) and those during the high solar activity years range ~ 83 – 170 s.f.u. The values, if taken daily, range ~ (65 – 93) s.f.u. and (76 – 253) s.f.u. during 2008 – 2010 and 2011 – 2014 periods respectively. Since the first half of the year 2011 has rapidly changing transitional F10.7 values, these values have fewer samples than the remaining period of high solar activity years. Inclusion of this period of data doesn't significantly alter the features of the climatology.

Fig 5.9 shows the distribution of the plasma irregularities with changing apex altitude for the years 2011-2014. Although the longitudinal and seasonal features of occurrence percentage of the irregularities remain similar as we go from low-apex altitudes to high-apex altitudes map, the occurrence percentage significantly decreases as we move higher. The equatorial plasma bubble (EPB) rates are generally high around equinoctial months and low around June solstice. *Tsunoda* [32] sought to explain the seasonal occurrence patterns of equatorial scintillation – suggestive of the bubble formation – by showing that the maxima in scintillation activity coincide with the times of the year when the solar terminator is most nearly aligned with the geomagnetic field lines. However, as suggested by Tsunoda himself in the paper, observational discrepancies in this explanation of the seasonal pattern of scintillation activity (bubble climatology) are ascribed to processes other than the generalized gradient drift (or Rayleigh-Taylor) instability in the creation of the ionospheric irregularities. The term generalized is used to include the different sources of free energy for the instability: gravity, neutral wind, electric fields and field-aligned currents. *Aarons* [33] and *Huang et al.* [34, 35] have confirmed the general features of Tsunoda's model of seasonal and longitudinal variations of the global equatorial plasma bubble rates. The longitudinal differences which remain unresolved by the Tsunoda model have been examined in the work of *Huang et al.* [35] in which they suggest the R-T irregularities should grow fastest at longitudes where the Earth's magnetic field at the equator is weakest. This is so because the linearized RT instability growth rate is directly proportional to vertical plasma drift ($V_p \propto E/B$) which in turn is inversely related to the magnetic field. But as *Burke et al.* [36] suggest, mother nature probably has a more complex scheme than this conjecture. Their observations, contrary to the inference of *Huang et al.* [35], indicate that the EPB rates are lower in the South American sector. They suggest this is due to the precipitation of magnetospheric electrons from the inner radiation belt which leads to an increase of E-region conductance and thereby inhibits nonlinear EPB growth. *McClure et al.* [37] proposed an alternative explanation of the seasonal and longitudinal variations of the equatorial plasma bubbles. They suggest $P_{EFI} = P_{seeds}P_{inst}$ where P_{EFI} is the probability for the Atmosphere Explorer E (AE-E) satellite encountering equatorial F region irregularities, P_{seeds} is the probability of having gravity wave induced 'seeds' for spread F irregularities in the post-sunset ionosphere, and P_{inst} is the probability that the bottomside F layer is Rayleigh-Taylor unstable. In this work, we only note that the general seasonal and longitudinal features of the climatology maps are consistent with previous studies [2, 18, 19, 22]. But we do not aim to add to any of the aforementioned explanations of the longitudinal and seasonal patterns of equatorial plasma bubbles. That is because we didn't investigate the C/NOFS data to find small density perturbations (e.g., TIDs) which act as seeds for the development of the RT instability. Furthermore, the overall climatological pattern of scintillation activity is reproduced by the climatology of the RT growth rate alone, so that the seed probability probably has more to do with the day-to-day variability of scintillation occurrence.

The longitude span in each monthly-Longitude-Localtime cell in the climatology map is 20 degree. The 20 degree longitude corresponds to ~ 2200 km of region. With a speed of 7.8 km/sec, the satellite makes ~ 282 (≈2200/ 7.8) secs of measurements in one orbit while passing through the 20 degree longitudinal region. With our bin defined every 11 secs, in one orbit it makes ~25(≈ 282/11) bins of measurements. Conversely, 25 bins of measurements by the satellite correspond to one orbit. In four hours of local time (20 – 24 LT), the satellite makes ~ 2.5 (≈ 4 hours/Orbital period of the satellite (93 mins)) orbits through a specific region. In a day, it will have 25 * 2.5 = 62.5 bins of measurements through the longitudinal region of a cell in the climatological map. In a specific month of all four years, there can be 62.5*30*4 = 7500 such bins. In each monthly Longitude-LocalTime bin (cell), the total number of orbits through four years of data can be maximum of ~ 7500/25 ~ 300 orbits without the magnitude latitude and the apex-altitude filters. In the climatology map for the years 2011-2014, with magnetic latitude (± 10) and apex-altitude (400 - 500 km) filters, we found the maximum number of orbits in a cell is 115 and the minimum is 6 , the median is 50, the mean is ~ 50 and the standard deviation is ~ 20.

The EPB rates maximize in the America-Atlantic-Africa region corresponding to the longitude sector 280° E (-80°) to 30°E. The global morphological features of the equatorial plasma bubbles are similar to those found in previous studies from DMSP, ROCSAT-1, AE-E satellites. The maximization of EPB rates in the American-Atlantic-Africa sector is observed in the distributions of irregularities from AE-E satellite as reported by *Kil and Heelis* [19] in their Figure 5, in the climatology map of the ROCSAT satellite data as reported by *Kil et al.* [3] in their Figure 6 and in the DMSP results as reported by *Gentile et al.* [2] in their Figure 2. *Kil and Heelis* included observations during high solar activity years 1978 – 1981 from AE-E. Similarly, *Kil et al.* included ROCSAT-1 data from high solar activity years 1999 – 2002 for the climatology map. Climatology studies from DMSP were made for both solar high and low activity years. In particular, we seek to compare our results with those from the DMSP satellites, which operated through more than one full solar cycle (1989 – 2004), and suggested a striking dependence on solar flux. But the operational life times for the AE-E and ROCSAT-1 orbiters were limited to a few years. A detailed review and comparison of results from past studies with C/NOFS results may be a topic of future investigation.

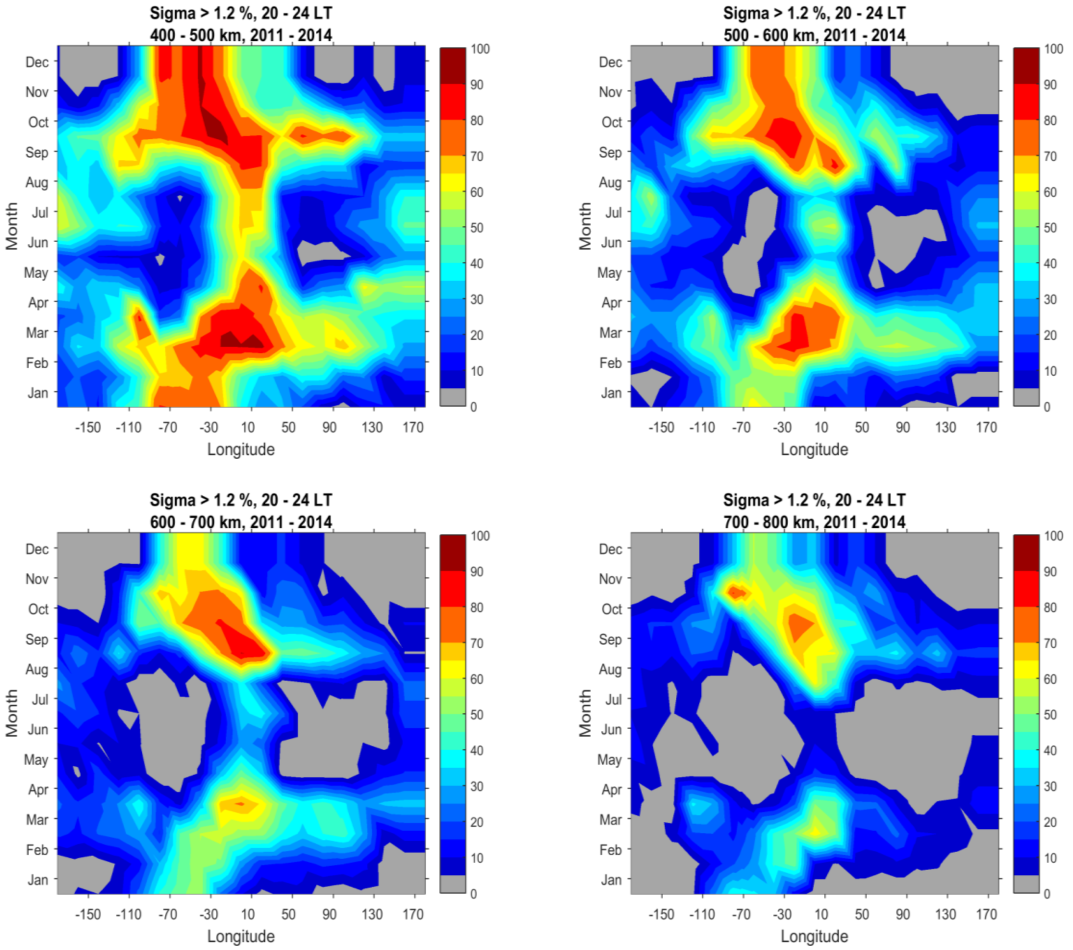

Figure 5.9: Equatorial Plasma Bubble (EPB) Occurrence percentage during high solar activity years (2011 – 2014) as a function of apex altitude. While the major seasonal and longitudinal features of the occurrence percentage remain similar as we go from lower apex-altitudes to higher apex-altitudes, the maximum occurrence percentage decreases significantly in large areas of the map.

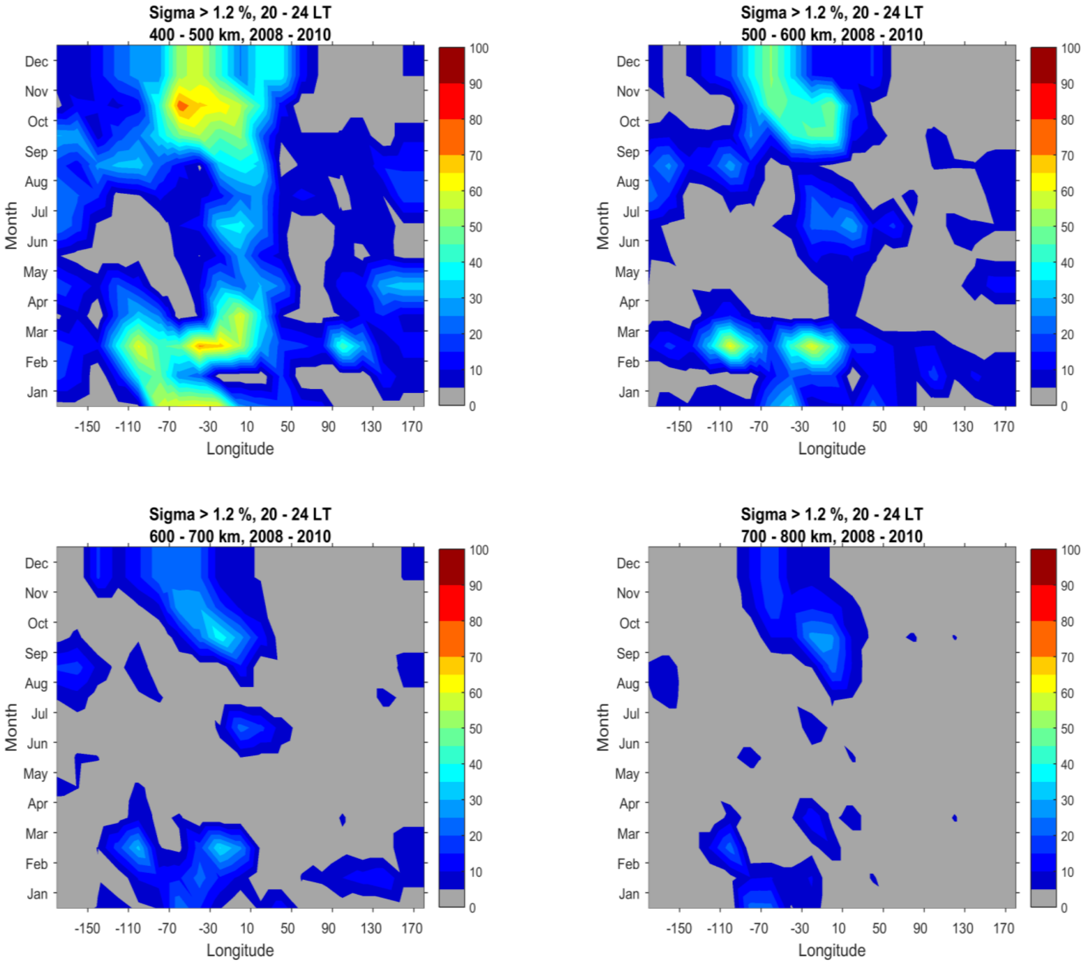

Figure 5.10: Equatorial Plasma Bubble (EPB) Occurrence Probability percentage results during low solar activity years (2008 - 2010) as a function of apex altitude. The lowest apex-altitude bin climatology map resembles similar seasonal and longitudinal features as during high solar activity years whereas the features become gradually less distinct in higher apex-altitude bin climatology maps. The activity in higher apex-altitude bins also drop significantly more rapidly as compared to that of the high activity years.

In Fig. 5.9, the maximum occurrence percentage decreases from 95 % to 81 % as we go from 400-500 km of apex-altitudes to 700-800 km of apex-altitudes. The larger regions of zero (or less than 5 %) occurrence percentage in the higher apex-altitude maps suggest not all the bubbles created at the lower apex altitudes reach higher apex-altitudes. This is similar to observations made by DMSP (Fig 5.11) in the studies by *Gentile et al.* [2] where the peak occurrence rates are close to 70 % during high solar activity years of 1989-1992 and are above 50 % in the high solar activity years 1999-2002. The discrepancy in peak occurrence during solar high activity years between DMSP and C/NOFS observations could be possibly due to difference in detection algorithms (automated vs manual inspection), sampled apex altitudes, apex-altitude range of the climatology maps, orbits of the two satellites (low vs high inclination) and the time periods analyzed. The DMSP satellites are polar-orbiting at an altitude of 840 km and the trajectories chosen for the aforementioned study crossed the magnetic equator in the post sunset local time (LT) sector (1900 – 2200 LT).

The C/NOFS climatology maps in our work have data between 20 – 24 LT. We cannot have a single altitude climatology map for the elliptically orbiting C/NOFS satellite and hence, the highest apex-altitude bin has been chosen to be 700-800 km for the climatology maps. Any bin slightly higher than this altitude and close to DMSP altitude of 840 km produces similar climatology (Fig. 5.12). The peak occurrence percentage further decreases to 71% as we go to 800 – 900 km of apex-altitude climatology map. The slight differences in occurrence percentage between DMSP and C/NOFS could also be due to the different values of F10.7 during different high solar activity periods. In

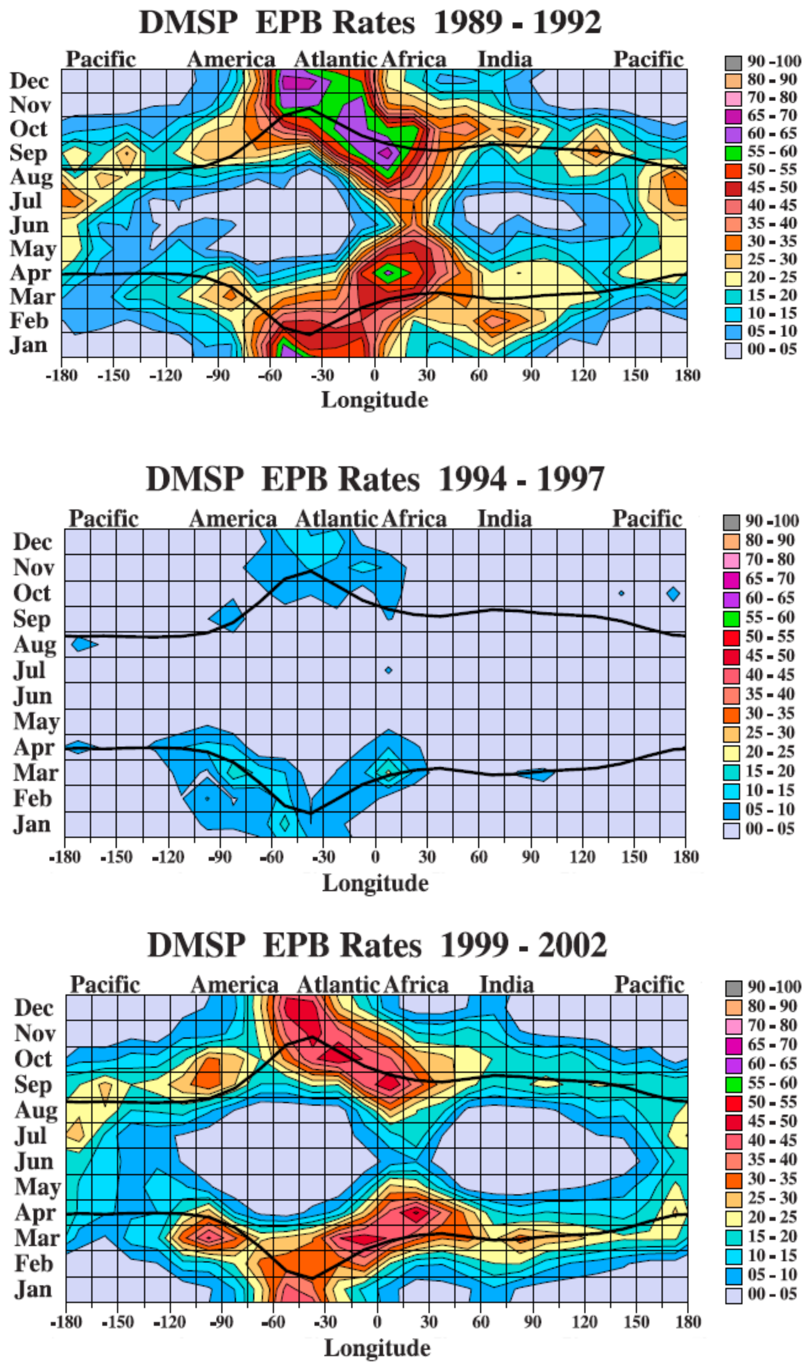

Figure 5.11: DMSP EPB Rates during solar maximum (top : 1989 - 1992 and bottom : 1999 - 2002) and minimum (middle : 1994 - 1997) years. The EPB rates during both solar maximum and minimum years maximize in the America-Atlantic-Africa sector but the EPB rates reduce sharply during the solar minimum years. These climatological maps suggest a striking dependence of equatorial plasma irregularities on solar activity at the polar-orbiting DMSP altitude of 840 km.

fact, a primary aim of this study is to understand the relationship between the F10.7 values and the apex-altitudes of the equatorial plasma bubbles.

Figure 5.10 shows the distribution of the plasma irregularities with changing apex altitude for the low solar flux years 2008 – 2010. The lowest apex-altitude bin climatology map resembles similar seasonal and longitudinal features as of those maps during high solar activity years whereas the features become gradually less distinct as we go to higher apex-altitude bin climatology maps. The maximum occurrence percentage decreases from 74 % to 27 % as we go from 400-500 km of apex-altitudes to 700-800 km of apex-altitudes. This is a significant drop in the occurrence percentage as compared to high solar activity years suggesting far fewer bubbles reach higher apex-altitudes during low solar activity years. This is easily demonstrated because the climatology map at the lowest apex-altitude bin shows significant bubble activity whereas that at 700-800 apex-altitude bin shows far less activity. The peak percentage of 27 % is in an isolated area and the percentage decreases further in a few other areas of activity. Most of the map is devoid of any bubble activity at all. But the total activity is also significantly less in the lowest apex-altitude bin during the low solar activity years as compared to that of the high solar activity years. This shows that not only are fewer bubbles created at the bottomside F-layer but also that far fewer of those created reach higher apex-altitudes during the low solar activity years as compared to high solar activity years. It is similar to what has been reported for DMSP by *Gentile et al.* in their aforementioned work. If we construct a C/NOFS climatology map closer to the DMSP altitude of 840 km, the maximum occurrence percentage further decreases to a lower level of 16 % (Fig. 5.12). The similarity between DMSP and C/NOFS observations at comparable apex-altitudes

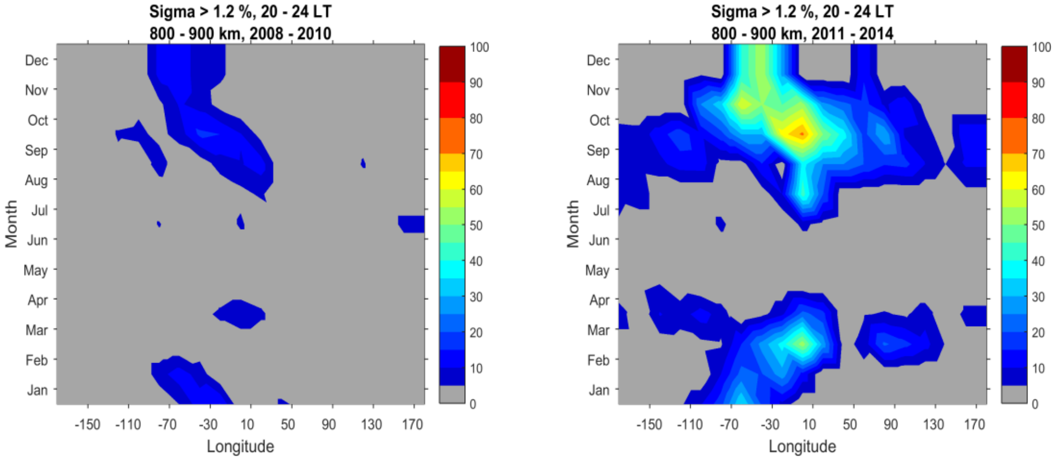

Figure 5.12: Occurrence Probability percentage results during low (2008 – 2010) and high (2011 – 2014) solar activity years of equatorial plasma irregularities at comparable altitude to that of DMSP altitude. The maximum occurrence percentage during low activity years further decreases to a lower level confirming the low-activity during DMSP low solar activity years.

and presence of significant bubble activity in C/NOFS observations at lower apex-altitudes confirms that the lack of activity in DMSP low solar activity climatology is indeed an apex-altitude effect. We also note the general pattern of scintillation climatology is found in the pattern of strong RT growth rates by Sultan (Fig. 9(a) and 9(b) in reference [41]) using climatological ionospheric models, and has been reproduced by a model of ionospheric irregularities and scintillation, i.e. PBMOD, in the work of *Retterer and Gentile* [38].

5.4 Flux-tube Mapping – Validation of the Climatology results

In this section, we seek to compare the irregularity detections from space-based in-situ observations with ground based scintillation observations by invoking the flux-tube paradigm of equatorial plasma bubble growth. Following the important works by *Haerendel* [1] and *Balsley et al.* [39], the disturbances in the equatorial ionospheric region – previously called by various names such as equatorial spread F (ESF), bubbles, and plumes owing to the diagnostic instruments used and structures reported by those instruments [40] – started to be understood as a flux-tube aligned interhemispheric effect explained by the gravitational Rayleigh-Taylor (GRT) flux tube interchange instability. In this scheme, the high plasma density magnetic flux tubes at the bottom-side of the ionospheric F region are replaced by the lower plasma density flux tubes from below similar to the hydrodynamic Rayleigh Taylor instability [41]. The magnetic field lines are horizontal at the equator contributing to the high vertical drift velocity, due to the polarization electric fields created by the disturbances in the plasma, of the plasma bubbles growing from the bottomside of the ionospheric F-region. Hence, the local density perturbation created by the exchange of magnetic flux tubes rises in altitude

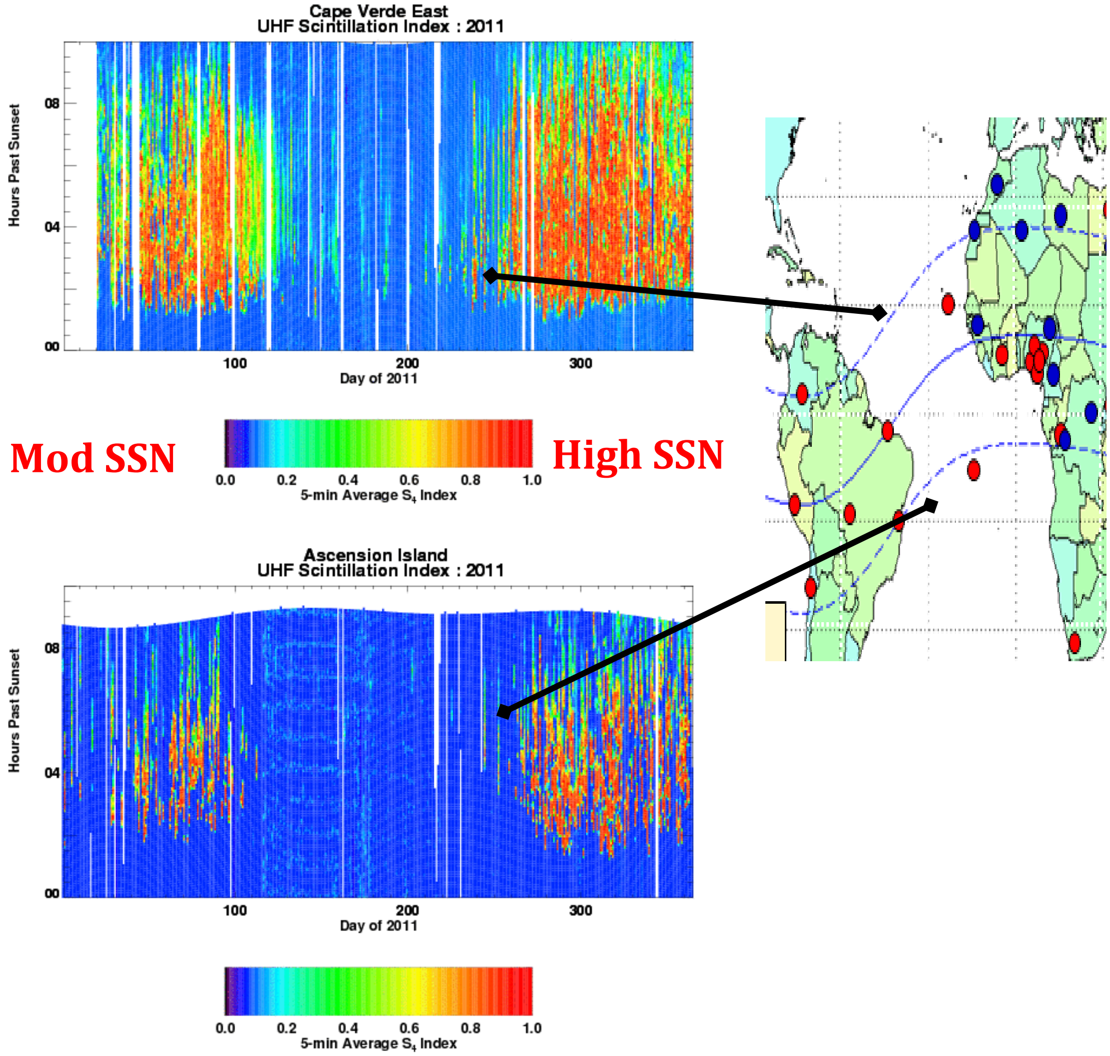

Figure 5.13: Scintillation observations in the year 2011 – the first part of which had moderate solar activity and the second part of which had high solar activity – in the two islands Ascension and Cape-Verde.

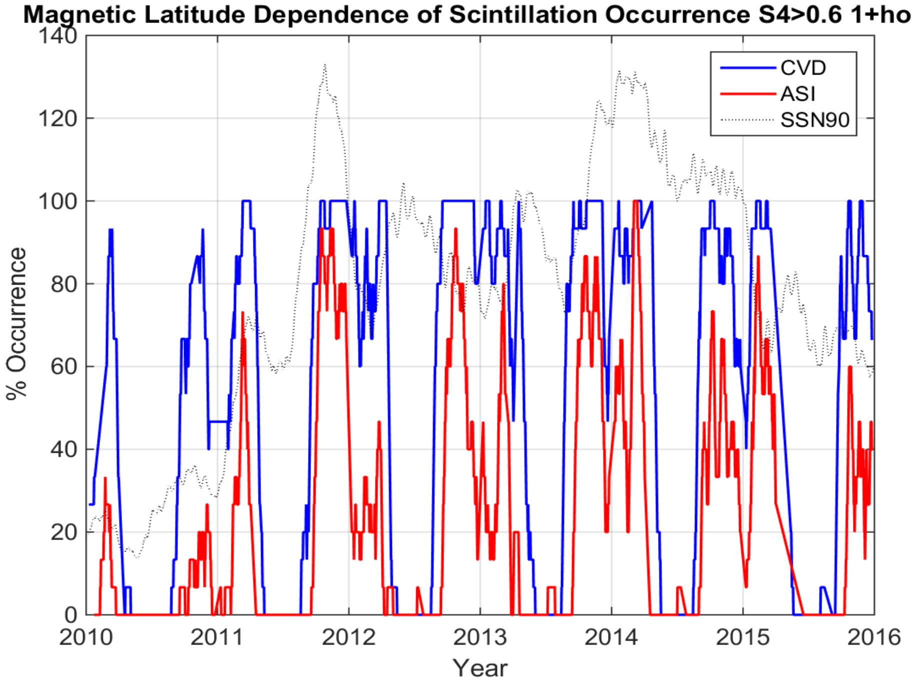

Figure 5.14: Nightly occurrence rates for S4 > 0.6 for at least one hour are shown in the plot for both Ascension and Cape Verde, where peak occurrence rates are essentially 100 % for periods of high solar flux.

through the topside region of ionosphere and moves polewards along the equipotential magnetic field lines as the electric fields map along the magnetic field lines. In this paradigm, the latitudinal extent of the irregularities is determined by the height of the bubbles at the magnetic equator. This unified explanation of the equatorial ionospheric irregularities has been tested before both theoretically and experimentally. The evidence of this field-aligned characteristics of equatorial ionospheric irregularities has been well studied in the works of *McClure et al*. [42] from the AE-C ion density measurements, *Weber et al.* [43] and *Moore and Weber* [44] from the air-glow emission observations, *Sobral et al* [45]*, Mendillo and Baumgardner* [46] from the all-sky images and scanning measurements of 6300-A^{o} emission, *Dyson and Benson* [47] from topside sounder results and *Aarons et al.* [48] from multi-station scintillation measurements. In this work, we seek to test this paradigm comparing C/NOFS observations with the ground-based scintillation observations made at Ascension Island and Cape-Verde Island (Fig. 5.13). The goal of the comparison between the space and the ground based observations is to check if our irregularity detection algorithm from the space based observations is consistent with the ground-based scintillation observations. To achieve this, we evoke the flux-tube paradigm of the equatorial plasma bubble growth to validate the space-based observation results as against the ground-based scintillation observations. This will achieve two goals – if it validates the space-based observations, it will validate the flux-tube paradigm as well.

To compare the ground and the space-based observations, we map the C/NOFS in situ observations into the magnetic field geometry at Ascension Island and Cape Verde Island respectively. We expect to see in situ irregularities whenever scintillation is observed on

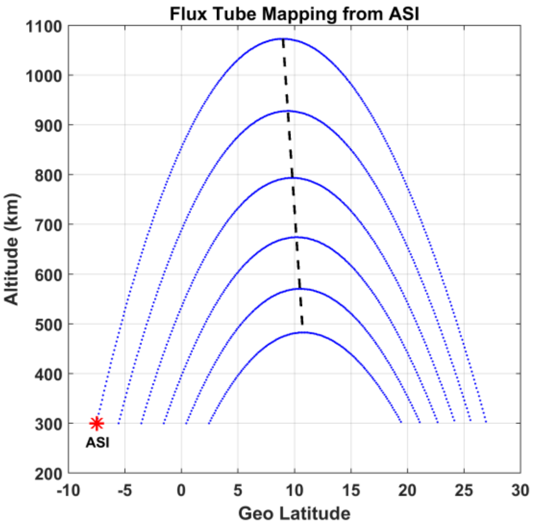

Figure 5.15: Illustration of the heights at magnetic equator corresponding to magnetic field lines from Ascension (Left) and Cape-Verde (right) Islands. Assuming bubble height determines the meridional extent, structures must rise to over 1000 km to reach Ascension but only above 400 km to reach Cape-Verde.

the ground and the satellite is sampling below the apex altitude of the F-region field lines above the site. Assuming bubble height determines the meridional extent, structures must rise to over 1000 km to reach Ascension but only 400 km to reach Cape-Verde (Fig 5.15).We use the International Geomagnetic Reference Field (IGRF) model to compute the magnetic field lines at the ionospheric pierce point from the VHF receiver at Ascension Island to the VHF satellite. The IGRF is a standard mathematical description of the Earth's main magnetic field that is widely used in studies of the Earth's deep interior, its crust and its ionosphere and magnetosphere [49]. As in the climatology maps, we compare irregularities between 20-24 Local Time. We draw magnetic field lines originating from the Ascension Island with correction made in latitude and longitude for the ionospheric pierce point at 300 km. Due to the magnetic declination of ~ 17 ^{o} west at the Ascension Island, the geographic longitude of the magnetic flux tube from Ascension ionospheric pierce point at 300 km to another hemisphere at 300 km varies with latitude by 6.3 degree (Fig. 5.16). Hence, while constructing the magnetic flux tube starting at the ionospheric pierce point at 300 km above Ascension Island and ending at 300 km in another hemisphere, we change the longitude values in ten steps with changing latitude values as given in the Figure 5.16. The longitude span for each of the ten latitude windows chosen is ±0.75 longitude degrees.

Since the look angle may not be pointed directly along the magnetic meridian, the ray path from the VHF satellite to the ionospheric pierce point for the receiver will cross magnetic field lines technically belonging to 'different flux tubes'. We calculated the distance the magnetic field line would vary in the east-west direction to be significantly less than the distance of the chosen longitudinal span corresponding to every latitude

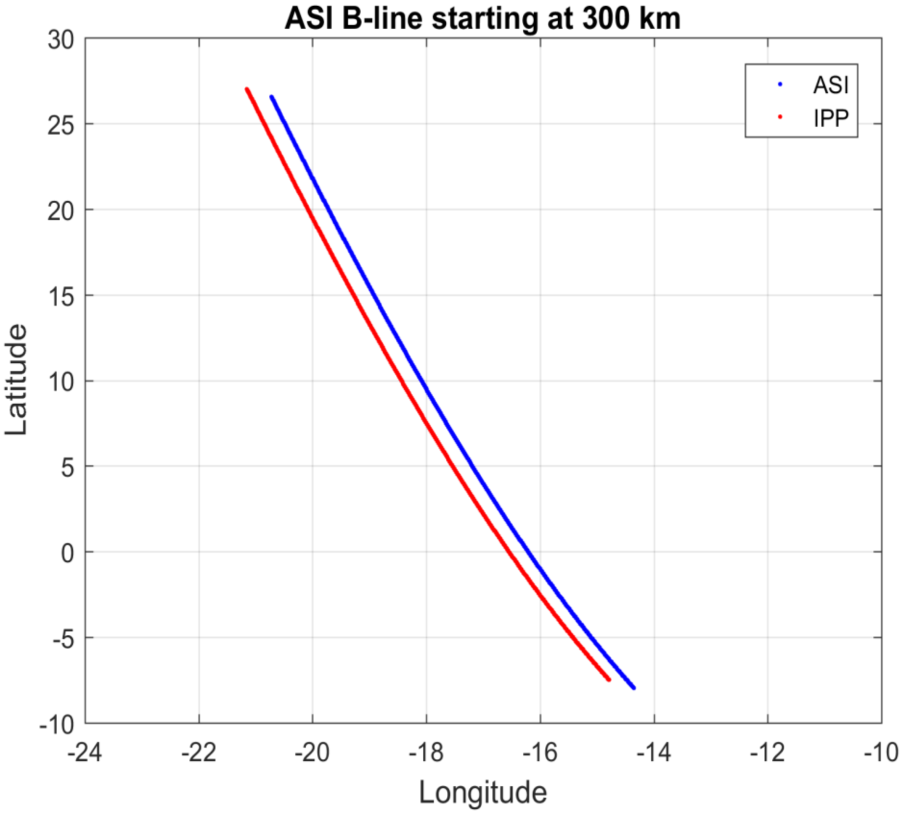

Figure 5.16: Variation of magnetic field line towards the northern hemisphere from the Ascension Island. The red line shows similar variation of magnetic field line for the ionospheric-pierce-point (IPP) corresponding to the Island.

window. Hence, we are constructing a 3-D flux tube from the Ascension Island to make the comparisons between ground based receiver observations with space based satellite observations. We count the number of passes that the satellite makes in our Longitude-Latitude-LocalTime windows in a day. For each pass observed in space, we take the mean Local-Time corresponding to the bin which has the maximum (peak) Sigma value. We find ground data closest to the calculated mean Local-Time, which let's say is the i^{th} position in the ground data. We take the mean value of scintillation index (S4) as recorded by the ground-based receiver for three data positions (i-1: i+1) to check if the ground has recorded scintillation. If the mean scintillation index for the fifteen minutes (as data is recorded every five minutes) exceeds the threshold value of 0.6, we count that the ground has reported scintillation. Based upon this criterion, there could be following four possible cases:

Color Key	**Ground S4 > 0.6**	**Space $\sigma > 1.2\%$**
🟥	**YES**	**YES**
⬛	**YES**	**NO**
🟦	**NO**	**YES**
🟩	**NO**	**NO**

To maximize the number of events for the correlation, we choose to make comparisons only for the active seasons observed both in the climatology maps and the ground-based scintillation observations (Fig. 5.17) for the years 2010 - 13. These set of years are chosen because both ground and space data are available for these years.

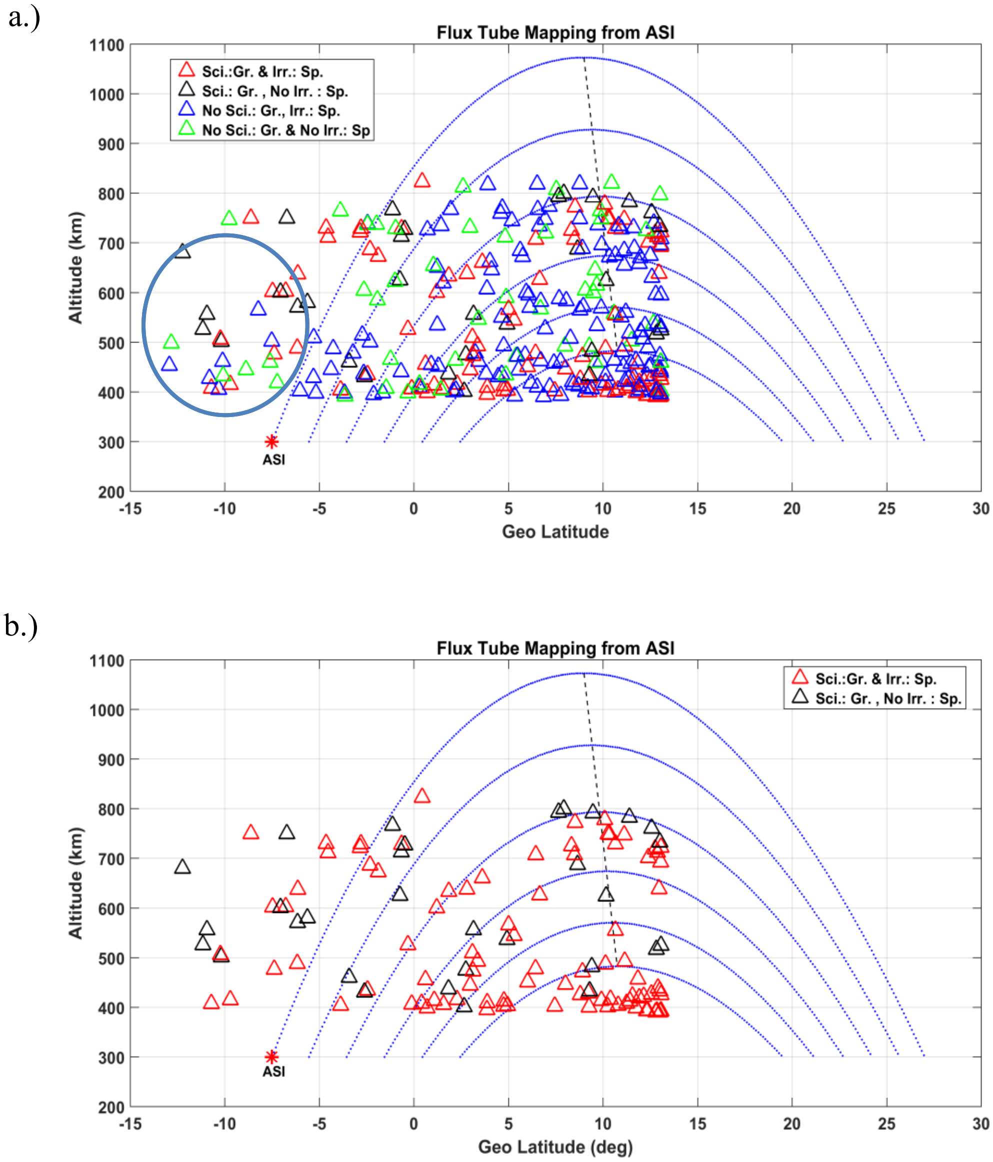

Figure 5.17: (a) Flux tube mapping of the satellite passes in the active seasons of the years 2010-11, 2011-12, 2012-13. The magnetic field line corresponding to the site, Ascension Island (red asterisk in the image), refers to an apex-altitude close to 1100 km at the magnetic equator (dashed black line). **(b)** Similar as (a) after removal of blue and green triangles. The black triangles below the magnetic field line corresponding to the ground receiver site are far less in number than the red triangles.

In Figure 5.17 (a), the red triangles correspond to the satellite passes which detect irregularities in space when ground based receiver also reports scintillation observations for the VHF satellite signals; that is, both sources "red" in the color key. For the ground receiver site to report scintillation, the bubbles must have risen as high as the apex-altitude corresponding to the site longitude's ionospheric pierce point at an altitude of 300 km. Because the bubbles rise from lower altitudes, it is assumed that the entire flux tube below the peak apex altitude is disturbed. Hence, a satellite pass below the magnetic field line corresponding to the site 'must' detect irregularity in space if the receiver site has reported scintillation observations. The black triangles within the magnetic flux tube, corresponding to cases where the ground site observed scintillation but the satellite did not detect any irregularities, are anomalies. They are far less numerous (Fig. 5.17 (b)) than the red triangles. The blue triangles, which are within the magnetic field line corresponding to Ascension Island, don't violate the flux tube formalism as it is plausible for the ground not to report scintillation if the bubbles didn't rise high enough at the magnetic equator to reach an apex-altitude mapping over Ascension Island. The blue triangles inside the blue circle in Figure 5.17 (a) which are beyond the magnetic field line corresponding to the Island are anomalies as well. They represent the cases in which the satellite detected irregularities in space but the ground receiver did not observe scintillation despite the bubbles rising higher than the apex-altitude corresponding to the Island. But these are far less numerous than the blue triangles within the magnetic field line corresponding to the site (6 out of 141). Three out of these 6 blue triangles have S4 ~ 0.5 which is close to the chosen threshold of S4 > 0.6. So, many of these anomalies could be due to the threshold assigned with scintillation and irregularity observations as no threshold can be expected to be perfect. Similarly, few of the black triangles turn into red when the longitudinal span in the flux-tube definition is increased suggesting the longitudinal drift – east or west – of the bubbles could also be the issue of the reported anomalies in our method. The green triangles don't warrant any specific attention as they represent cases when both ground and space don't detect activity.

In Figure 5.17 (b), there are 121 passes for which the ground reported scintillation observations. Out of these 121, 100 are within the magnetic field lines corresponding to the site Ascension. 77 out of these 100 are detected to have irregularities in space as well. This is 77 % of 'congruent' observations both in space and ground. As seen in the Sigma vs S4 colorbar plot (Fig. 5.18) of these 100 passes, many of the cases for which the space observations don't detect irregularities are close to the chosen threshold value of Sigma > 1.2 and most of the them are above the nominal noise floor of Sigma ~ 0.5.

	Ground (S4 > 0.6)	Space (σ > 1.2)
No. of passes	100	77

Table 5.1: Bubble Bin Statistics

Similarly, we mapped the nightly comparisons of C/NOFS and ground observations in the magnetic field lines in the active seasons of the years 2010-11, 2011-12 and 2012-13 (Fig. 5.19) for the station Cape-Verde. For this station, we didn't aim for pass-to-pass comparison as we did for Ascension Island. This is because Cape-Verde is close to the magnetic equator and the apex altitude corresponding to the station is close to 450 km. Hence, we expect the comparison to be less sensitive to the corrections introduced by IPP

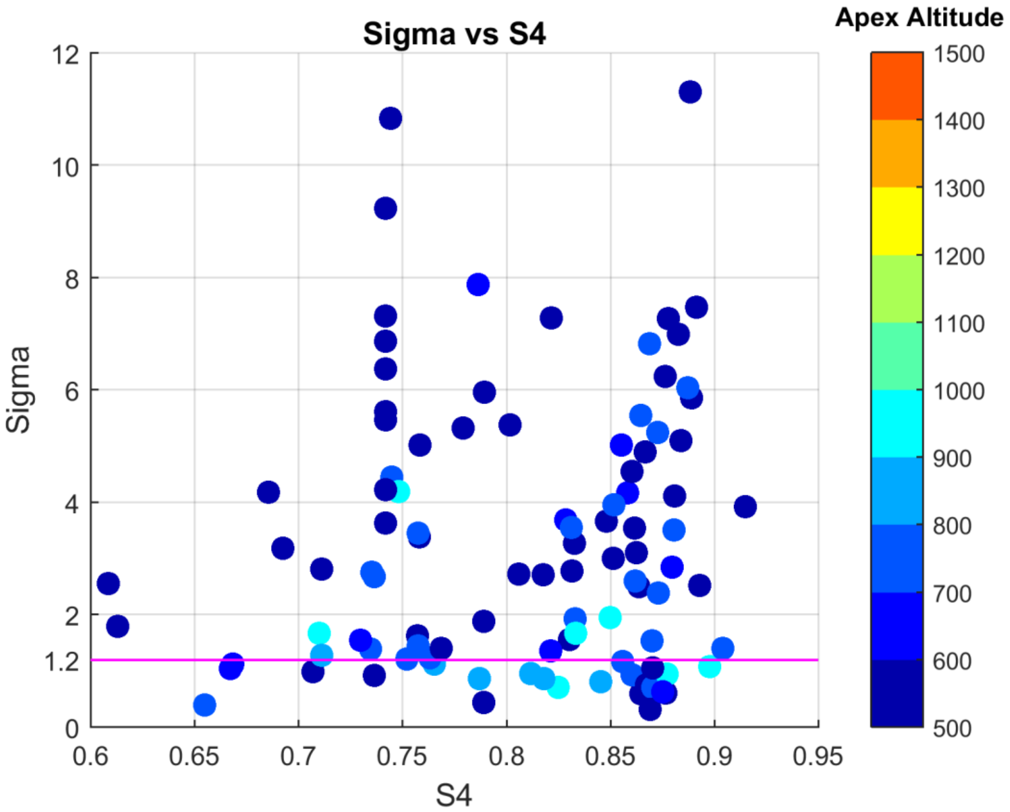

Figure 5.18 : Sigma vs S4 Colorbar plot - The space observations which don't 'detect irregularities' are close to the chosen threshold value of Sigma > 1.2 and most of the them are above the nominal noise floor of Sigma ~ 0.5.

magnetic field lines applied in the pass-to-pass comparison as in case of Ascension Island.

Since the apex-altitude corresponding to the station is relatively low, we expect the ground to report scintillation most of the times whenever the satellite observes irregularity. This is so because the satellite orbits in an elliptical path of 400 - 850 km and unless it is very close to magnetic equator while at perigee, its corresponding apex-altitude must be equal or higher than that corresponding to the receiver station Cape-Verde. In Figure 5.19, there are 238 nights for which irregularities were detected in space and 231 out of these 238 reported scintillation in ground as well. This is 97 % of 'congruent' observations both in space and ground. As expected, we see higher correlation pertaining to the Cape-Verde Island as it is close to the magnetic equator.

	Space ($\sigma > 1.2$)	Ground (S4 > 0.6)
No. of passes	238	231

Table 5.2: Bubble Bin Statistics for CVD Island

Unlike the Ascension Island, Cape-Verde is at low magnetic latitude and it is possible the scintillation observed on the ground did not reach the height of the space observations which correspond to the black triangles in the Figure 5.19. The black triangles in the case of Cape-Verde are consistent with the flux-tube paradigm. The green triangles, like in the Ascension Island case, are also consistent. It is the blue triangles – corresponding to the cases where scintillation is not reported on the ground but irregularities are observed in space – which need explanation. How can one observe irregularities in space where the irregularities are well above the apex altitude needed to reach the station but no

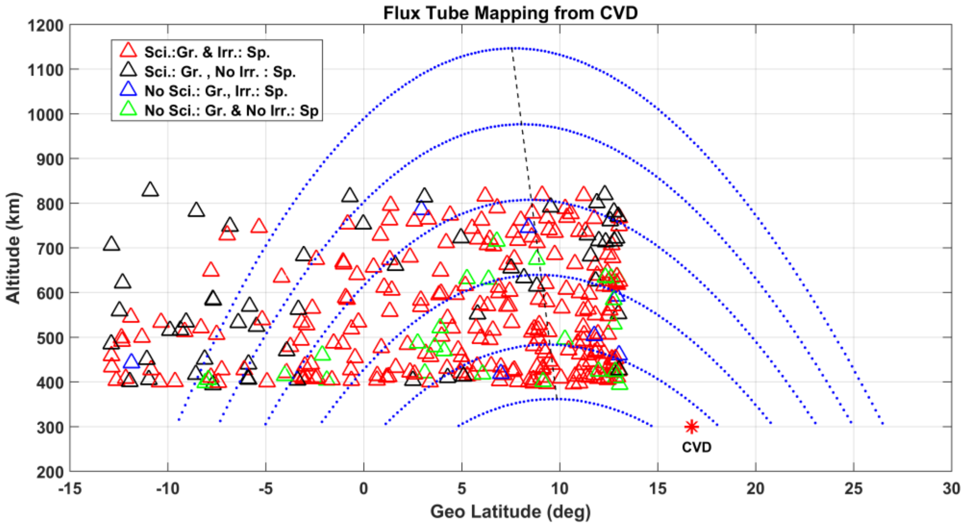

Figure 5.19: Flux tube mapping of the nightly comparisons of C/NOFS observations and ground observations at the Cape-Verde site in the active seasons of the years 2010-13. The magnetic field line corresponding to the site, Cape-Verde (red asterisk in the image), refers to an apex-altitude close to 450 km at the magnetic equator (dashed black line). We see higher correlation between the ground and the space observations (more number of red triangles) as bubbles need only rise to 450 km for the ground to report scintillation.

scintillation is observed on the ground? These could, as in the case of Ascension Island, represent instances where the background density is sufficiently low that the scintillation didn't exceed our absolute threshold of S4 > 0.6 even though our relative space based parameter exceeded 1.2 %. Since these are few (7 nights out of 319 nights) in numbers in the entire data-set of comparisons, our space-based algorithm of equatorial ionospheric irregularities detection is confirmed to be consistent with ground-based scintillation observations. While confirming this, we validate the flux-tube paradigm of equatorial plasma bubble growth as well.

5.5 Apex Altitude Distribution during low and high solar activity years

5.5.1 Objective

Since we have demonstrated that our irregularity detection algorithm is consistent with ground-based scintillation observations associated with equatorial plasma bubbles, we now proceed with our fundamental objective of determining the apex-altitude distribution of the bubbles. Since the first half of 2011 has transitional F10.7 values, we include data from the second half of 2011 through 2014 as high solar activity period. We take data from 2008 through 2010 as low solar activity period as in the preceding sections. The sampling window for both solar low and high activity years includes active seasons Jan – April and Sep – Dec., Local-Time 20 – 24 LT and longitudinal region: 80^o W: 10^o E.

We are interested in finding out the 'True Distribution' of peak-altitudes of the bubbles at the magnetic equator. It is the peak altitudes of the bubbles at the magnetic equator which determine their latitudinal extent as the irregularities map along the equipotential magnetic field lines in either side of the hemispheres. It is important because we think and we will test in this section the ‘True Distribution’ of peak-altitude of bubbles at the magnetic equator is markedly different than the ‘Observed Apex-Altitude Distribution’ of the bubbles (by the satellite).

5.5.2 Methodology

5.5.2.1 Mono-Altitude True Distribution Illustration

The below flow-chart and illustration shows a simple example how the ‘Observed Distribution’ doesn’t represent the ‘True Distribution’ of the bubbles. But it also shows that the ‘Estimated True Distribution’ replicates the shape of ‘True Distribution’. The Observed Distribution shows what a satellite sampling uniformly in apex altitude would observe given the ‘monochromatic’ True Distribution defined in the first subplot. The True Distribution in the final subplot of Fig. 5.20 is estimated from the Observed Distribution based on the physical reality that the number of observed distribution at an apex altitude is integral of the true distribution at apex-altitudes equal and higher than that of the observed distribution. Conversely, all higher altitude bubbles at the magnetic equator pass through the lower altitudes beneath them. Mathematically,

$$M_{zo} \quad = \quad \int_{zo}^{\infty} N(z)dz \,, \qquad \text{----------- (3)}$$

M_{zo} is observed distribution,

N(z) is true distribution.

For discrete data, $M_{zo} \quad = \quad \sum_{zo}^{\infty} N(z) \qquad \text{----------- (4)}$

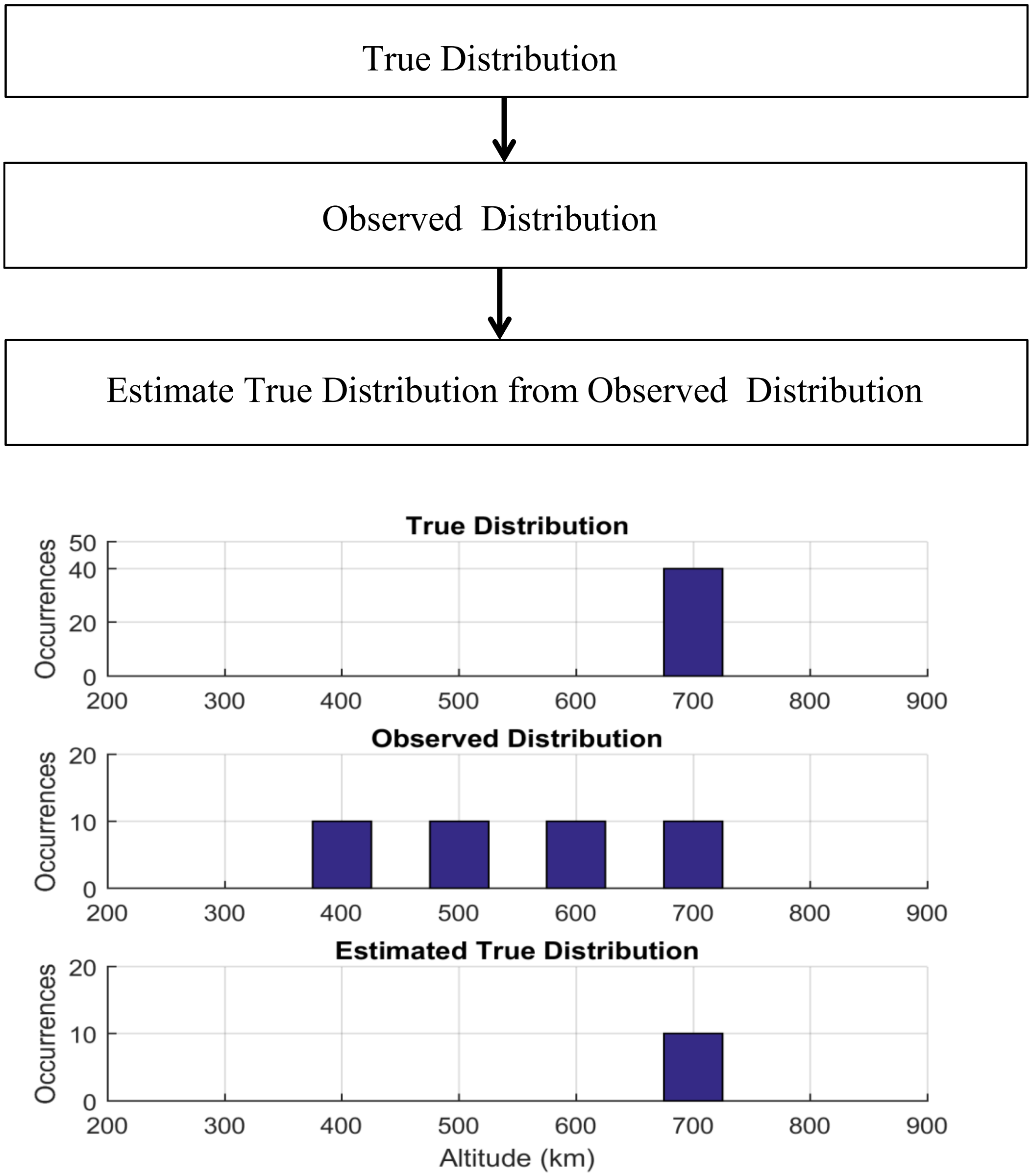

Figure 5.20: The flowchart above outlines the steps involved in the simulation. The plot below illustrates the simulation with one simple example. A 'monochromatic' true distribution is defined (1st subplot). With assumed uniform sampling, altitude bins less than or equal to that of True Distribution have 'Occurrences' distributed uniformly in 'Observed Distribution' (2nd subplot). In the final subplot, 'True Distribution' is estimated from the 'Observed Distribution' which is essentially subtracting the number of Occurrences at a previous bin from that at a bin – starting at the highest altitude bin, i.e. TrueDist(N) = Obs(N) – Obs(N+1). The steps are explained in detail in the text.

This is equivalent to subtracting the number of bubbles at a previous bin from that at a bin while starting at the highest apex-altitude bin in the Observed Distribution, i.e. TrueDist(N) = Obs(N) – Obs(N+1). The Estimated True Distribution has the right 'shape' of the initially defined 'True Distribution'. While we are applying this exercise to estimate the true distribution from the observed distribution, we also identify that the same can be achieved through familiar functions in statistics. The observed distribution is in fact the Complementary Cumulative Distribution Function (CCDF) and we can deduce Cumulative Distribution Function (CDF) from the CCDF from the following relation:

$$\text{CDF} = 1 - \text{CCDF}.$$

where, CDF is the probability that N will take a value less than or equal to n:

$$F_N(n) = P(N \leq n) \text{ and}$$

the CCDF is the probability that N will take a value more than n:

$$F_N(n) = P(N > n).$$

And we can estimate the true distribution via differentiation of the CDF(or in the discrete case, by applying difference appropriately).

5.5.2.2 Simulation for non-trivial True Distributions

In another simulation, we extend the illustration in the preceding sub-section to initially defined True Distributions which aren't as simple as 'monochromatic'. We will seek to test if the 'Estimated True Distribution' in this case also replicates the shape of the initially defined 'True Distribution'. If that's the case, we will be more confident of our

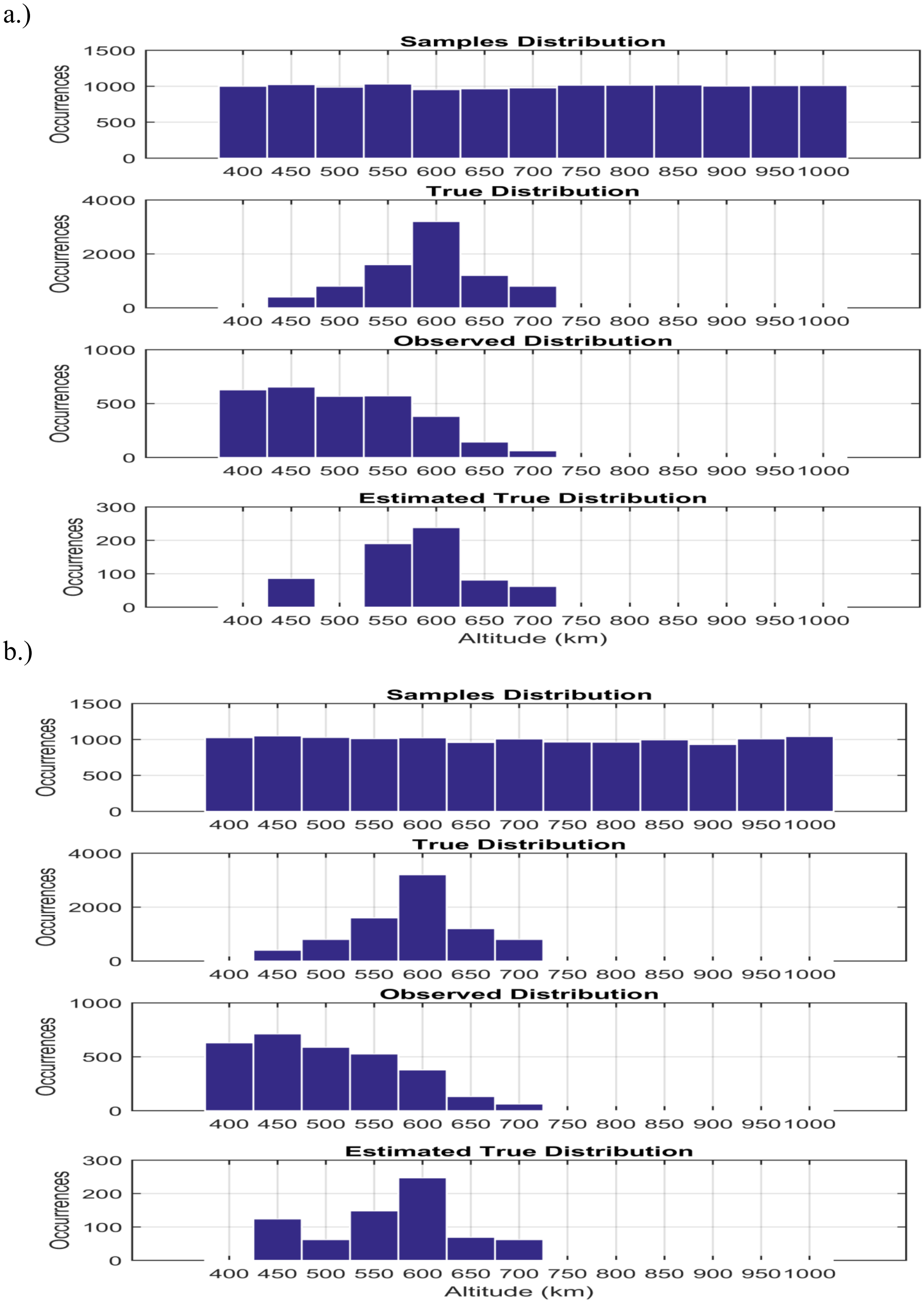

Figure 5.21: Two runs (a, b) of a simulation to estimate the true distribution of bubble activity from an initially assumed true distribution. The estimated true distributions are seen to depend upon the initial Sample Distribution and the Observed Distribution.

approach in constructing the ‘Estimated True Distribution’. We also seek to learn how the initial sampling density influences the shape of the final ‘Estimated True Distribution’. We start by randomizing a ‘Sample Distribution’ of apex-altitudes within a chosen range (e.g.: 375 – 1025 km). We then define a ‘True Distribution’ which determines the number of bubbles at specific altitude-bins. Based upon the ‘True Distribution’, we ‘retrieve’ an ‘Observed Distribution’ from a virtual satellite we fly through our initial sample-space. And based upon the virtual ‘Observed Distribution’, we build the ‘Estimated True Distribution’. The steps briefly outlined here are described in little more detail in the paragraph following this. Here, we are only trying to initiate the reader to the processes involved in the simulation.

We start by randomizing the initial sample distribution for 13000 samples. Each sample is taken at a random altitude but the overall distribution of 13,000 samples is uniform over the altitude range (375 – 1025 km). This ‘large’ number of samples with uniform sampling over the altitudinal range is to ensure good statistics in the simulation comparable to real data. Each sample can be thought as a ‘pass’ of an imaginary satellite involved in this simulation or as a data-point for every ‘night’ the satellite is in operation. Each sample corresponds to an altitude which we take to be the altitude of the satellite in this simulation. We then specify true bubble distribution. The number of bubbles shall not exceed the number of samples. In Figure 5.21, we choose a True Bubble Distribution to be of semi-Gaussian shape that peaks at 600 km. The bubbles are at certain altitude but satellite positions can be anywhere throughout the sample space. As an example, if we have chosen to have 3000 number of bubbles at the apex-altitude bin centered at 600, the corresponding 3000 satellite positions are distributed randomly over all 13,000 samples.

Though the corresponding satellite positions are randomly distributed, the (maximum) bubble altitude for these bubbles will remain 625. The satellite will observe a bubble if it is below or equal to the bubble altitude but it will miss the bubble if it is above the bubble altitude. Hence, the observed distribution is determined by checking the altitude of the satellite for each pass where a bubble was present. We seek to estimate the true distribution from the observed distribution and compare the estimated true distribution with the 'original' true distribution we started with to construct the observed distribution. The true distribution is estimated based on the physical reality that higher altitude bubbles at the magnetic equator pass through the lower altitudes beneath them as expressed in the equations (3) and (4) above. This is equivalent to subtracting the number of bubbles at a previous bin from that at a bin while starting at the highest apex-altitude bin in the observed distribution. The goal is to see if we can successfully estimate the True Distribution (from the Observed Distribution) to be similar as initially defined True Distribution. We made five runs of the simulation for every true distribution. In Figure 5.21(a), the shape of the True Distribution and the Estimated True Distribution look closely similar. But, the estimated true distribution doesn't report bubble activity in the apex altitude bin centered at 500 km. This can be traced to the relatively less number of bins in the corresponding bin in the Samples and the Observed Distribution. In another example from another run (Fig. 5.21 (b)), the shape of the True Distribution and the Estimated True Distribution also look closely similar. But, the estimated true distribution has slightly higher bubble activity in the apex altitude bin centered at 450 km. This can again be traced to the relatively more number of bins in the corresponding bin in the Samples and the Observed Distribution. In both Fig. 5.21(a) and 5.21(b), the estimated

True Distributions aren’t very dissimilar than the initially defined True Distribution. This shows that the estimated True Distribution closely resembles the initially defined True Distribution with the assumptions made in the simulation. It also shows that the initial statistics of the sample distribution influences the final estimation of the True Distribution.

5.5.2.3 Processing the Results: C/NOFS Bubble Distributions

With example and simulation in preceding two sub-sections establishing that the ‘Observed Distribution’ of bubbles by a satellite is markedly different than the ‘True Distribution’ of the peak-altitude of the bubbles at the magnetic equator, we present how we seek to process the bubble distribution results from C/NOFS observations in this sub-section. We start with the following flow-chart. The results themselves are presented in the next section.

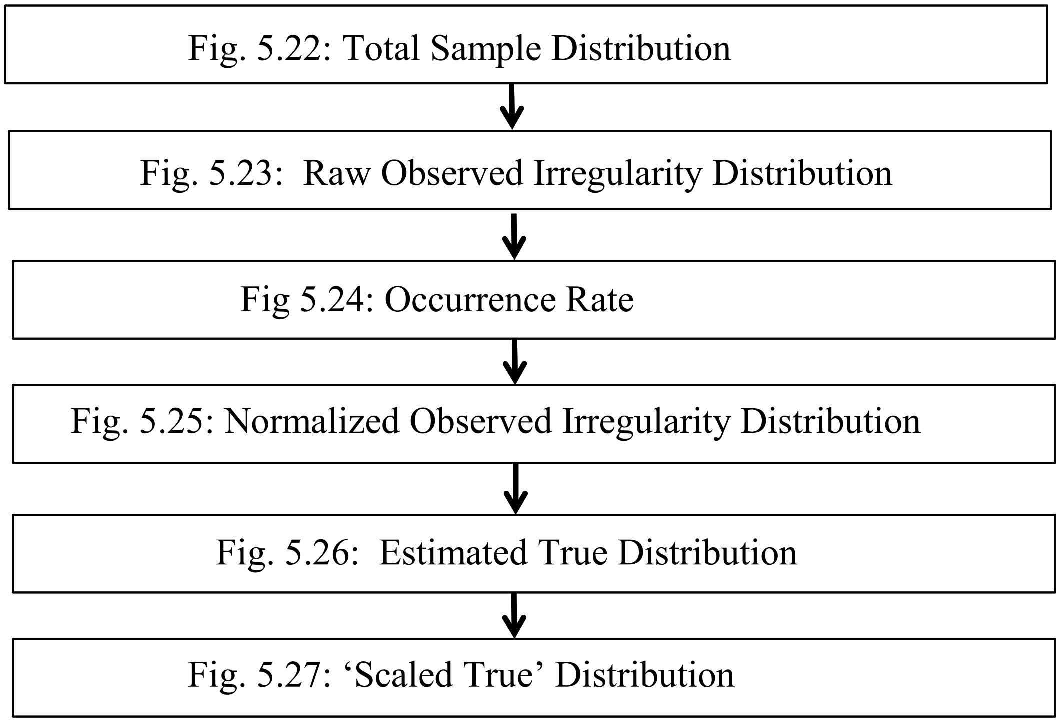

We start with the ‘Sample Distribution’ and the ‘Raw Observed Irregularity Distribution’ for both high and low solar activity periods. The sampling and the observed irregularity apex-altitude distributions will allow us to see how farther do bubbles rise to higher apex-altitudes. While examining the total sampling apex-altitude distributions, we include all apex-altitudes for which an appreciable number of bubbles were observed. We then calculate the occurrence rate of ionospheric irregularities for both solar low and high activity years. We recognize that the altitude sample distribution has a direct influence upon the observed irregularity distribution as confirmed in the simulation in preceding sub-section. Put more simply, the more samples acquired in a given altitude range the more bubbles one is likely to detect in that range. To correct the bias introduced due to sampling density, we ‘normalize’ the observed irregularity distribution and present the normalized observed irregularity distribution for both solar low and high activity years. But, the raw observation of irregularities by a uniformly sampling satellite can ‘statistically overlook’ the physical reality that all higher altitude bubbles at the magnetic equator pass through the lower altitudes beneath them. That this physical reality is indeed valid was established in the simulation in the preceding sub-section by the closely similar ‘True Distribution’ and ‘Estimated True Distribution’. To recall, the ‘Estimated True Distribution’ was constructed from the ‘Observed Distribution’ by applying the physical reality we are referring here. Similarly, we construct an ‘Estimated True Distribution’ from the ‘Normalized Observed Distribution’ in C/NOFS results. The ‘Estimated True Distribution’ is the distribution of bubble peak-altitudes at the magnetic equator. We construct ‘Scaled True Distribution’ from the ‘Estimated True Distribution’. We are saying ‘Scaled True Distribution’ as we rescale the ‘Estimated True Distribution’ in an attempt to get close to the actual number of bubbles in the ‘True Distribution’.

5.5.3 Results: C/NOFS Bubble Distributions

In Fig. 5.22, we show the distribution of apex-altitudes sampled is predominantly below 1000 km, but the full range of expected bubble altitudes is covered. These are simply the distribution of samples acquired by C/NOFS satellite through 2008-2014. The distributions during low and high solar activity years are similar but not identical. The change in the sampling statistics for two periods is mostly due to the change in C/NOFS orbit as the apogee decreases over time and the sampling density tends towards lower altitudes.

The apex altitude distributions with irregularities defined by Sigma > 1.2 during low and high solar activity years (Fig. 5.23) show higher number of irregularities detected during high solar activity years. It also shows the irregularities rise higher during high solar activity years as compared to low solar activity years. The irregularities included in the distributions exclude enhancements and also ‘smooth reductions’ in ion density as defined by delN/N < 0.02 as elsewhere in this study. The occurrence rate (Fig. 5.24) plot is obtained by dividing the number of observed irregularity bins in each apex-altitude bin by the number of total sample bins in the corresponding apex-altitude bin. The plot shows that the occurrence rate of irregularities decreases more rapidly at solar minimum years relative to solar maximum years. While going from 400-500 km apex-altitude bin to 800-900 km apex-altitude bin, the occurrence rate decreases from 26.7 % to 8.9 % during high solar activity years while it decreases from 12.1 % to 1.5 % during low solar

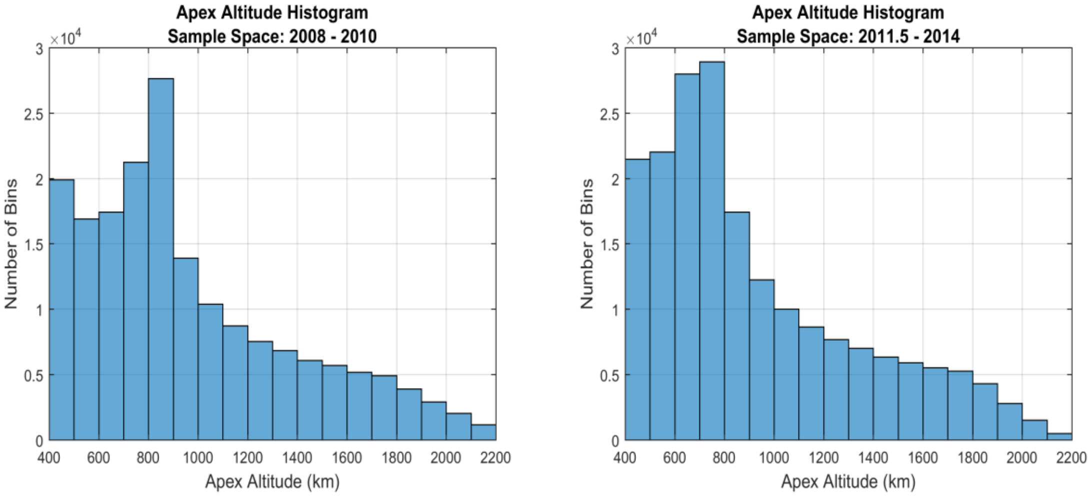
Apex Altitude Histogram
Sample Space: 2008 - 2010

Apex Altitude Histogram
Sample Space: 2011.5 - 2014

Figure 5.22: Apex-Altitude Distribution sampled during low and high solar activity years (2008 – 2014) by C/NOFS satellite. The sample space shown is for active longitude (-80^o : 10^o) and seasons (Jan – Apr, Sep – Dec) and between 20 – 24 LT. The sampling density trends towards lower altitudes (right image) due to decrease of C/NOFS apogee during later years of operation.

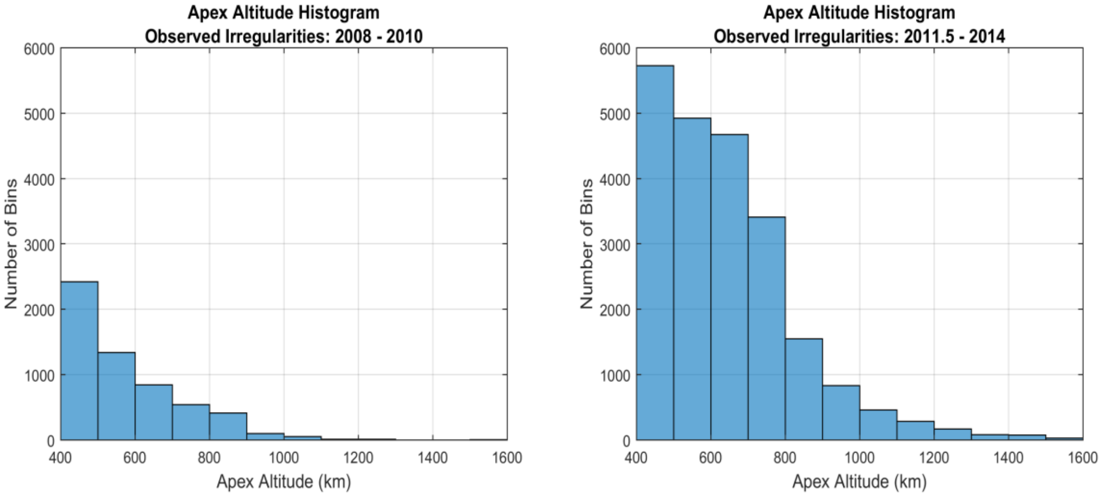

Figure 5.23: Raw Observed Apex Altitude Distribution with irregularities defined by Sigma > 1.2 during low and high solar activity years. The irregularities in the distributions exclude enhancements and 'smooth reductions' in ion density as defined by $\Delta N/N < 0.02$. The distributions shown are for active longitude (-80^o: 10^o) and seasons (Jan – Apr, Sep – Dec) and between 20 – 24 LT. The high solar activity years have more activity rising to higher altitudes as compared to low solar activity years.

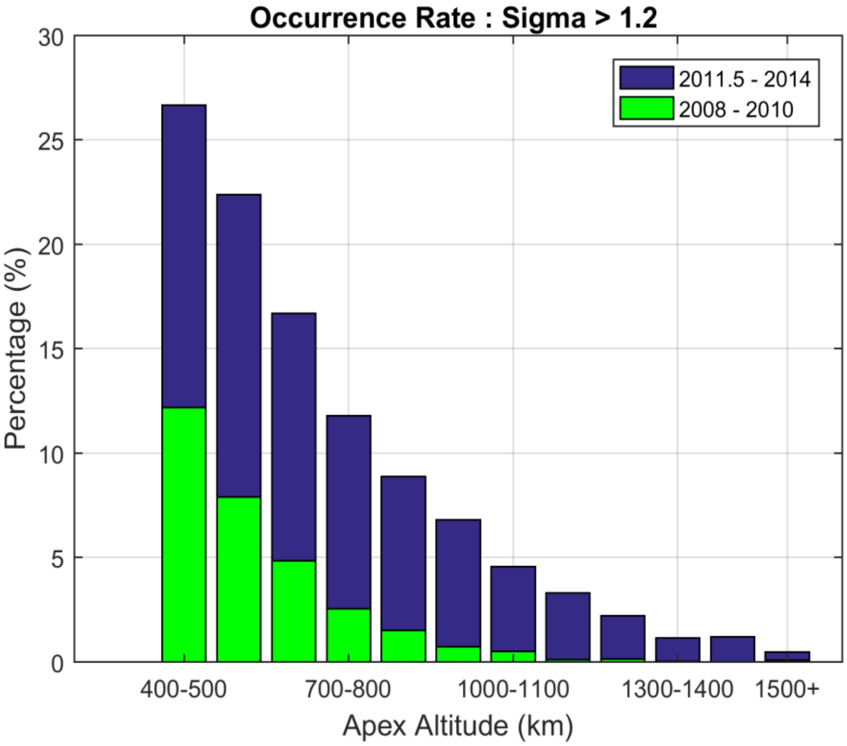

Figure 5.24: Occurrence Percentage: Irregularity detections normalized by total samples. The irregularities detected exclude enhancements and 'smooth reductions' in ion density as defined by delN/N < 0.02. The occurrence rate decreases more rapidly at solar minimum years as compared to solar maximum years.

activity years. This is more than twice (~ 2.7) as rapid a decrease during low solar activity years as compared to high solar activity years in this apex-altitude bin. In the DMSP climatology results, the peak occurrence percentage decreases nearly four times during solar minimum years as compared to solar maximum years. The disparity in occurrence rate during low solar flux years is nearly twice as high with DMSP data as it is in the C/NOFS data sets analyzed here despite the solar flux being lower for both the high and the low solar flux periods for C/NOFS. While the methodology to calculate the occurrence percentage for DMSP climatology and here in Figure 5.24 are different, it confirms that the very low occurrence rates reported by DMSP during solar minimum are partly due to altitude bias. The satellite sampled at a constant altitude of 840 km and observed far fewer bubbles during solar minimum years. We say – partly – as not only were less bubbles were observed during solar minimum years but also fewer bubbles were observed at the lowest apex-altitude bin as seen in Figure 5.24.

To correct the bias introduced due to the sampling density, we seek to normalize the 'Raw Observed Distribution' (Fig. 5.23) based on the 'Sample Distribution' (Fig. 5.22). We normalized the 'Raw Observed Distribution' based on the number of bins in the first apex-altitude bin of the 'Sample Distribution'. The 'Estimated True Distribution' is constructed out of the 'Normalized Observed Distribution' (Fig. 5.25) and is rescaled to deduce 'Scaled True Distribution' as shown in Figure 5.26. The rescaling is done to conserve the initial number of bins in 'Normalized Observed Distribution'. This allows us to construct 'True Distribution per night' by dividing the number of bubble bins in every apex-altitude bin of 'Scaled True Distribution' by successive number of nights the

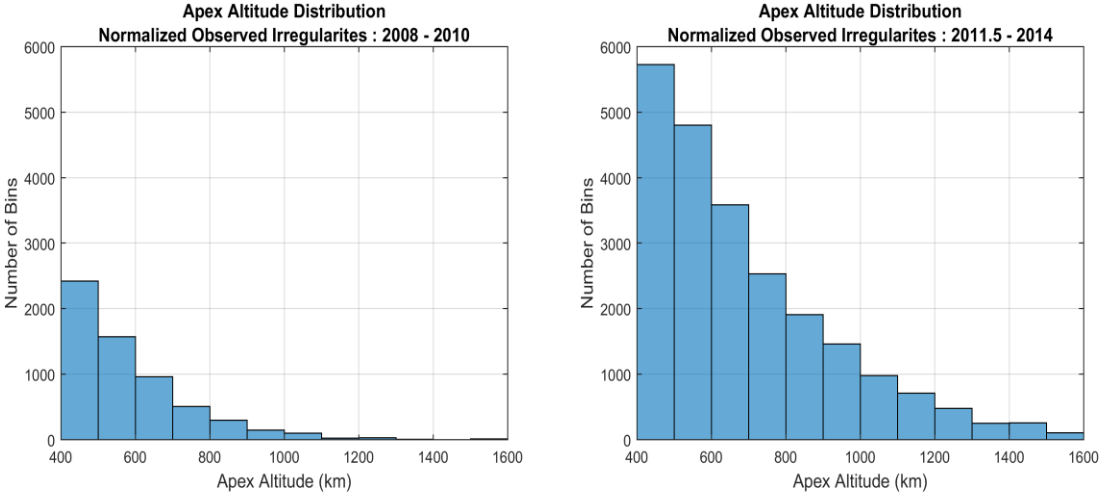

Figure 5.25: 'Normalized Apex Altitude Distribution' of ionospheric irregularities during low and high solar activity years. The distributions shown are for active longitude (-80° : 10°) and seasons (Jan – Apr, Sep – Dec) and between 20 – 24 LT. The normalization of the Observed Irregularity Distributions (Fig. 5.23) was based on the first apex-altitude bin of the initial Sample distributions (Fig. 5.22).

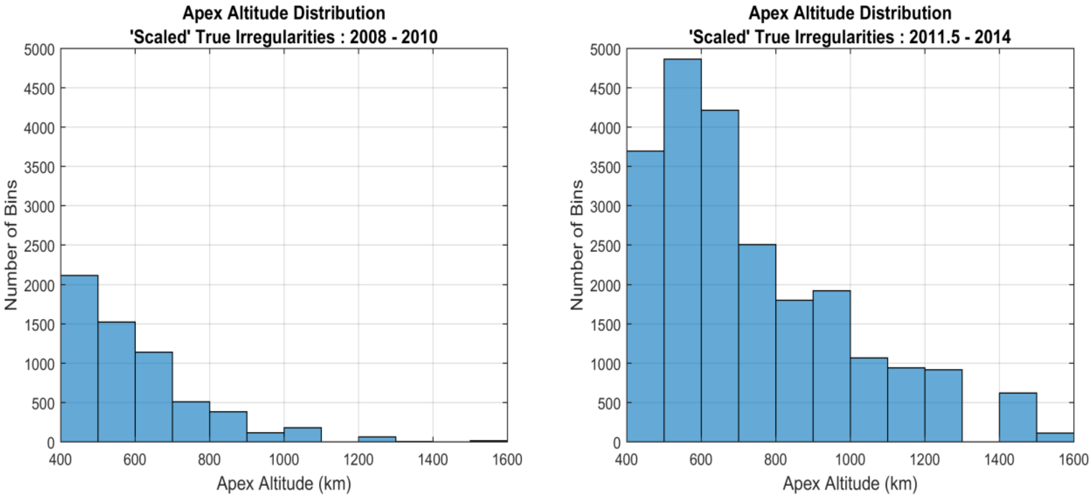

Figure 5.26: 'Scaled True Distribution' of Irregularities for low and high solar activity years. The distributions shown are for active longitude (-80^o:10^o) and seasons (Jan – Apr, Sep – Dec) and between 20 – 24 LT. The 'Scaled True Distribution' is achieved by rescaling the 'Estimated True Distribution'. The rescaling is done to preserve the initial number of bins in Normalized Observed Distribution.

satellite was in operation during both low and high solar activity years. In next section, we use this 'True Distribution per night' to run a numerical simulation in which we seek to reproduce the initial 'Observed Distribution' by 'numerically' flying a 'satellite' on the C/NOFS trajectory through the randomly distributed bubbles.

5.6 Numerical Simulation

The continuous in-situ observations made onboard C/NOFS satellite during both high and low solar activity years avails data to analyze the effects of solar-activity on the altitude distribution of the ionospheric irregularities at the magnetic equator. But, we also seek to ask: what is the 'reasonable' period of time to make statistically meaningful inferences from the distributions? We ask the question because it is required to pursue our primary aim of this study to understand the relationship between the F10.7 values and the peak apex-altitudes of the equatorial plasma bubbles. If we want to examine the dependence of bubble peak altitude on solar flux, we need to understand the statistics of our observations over the time scales on which solar flux varies.

We try to run a numerical simulation to find the answers. We randomize longitude positions in every apex-altitude bin of true distribution for nightly bubble observations. The 'True Distribution per night' (Fig. 5.27), as discussed in preceding section, becomes the numeric bubble distribution for every night in this simulation. The upper value of each apex altitude bin is now taken as the apex-altitude for the number of numeric bubble bins in that bin. For every randomized longitude position of a numeric bubble bin, we find the closest C/NOFS satellite longitude position to compare the C/NOFS apex altitude with the numeric bubble bin apex-altitude. It is virtually flying a 'satellite' through the ‘true bubble distribution’ and reporting a bubble if the C/NOFS apex altitude corresponding to the randomized longitude position of a numeric bubble bin is less than or equal to the numeric bubble apex-altitude. The steps are:

1. Start with the True Bubble Distribution Per night. This becomes the Numeric Bubble Distribution per night,
2. Randomize the longitude positions within the active window (-80° : 10 °) for the number of bubbles in every apex-altitude bin of the Numeric Bubble Distribution,
3. Get the apex-altitude from C/NOFS data corresponding to the randomized longitude positions for each pass. The analysis is performed for the active longitude sector (-80° : 10 °), active seasons (Jan – Apr, Sep – Dec) and the evening local time (20 – 24 LT),
4. Report a bubble if C/NOFS Apex Altitude is less or equal than numeric bubble Apex Altitude,
5. Build a Numeric Observed Distribution after running the simulation for as many nights as C/NOFS was in operation for low and high solar activity years,
6. Compare the Numeric Observed Distribution with the C/NOFS Observed Distribution.

The following cartoon illustrates the simulation:

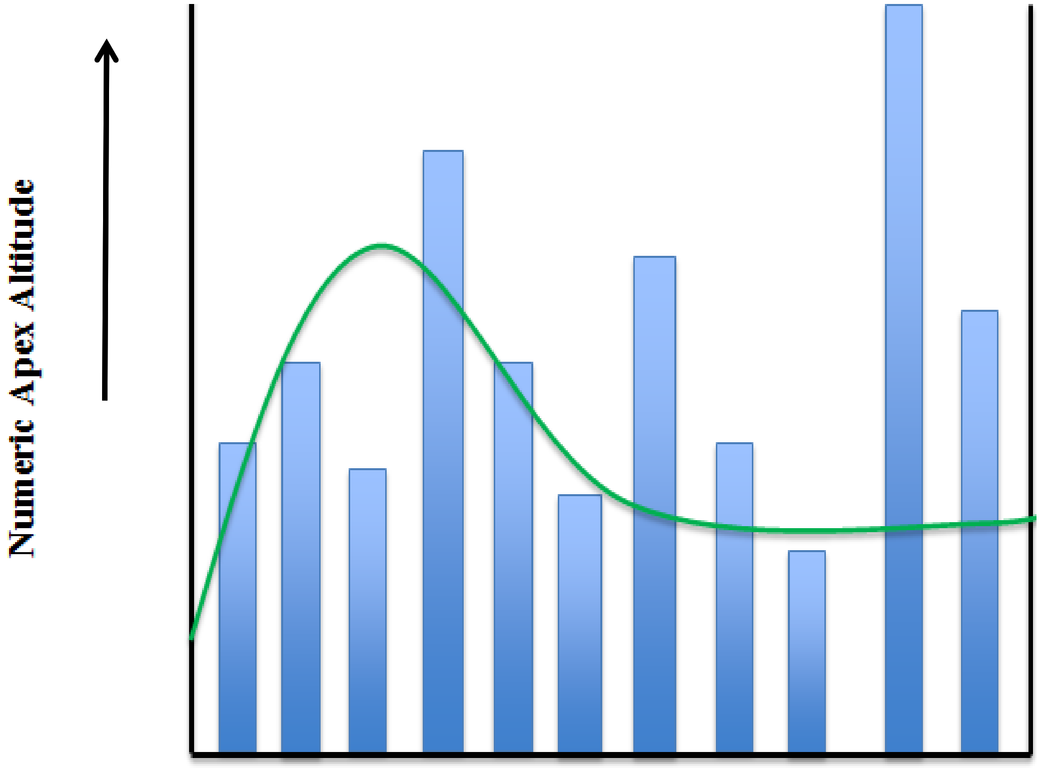

Cartoon 5.1: The green line shows a possible path of a ‘satellite’ passing through numeric bubble bins at various apex altitudes. The path is taken from C/NOFS data. For every numeric bubble bin, a position is randomized to be taken as the longitude position of the satellite in C/NOFS data. If the apex altitude of a corresponding longitude position in C/NOFS data is less or equal than the apex altitude of the numeric bubble bin, the satellite will detect an irregularity. If,

$$\mathbf{Z_{AP\ (C/NOFS)} <= Z_{AP\ (NUMERIC\ BUBBLE)},}$$

$$\mathbf{detect\ \ \sigma > 1.2\ .}$$

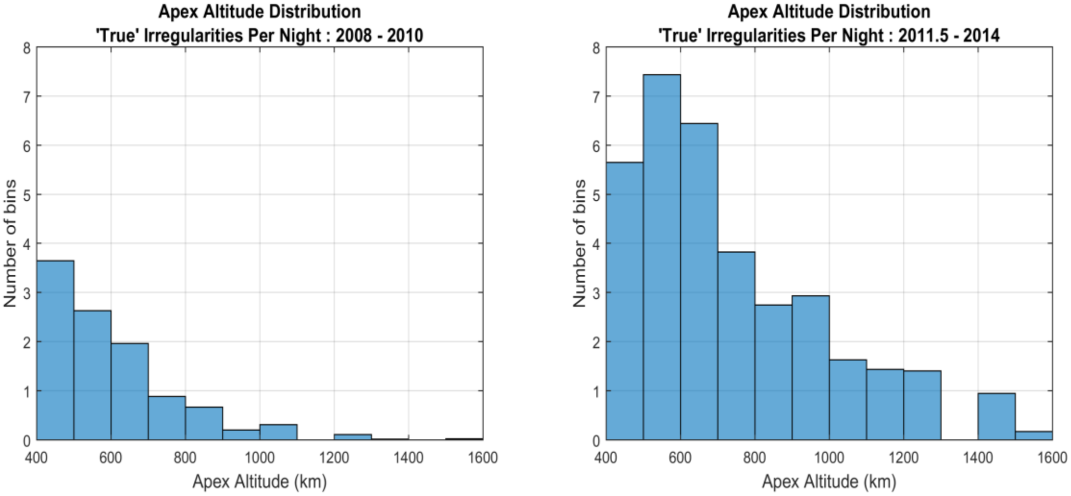

Figure 5.27: Estimated True Distribution per night for solar low and high activity years. The distributions shown are for active longitude (-80^o : 10^o) and seasons (Jan – Apr, Sep – Dec) and between 20 – 24 LT. The True Distribution per night is used in numerically simulating the 'C/NOFS experiment'.

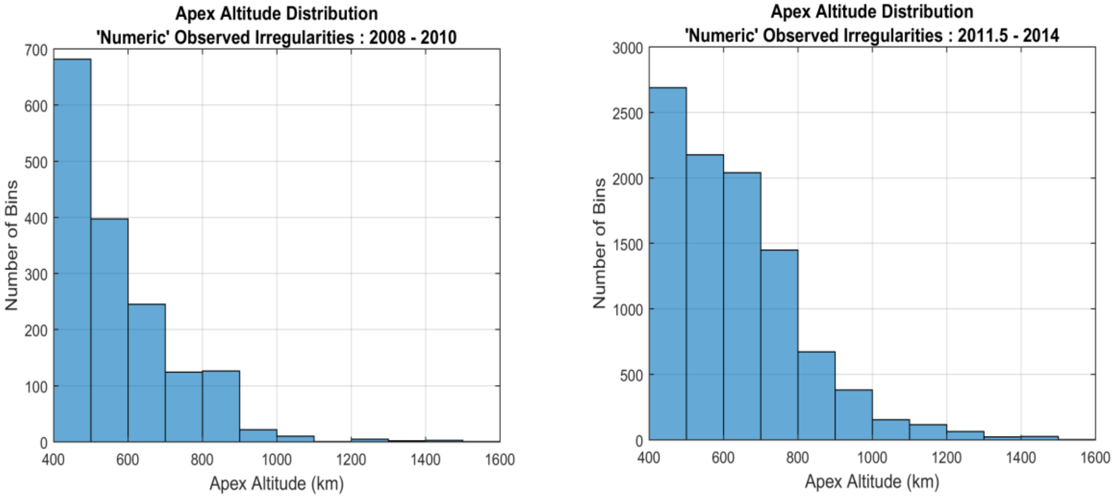

Figure 5.28: Apex Altitude Distributions of ionospheric irregularities as observed in the numeric simulation. The distributions shown are for active longitude (-80^o : 10^o) and seasons (Jan – Apr, Sep – Dec) and between 20 – 24 LT. The distributions mirror the C/NOFS Observed Irregularity Distributions (Fig 5.23)). The ratio of number of bubble bins observed in the numeric simulation to the number of bubble bins in C/NOFS observed irregularity distributions allow us to estimate the percentage of the bubble bins C/NOFS possibly could have sampled out of the actual bubble bins present in the ionosphere during its years of operation.

The ‘success’ of this exercise lays in the observed distribution results of the numeric simulation (Fig. 5.28). The numeric observed distribution does mirror the C/NOFS observed distribution (Fig. 5.23). It demonstrates that we get numeric irregularity observations akin to C/NOFS irregularity observations after applying our assumptions to the initial observed distribution to obtain the true distribution and using the true distribution to run the numerical simulation. This validates our assumption of the physical reality that all higher altitude bubbles at the magnetic equator pass through the lower altitudes beneath them. This also validates the need to normalize the observed distribution to obtain the true distribution. The ratio of number of bubble bins observed in the numeric simulation to the number of bubble bins in C/NOFS sample space also give us an idea of the percentage of the bubble bins C/NOFS possibly could have sampled out of the actual bubble bins present in the ionosphere during its years of operation. In the numeric simulation, 44 % of the bubble bins existing in the C/NOFS data are observed during high solar activity years whereas the percentage is 28 % during low solar activity years (Table 5.3). The smaller percentage of detection during low solar activity years is possibly due to combination of low true distribution per night and low number of sample space (C/NOFS bubble bins). We run the simulation multiple times (~ 100) changing seed for the random number generator in MATLAB used to randomize the longitude positions for each run of the simulation.

	C/NOFS	Numerical	Percentage (%)
High Activity Years	22,221	9,797	44.09
Low Activity Years	5,736	1,618	28.21

Table 5.3: Bubble Bin Statistics: Numeric simulation and C/NOFS satellite results

This allows us to define error bar in each apex-altitude bin so that we can run the simulation for smaller sample size and define a reasonable time interval over which we can apply the algorithm. The standard deviation calculated from 100 run of the numeric simulations is more than 10% of the number of bubble bins since sixth apex-altitude bin (Fig. 5.29). The sixth bin corresponds to 900 – 1000 km. Most of our comparisons are at lower altitudes in the range of 700-900 km. So, we conclude to take 12 month period of data as a reasonable time interval to analyze data for the effects of solar activity. We start in the year 2008, take a year of data and analyze the bubble altitude characteristics. We slide the window by six months and again take a year of data and repeat the process until the end of the C/NOFS data period.

Figure 5.30 shows the evolution of the median percentile apex altitudes from low solar activity year 2008 to high solar activity year 2014. The F10.7 values in the x-axis are the mean of the 13-month smoothed values of monthly averaged data of the months corresponding to the yearly time-window.

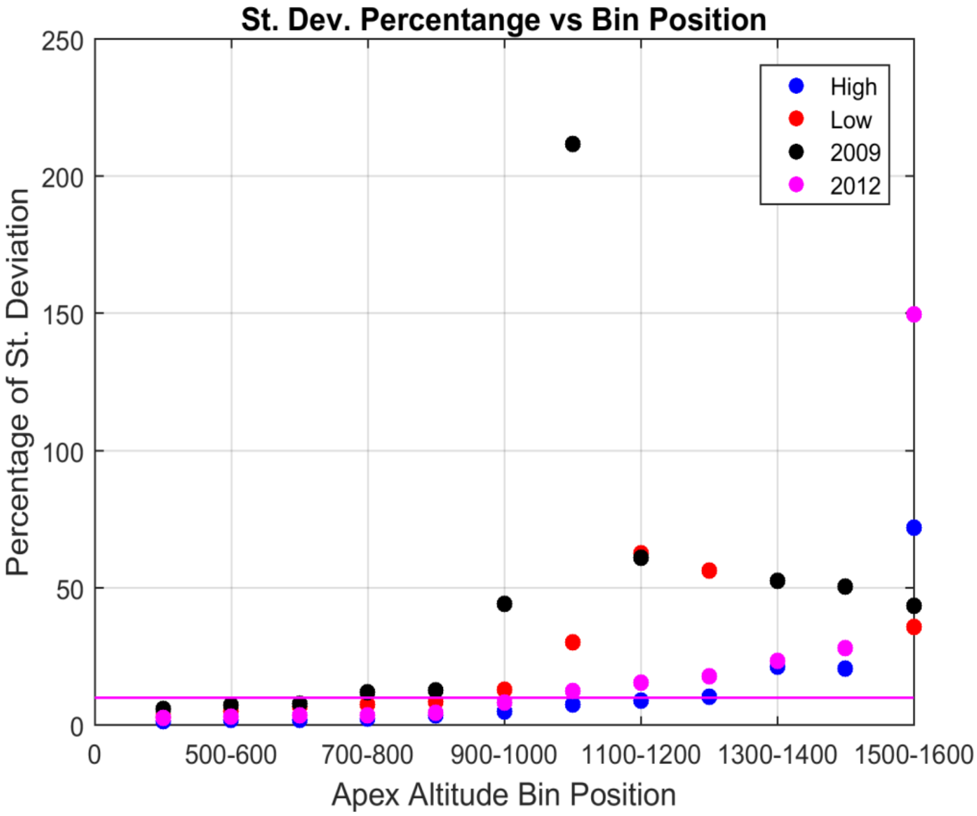

Figure 5.29: The percentage of standard deviation as compared to number of bubble bins in each apex-altitude bin for the year 2009, 2012 ; and for low and high solar activity years. The standard deviation is calculated from 100 run of the numeric simulations.

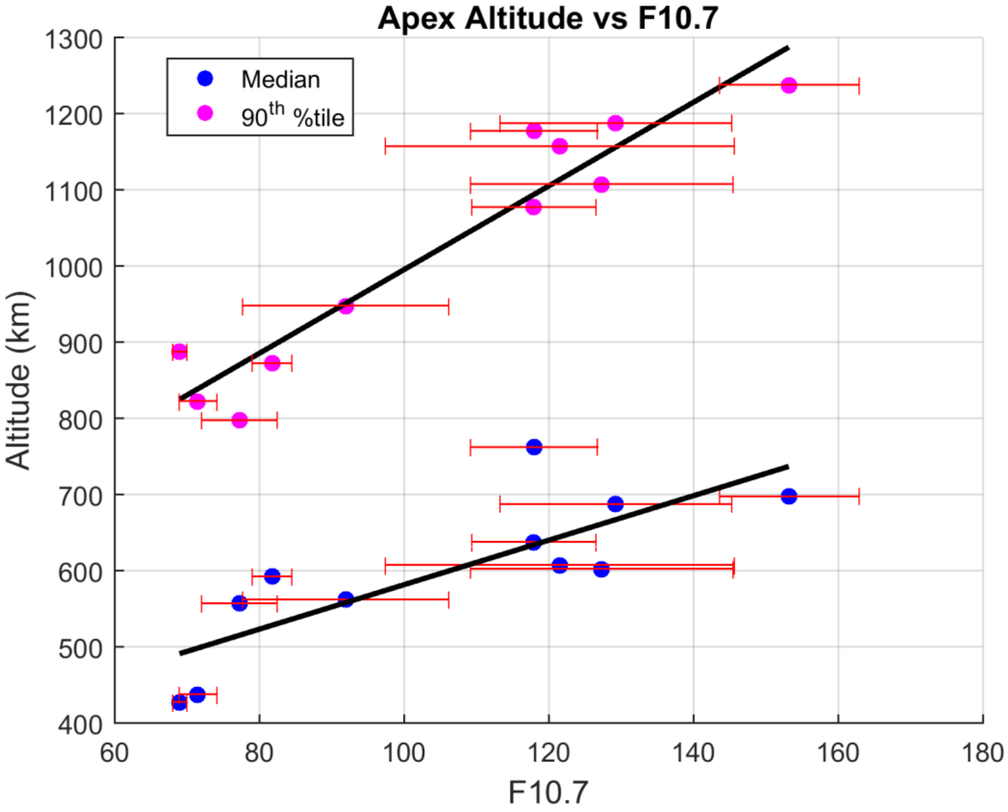

Figure 5.30: Apex Altitude vs F10.7 plot shows the evolution of the median peak apex-altitudes from low solar activity year 2008 to high solar activity year 2014. The line fit shows that the irregularities rise from about 491 km at solar minimum to 737 km during solar maximum. The line fit has higher slope for the 90th percentile peak apex-altitudes.

5.7 Local-Time Effects

We sought to understand the bubble altitude characteristics in the 20 - 24 LT as reported by the C/NOFS satellite observations. It has been established [50, 51] that the height of the nighttime F layer is the single most important factor controlling the occurrence of spread F. This height, in turn, is determined by the equatorial vertical plasma drift velocity which peaks before 20 LT in the equatorial region [52]. So, the time window 20 - 24 LT offers a period to observe fully grown irregularities in the equatorial region. But, we also like to check how significantly the apex-altitude distribution of the ionospheric irregularities as observed by C/NOFS varies if we divide the time window in two halves. If the 20-22 LT and the 22-24 LT periods have essentially the same statistics it implies that the bubble growth is largely complete within the first two hours of sunset by 20 LT and our approach of including as many observations between 20-24 LT will be justified. We want to check if our results are skewed by the growth time of the bubbles.

The sample space in each halves of the window has similar distribution without significant differences for both solar high and low activity years (Fig. 5.31 & Fig. 5.32). This is obvious as the satellite should be sampling similar space in every two hours – the time for each half of the total time window. Of interest are the distributions of the irregularities – we include the normalized distribution of apex altitude bins with irregularities and also the ‘Total True’ Distribution deduced from those irregularities.

From the total true distributions in Figures 5.31 & 5.32, we see the lowest apex altitude bin has higher number of ‘true’ irregular bins in the latter half of the time window (22 – 24 LT) for both low and high solar activity years. This suggests the bubble activity is more in the second half of the time window than the first half in the lowest apex-altitude bin for both low and high solar activity years. The number of irregularity bins is lower in first half of the time window than the second half in the low solar activity years whereas it is opposite in case of the high solar activity years. This is valid in all altitudinal ranges as defined in Table 5.4. This suggests more number of bubbles reach higher in the second half of the time window during low solar activity years but not in the high solar activity years. A similar inference can also been drawn from the normalized irregularity detections. A possible consequence of these observations is that the bubble grew slightly slowly in the early period than the later period of time window 20-24 LT during the low solar activity years whereas they had already matured in the early period and possibly slowed during the later period during the high solar activity years. More work is needed to reach unambiguous conclusions and to make a judicious choice of local time-window in both low and high solar activity years of observations. The observations are summarized in Table 5.4.

Apex Altitude range (km)	Low Solar Activity Years No. of 'true' bubble bins		High Solar Activity Years No. of 'true' bubble bins	
	First Half	Second Half	First Half	Second Half
400 -1700	2,863 (↓)	3,223 (↑)	12,402 (↑)	10,074 (↓)
700-1700	629(↓)	670(↑)	5,905(↑)	3,894(↓)
1000-1700	93(↓)	122(↑)	2,392(↑)	1,359(↓)

Table 5.4: Number of Bubble bins in two halves of the time window 20 – 24 LT for low and high solar activity years.

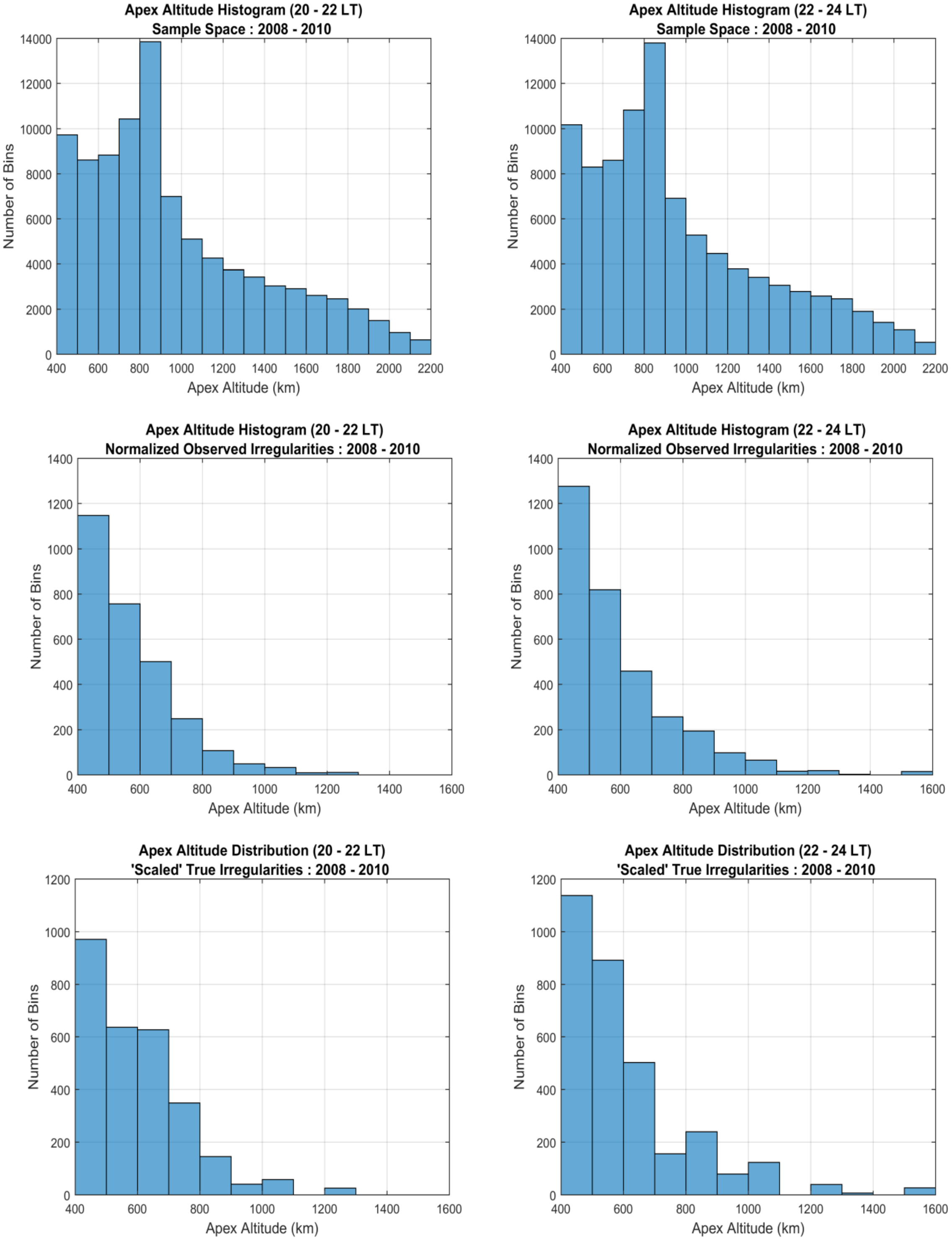

Figure 5.31: The apex-altitude distributions during low solar activity years for the Sample Space (top), the Normalized Observed Irregularities (middle) and the 'Total True' Observed Irregularities (bottom) for the former half 20 – 22 LT (left) and the latter half 22 – 24 LT (right) of the time window 20 – 24 LT. The distributions shown are for active longitude (-80° : 10°) and seasons (Jan – Apr, Sep – Dec). The distributions show that the bubble grew slightly slowly in the early period (20 – 22 LT) than the later period (22 – 24 LT) during the low solar activity years.

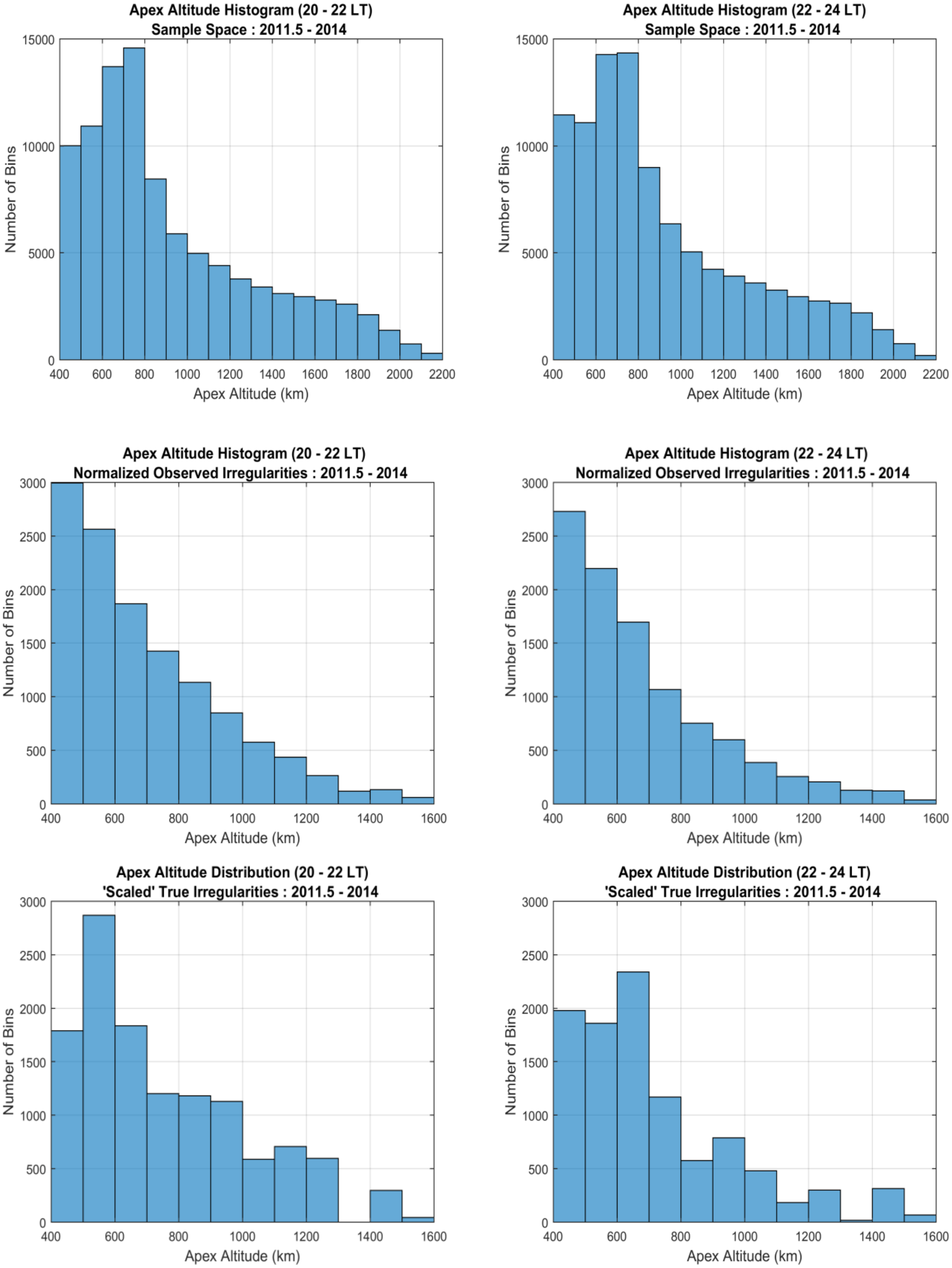

Figure 5.32: The apex-altitude distributions during high solar activity years for the sample space (top) , the Normalized Observed Irregularities (middle) and the 'Total True' Observed Irregularities (bottom) for the earlier half 20 – 22 LT (left) and the latter half 22 – 24 LT (right) of the time window 20 – 24 LT. The distributions shown are for active longitude (-80^{o} : 10^{o}) and seasons (Jan – Apr, Sep – Dec). The distributions show that the bubbles had matured in the early period (20 – 22 LT) and possibly slowed during the later period (22 – 24 LT) during the high solar activity years.

5.8 Modeling the rise of equatorial ionospheric irregularities

As we have demonstrated that the apex-altitude of bubbles increases with solar flux from satellite observations, we seek to apply a physics-based model to see if the model predicts similar effects and if it can help us understand the physical processes responsible for the effects. We use PBMOD (*P*hysics *B*ased *MOD*els) to model the effects of solar activity on the altitude of ionospheric irregularities at magnetic equator. PBMOD [53] ionospheric model, as described in the reference, is a system of *P*hysics *B*ased *MOD*els that describes the three-dimensional time-dependent evolution of the low-latitude ionosphere on several different spatial scales: globally it provides the plasma density and composition at altitudes between 90 and 2000 km; at finer scales it describes the development of fluid plasma turbulence within this region and the resulting radio scintillation.

We ran a series of PBMOD at four levels of solar activity, F10.7 = 90, 120, 150 and 180 (Fig. 5.33) at 280 deg longitude (Jicamarca). The model was also run with changing values of the magnitude of the initial density perturbation for the aforementioned values of solar activity. The initial seed of perturbations were changed as S001 = ± 50 x $10^{\wedge 3}$ cm^{-3}, S002 = ± 25 x $10^{\wedge 3}$ cm^{-3}, S003 = ± 12 x $10^{\wedge 3}$ cm^{-3}, S004 = ± 6 x $10^{\wedge 3}$ cm^{-3}. The initial magnitude of the seed plays a role until the magnitude reached a threshold after which it is no longer an important factor in determining bubble altitude at magnetic equator. For the longitude sector and the active periods we are analyzing C/NOFS observations, we don't see any variability in the bubble activity. It allows us to assume the initial perturbation was well above the minimum threshold for bubble growth and probably not a factor in determining the bubble altitude for the C/NOFS observations we are analyzing in the active periods and the longitude sector. In our runs, the non-linear development of plumes didn't occur with the seed level S004 = ± 6 x $10^{\wedge 3}$ cm^{-3} at F10.7 = 90 and 120. Hence, we choose to infer the peak bubble altitude for all solar activity levels with initial seed perturbation of S003 = ± 12 x $10^{\wedge 3}$ cm^{-3} to compare with the relationship between bubble altitude and F10.7 obtained from C/NOFS observations.

In Figure 5.33, the images show a history of the peak magnitude of the deviation of density in the equatorial plane across the zonal direction as a function of height (apex altitude) and local time. For the first image, the F090 in the title suggests the F10.7 value of 90 solar flux units (s.f.u.) and S001 suggests the 1st of the seed values (± 50 x $10^{\wedge 3}$ cm^{-3}) the model was run with. Equatorial plasma bubbles rise to higher apex altitudes with increasing solar flux as seen in the Figure 5.33. We estimated the maximum altitude these bubbles rise in the equatorial plane to compare with the earlier results from C/NOFS observations (Fig. 5.34). The variation of plasma bubble apex altitude from PBMOD results for the third seed S003 matches closely with that of the median values of the apex-altitude distributions from C/NOFS observations. *Krall et al.* [54] report the three dimensional simulations of equatorial spread F bubbles. They argue that the bubbles stop rising when the flux-tube integrated ion mass density just inside the bubble is equal to that of the adjacent background. In the case of single-ion ionosphere, the condition is equivalent to the hypothesis of *Mendillo et al.* [55] which says the bubbles stop rising when there is balance between the flux-tube integrated electron densities inside and outside the flux-tube. The question "Why do equatorial plasma bubbles stop rising?" has been asked before in the works by *Ott* [56], *Ossakow and Chaturvedi* [57]. In *Ott*'s paper

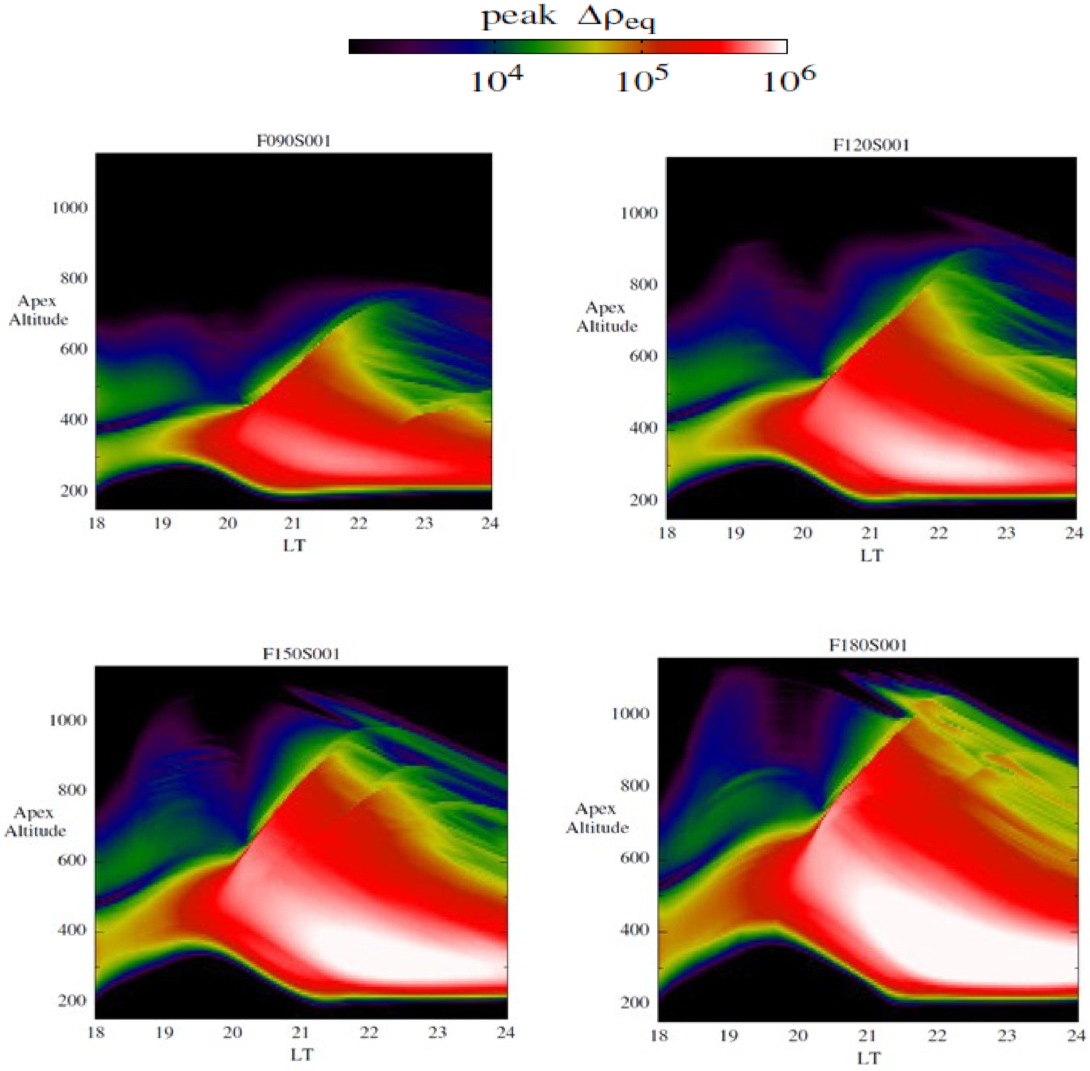

Figure 5.33: The images show a history of the peak magnitude of the deviation of density in the equatorial plane across the zonal direction as a function of apex altitude and local time. For the first image, the F090 in the title suggests the F10.7 value of 90 solar flux units (s.f.u.) and S001 suggests the 1^{st} of the seed values (± 50 x $10^{\wedge 3}$ cm^{-3}) the model was run with. The equatorial plasma bubbles rise to higher apex altitudes with increasing solar flux as seen.

the final expression for the vertical speed in case for collision-dominated plasma bubble is given to be:

$$U = \frac{(n_o - n_b)}{(n_o + n_b)} \frac{g}{v_{in}} \qquad \text{---- (5)}$$

In equation (5), n_o and n_b are respectively the background and the "bubble" densities, g is the acceleration due to gravity and v_{in} is the ion-neutral collision frequency. The equation is essentially a manifestation of a buoyancy argument. It shows that the bubble will rise at the bottomside of the F-region with a certain value of vertical speed which will reach zero at altitudes where the density of the bubble equals the background density.

Ossakow and Chaturvedi describe in context of the Figure 1 in their article about the amplification of total electric field inside depleted plasma due to density differences inside and outside the bubble. The enhanced electric field results in the faster upward drift of the center of the bubble. They calculate the expressions for various – linear, non-linear sheet and non-linear elliptical – bubble models. All of the models described in the paper have the vertical bubble rise velocity of the form:

$$V_B = \frac{g}{v_{in}} f\left(\frac{\delta n}{n_o}\right) \qquad \text{---- (6)}$$

where the factor $f\left(\frac{\delta n}{n_o}\right)$ is some function of $\frac{\delta n}{n_o}$. *Ossakow and Chaturvedi* further write in their paper, "The factor f increases with increasing with $\frac{\delta n}{n_o}$. According to linear theory $\frac{\delta n}{n_o}$ increases with altitude and decreasing bottomside electron density gradient scale length. These ideas indicate that there is a range of bubble vertical rise velocities but these rise velocities depend on ambient equatorial F region ionospheric conditions, e.g., the height of the F peak and bottomside gradient scale length. …. Moreover, it should be pointed out that for $\frac{\delta n}{n_o} = 0$, i.e., for bubbles which have the same density as the background ionosphere, the induced (polarization) electric field, which causes the bubble to rise through E x B, becomes zero as does the attendant vertical bubble velocity. This simply states that a bubble created on the bottomside of the F region will rise until its density equals the topside background ionospheric density." Since the variation of the apex-altitude of equatorial plasma bubbles in PBMOD matches well with the similar variation in C/NOFS observations, we seek to emulate the 'buoyancy hypothesis' by taking physical quantities attainable in PBMOD runs as proxies for the flux-tube-integrated-density equivalence inside and outside the bubble as proposed in Krall's work. Physically, the reduction in polarization electric field which gives rise to the motion of the plume is controlled by the conductivity and in the aforementioned works, it has been argued that density can be a proxy for the conductivity to estimate how high bubbles would rise at magnetic equator. We seek to check both conductivity (which controls the polarization electric field) and TEC (which represents the flux-tube-integrated density and has been taken as proxy for the conductivity or the electric field) in PBMOD runs to examine the "buoyancy hypothesis" (private communication with John Retterer). The value of conductance/TEC below the bottomside that we choose at the start of the simulation shall be captured in the rising bubbles and so, assuming it remained unchanged by other processes, would represent conductivity/TEC within the bubbles at later times. The average conductivity/TEC in the topside we look for at the time of maximum bubble height would represent the flux-tube content outside the bubbles. Thus,

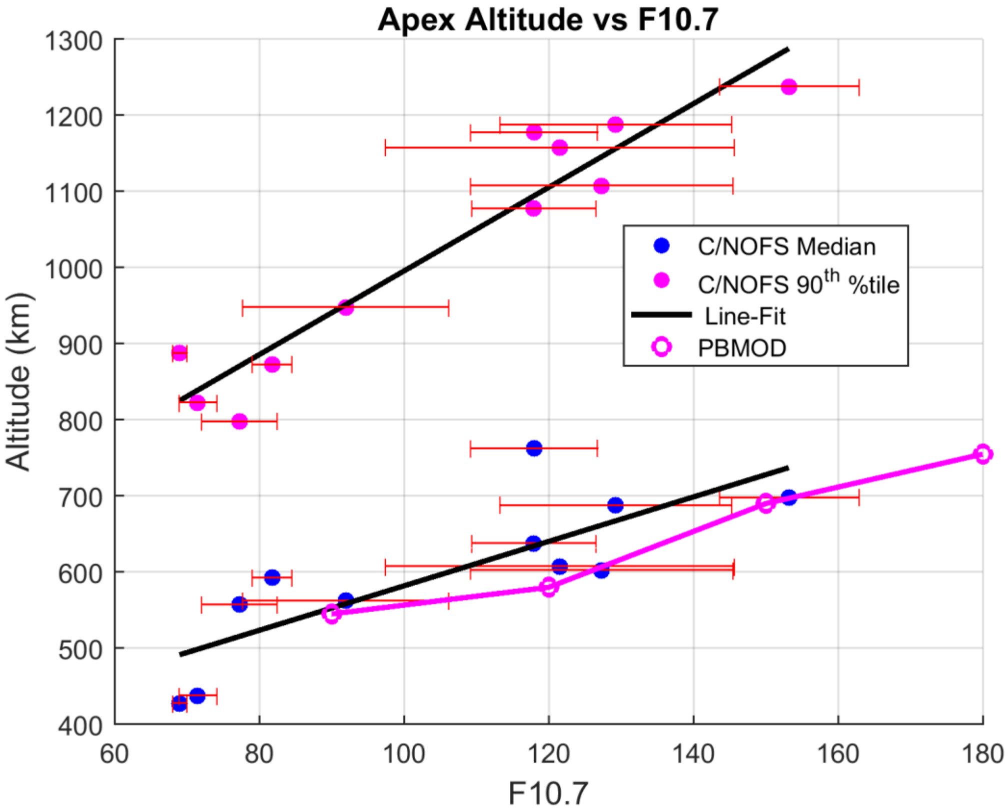

Figure 5.34: The PBMOD results for the variation of the plasma bubble apex altitude with solar flux matches closely with that of the median values of the peak apex-altitude distributions deduced from C/NOFS observations. The PBMOD was run with initial seed perturbation of S003 = ± 12 x $10^{\wedge 3}$ cm^{-3}.

matching the bottomside conductivity/TEC from early times to the average conductivity/TEC at later times mean matching the flux-tube content inside and outside the bubbles, as suggested in Krall's heuristic. But we initially examine if the conductivity or the TEC are indeed good candidates to check the buoyancy of the bubbles (Fig. 5.35).

In Figure 5.35, the upper panel shows the variation of conductivity at two times - when bubbles are just beginning to emerge and when the bubbles have attained maximum height. The lower panel shows the variation of TEC at those same times. The level of conductivity and TEC entrained in the rising plasma of the bubbles from the bottomside is seen in the images at 21.598 LT – black or dark purplish color in the color scale of the pictures. The images at 23.498 LT show that while the conductivity has similar value outside and inside the maximum bubble height, the TEC doesn't. In the TEC plot the height where the background TEC matches the original bubble TEC is well above the height of the bubbles. This clearly illustrates that TEC cannot be a (good) proxy for estimating bubble altitude. It can also be seen that the TEC within the bubbles near the maximum height has also been modified more than the conductivity has been (to a bluish color in the color scale) – probably by diffusion of plasma into the bubbles or plumes. This tendency further complicates the use of TEC as a forecaster of bubble rise altitude. In Figures 5.36 – 5.37, we illustrate a couple of cases as applications of flux-tube-integrated-Pedersen-conductivity as a proxy for examining the buoyancy hypothesis to understand if it provides a reasonable guess for how high the plumes will rise. In Figure 5.36, the plume rises a maximum height of 550 – 600 km around 23.5 LT as seen in the upper plot of PBMOD run showing the peak density deviation across the zonal direction

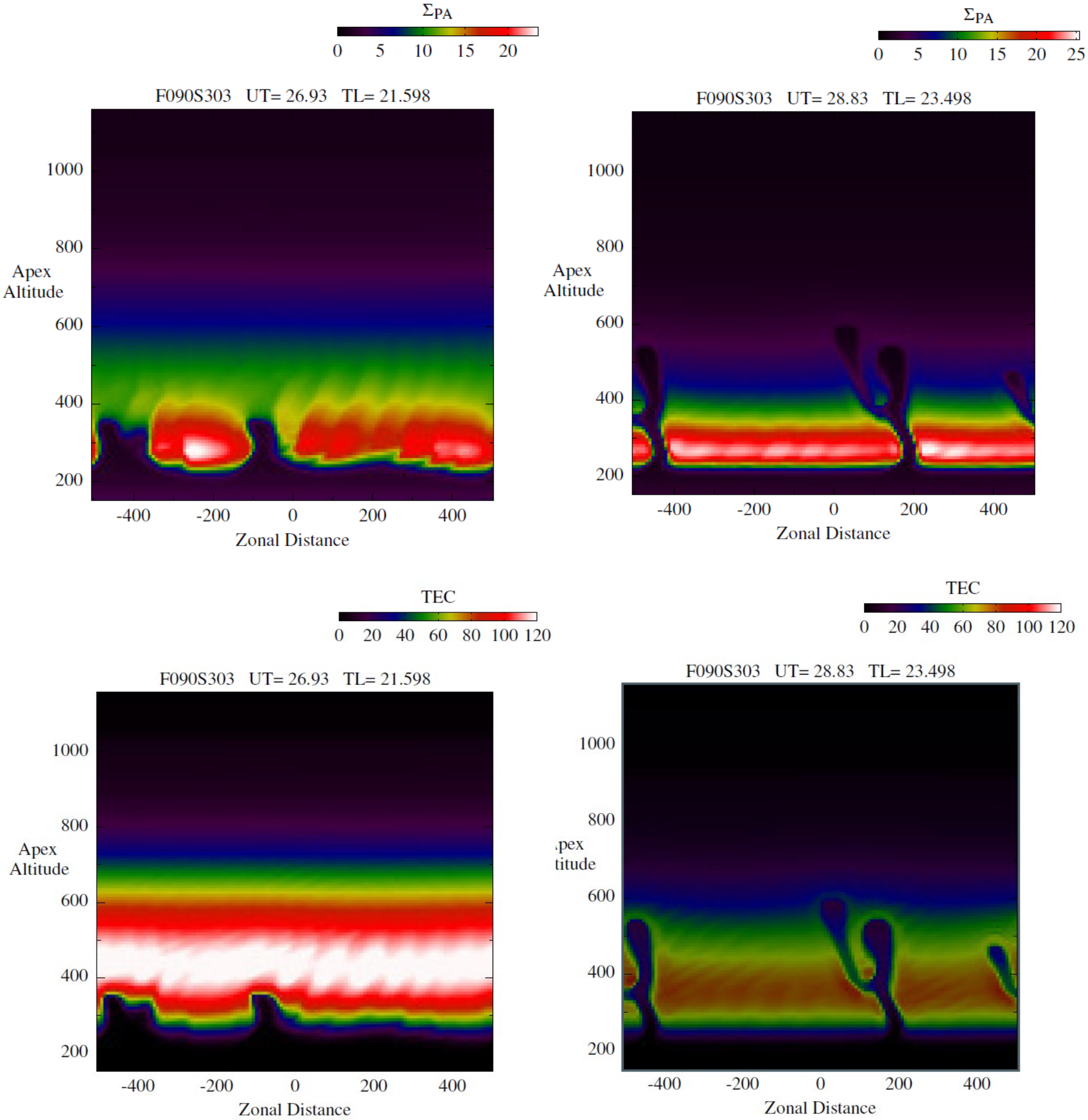

Figure 5.35: The variation of conductivity (upper panel) and TEC (lower panel) at two times - when bubbles are just beginning to emerge and when the bubbles have attained maximum height are shown. The level of conductivity and TEC associated in the rising plasma of the bubbles from the bottomside (black or dark purplish color) is seen in the images at 21.5 LT (left column). The images at 23.4 LT (right column) show while the conductivity has similar value outside and inside the maximum bubble height, the TEC doesn't. In the TEC plot, the height where the background TEC matches the original bubble TEC is well above the height of the bubbles. This illustrates that TEC cannot be a (good) proxy for estimating bubble altitude.

in the equatorial plane at solar activity level F10.7 of 90 sfu. In the profile of conductivity (bottom) at the time of maximum extent of the plume, the height where the conductivity equals the conductivity initially just below the F layer (4 mhos) is about 520 km, close to the maximum height of the plume containing the plasma initially from that place. In Figure 5.37, we make similar comparison for a PBMOD run at F10.7 = 180 sfu level. The maximum height of the plume in the PBMOD run is about 800 - 850 km around 23.5 LT. In the conductivity profile, the conductivity just below F-region bottomside is matched at the topside at an altitude little over 800 km. While testing the "buoyancy hypothesis", we tried to match the bottomside and topside conductivity from the PBMOD runs. The topside altitude represents the maximum altitude the bubbles possibly may have risen. These examples illustrate that the heuristic of matching the bottomside conductivity with the conductivity on the topside does seem to provide a reasonable guess for maximum altitude plumes may rise. The caveats associated with this approach are – (i) plume height and time of arrival depend on initial density perturbation which have been ignored in this method, (ii) the substantial slope in the conductivity below the F-layer bottomside introduces ambiguity in what conductivity to match on the topside, (iii) Plasma gets modified as it rises and evolves (diffusion fills in evacuated plume, modifying conductivity). Smaller F10.7 means slower rise, thus more modification, (iv) Need to know time of arrival at maximum extent to know the height (but 23.5 LT seems a reasonable guess), (v) Used actual profile of conductivity in simulation, not the background conductivity, which is the only profile known before simulation run.

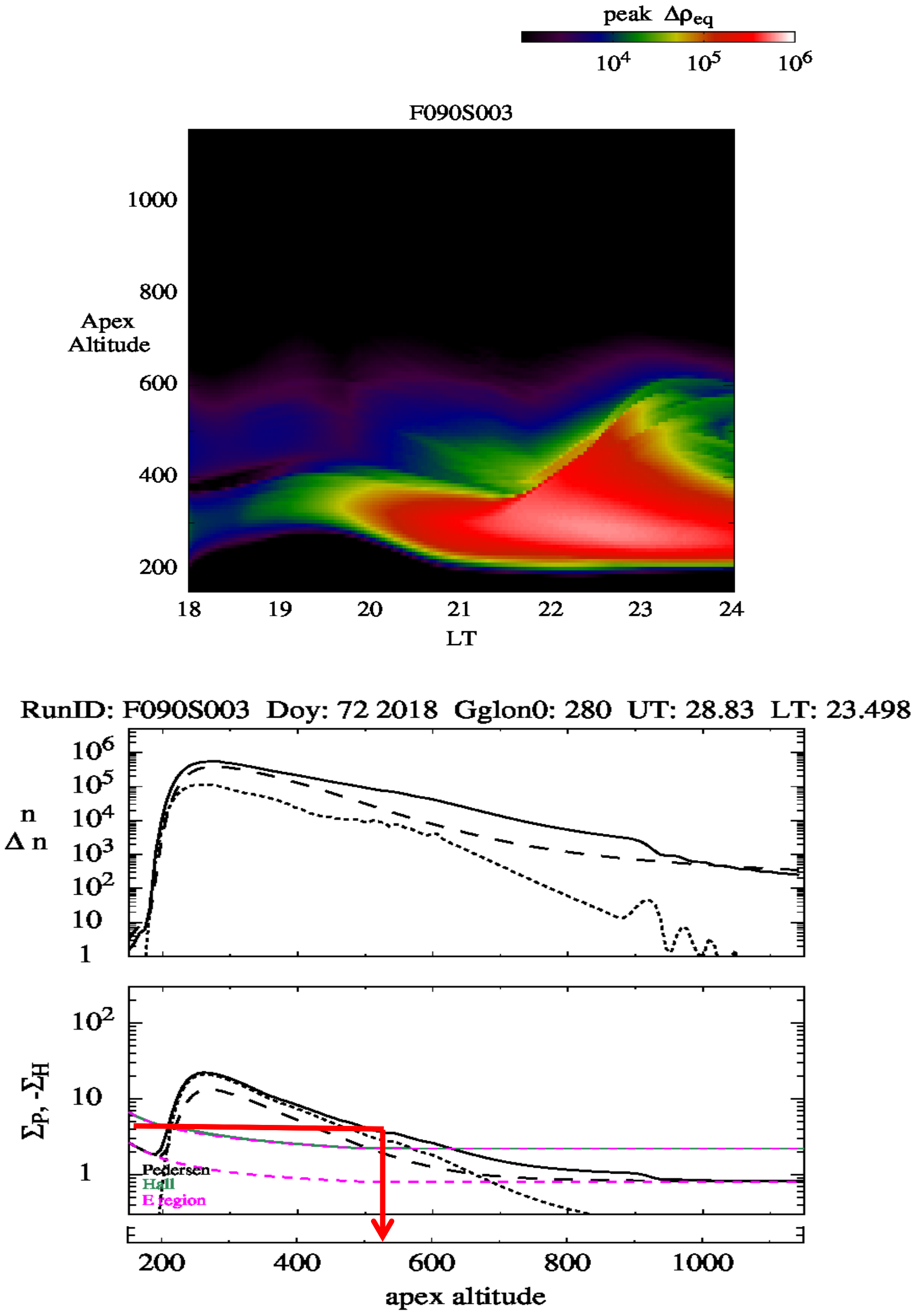

Figure 5.36: When the plume rises, it reaches a maximum height of 550 – 600 km, around 23.5 LT (top). In the profile of Pedersen conductance (bottom) at the time of maximum extent of the plume, the height where the conductance equals the conductance initially just below the F layer (4 mhos) is about 520 km, close to the maximum height of the plume containing the plasma initially from that place.

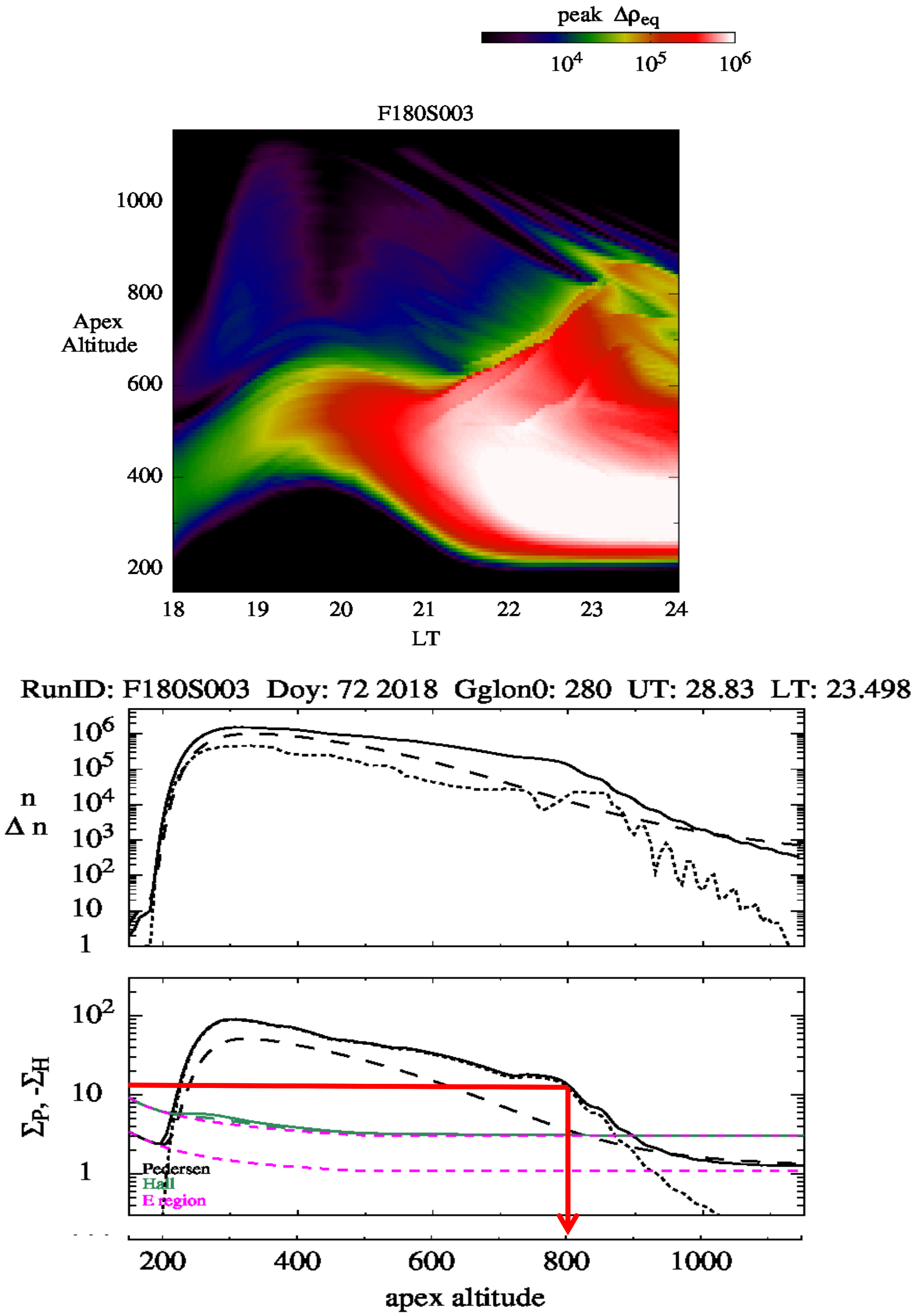

Figure 5.37: Similar illustration as of Fig. 5.36 but at solar activity level of F10.7 = 180 sfu. The maximum plume height is about 850 km, at 23.5 LT. Predicted maximum height by the approach of matching bottomside to topside conductance is little over 800 (km)

Conclusions

The research results presented in this chapter make a comprehensive investigation into altitude distributions of equatorial ionospheric irregularities at the magnetic equator. We presented the climatological maps of equatorial ionospheric irregularities as observed by the elliptically orbiting low-inclination C/NOFS satellite. We compared the space-based C/NOFS satellite observations with ground-based scintillation observations to confirm our irregularity detection algorithm for the space-based in-situ observations. To our knowledge, it is the first such day-to-day comparison of space-based observations with those of the ground. While making the aforementioned comparison, we invoked the flux-tube paradigm of equatorial plasma bubble growth and consequently, by confirming the correlation between space and ground based observations, we validated the paradigm as well. We studied the apex-altitude distributions of equatorial ionospheric irregularities for low and high solar activity years. We ran numerical simulations to validate our methodology and find a reasonable time period for which we can have good statistics to analyze the effects of solar activity on the apex-altitude distribution of equatorial ionospheric irregularities. The numerical simulations aided in our analysis of C/NOFS observations to achieve a relationship between solar activity index F10.7 and apex-altitude distribution of equatorial ionospheric irregularities. We used PBMOD (*P*hysics *B*ased *MOD*els) to see if model predicts similar effects of solar activity on the altitude of ionospheric irregularities at magnetic equator as of C/NOFS observations. We also used the model results to understand the physical processes responsible for the effects. We summarize our investigation results as following:

1. Our results are consistent with past studies examining the longitudinal and seasonal occurrence rate of equatorial ionospheric irregularities. We found the equatorial plasma bubble (EPB) occurrence rates were generally high around equinoctial months and low around June solstice. The EPB occurrence rates maximized in the America-Atlantic-Africa region corresponding to the longitude sector -80^{o} W to 30^{o} E.

2. Previous studies (e.g., DMSP) showed almost no activity during solar minimum. Our results show a near absence of activity at DMSP altitudes during solar minimum, but the maximum occurrence percentage as observed in the climatological plots at the lowest apex-altitude bin appears to decrease by approximately 95 % at solar minimum to 73.58 %.

3. We thus attribute the lack of detection by DMSP to satellite altitude bias, sampling a bubble altitude distribution that depends on solar flux.

4. Careful analysis indicates that the median height distribution of bubbles increases linearly from about 491 km at solar minimum to 737 km during solar maximum. These results apply to the -80^{o} W to 10^{o} E longitude sector. Other longitude sectors may have different altitude distributions. Our occurrence statistics suggest that bubbles in this longitude sectors are higher than in other regions on average.

5. A physics-based model was used to confirm our findings. In the model it appears that field-line integrated conductivity is the key determinant of terminal bubble altitude. Specifically, when the field-line integrated conductivity inside the bubble

is equal to that of the background ionosphere the polarization electric field that propels the bubble upwards vanishes and the bubble ceases to rise further.

6. Conductivity is determined by a combination of electron density and collision frequency [58] : $\sum_P = \sum n_i q^2 \left(\frac{\upsilon_i}{m_i(\upsilon_i^2 + \omega_i^2)} + \frac{\upsilon_e}{m_e(\upsilon_e^2 + \omega_e^2)} \right)$, in which $\sum_P$ is Pedersen Conductivity , n_i is the density of ion species i, the sum is over ion species, the quasi-neutrality condition of the ion densities being equal to the electron density is assumed and m , υ , ω are mass, collision frequency and cyclotron frequency respectively of the charge species , the charge species being ions (i) and electrons (e). All other parameters being equal, the field-line integrated plasma density, as suggested by other investigators [54, 55] is not a reasonable proxy for conductivity due to the higher weight given by the collision-frequency factor at lower altitudes in the field-line conductance integral whereas no such weight at any altitude occurs in the field-line integration of the density due to the absence of collision frequency factor.

7. These results are the first observational confirmation of bubble altitude as a function of solar flux and are valuable to the development of improved scintillation mapping models for both real-time and post-processing applications.

References:

[1] Haerendel, G. (1973), Theory of equatorial spread F, technical report, Max Planck Inst. fur Extraterr. Phys. Munich, Germany.

[2] Gentile, L. C., W. J. Burke, and F. J. Rich (2006), A climatology of equatorial plasma bubbles from DMSP 1989– 2004, *Radio Sci.*, 41, RS5S21, doi: 10.1029/2005RS003340.

[3] Kil, H., L. J. Paxton, and S.-J. Oh (2009), Global bubble distribution seen from ROCSAT-1 and its association with the evening prereversal enhancement, *J. Geophys. Res.*, 114, A06307, doi: 10.1029/2008JA013672.

[4] Kelley, M.C., The Earth's Ionosphere, Academic Press, Inc., 1989.

[5] Huang, C.-S., O. de La Beaujardiere, P. A. Roddy, D. E. Hunton, R. F. Pfaff, C. E. Valladares, and J. O. Ballenthin (2011), Evolution of equatorial ionospheric plasma bubbles and formation of broad plasma depletions measured by the C/NOFS satellite during deep solar minimum, *J. Geophys. Res.*, 116, A03309, doi: 10.1029/2010JA015982.

[6] Berkner, L. V., and H. W. Wells (1934), *F*-region ionosphere-investigations at low latitudes, *Terr. Magn. Atmos. Electr.*, 39(3), 215–230, doi: 10.1029/TE039i003p00215.

[7] Hysell, D. L., R. B. Hedden, J. L. Chau, F. R. Galindo, P. A. Roddy, and R. F. Pfaff (2009), Comparing *F* region ionospheric irregularity observations from C/NOFS and Jicamarca, *Geophys. Res. Lett.*, 36, L00C01, doi: 10.1029/2009GL038983.

[8] Rodrigues, F. S., M. C. Kelley, P. A. Roddy, D. E. Hunton, R. F. Pfaff, O. de La Beaujardière, and G. S. Bust (2009), C/NOFS observations of intermediate and transitional scale-size equatorial spread *F* irregularities, *Geophys. Res. Lett.*, 36, L00C05, doi: 10.1029/2009GL038905.

[9] Thampi, S. V., M. Yamamoto, R. T. Tsunoda, Y. Otsuka, T. Tsugawa, J. Uemoto, and M. Ishii (2009), First observations of large-scale wave structure and equatorial spread F using CERTO radio beacon on the C/NOFS satellite, *Geophys. Res. Lett.*, 36, L18111, doi: 10.1029/2009GL039887.

[10] de la Beaujardiere, O., et al. (2004), C/NOFS: A mission to forecast scintillation, *J. Atmos. Terr. Phys.*, 66, 1573, doi:10.1016/j.jastp.2004.07.030.

[11] https://www.nasa.gov/directorates/heo/scan/services/missions/earth/CNOFS.html.

[12] https://directory.eoportal.org/web/eoportal/satellite-missions/c-missions/cnofs.

[13] https://www.nasa.gov/mission_pages/sunearth/missions/mission_cindi.html.

[14] T. Abe and K. Oyama (2013), "Langmuir probe", An introduction to space instrumentation. Edited by K. Oyama and C.Z. Cheng. pp. 63–75 (Terra, Pub.), doi:10.5047/aisi.010.

[15] Roddy, P. A., D. E. Hunton, J. O. Ballenthin, and K. M. Groves (2010), Correlation of in situ measurements of plasma irregularities with ground-based scintillation observations, *J. Geophys. Res.*, **115**, A06303, doi: 10.1029/2010JA015288.

[16] Tapping, K. F. (2013), The 10.7 cm solar radio flux ($F_{10.7}$), *Space Weather*, 11, 394–406, doi:10.1002/swe.20064.

[17] Dudok de Wit T & Bruinsma S. (2017), The 30 cm radio flux as a solar proxy for thermosphere density modelling, *J. Space Weather Space Clim.*, 7, A9, doi: 10.1051/swsc/2017008.

[18] Huang, C.-S., O. de La Beaujardiere, P. A. Roddy, D. E. Hunton, J. Y. Liu, and S. P. Chen (2014), Occurrence probability and amplitude of equatorial ionospheric irregularities associated with plasma bubbles during low and moderate solar activities (2008–2012), *J. Geophys. Res. Space Physics*, 119, 1186–1199, doi: 10.1002/2013JA019212.

[19] Kil, H., and R. A. Heelis (1998), Global distribution of density irregularities in the equatorial ionosphere, *J. Geophys. Res.*, 103(A1), 407–417, doi: 10.1029/97JA02698.

[20] McClure, J. P., S. Singh, D. K. Bamgboye, F. S. Johnson, and H. Kil (1998), Occurrence of equatorial F region irregularities: Evidence for tropospheric seeding, *J. Geophys. Res.*, 103(A12), 29119–29135, doi: 10.1029/98JA02749.

[21] Su, S.-Y., C. H. Liu, H. H. Ho, and C. K. Chao (2006), Distribution characteristics of topside ionospheric density irregularities: Equatorial versus midlatitude regions, *J. Geophys. Res.*, 111, A06305, doi: 10.1029/2005JA011330.

[22] Kil, H., L. J. Paxton, and S.-J. Oh (2009), Global bubble distribution seen from ROCSAT-1 and its association with the evening prereversal enhancement, *J. Geophys. Res.*, 114, A06307, doi: 10.1029/2008JA013672.

[23] Retterer, J. M., and P. Roddy (2014), Faith in a seed: On the origin of equatorial plasma bubbles, *Ann. Geophys.*, **32**, 485–498, doi: 10.5194/angeo-32-485-2014.

[24] Huang, C., and M. R. Hairston (2015), The post sunset vertical plasma drift and its effects on the generation of equatorial plasma bubbles observed by the C/NOFS satellite, *J. Geophys. Res. Space Physics*, 120, 2263–2275, doi: 10.1002/2014JA020735.

[25] Huang, C.-S., G. Le, O. de La Beaujardiere, P. A. Roddy, D. E. Hunton, R. F. Pfaff, and M. R. Hairston (2014), Relationship between plasma bubbles and density enhancements: Observations and interpretation, *J. Geophys. Res. Space Physics*, 119, 1325–1336, doi: 10.1002/2013JA019579.

[26] Kil, H., Y.-S. Kwak, W. K. Lee, E. S. Miller, S.-J. Oh, and H.-S. Choi (2015), The causal relationship between plasma bubbles and blobs in the low-latitude *F* region during a solar minimum, *J. Geophys. Res.*, Space Physics, 120, 3961–3969, doi: 10.1002/2014JA020847.

[27] Ogawa, T., K. Igarashi, K. Aikyo, and H. Maeno (1987), NNSS satellite observations of medium-scale traveling ionospheric disturbances at southern high-latitudes, *J. Geomagn. Geoelectr.*, **39**, 709–721.

[28] Tsunoda, R. T., & White, B. R. (1981), On the generation and growth of equatorial backscatter plumes, 1. Wave structure in the bottomside F layer, *Journal of Geophysical Research*, 86, 3610, https://doi.org/10.1029/JA086iA05p03610.

[29] Tulasi Ram, S., M. Yamamoto, R. T. Tsunoda, S. V. Thampi, and S. Gurubaran (2012), On the application of differential phase measurements to study the zonal large

scale wave structure (LSWS) in the ionospheric electron content, *Radio Sci.*, **47**, RS2001, doi:10.1029/2011RS004870.

[30] Gershman, B.N., and G.I. Grigorev (1968), Traveling ionospheric disturbances – a review, *Radiophys. Quantum Electron.,* 11(1), 1–13, doi: 10.1007/BF01033534.

[31] Tsugawa, T., A. Saito, Y. Otsuka, and M. Yamamoto (2003), Damping of large-scale traveling ionospheric disturbances detected with GPS networks during the geomagnetic storm, *J. Geophys. Res.*, **108**(A3), 1127, doi: 10.1029/2002JA009433.

[32] Tsunoda, R. T. (1985), Control of the seasonal and longitudinal occurrence of equatorial scintillations by the longitudinal gradient in integrated *E* region Pedersen conductivity, *J. Geophys. Res.*, 90(A1), 447–456, doi: 10.1029/JA090iA01p00447.

[33] Aarons, J. (1993), The longitudinal morphology of equatorial *F* layer irregularities relevant to their occurrence, *Space Sci. Rev.*, **63**, 209.

[34] Huang, C. Y., W. J. Burke, J. S. Machuzak, L. C. Gentile, and P. J. Sultan (2001), DMSP observations of equatorial plasma bubbles in the topside ionosphere near solar maximum, *J. Geophys. Res.*, **106**, 8131.

[35] Huang, C. Y., W. J. Burke, J. S. Machuzak, L. C. Gentile, and P. J. Sultan (2002), Equatorial plasma bubbles observed by DMSP satellites during a full solar cycle: Toward a global climatology, *J. Geophys. Res.*, **107**(A12), 1434, doi:10.1029/2002JA009452.

[36] Burke, W. J., C. Y. Huang, L. C. Gentile, and L. Bauer (2004), Seasonal-longitudinal variability of equatorial plasma bubble occurrence, *Ann. Geophys.*, **22**, 3089.

[37] McClure, J. P., S. Singh, D. K. Bamgboye, F. S. Johnson, and Hyosub Kil (1998), Occurrence of equatorial *F* region irregularities: Evidence for tropospheric seeding, *J. Geophys. Res.*, **103**, 29,119.

[38] Retterer, J. M., and L. C. Gentile (2009), Modeling the climatology of equatorial plasma bubbles observed by DMSP, *Radio Sci.*, **44**, RS0A31, doi:10.1029/2008RS004057.

[39] Balsley, B. B., G. Haerendel, and R. A. Greenwald (1972), Equatorial spread *F*: Recent observations and a new interpretation, *J. Geophys. Res.*, 77(28), 5625–5628, doi: 10.1029/JA077i028p05625.

[40] Mendillo, M., E. Zesta, S. Shodhan, P. J. Sultan, R. Doe, Y. Sahai, and J. Baumgardner (2005), Observations and modeling of the coupled latitude-altitude patterns of equatorial plasma depletions, *J. Geophys. Res.*, 110, A09303, doi: 10.1029/2005JA011157.

[41] Sultan, P. J. (1996), Linear theory and modeling of the Rayleigh-Taylor instability leading to the occurrence of equatorial spread F, *J. Geophys. Res*., 101(A12), 26875–26891, doi: 10.1029/96JA00682.

[42] McClure, J. P., Hanson, W. B., & Hoffman, J. H. (1977), Plasma bubbles and irregularities in the equatorial ionosphere, *Journal of Geophysical Research*, **82**(19), 2650–2656, https://doi.org/10.1029/JA082i019p02650.

[43] Weber, E. J., J. Buchau, R. H. Eather, S. B. Mende (1978), North-south aligned equatorial airglow depletions, *J. Geophys. Res.*, **83**, 712–716, https://doi.org/10.1029/JA083iA02p00712.

[44] Moore, J. G., E. J. Weber (1981), OI 6300 and 7774 A^o airglow measurements of equatorial plasma depletions, *J. Atmos. Terr. Phys.*, **43**, 851–858.

[45] Sobral, J. H. A., M. A. Abdu, I. S. Batista (1980), Airglow studies on the ionosphere dynamics over low latitude in Brazil, *Ann. Geophys.*, **36**, 199–204.

[46] Mendillo, M., J. Baumgardner (1982), Airglow characteristics of equatorial plasma depletions, *J. Geophys. Res.*, **87**, 7641–7652.

[47] Dyson, P. L., R. I. Benson (1978), Topside sounder observation of equatorial bubbles, *Geophys. Res. Lett.*, **5**, 795–798.

[48] Aarons, J., J. P. Mullen, J. R. Koster, R. F. da Silva, J. R. Medeiros, R. T. Medeiros, A. Bushpy, J. Pantoja, J. Lanai, M. R. Paulson (1980), Seasonal and geomagnetic control of equatorial scintillations in two longitudinal sectors, *J. Atmos. Terr. Phys.*, **42**, 861–866.

[49] https://www.ngdc.noaa.gov/IAGA/vmod/igrf.html.

[50] Ossakow S L, Zalesak S T, McDonald B E and Chaturvedi P K (1979), Nonlinear equatorial spread F: Dependence on altitude of the F peak and bottom side background electron density gradient length; *J. Geophys. Res.* **84** 17–29.

[51] Fejer, B. G., L. Scherliess, and E. R. dePaula (1999), Effects of the vertical plasma drift velocity on the generation and evolution of equatorial spread F, *J. Geophys. Res.*, **104**, 19,859–19,869, doi: 10.1029/1999JA900271.

[52] Fejer, B. G., E. R. dePaula, S. A. González, and R. F. Woodman (1991), Average vertical and zonal *F* region plasma drifts over Jicamarca, *J. Geophys. Res.*, **96**(A8), 13,901–13,906, doi: 10.1029/91JA01171.

[53] https://ccmc.gsfc.nasa.gov/RoR_WWW/pbmod-rt/PBMOD-Text.html.

[54] Krall, J., J. D. Huba, S. L. Ossakow, and G. Joyce (2010), Why do equatorial ionospheric bubbles stop rising?, *Geophys. Res. Lett.*, **37**, L09105, doi: 10.1029/2010GL043128.

[55] Mendillo, M., Zesta, E., Shodhan, S., Sultan, P., Doe, R., Sahai, Y., & Baumgardner, J. (2005),Observations and modeling of the coupled latitude-altitude patterns of equatorial plasma depletions, *Journal of Geophysical Research*, **110**, A09303, https://doi.org/10.1029/2005JA011157.

[56] Ott, E. (1978), Theory of Rayleigh-Taylor bubbles in the equatorial ionosphere, *J. Geophys. Res.*, **83**(A5), 2066–2070, doi: 10.1029/JA083iA05p02066.

[57] Ossakow, S. L., and P. K. Chaturvedi (1978), Morphological studies of rising spread F bubbles, *J. Geophys. Res.*, **83**(A5), 2085–2090, doi: 10.1029/JA083iA05p02085.

[58] Retterer, J. M. (2010), Forecasting low-latitude radio scintillation with 3-D ionospheric plume models: 1. Plume model, *J. Geophys. Res.*, **115**, A03306, doi: 10.1029/2008JA013839.

CHAPTER 6 CONCLUSIONS AND FUTURE DIRECTION OF RESEARCH

6.1 Conclusions

In this dissertation work, we analyzed data from the Metal Oxide Space Cloud (MOSC) experiment and C/NOFS satellite mission to understand the ionospheric irregularities in the equatorial ionosphere. In the MOSC experiment, we analyzed the high frequency (HF) propagation effects of artificial ionospheric modification in the lower F-region in the equatorial ionosphere. We also analyzed the HF data during the MOSC campaign to understand the factors influencing the growth rate of the generalized Rayleigh-Taylor instability. The Planar Langmuir Probe (PLP) in-situ observations made onboard C/NOFS satellite have been analyzed to understand the effects of solar activity on the altitude-distributions of the equatorial ionospheric irregularities at the magnetic equator.

In Chapter 1, we presented an overview of this dissertation outlining the details of the following chapters.

In Chapter 2, we presented a basic introduction of the ionosphere – variation of its profile with altitude and the composition of its chemical constituents. We discussed artificial ionospheric modification and presented theoretical treatment of the radio wave propagation through an ionized layer of the upper atmosphere.

In Chapter 3, we presented the High Frequency propagation results from the Metal Oxide Space Cloud (Experiment). We analyzed data from high frequency (HF) radio links and ALTAIR incoherent scatter radar to understand the impacts of the artificial ionization on the radio wave propagation. We also presented the modeling results done with the aid of the HF radio wave ray-tracing toolbox PHaRLAP along with ionospheric models. The results accounted for the features of the modified HF propagation environment observed at early times during the MOSC samarium release experiments. We showed that ray tracing techniques can be successfully used to model the disturbances caused by artificial ionospheric modification. The modeling identified three additional HF propagation paths created by the samarium plasma clouds in the ionosphere. These effects were observed both on a great circle path and a markedly non-great circle path where the refraction angle exceeded 90°. For modeling the background plasma the Parameterized Ionospheric Model (PIM), constrained by ALTAIR radar observations, provided an excellent representation of the low latitude ionosphere during quiet conditions. But, neither PIM nor IRI were able to accurately specify local gradients of a magnetically disturbed ionosphere. However, IRI's flexibility and convenient access to parameters within the model supported the use of the Nelder-Mead minimization technique for constructing a regional ionosphere.

In Chapter 4, we presented the calculation of various parameters in the growth rate of the Rayleigh-Taylor Instability and the growth rate as well from thirteen days of High-Frequency (HF) radar data during the Metal-Oxide Space Cloud (MOSC) campaign. The parameters and the growth rate were also calculated from model ionospheric profiles optimized to match time-delays in corresponding HF observations. We also made comparisons of the calculated growth rate with the ground based scintillation observations as quantified by the total hourly mean S4 (THMS4) index. The vertical plasma drift was shown to be an important factor in the growth of instability in the equatorial F-region. The vertical plasma drift $(V_p) \sim 20$ m/sec was seen to be a threshold value for moderate/high level of scintillation observations. The cumulative effect of the various ionospheric parameters was captured in the growth rate and hence was shown to be a better indicator to correlate with scintillation activity instead of any single parameter in the growth rate expression. The growth rate calculated from the HF link data or the optimized model ionospheric profiles accurately predicted the instability development as reflected by the scintillation index THMS4.The assumptions made in our work can be the possible sources of small discrepancies between the calculated growth rate and the scintillation observations: constant vertical neutral wind, disappearance of E-region conductivity. The other possible sources of the discrepancies can be seed perturbations in the bottomside F-layer, transequatorial neutral wind and choice of scintillation index.

In Chapter 5, we presented an investigation on the variation of apex-altitude distribution of equatorial ionospheric irregularities with solar activity. We analyzed the data from Communications/Navigations Outage Forecasting System (C/NOFS) satellite mission to understand the effects of the solar activity on the occurrence of the equatorial ionospheric irregularities. We also analyzed Physics Based Model (PBMOD) ionospheric model results to determine if a physics-based model can reproduce the observed dependence of bubble height on solar activity. Our results are consistent with similar past studies examining the longitudinal and seasonal occurrence statistics of equatorial ionospheric irregularities. We found the equatorial plasma bubble (EPB) occurrence rates were generally high around equinoctial months and low around June solstice. We compared the irregularity detections from space-based in-situ observations with ground based scintillation observations and found that they were consistent under the assumption that the disturbance electric fields map efficiently along the magnetic fields of equatorial plasma bubble growth. Our space-based algorithm of equatorial ionospheric irregularities detection was confirmed to be consistent with ground-based scintillation observations. While confirming this, we validated the flux-tube paradigm of equatorial plasma bubble growth as well. In the climatology maps, the EPB occurrence rates maximized in the America-Atlantic-Africa region corresponding to the longitude sector -80^o W to 30^o E. Previous studies (e.g., DMSP) showed almost no activity during solar minimum. Our results show a near absence of activity at DMSP altitudes during solar minimum, but total bubble activity as observed in the lowest apex-altitude bin decreases to 12.18 % at solar minimum as compared to 26.67 % at solar maximum. The lack of detection by DMSP can thus be attributed to a bubble altitude distribution that depends on solar flux. The median height distribution of bubbles increases linearly from about 491 km at solar minimum to 737 km during solar maximum in the longitude sector -80^o W to 30^o E [1]. Other longitude sectors may have different altitude distributions. The occurrence statistics suggested that bubbles in this longitude sector are higher than in other regions on average. A physics-based model (PBMOD) was used to confirm our findings. In the model we found that field-line integrated conductivity is the key determinant of terminal bubble altitude. Specifically, when the field-line integrated conductivity inside the bubble is equal to that of the background ionosphere, the polarization electric field that drives the bubble upwards disappears and the bubble stops rising. We also found that the field-line integrated plasma density is not a reasonable proxy for conductivity due to the higher weight given by the collision-frequency factor at lower altitudes in the field-line conductance integral whereas no such weight at any altitude occurs in the field-line integration of the density due to the absence of the collision frequency factor. These results from our comprehensive investigation into altitude distributions of equatorial ionospheric irregularities at the magnetic equator are the first observational confirmation of bubble altitude changes as a function of solar flux and are valuable to the development of improved scintillation mapping models for both real-time and post-processing applications.

6.2 Directions for Future Research

This dissertation opens doors to many important research questions to expand upon this work to newer and more exciting frontiers. A companion paper [2] published in *Radio Science* in the special issue of *2013 Equatorial Ionospheric Sounding Rocket Campaign from Kwajalein Atoll* has attempted to study the electrodynamic environment in the equatorial ionosphere produced by the artificial plasma clouds created in the MOSC experiment via simulations. *Retterer et al.* [2] show through their simulations that a moderately denser cloud than the MOSC cloud, close to the bottom-side of the F layer, could indeed suppress the development of the low-density plumes and the shorter-wavelength irregularities associated with radio scintillation that form with the Rayleigh-Taylor instability in the equatorial ionosphere. The ability to artificially quench bottomside equatorial ionospheric irregularities can be an ‘eureka’ moment for the space-weather research community as it could also mean the suppression of radio-wave scintillation which directly points to active mitigation of adverse impacts of ionospheric irregularities and radio wave scintillations on communication and navigation systems. So, future artifical ionospheric modification experiments can be used to test the results from the simulations in the aforementioned work to check if it indeed could be possible to quench the ionospheric bottomside instabilities by increasing the density of the chemical (Sm+) used to create the artifical plasma.

In our work, we modeled the tailored ambient propagation environment generated through artificial ionospheric modification in the MOSC experiment by taking a spherical cloud of constant size. In the future, we can include the temporal and the spatial changes of a dynamic plasma cloud in the modeling work to better understand the change in the ambient propagation environment. HF data from the ionosonde can also be used to investigate the role of precursor conditions to instability development in the equatorial ionosphere to expand and build upon the published literature [3, 4] in the field. The wave structures can be identified through the iso-density ionospheric plasma contours from HF radar echoes to understand the complementary roles they play in the development of equatorial spread F. Such investigations can be taken at various longitude sectors to determine if a similar pattern of the complementarity is observed in all the longitude sectors. The results from statistical studies in such investigations shall also be tested against a daily case-by-case basis to check if they confirm or refute the statistical results.

The various sensor observations made onboard C/NOFS satellite spanning half a solar cycle ranging from low solar activity to high solar activity years (2008 – 2014) presents an unprecedented opportunity to investigate a repertoire of science questions vis-a-vis the equatorial ionosphere. In this dissertation work, we analyzed PLP sensor observations to understand the effects of solar activity on the apex-altitude distribution of equatorial ionospheric irregularities in the longitude sector 280^{o} E (-80^{o}) to 30°E. We focused on this longitude sector as we found – in concurrence with similar past studies – the ionospheric irregularities maximized in this sector. We found a linear relationship between the apex altitude of ionospheric irregularities and the F10.7 index in this longitude sector with a positive slope. This investigation can be extended to more clearly defined longitude sectors to check if similar relationships exist between the apex altitude of ionospheric irregularities and the F10.7 index. We refined the existing algorithm for identifying equatorial ionospheric irregularities but more work can be done to further isolate the depletions in the data from other type of disturbances. Since the 200-point moving median baseline follows the background ion-density, the baseline can be elevated or depressed to make a tight envelope to the background ionospheric density at places it hasn't fluctuated 'rapidly'. The identified depletions under this scheme can be categorized based upon their depth for further analysis. A similar approach is used in a work by *Costa et al.* (from an unpublished manuscript). The PLP sensor observations can also be studied to analyze the spectral slopes of the ionospheric irregularities. It has been hypothesized that there is less scintillation at the magnetic equator because the slope of the irregularity spectrum is steeper there [5]. The implication is that the spectra are steep at low apex-altitudes and increasingly shallow as one goes to higher apex altitudes. A study on the spectral slopes of equatorial plasma bubbles and their dependence on apex altitude can demonstrate the validity of the hypothesis and improve an ability to model and predict low-latitude scintillation. For Radio Occultation (RO) observations, the more apriori constraints we can put in the data, the better we can localize the irregularities. Hence, knowing bubble apex altitude based on solar activity, as from this thesis work, can be helpful in future radio-occultation experiments. The data from sensors onboard C/NOFS satellite can also be studied to analyze the gravity wave phenomena such as Large Scale Wave Structures (LSWSs) [6], Traveling Ionospheric Disturbances (TIDs)

[7] in ionosphere-thermosphere system which could play a role in seeding the RT instability leading to equatorial plasma bubbles. We can also seek to characterize other density structures we observed in the PLP ion-density observations such as positive enhancements (blobs) and sinusoidal or periodic variations to understand their morphology to find physical processes responsible.

References:

[1] Joshi, D., J. Retterer, P. Roddy, K. Groves (2019), Peak Height Distributions of Equatorial Ionospheric Irregularities deduced from the C/NOFS satellite mission *(under preparation).*

[2] Retterer, J., K. Groves, T. Pedersen, and R. Caton (2017), The electrodynamic effects of MOSC-like plasma clouds, *Radio Sci.*, **52**, doi: 10.1002/2016RS006085.

[3] Abdu, M. A., Souza, J. R., Kherani, E. A., Batista, I. S., MacDougall, J. W., & Sobral, J. H. A. (2015), Wave structure and polarization electric field development in the bottomside *F* layer leading to postsunset equatorial spread F, *Journal of Geophysical Research: Space Physics*, **120**, 6930–6940, https://doi.org/10.1002/2015JA021235.

[4] Abdu, M. A., E. Alam Kherani, I. S. Batista, E. R. de Paula, D. C. Fritts, and J. H. A. Sobral (2009), Gravity wave initiation of equatorial spread F/plasma bubble irregularities based on observational data from the SpreadFEx campaign, *Ann. Geophys.*, **27**, 2607–2622, doi:10.5194/angeo-27-2607-2009.

[5] Bhattacharya, A., Kakad, B., Sripathi, S., Jeeva, K., & Nair, K. (2014), Development of intermediate scale structure near the peak of the *F* region within an equatorial plasma bubble, *Journal of Geophysical Research: Space Physics*, **119**, 3066–3076, https://doi.org/10.1002/2013JA019619.

[6] Thampi, S. V., M. Yamamoto, R. T. Tsunoda, Y. Otsuka, T. Tsugawa, J. Uemoto, and M. Ishii (2009), First observations of large-scale wave structure and equatorial spread

F using CERTO radio beacon on the C/NOFS satellite, *Geophys. Res. Lett.*, **36**, L18111, doi: 10.1029/2009GL039887.

[7] Huang, C.-S. (2016), Plasma drifts and polarization electric fields associated with TID-like disturbances in the low-latitude ionosphere: C/NOFS observations, *Journal of Geophysical Research: Space Physics*, **121**, 1802–1812, https://doi.org/10.1002/2015JA022201.

Appendix I

Joshi, D., Groves, K., McNeil, W., Carrano, C., Caton, R., Parris, R. T., Pedersen, T., Cannon, P., Angling, M., and Jackson-Booth, N. (2017), HF propagation results from the Metal Oxide Space Cloud (MOSC) Experiment, *Radio Sci., 52*, doi:10.1002/2016RS006164.

AGU PUBLICATIONS

Radio Science

RESEARCH ARTICLE

10.1002/2016RS006164

Special Section:
2013 Equatorial Ionospheric Sounding Rocket Campaign from Kwajalein Atoll

Key Points:

- High-frequency propagation effects due to an artificial plasma cloud successfully modeled
- Effects of arbitrary plasma environments shown to be predicted with accuracy by ray-tracing
- Ray tracing can be applied to selectively adjust ionospheric models effectively for HF applications

Correspondence to:
D. Joshi,
dev.joshi@bc.edu

Citation:
Joshi, D., K. M. Groves, W. McNeil, C. Carrano, R. G. Caton, R. T. Parris, T. R. Pederson, P. S. Cannon, M. Angling, and N. Jackson-Booth (2017), HF propagation results from the Metal Oxide Space Cloud (MOSC) experiment, *Radio Sci.*, *52*, doi:10.1002/2016RS006164.

Received 1 SEP 2016
Accepted 11 APR 2017
Accepted article online 25 APR 2017

HF propagation results from the Metal Oxide Space Cloud (MOSC) experiment

Dev Joshi[1,2], Keith M. Groves[1], William McNeil[1], Charles Carrano[1], Ronald G. Caton[3], Richard T. Parris[3], Todd R. Pederson[3], Paul S. Cannon[4,5], Matthew Angling[5], and Natasha Jackson-Booth[4]

[1]Institute for Scientific Research, Boston College, Chestnut Hill, Massachusetts, USA, [2]Department of Physics, Boston College, Chestnut Hill, Massachusetts, USA, [3]Space Vehicles Directorate, Air Force Research Laboratory, Kirtland Air Force Base, Albuquerque, New Mexico, USA, [4]QinetiQ, Malvern, United Kingdom, [5]Now at University of Birmingham, Birmingham, United Kingdom

Abstract With support from the NASA sounding rocket program, the Air Force Research Laboratory launched two sounding rockets in the Kwajalein Atoll, Marshall Islands in May 2013 known as the Metal Oxide Space Cloud experiment. The rockets released samarium metal vapor at preselected altitudes in the lower *F* region that ionized forming a plasma cloud. Data from Advanced Research Project Agency Long-range Tracking and Identification Radar incoherent scatter radar and high-frequency (HF) radio links have been analyzed to understand the impacts of the artificial ionization on radio wave propagation. The HF radio wave ray-tracing toolbox PHaRLAP along with ionospheric models constrained by electron density profiles measured with the ALTAIR radar have been used to successfully model the effects of the cloud on HF propagation. Up to three new propagation paths were created by the artificial plasma injections. Observations and modeling confirm that the small amounts of ionized material injected in the lower *F* region resulted in significant changes to the natural HF propagation environment.

1. Introduction

Since the 1950s after the availability of rockets for research purposes, experiments have been conducted to inject various materials into the atmosphere for the purpose of creating perturbations to the ambient medium [*Bedinger et al.*, 1958; *Rosenberg*, 1963; *Corliss*, 1971; *Davis*, 1979; *Wand and Mendillo*, 1984; *Bernhardt et al.*, 2012]. Such ionospheric modification experiments in the form of chemical releases have been used for various goals such as to measure neutral wind directions and shears, to detect plasma drift velocities and electric fields, to exploit the ionosphere as a plasma laboratory without walls, to modify the plasma density in the ionosphere to trigger larger scale phenomena, and many other uses [*Bernhardt*, 1987; *Hu et al.*, 2011; *Shuman et al.*, 2015]. The Air Force Research Laboratory (AFRL) launched two sounding rockets in the Kwajalein Atoll, Marshall Islands, in May 2013 known as the Metal Oxide Space Cloud (MOSC) experiment. The sounding rockets, each carrying a payload of two 2.5 kg canisters of powdered samarium metal in a thermite mixture, released samarium metal vapor at dusk at 170 and 180 km altitude, respectively. A fraction of the samarium metal vapor ionized in the ambient environment, creating an additional layer of plasma. The objectives of the experiments were to understand the dynamics, evolution, and chemistry of Sm atoms in the Earth's upper atmosphere; to understand the interactions of artificial ionization and the background plasma; and to measure the effects on high-frequency (HF) radio wave propagation. A host of diagnostic instruments were used to probe and characterize the cloud including the Advanced Research Project Agency Long-range Tracking and Identification Radar (ALTAIR) incoherent scatter radar, multiple GPS, and optical instruments, satellite radio beacons, and a dedicated network of high-frequency (HF) radio links [*Caton et al.*, 2017]. In this paper, we report the results from the HF sounder observations and modeling those results with the ALTAIR radar data using the HF radio wave ray-tracing MATLAB toolbox PHaRLAP. The modeling results enable us to understand the changes caused by the samarium plasma cloud in the HF propagation environment and thus validate the extent to which we can model HF propagation for other specified plasma perturbations. We have developed a new technique to model an anomalous background ionosphere by assimilating oblique ionosonde data specifically to match observed HF signal delays. The approach may have numerous applications for ionospheric specification for HF propagation.

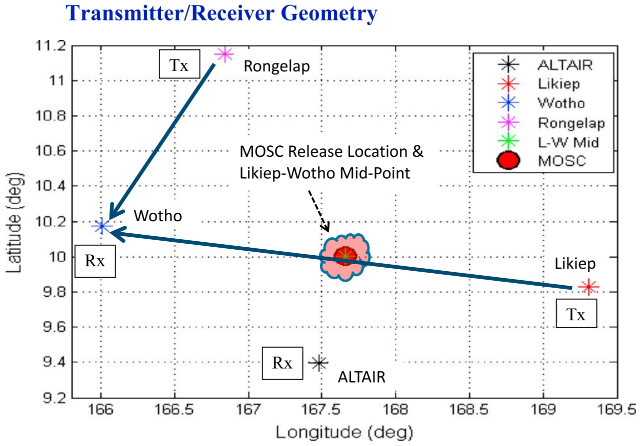

Figure 1. Site locations in Marshall Islands. Tx = transmitter, Rx = receiver. The MOSC release point is midway between Likiep and Wotho.

In Figure 1, the site locations corresponding to the HF links and the ALTAIR incoherent scatter radar are shown. In this work, we focus on the signals received at Wotho from transmitters at Rongelap and Likiep. The Rongelap-Wotho link geometry is predominantly N-S and the release region is far from the great circle path, whereas the Likiep-Wotho path is nearly magnetic E-W and the release point lies close to the midpoint of the link. Geographic coordinates for the sites may be found in Table 1.

The first sounding rocket launch occurred on 1 May 2013 at 07:38 UT, and the samarium metal vapor release occurred at 07:40:40 UT. The second sounding rocket launch occurred on 9 May 2013 at 07:23 UT, and the release occurred at 07:25:40 UT. In both releases, approximately 10% of the samarium metal in the canisters ionized.

2. Observations

The Advanced Research Project Agency Long-range Tracking and Identification Radar (ALTAIR) at Kwajalein Atoll was used to monitor the ionospheric state and track the evolution of the metal oxide space cloud. Range-time-intensity displays of each release event are shown in Figure 2. The data gap during the first release shown in Figure 2a was an intentional data management action to avoid a data file size limitation. Recording was turned off for a period of about 2 min and turned back on approximately 30 s prior to the samarium release. Improved prelaunch file management on the night of 9 May precluded the need to limit data sampling during the second rocket flight as shown in Figure 2b.

The ionograms (Figures 3 and 4) from the oblique sounder data for the releases on 1 and 9 May 2013 show the evolution of the ionosphere before and after the release of the samarium metal vapor in the ambient environment. Both Likiep and Rongelap used broadband folded dipole transmit antennas approximately 12 m long connected to 100 W power amplifiers to transmit swept frequency waveforms from 2–30 MHz every 5 min at the rate of 100 KHz/s. The timing for both transmitters and receivers was synchronized by GPS-disciplined clocks. The ionograms shown in the figures were recorded at Wotho using a simple 1 m diameter loop antenna. Plots show data from only 2–14 MHz since no signatures were observed at higher frequencies. The titles include the start time of the frequency sweep (2 MHz); end time at 14 MHz is 120 s later. In prerelease sweeps on 1 May, *E*-layer traces are also seen in the ionograms in addition to the ground wave and *F* region traces, whereas the *E*-layer trace is not seen on 9 May, suggesting that the *E* region is not present during the second release. The *E*-layer echoes present on 1 May are due to sporadic *E* [*Davies*, 1990], as the traces extend to 10 MHz or so, well beyond the peak plasma frequency expected in the *E* region at this local time (approximately 18:20 LT). The *F* region traces are further seen to be split into two characteristic components: ordinary and extraordinary waves. The effects of the artificial plasma cloud are clearly seen in the postrelease sweeps along both Rongelap-Wotho and Likiep-Wotho paths. Two additional traces, denoted as the “MOSC” layer and the secondary *F* region echo, are evident, suggesting significant change in the propagation environment of the HF radio waves due to the metal oxide plasma cloud. SmO+ layer density (approximately 10 MHz at early times) is similar in both cases and observed initially on all links. The density of the artificial cloud is observed to fall rapidly over time scales of a few minutes, and the signatures disappear completely within about 15 min. The difference between the secondary *F* region echo

Table 1. Geographic Co-Ordinates

Site	Latitude (°N)	Longitude (°E)
Rongelap	11.152	166.838
Likiep	9.826	169.307
Wotho	10.174	166.005
ALTAIR	9.395	167.479

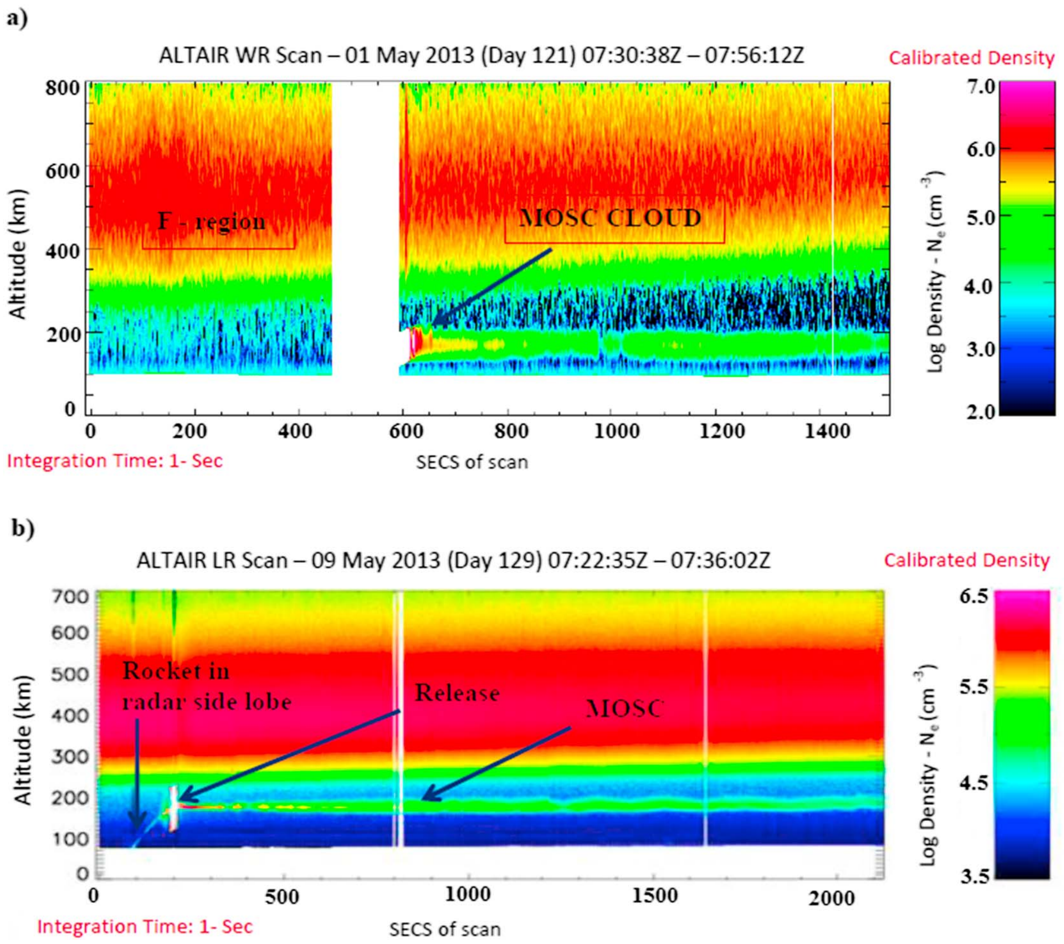

Figure 2. (a) First release: (top) the ALTAIR radar range-time-intensity (RTI) plot shows a rapidly rising *F*-layer of the ionosphere (disturbed condition). (b) Second release: (bottom) the RTI plot shows a quiescent ionosphere typical of the equatorial region just prior to the onset of the prereversal enhancement period.

and *F* region trace is smaller along the Likiep-Wotho path compared to the Rongelap-Wotho path, the reason of which is explained in section 4.2. A more detailed description of the cloud's evolution can be found in *Pedersen et al.* [2017]; here we focus on modeling the HF propagation observed during the first few minutes after the release. The SmO+ plasma also triggered significant modification of HF propagation in the *F* region.

In the first postrelease frequency sweep initiated less than 40 s after the release on 1 May, the Likiep-Wotho path has an MOSC signature only in the high end of the frequency sweep above $f = 8$ MHz (Figure 3d), yet the Rongelap link shows a robust signature beginning at less than 4 MHz (Figure 3c). The subsequent sweep 5 min later shows a solid MOSC trace at lower frequencies only on both paths (Figures 3e and 3f). Moreover, MOSC signature is present across most of the frequency bands on both links in the second release during all phases of the observations (Figures 4c–4f). Potential reasons for the lack of signals on the Likiep-Wotho path in the lower portion of the HF frequency band during the first release will be discussed later in this paper.

3. Modeling

Since *Haselgrove* [1955] set down the differential equations governing raypaths in an anisotropic medium for numerical integration techniques [*Haselgrove*, 1955], the equations have been used extensively [*Jones and Stephenson*, 1975; *Coleman*, 1993; *Zawdie et al.*, 2016] to study the propagation of HF energy through the ionosphere. In our work to model the HF sounder observations, we have used PHaRLAP, a HF radio wave ray tracing MATLAB toolbox developed by Dr. Manuel Cervera, that contains a variety of ray tracing engines of various sophistications from 2-D ray tracing to full 3-D magnetoionic ray tracing [*Cervera and Harris*, 2014].

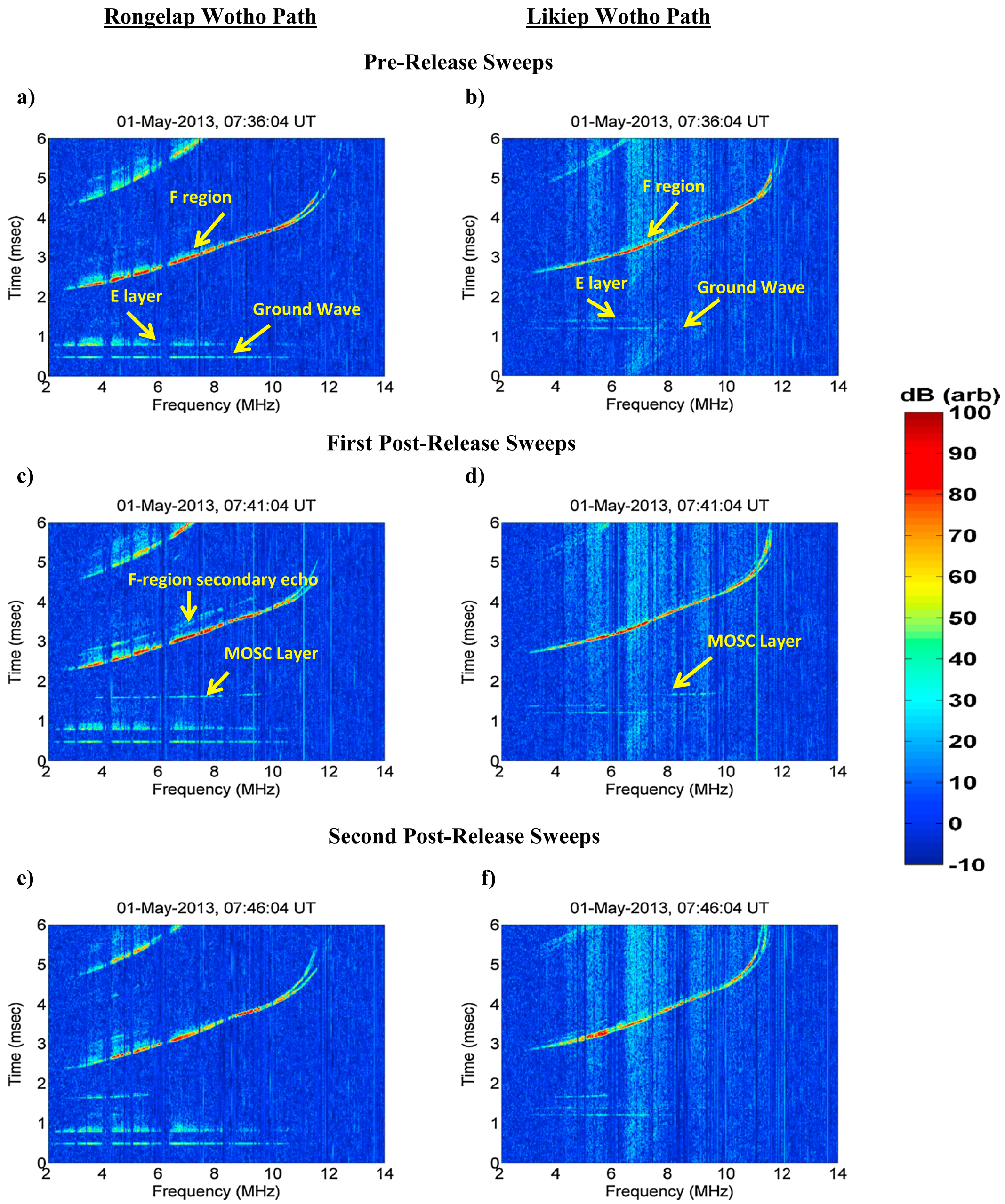

Figure 3. First release: sounder observations of the ionosphere before and after the release of the samarium metal vapor (a, c, and e) along Rongelap-Wotho path and (b, d, and f) along Likiep-Wotho path.

Modeling the sounder observations involved insertion of a three-dimensional plasma cloud representing the MOSC into a background ionosphere and then using full 3-D magnetoionic ray-tracing to understand the various propagation modes induced by introduction of Sm+ ions in the ambient plasma. Prior to the first release on 1 May the ionosphere was rising rapidly ($v_z \geq 50$ m/s), potentially responding to a minor magnetic perturbation ($Dst \sim -50$), and spreads *F* formed within minutes after the release as observed in the sounder data and ALTAIR radar scan. For the second release, the ionosphere was quiescent as seen in the sounder observations and the radar scan. Hence, we present the modeling efforts for the background ionosphere and samarium cloud for the second release in section 3.1 before those for the first release (section 3.2).

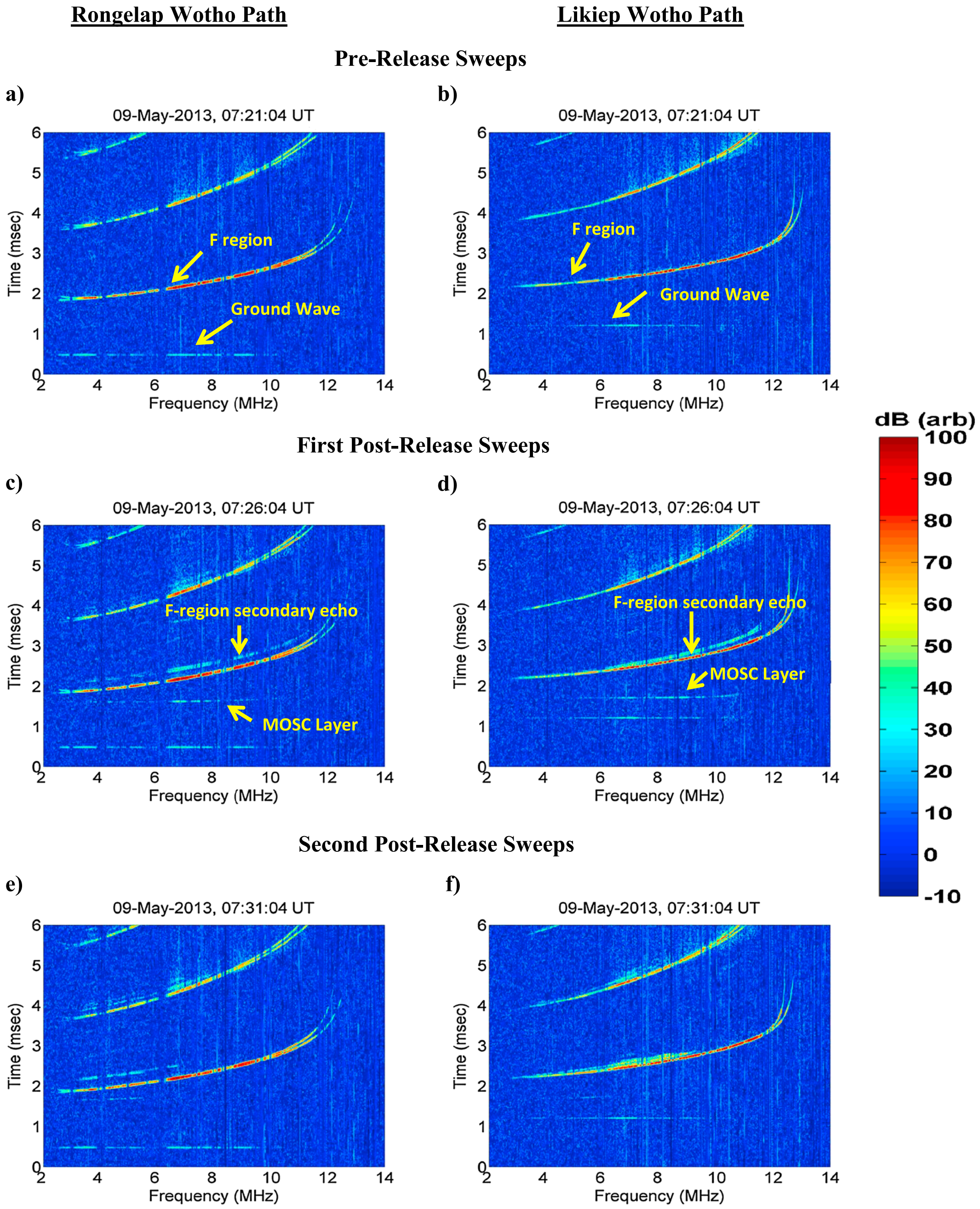

Figure 4. Second release: sounder observations of the ionosphere before and after the release of the samarium metal vapor (a, c, and e) along Rongelap-Wotho path and (b, d, and f) along Likiep-Wotho path.

At early times immediately after the release, the cloud appeared to be symmetric optically and the ALTAIR radar scan also showed a symmetric density profile [*Caton et al.*, 2017]. Before- and after-release density profiles along with the symmetric 3-D representation for the samarium plasma cloud derived from ALTAIR are shown in Figure 5 where a prerelease electron density profile (Figure 5a) and a postrelease profile (Figure 5b) clearly show the contribution of the samarium plasma. A model cloud based on these observations was inserted into the background ionosphere for ray-tracing. A graphical representation of the digitized cloud is shown in Figure 5c, while a false-color image of the cloud itself is shown in Figure 5d. The image was acquired with the AFRL bare CCD camera through a 630 nm filter approximately 4 min after release. The cloud still appears spherical at this time which corresponds to the end of the first postrelease HF frequency scans presented in Figure 4.

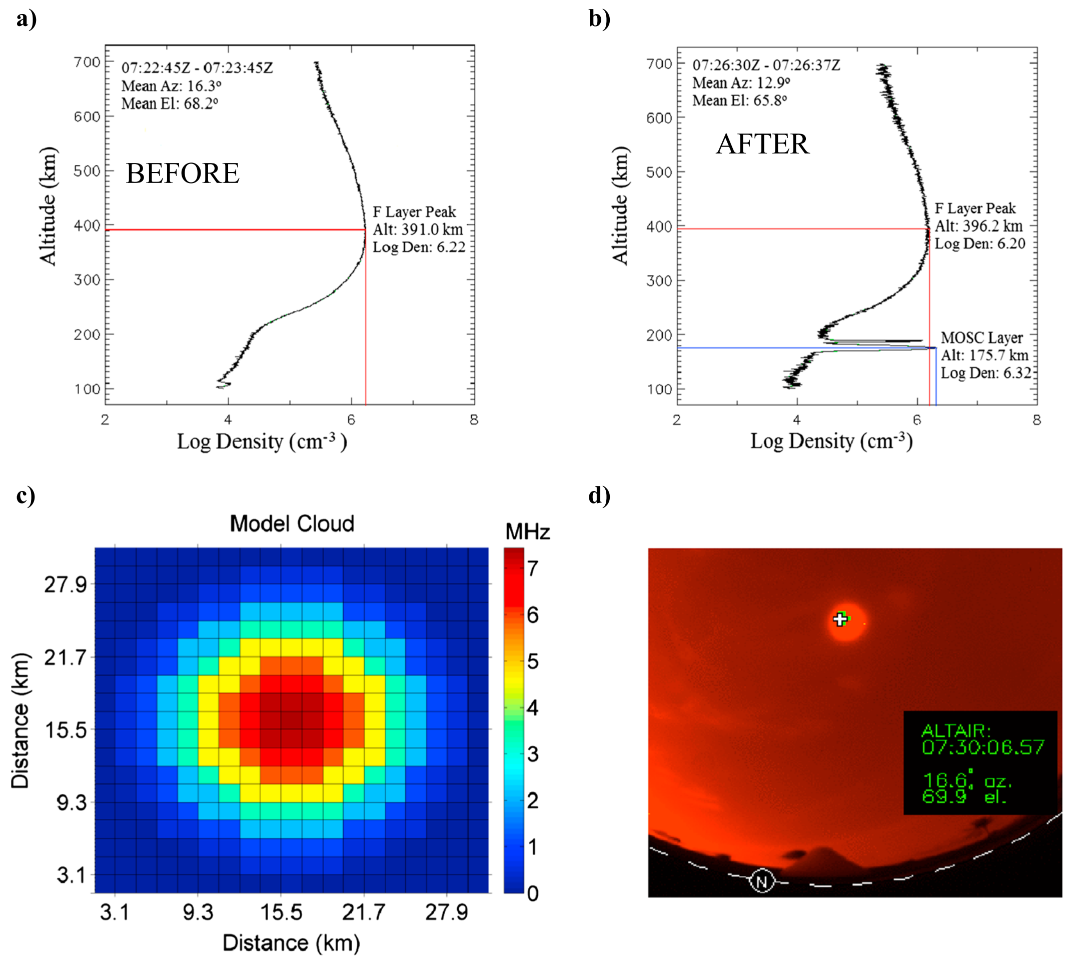

Figure 5. (a) The ALTAIR radar profile before the release of the samarium metal vapor. (b) The radar profile approximately 30 s postrelease. (c) The two-dimensional view of the model cloud through its center is shown. The central pixel corresponds to f_{pe} = 7.44 MHz. (d) A false-color image of the illuminated cloud acquired with the AFRL bare CCD all-sky imager approximately 4 min after release on 9 May 2013. The cross-hair indicates the look-angle of the ALTAIR radar.

An ionospheric model was used for the background because we did not have adequate knowledge of the ionosphere across the whole region of interest. The approach was to constrain the background model with calibrated ALTAIR radar observations at a specific location and then use the model to represent the ionosphere across a region that extended approximately 200 km north and ±200 km E-W from the point of the radar observations. We used the Parameterized Ionospheric Model (PIM) [*Daniell et al.*, 1995] and the International Reference Ionosphere (IRI-2012) [*Bilitza et al.*, 2014] as the background model ionospheres for ray-tracing. The reason for using two models rather than just one will be made clear shortly.

The IRI is an empirical model ionosphere developed as a joint project of the Committee on Space Research and the Union Radio Scientifique Internationale. For a given location, time, and date, IRI provides the median monthly values of electron density, the electron temperature, and ion composition in the altitude range from 50 km to 2000 km. The major data sources for the IRI model are the worldwide network of ionosondes, the powerful incoherent scatter radars, (Jicamarca, Arecibo, Millstone Hill, Malvern, St. Santin), the International Satellites for Ionospheric Studies and Alouette topside sounders, and in situ instruments on several satellites and rockets.

The PIM is a global ionospheric and plasmaspheric model based on combined output from the Global Theoretical Ionospheric Model for low and middle latitudes. PIM produces electron density profiles between 90 and 25,000 km altitude, in addition to other profile parameters such as corresponding critical frequencies and heights for the ionospheric E and F_2 regions, and total electron content.

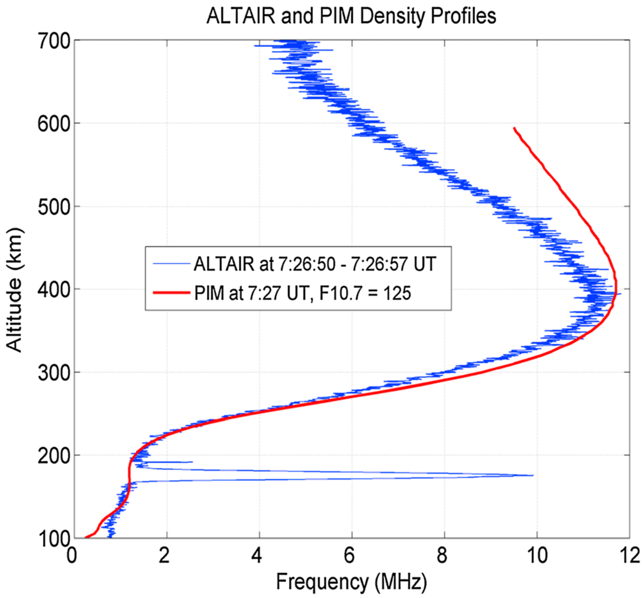

Figure 6. PIM and ALTAIR radar electron density (N_e) profiles displayed as equivalent plasma frequency ($f_p \approx \sqrt{N_e}$, in MKS units). The PIM bottomside fits well with the observed ATLAIR profile. The disparity below about 125 km corresponds to a very low density/frequency ($<10^3$ cm^{-3}/1 MHz) that will not have an appreciable effect on radio waves propagating above about 2 MHz.

3.1. Ionospheric Model for Samarium Release on 9 May

For the second release in which the background ionosphere exhibited typical quiescent characteristics, good agreement between the PIM model and the ALTAIR radar observations were obtained by making a small change in the F10.7 flux input to the model, as shown in Figure 6. The objective was to obtain a good fit primarily to the bottomside to ensure accurate HF propagation modeling.

3.2. Ionospheric Model for Samarium Release on 1 May

For the first release which had a disturbed and rapidly rising ionosphere, no standard model could be fitted to match the background ionosphere. We tried to minimize the difference between the model ionospheric profile and the ALTAIR radar profile at the MOSC release location by an optimization technique known as the Nelder-Mead Downhill Simplex method [*Nelder and Mead*, 1965; *Press et al.*, 2007]. We used the native “fminsearch” function in MATLAB to optimize the difference between the ALTAIR radar ionospheric profile and the model profile (Figure 7a). Since PIM did not have enough accessible degrees of freedom, this optimization technique gave good results only with the IRI model. An altitude-dependent scale vector was obtained by dividing the optimized IRI profile by the initial IRI profile, and this was subsequently used to scale the entire IRI 3-D grid. However, when the optimized results were used on the Rongelap-Wotho path (~150 km NW of ALTAIR scan), the modeled delay did not match observations with sufficient accuracy, presumably because the disturbed ionosphere gradients were not well represented by the scaled climatological model output. After experimenting with a number of approaches we succeeded in modeling the background ionosphere along the raypath by applying frequency-specific multipliers to the altitude-dependent scale vector; results are shown in Figure 7b. The variations in the multipliers were not large, but they facilitated a good fit between the modeled and observed profiles. The multipliers were determined by adjusting the ionosphere using ray tracing to minimize the difference between the observed and modeled signal delays. The primary objective is not to develop a good model of the ionosphere, but rather, to optimize our ability to model the HF propagation environment. The priority is for the primary *F* region modes to match the observations with high fidelity, so when the samarium cloud is introduced one can have high confidence in the propagation model results.

4. HF Propagation Modeling Results and Discussion

Ray-tracing was performed for both the releases after inserting the 3-D plasma cloud into the background ionosphere. It confirmed and explained the changes in propagation modes of the HF radio waves due to the artificial plasma cloud.

4.1. Rongelap-Wotho Path

As shown in Figure 8a, the Rongelap-Wotho path is nearly N-S and the release point is well off the great circle path connecting the two atolls. Up to three additional paths due to the presence of the samarium plasma cloud for the received HF energy have been identified. Rays reflected directly from the transmitter off the cloud account for the low delay MOSC trace. Meanwhile, the secondary *F* region traces may be formed in two ways. One path consists of reflection first by the *F*-layer to the MOSC cloud and subsequent reflection

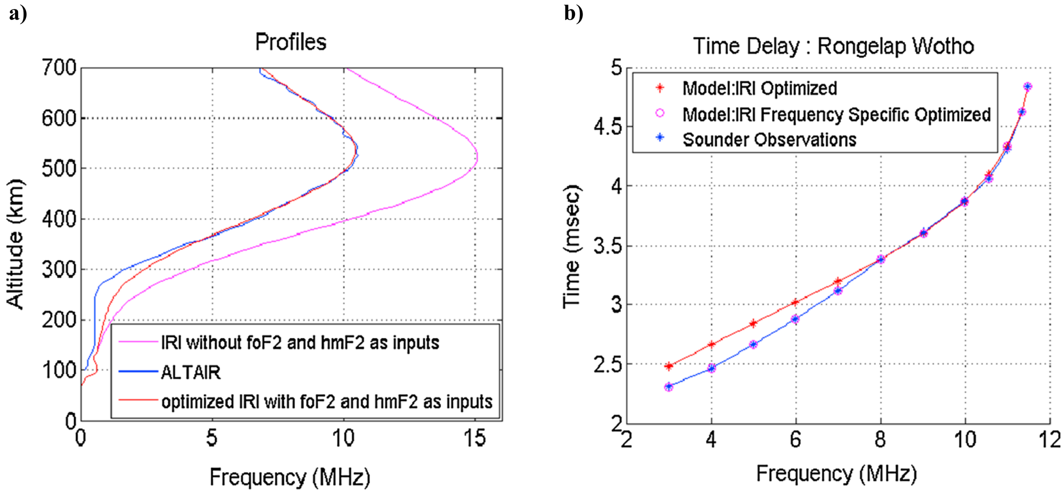

Figure 7. (a) The Nelder-Mead Downhill Simplex method applied to optimize IRI in the vicinity of ALTAIR radar data. (b) A second frequency-dependent optimization procedure was applied to assimilate the sounder data along the R-W path.

to the receiver site (high elevation). The other path is defined by waves that propagate directly to the samarium cloud, reflect to the *F* region, and are then reflected to the receiver (low elevation). The elevation angles so defined refer to the angle between the transmitted HF signal and the ground at the transmitter. Figure 8b shows a graphical representation of the various propagation modes identified to model the time delays shown in Figure 8c. The match between the observations and the model results suggests that both the high- and low-elevation angle paths contributed to the observed *F* region secondary layers. We note that the low-elevation propagation mode corresponds to smaller delay compared to that of the high-elevation propagation mode in the *F* region secondary trace (Figure 8c). This is as expected as the low-elevation mode has a shorter path. From the geometry all the observed signatures confirm that the cloud scattered and/or refracted HF energy well off the great circle path. Rays were traced for a number of selected frequencies. Ray-tracing gave excellent results which agree with the sounder observations (Figures 8c and 8d). For the first release (Figure 8d), the additional MOSC and *F* region secondary layers are also modeled to be close to the observed layers validating the modeling approach and the technique developed to build a disturbed background ionosphere.

For both releases, the sounder observations show greater frequency extent for both the MOSC samarium layer and the *F* region secondary layer than the model results. Reasons for the discrepancy include inadequate spatial resolution of the MOSC plasma cloud in the model and a low estimate of the peak plasma density in the cloud obtained from the radar observations. The high-density center of the cloud is contained in a layer just a few hundred meters on a side, which represents a very small target for ray tracing calculations, particularly for accurately homing rays from a transmitter to a receiver. In fact, it is challenging to resolve the structure adequately in both space and time with the ALTAIR radar. The observations presented in Figure 5b are the true cloud density convolved spatially with the radar beam width and pulse resolution and the time period over which the measurements were integrated. The measurements provide a good estimate of the average parameters of the cloud over a 60 s window, but they do not represent a precise characterization of the plasma cloud at the subkilometer resolution needed to describe the structure in full detail. This does not present a critical problem, however, because the primary objectives to identify and characterize the new propagation modes introduced by the cloud can be achieved without an extremely high fidelity representation of the electron density in the cloud. The radar-derived spatial and plasma parameters are sufficient for this purpose.

4.2. Likiep-Wotho Path

Similar analysis was performed along the Likiep-Wotho path, shown in Figure 9a. This path was selected because the samarium release point lies nearly at the midpoint of the great circle path between the transmitter (Likiep) and the receiver (Wotho). The same modes to/from the cloud and the *F* region were observed in

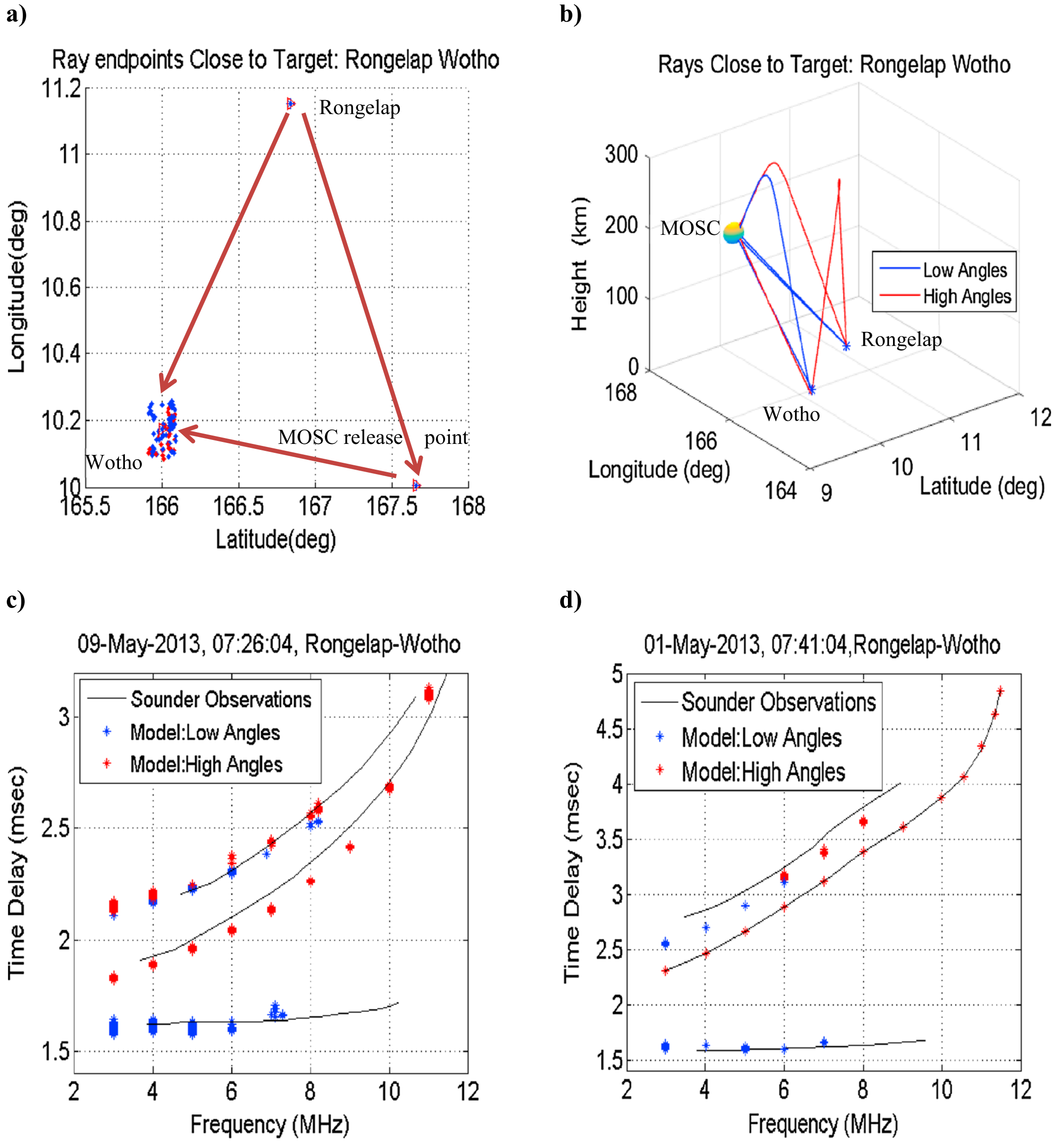

Figure 8. (a) Rongelap-Wotho geometry. (b) Various propagation modes for 6 MHz in second release. Excellent agreement between model and observations: (c) second release and (d) first release.

this geometry, but the differences in delay between the normal *F*-layer path and the delayed paths (*F* region to cloud; cloud to *F* region) were significantly smaller than for the Rongelap-Wotho geometry as expected due to the coplanar geometry (see Figure 9b). Rays traced for various frequencies reproduced the additional MOSC and *F* region secondary layers close to the observations for both releases (Figure 9). As mentioned previously, one significant feature of the observations that remains to be explained is the absence of lower frequency signals (below ~8 MHz) refracted directly from the samarium cloud to the receiver on the Likiep-Wotho path within the first few minutes postrelease on 1 May 2013.

The lack of lower frequency signals on the nearly great circle path is noteworthy because relatively strong lower frequency signals are observed on the distinctly nongreat circle Rongelap-Wotho link at the same time. Moreover, lower frequency signals are present on both links throughout the observing period during the second release on 9 May. One possible explanation is enhanced absorption during the early scan period on the Likiep-Wotho path. This absorption is frequency-dependent and would normally be associated with an enhanced *E*- or *D* region not expected to be present at the time of the observations (18:47 SLT). A

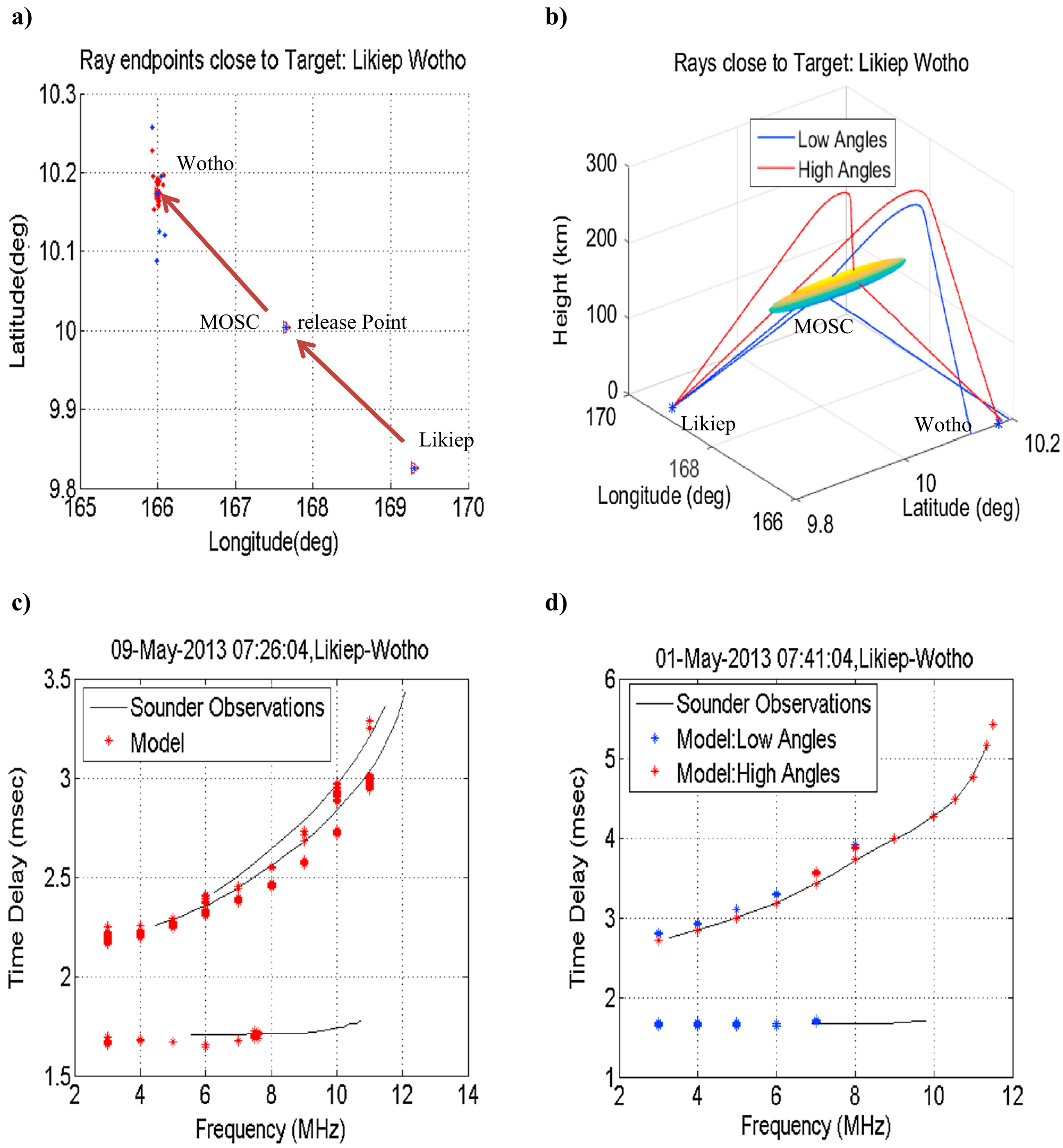

Figure 9. (a) Likiep-Wotho geometry. (b) Various propagation modes for 6 MHz in second release. Close agreement between model and observations: (c) second release and (d) first release.

comparison of the relative intensities of the *F* region traces at frequencies below 8 MHz clearly shows that there is little to no difference between the first and second postrelease scans on 1 May or the scans from the second release on 9 May. Absorption does not appear to be a viable mechanism for the observed absence of power.

The primary geophysical difference between the 1 May and the 9 May releases was the presence of sporadic *E* (Es) on the night of the first release. A reasonably strong Es layer is visible on the Rongelap-Wotho link (Figures 3a, 3c, and 3e) extending to about 10 MHz frequency. A faint Es trace may be observed during the same time on the Likiep-Wotho path. On neither path does the layer appear to be blanketing in terms of masking the *F* region returns or the return from the samarium cloud on the Rongelap path. But that does not preclude the possibility that the path to the samarium cloud from Likiep, which is significantly different than the direct paths to both the *F* and *E* regions, may have been partially or wholly obscured by local sporadic *E* at the lower frequencies consistent with the lack of power observed below 6 MHz on the night of 1 May.

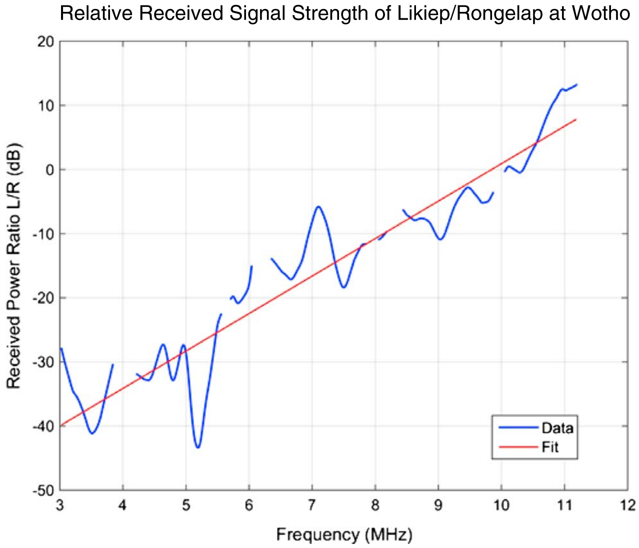

Figure 10. HF power received at Wotho from Likiep relative to Rongelap as a function of signal frequency (Likiep/Rongelap). The straight line shows a linear fit of the data. The received power from Rongelap was considerably higher at low frequencies.

The severity of the effect may have been exacerbated by the reduced received power at low frequencies on the Likiep-Wotho path relative to the Rongelap-Wotho path. HF transmissions at Likiep were weaker overall than those from Rongelap and considerably weaker at frequencies below 8 MHz. In fact, between 2 and 6 MHz the observed average signal strengths at Wotho were more than 20 dB below the corresponding signals from Rongelap, as shown in Figure 10. The curve in the figure shows the ratio of power from Likiep/Rongelap as a function of frequency and was derived from averaging 10 scans during different quiet periods characterized by an absence of spread *F* and low *E* region density. A straight line fit to the data is also plotted to demonstrate the trend of the frequency dependence. Differences in path length between the two sites account for some of the observed SNR differences, approximately 6 and 2.5 dB for *E* and *F* region paths, respectively. A more significant contribution to the disparity may result from the transmit antenna installations at the two sites. The antenna at Rongelap was mounted on a tower some 18 m above ground, while the Likiep antenna was suspended from trees at a height of just 4 m. Although we do not have sufficient details to calculate the exact differences in gain at the two sites, it is well known that the impedance of a dipole antenna changes dramatically as the installation height decreases below one-fourth wavelength (see, e.g., *ARRL Antenna Handbook* [*American Radio Relay League*, 1974]); the resulting impedance mismatch greatly reduces the radiation efficiency of the antenna. The 18 m height of the antenna at Rongelap corresponds to one-fourth wavelength at about 4.2 MHz; the 4 m high antenna at Likiep would transmit much less efficiently at this frequency, though the relative response would be expected to improve rapidly as the frequency increases, as has been observed. Similarly, one would expect the masking efficiency of Es to decrease as the transmitted frequency increases. Thus, we believe that a combination of factors including path length, antenna efficiency, and Es masking effectiveness was responsible for the absence of lower frequency signals scattered by the samarium cloud from Likiep on the evening of 1 May. Of course, differences in the path lengths and antenna efficiencies were common to all the observations, while sporadic *E* was present only during the first release. However, the reduced signal strengths imposed by the common propagation factors from Likiep mean that relatively modest Es masking is needed to explain the observations.

A high-density plasmasphere placed in a low-density plasma background behaves as a divergent lens for radio waves; the signals will always be refracted away from the center. Figure 11 (top) shows such a simulated sphere, while Figure 11 (bottom) displays the relative signal strength for an 8 MHz plane wave traveling from left to right in the figure. The propagation results, derived from a wave-optics calculation [*Hocke and Igarashi*, 2003], show clearly how the power diverges as the wave propagates through the sphere. In this scenario it is plausible that the power from waves below 8 MHz was refracted off axis passing through the samarium cloud and was not received along the great circle path at Wotho; signals at higher frequencies would suffer less refraction and could thus reach Wotho. Meanwhile, the same plasma cloud could refract (or scatter) energy through acute angles such that signals from Rongelap were observed far off the great circle path, consistent with the actual observations. A detailed analysis of the cloud and geometry for the MOSC releases was performed. The results show that the region where refractive effects would be most effective in creating a signal void ("shadow") lies beyond Wotho. Indeed, the ray tracing results shown in Figure 9d specifically predict a signature at the lower frequencies where none is observed. Although it is treated as a sphere in our

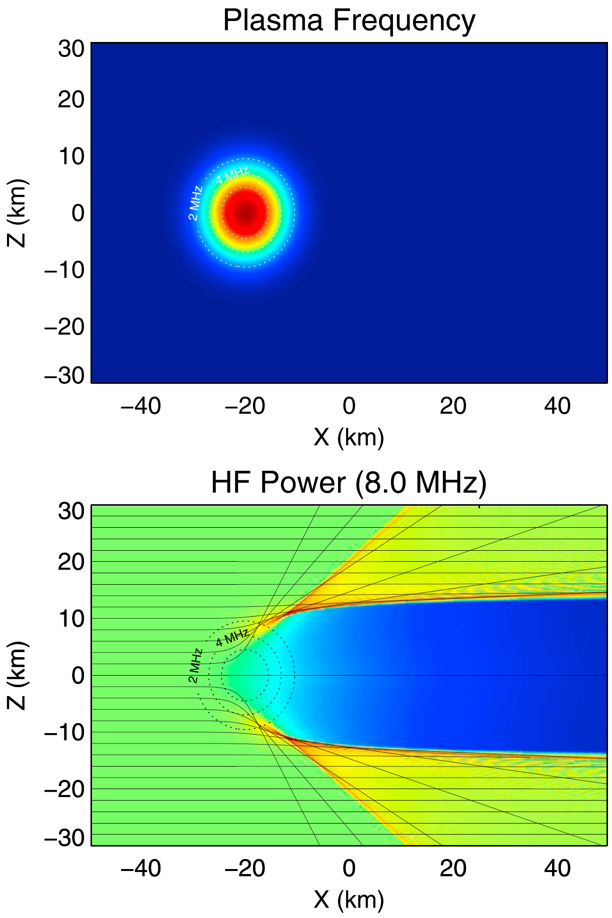

Figure 11. (top) Background environment and plasma distribution for a spherical artificial cloud. (bottom) Wave-optical calculation for 8 MHz radio wave propagation through the artificial cloud.

model, the actual shape and density distribution of the cloud determine the detailed HF propagation effects. Some elongation along the magnetic field is expected, even at early times, and the true shape undoubtedly differs from our simple model. Interestingly, the divergent effects of the cloud would be expected to persist much longer than the effects visible on the oblique ionograms shown in Figures 3 and 4. The divergence effect requires only small refraction angles along the direction of propagation, while large refraction angles are required to generate traces directly from the artificial plasma cloud. Thus, even signals at frequencies well above the maximum plasma frequency in the cloud will experience some level of divergence as they pass through.

5. Conclusions

The results presented here account for the features of the modified HF propagation environment observed at early times during the MOSC samarium release experiments. We have shown that ray tracing techniques may be used to model the disturbances caused by artificial ionospheric modification. The samarium plasma clouds created at least three additional HF propagation paths in the ionosphere. One path is directly from the transmitter to the cloud to the receiver, while two others involve propagation between the *F* region and the cloud: in one case interacting with the cloud first, reflecting off the *F* region to the receiver, and in the other reflecting from the *F* region first and then reaching the receiver antenna by refraction from the cloud. These effects were observed both on a great circle path and a markedly nongreat circle path where the refraction angle exceeds 90°. Additionally, a dropout in the lower portion of the HF band was observed on the great circle path between Likiep and Wotho minutes after the first release. An analysis of several potential causes reveals that the most probable explanation is masking due to sporadic *E* which is exacerbated by the greater distance from Likiep to Wotho and the lower transmitted signal power relative to Rongelap.

For modeling the background plasma, when constrained by ALTAIR radar electron density profiles, the Parameterized Ionospheric Model (PIM) provided an excellent representation of the low-latitude ionosphere during quiet conditions. Not surprisingly, neither PIM nor IRI was able to accurately specify local gradients during a modest magnetic disturbance. However, IRI's flexibility and convenient access to parameters within the model supported the use of a minimization technique for constructing a valid regional ionosphere. Ray-tracing confirms the sounder observations to a high degree of fidelity. Changes in the natural propagation environment can thus be successfully modeled, and the effects from arbitrary artificial plasma environments can be predicted with accuracy. Finally, though not observed directly in these measurements, modeling predicts that the samarium cloud will behave like a divergent lens resulting in “HF voids” or shadow zones where the HF signal is excluded downstream from the sphere. For the geometry in the present experiment the shadow zones are predicted to lie beyond the range of the most distant receiver site, but such effects could readily be characterized in future experiments.

Acknowledgments

The authors from the Boston College Institute for Scientific Research gratefully acknowledge support through the Naval Postgraduate School from the National Consortium for Measurement and Signature Intelligence (MASINT) Research Program award N00244-12-1-0049. We would also like to acknowledge the valuable contributions of the reviewers to this manuscript, specifically in regard to the role of sporadic *E* in interpreting the propagation results (reviewer #2). We would like to thank the U.S. Department of Defense Space Test Program for their support in providing the launch vehicles and launch support for the MOSC payloads. Requests for access to data collected during the MOSC experiment will be processed on a case-by-case basis pursuant to official Air Force Research Laboratory policy for public release of information.

References

American Radio Relay League (1974), *The ARRL Antenna Handbook*, 13th ed., edited by G. Hall, pp. 49–57, American Radio Relay League, Newington, Conn.

Bedinger, J. F., E. R. Manring, and S. N. Ghosh (1958), Study of sodium vapor ejected into the upper atmosphere, *J. Geophys. Res.*, *63*(1), 19–29, doi:10.1029/JZ063i001p0019.

Bernhardt, P. A. (1987), A critical comparison of ionospheric depletion chemicals, *J. Geophys. Res.*, *92*(A5), 4617–4628, doi:10.1029/JA092iA05p04617.

Bernhardt, P. A., et al. (2012), Ground and space-based measurement of rocket engine burns in the ionosphere, *IEEE Trans. Plasma Sci.*, *40*, 1267–1286, doi:10.1109/TPS.2012.2185814.

Bilitza, D., D. Altadill, Y. Zhang, C. Mertens, V. Truhlik, P. Richards, L.-A. McKinnell, and B. Reinisch (2014), The International Reference Ionosphere 2012—A model of international collaboration, *J. Space Weather Space Clim.*, *4*, A07, doi:10.1051/swsc/2014004.

Caton, R. G., et al. (2017), Artificial ionospheric modification—The Metal Oxide Space Cloud experiment, *Radio Sci.*, *52*, doi:10.1002/2016RS005988.

Cervera, M. A., and T. J. Harris (2014), Modeling ionospheric disturbance features in quasi-vertically incident ionograms using 3-D magnetoionic ray tracing and atmospheric gravity waves, *J. Geophys. Res. Space Physics*, *119*, 431–440, doi:10.1002/2013JA019247.

Coleman, C. J. (1993), A general purpose ionospheric ray tracing procedure, Tech. Rep., SRL-0131-TR, Defence Science Technology Organization, Adelaide, Australia.

Corliss, W. R. (1971), NASA sounding rockets, 1958–1968: A historical summary, Tech. Rep. NASA SP- 4401, National Aeronautics and Space Administration, Washington, D. C.

Davies, K. (1990), *Ionospheric Radio*, pp. 143–146, Peter Peregrinus, London, U. K.

Davis, T. N. (1979), Chemical releases in the ionosphere, *Rep. Prog. Phys.*, *42*, 1565, doi:10.1088/0034-4885/42/9/003.

Daniell, R. E., Jr., L. D. Brown, D. N. Anderson, M. W. Fox, P. H. Doherty, D. T. Decker, J. J. Sojka, and R. W. Schunk (1995), Parameterized ionospheric model: A global ionospheric parameterization based on first principles models, *Radio Sci.*, *30*(5), 1499–1510, doi:10.1029/95RS01826.

Haselgrove, J. (1955), Ray theory and a new method for raytracing, in *Physics of the Ionosphere*, pp. 355–364, Physical Society, London.

Hocke, K., and K. Igarashi (2003), Wave-optical simulation of the oblique HF radio field, *Radio Sci.*, *38*(3), 1039, doi:10.1029/2002RS002691.

Hu, Y., Z. Zhao, and Y. Zhang (2011), Ionospheric disturbances produced by chemical releases and the resultant effects on short-wave ionospheric propagation, *J. Geophys. Res.*, *116*, A07307, doi:10.1029/2011JA016438.

Jones, R. M., and J. J. Stephenson (1975), A versatile three-dimensional ray tracing computer program for radio waves in the ionosphere, NASA STI/Recon Tech. Rep., 76, 25,476, U.S. Dep. of Commer., Off. of Telecommun., Washington, D. C.

Nelder, J., and R. Mead (1965), A simplex method for function minimization, *Comput. J.*, *7*, 749–756, doi:10.1093/comjnl/7.4.308.

Pedersen, T. R., R. G. Caton, D. Miller, J. M. Holmes, K. M. Groves, and E. Sutton (2017), Empirical modeling of plasma clouds produced by the Metal Oxide Space Clouds experiment, *Radio Sci.*, *52*, doi:10.1002/2016RS006079.

Press, W. H., S. A. Teukolsky, W. T. Vetterling, and B. P. Flannery (2007), *Numerical Recipes 3rd Edition: The Art of Scientific Computing*, pp. 487–555, Cambridge Univ. Press, New York.

Rosenberg, N. W. (1963), Chemical releases in the upper atmosphere (Project Firefly), a summary report, *J. Geophys. Res.*, *68*(10), 3057–3063, doi:10.1029/JZ068i010p03057.

Shuman, N. S., D. E. Hunton, and A. A. Viggiano (2015), Ambient and modified atmospheric ion chemistry: From top to bottom, *Chem. Rev.*, *115*(10), 4542–4570, doi:10.1021/cr5003479.

Wand, R. H., and M. Mendillo (1984), Incoherent scatter observations of an artificially modified ionosphere, *J. Geophys. Res.*, *89*(A1), 203–215, doi:10.1029/JA089iA01p00203.

Zawdie, K. A., D. P. Drob, J. D. Huba, and C. Coker (2016), Effect of time-dependent 3-D electron density gradients on high angle of incidence HF radio wave propagation, *Radio Sci.*, *51*, 1131–1141, doi:10.1002/2015RS005843.